THE STEADY-STATE AND DYNAMIC PERFORMANCE OF GAS LUBRICATED UNIFORM FILM POROUS THRUST BEARINGS

by

ROY TAYLOR

A thesis submitted for the degree of Doctor of Philosophy at the University of Aston in Birmingham

March 1975

SUMMARY

Air lubricated externally pressurised thrust bearings are commonly used in industry since, even at slow speeds, they have exceedingly low frictional coefficients.

Conventional capillary or orifice compensated bearings have, however, low load capacities for the high supply pressures and feed rates required and their operating range is often limited by pneumatic instability of the air film. These disadvantages may be overcome by using a porous pad in place of the combination of a solid pad and compensating element, ensuring greater positional accuracy and a smaller tendancy to fail through blockage.

The present investigation is concerned with methods of predicting the steady-state and dynamic performance characteristics of a uniform film porous thrust bearing. Analytic predictions are made, based on the laminar flow through the bearing of a perfect gas.

A series solution of the pressure distribution throughout the porous pad and air film is presented for the steady operation of the bearing. The performance characteristics are presented in design curves for a range of bearing aspect ratio and supply pressure. The complexities involved in the time dependent situation prevent an analytic solution. In order to obtain theoretical predictions of the bearing dynamic character-

istics a complex numerical technique was developed. Theoretical predictions are based on the assumption that the bearing can be modelled as a linear dynamic system.

The design of a porous thrust test bearing and associated equipment as described. The experimental results for steady operation are presented as dimensionless performance characteristics as represented by load capacity and mass flow rate. Good agreement is obtained with predictions from the analysis. The experimental results for the forced vibration tests are presented as dimensionless performance characteristics as represented by dynamic spring force and damping force and it is found that the simple linear model breaks down for large amplitudes of vibration.

ACKNOWLEDGEMENTS

The author wishes to express his gratitude to the Senate of the University of Aston in Birmingham for permission to work for this degree.

Thanks are offered to the Special Projects Division of the National Engineering Laboratory for the sponsoring of this research programme. Special thanks are offered to Mr. J. Kerr of this Division whose constructive criticism led to many improvements of the experimental techniques.

Thanks are also extended to Professor A. J. Ede, Head of the Department for the use of the facilities of the Mechanical Engineering Department. Special thanks are offered to Professor E. Downham for his help and for the loan of valuable equipment.

Sincere thanks are offered to Dr. G. K. Lewis and Mr. J. Reed for their constant encouragement in their capacity as Supervisors.

Many improvements in the experimental approach arose from stimulating and fruitful discussion with Dr. J. Penny and Messrs. Kinsman, Schooler and Stanojevic; I thank them.

The author wishes to extend his gratitude to the late Mr. E. Denchfield, Mr. G. Rickers, Head Technician and his staff for their help in the acquisition and manufacture of components; in particular Messrs. Pizey,

Pratt and Smith for their assistance in the manufacture and development of apparatus.

My profound thanks are given to my wife for her constant help and encouragement during the course of this investigation.

CONTENTS

APPENDICES

FIGURES

Figure No. Page

LIST OF PLATES

NOMENCLATURE

A	Flow area
A'	Load parameter perturbation defined by equation 7.3.10
A_b	Coefficient, defined in equation 2.2.10
A_o	Steady-state load parameter defined by equation 7.3.12
A_1, A_2	Constants of Integration
A_3, A_4, A_5	Coefficients, defined in equation A.2.15
A_7	Constant of Integration
aij,aiJ,aji	Two dimensional arrays used in the time dependent solution
a_n	Coefficients of a polynomial (n = 1,2,3,...)
$\hat{a}$	Acceleration amplitude for forced vibration
$\hat{a}_r$	Resonance acceleration amplitude
a_o	$= 2 \overline{P}_o$
a_1	Coefficient, defined in equation 2.2.3
a_2	Coefficient, defined in equation 2.2.4
a_3	Coefficient, defined in equation 2.2.5
a_4	Coefficient, defined in equation 2.2.6
a_5	Coefficient, defined in equation 2.2.7
a_6	Coefficient, defined in equation 2.2.13
B, B_1, B_2	Constants of Integration
B_3, B_4, B_5	Coefficients, defined in equation A.3.12
bij,biJ,bji	Two dimensional arrays used in the time time dependent solution

b_n	Coefficients of a polynomial (n = 1,2,3,...)
b_1	Coefficient, defined in equation 2.2.3
b_2	Coefficient, defined in equation 2.2.4
b_3	Coefficient, defined in equation 2.2.5
b_4	Coefficient, defined in equation 2.2.13
C	Viscous damping coefficient
C_c	Critical damping coefficient
C_{n2}	Coeficients, (n = 2,3,4,...)
C_2	Constant defined by equation 3.3.10
c_n	Coefficient of a polynomial (n = 0,1,2,...)
c_2	Coefficient, defined in equation 2.2.4
c_3	Coefficient, defined in equation 2.2.5
D_f	Dimensionless dynamic damping force
$[D_i]_j, [D_i]_J$ $[D_j]_i, [D_J]_i$	Two dimensional arrays used in time dependent solution
D_1, D_2	Constants of integration
d_h	Pressure drop across the filter bed
d_1	Diameter factor for porous material
d_2	Constant, defined in equation 2.2.10
$[E_i]_j, [E_i]_J$ $[E_j]_i, [E_J]_i$	Two dimensional arrays used in the time dependent solution
E_n	Coefficients, (n = 2,3,4,...)
E_1, E_2, E_3	Coefficients, defined in equation A.5.15
e_n	Coefficients of a polynomial (n = 0,1,2,...)
$[F_i]_j, [F_i]_J$ $[F_j]_i$	Two dimensional arrays used in the time dependent solution

F_o	Amplitude of applied vibrational force
F_1, F_2	Coefficients, defined in equation A.4.24
F_3	Constant of Integration
F_4	Coefficient, defined in equation A.2.8
F_5, F_6	Coefficients, defined in equation A.2.9
F_7, F_8	Coefficients, defined in equation A.2.10
f, f_1, f_2, f_3	Functions
f_n	Coefficients of a polynomial (n=1,2,3...)
$[G_i]_j, [G_i]_J$	Two dimensional arrays used in the time
$[G_j]_i, [G_J]_i$	dependent solution
G_1, G_2	Coefficients, defined in equation A.2.11
gij, giJ, gji	Two dimensional arrays used in the time dependent solution
g_n	Coefficients of a polynomial (n=1,2,3,...)
H	Porous pad thickness
h	Air film thickness
h_b	Height of filter bed
h_d	Derived film thickness
h_m	Measured bearing lift
h_o	Steady-state film thickness
h'	Perturbation about steady-state film thickness
$\dot{h}'$	First derivative of h' with respect to time
$\ddot{h}'$	Second derivative of h' with respect to time
$\dddot{h}'$	Third derivative of h' with respect to time
I	Maximum value of i

i	Numerical counter in radial direction
J	Maximum value of j
J_o	Bessel Function of the first kind of order zero
J_1	Bessel Function of the first kind of order unity
j	Numerical counter in the axial direction
K	Viscous permeability ratio = Φ_r/Φ_y
K_f	Dimensionless dynamic spring force
K_o	Bessel Function of the second kind of order zero
K_1	Darcy's coefficient
K_2	Ratio of Inertia permeabilities = ϕ_r/ϕ_y
K_3	Dynamic spring stiffness
k	Constant of integration
k_c	Capillary coefficient
k_n	Roots of the equation $J_1(k_n) = 0$ $(n = 2,3,4,\ldots)$
l, l_1, l_2	Exponential powers
M	Mass flow rate
$\overline{M}$	Dimensionless mass flow rate $= \dfrac{2M\eta RTH}{\pi r_o^2 (p_s^2 - p_a^2)\Phi_y}$
$\overline{M}_c$	Dimensionless mass flow rate through a circular step bearing = $\dfrac{2m_c \eta RT}{(p_s^2 - p_a^2) k_c}$
$\underline{M}$	Maximum value of m
m	Numerical counter in time
m_b	Mass of gas contained in porous bearing

m_b'	Time rate of change of m_b
m_c	Mass flow rate through a circular step bearing
m_f	Mass of gas contained in air film
m_{fr}	Mass flow rate in air film at radial position r
m_{fR}	Mass flow rate in air film at dimensionless radial position R
m_{in}	Mass inflow to bearing
m_{out}	Mass outflow from bearing
m_p	Mass of gas contained in porous pad
m_1	Mass flow through a capillary
m_2	Mass flow out of a circular step bearing
m_3	Coefficient, defined in equation 2.2.7
m_4	Vibrating mass
N	Maximum value of n
n	Numerical counter
p	$= \hat{a} / \hat{a}_r$
$\overline{P}$	Dimensionless pressure = p / p_a
$\overline{P}_f$	Dimensionless pressure force vector
$\overline{P}_f'$	Dimensionless film pressure perturbation
$\overline{P}_{film}$	Dimensionless steady-state film pressure
$\overline{P}_{fo}$	Dimensionless steady-state film pressure
$\overline{P}'$	Dimensionless pressure perturbation
$\overline{P}_m$	Finite value of pressure
$\overline{P}_o$	Dimensionless steady-state pressure
$\overline{P}_p$	Dimensionless port pressure for circular step bearing

$\overline{P}_{pad}$	Dimensionless pad pressure
$\overline{P}_s$	Dimensionless supply pressure
p	Pressure
p'	Perturbation about steady-state pressure
p_a	Atmospheric pressure
p_f	Pressure force vector
p_p	Port pressure forcircular step bearing
p_s	Supply pressure
p_1	Initial pressure in container A of porosity rig
p_2	Final pressure in container A of porosity rig
Q	Volumetric flow rate
Q_m	Volumetric flow rate at mean pressure
Q_r	Volumetric flow rate at radial position r
Q_R	Volumetric flow rate at dimensionless radial position R
R	Dimensionless radial position
Re	Reynolds number for porous media
Rel	Relaxation parameter
R_p	Dimensionless port radius for circular step bearing
R	Gas constant
r	Radial position
r_p	Port radius for circular step bearing
r_o	Outer radius of bearing
r_1, r_2, r_3	Coefficients, defined in equation 2.2.10
S	Porous pad aspect ratio = H/r_o

SF	Mean pneumatic clearance
T	Absolute temperature of gas
$\overline{T}$	Dimensionless time
t	Time
U	Gas velocity in radial direction
U_c	Gas velocity of flow through circular step bearing
V_A	Volume of container A of porosity rig
V_B	Volume of container B of porosity rig
V_p	Volume of intercommunicative pores in porous specimen
V_s	Volume of porous specimen
v	Gas velocity in axial direction
W	Bearing load
$\overline{W}$	Dimensionless bearing load = $W/\pi r_o^2(p_s-p_a)$
W_c	Bearing load for circular step bearing
$\overline{W}_c$	Dimensionless bearing load for circular step bearing = $W_c/\pi r_o^2(p_s-p_a)$
w	Gas velocity in angular direction
X	Static stiffness
$\overline{X}$	Dimensionless static stiffness $= \frac{Xh_o(h_o^2+6\Phi_r)}{\pi r_o^2(p_s-p_a)(h_o^2+2\Phi_r)}$
X_c	Static stiffness of circular step bearing
$\overline{X}_c$	Dimensionless static stiffness of circular step bearing = $X_c h/\pi r_o^2(p_s-p_a)$
Y	Dimensionless axial position = y/H
y	Axial position

y_1	Axial movement of top plate of circular step bearing
Z	Differentiable parameter
Z_1, Z_2, Z_3, Z_4	Coefficients, defined in equation 7.3.27
z_1, z_2	Constants of integration
α	Frequency factor = $H^2 \eta P^* \omega / \Phi_y p_a$
α_1	Dimensionless parameter = $2H\Phi_y P^* \omega p_a / \phi_y \eta R T$
α_2	Dimensionless parameter = $2\Phi_r{}^2 p_a{}^2 / \phi_r \eta^2 R T r_o$
α_3	Dimensionless parameter = $6 r_o \eta^2 \phi_r R T / h^2 \Phi_r p_a{}^2$
α_4	Dimensionless parameter = $2 r_o K \alpha_3 / h K_1$
β	Frequency factor = $12 r_o{}^2 \eta \omega / (h^2 + 6\Phi_r) p_a$
β_1	Dimensionless parameter = $12 r_o{}^2 \eta \omega / h^2 p_a$
γ	Velocity factor = $24 r_o{}^2 \eta \frac{dh}{dt} / h(h^2 + 6\Phi_r) p_a$
γ_1	Dimensionless parameter = $24 r_o{}^2 \eta \frac{dh}{dt} / h^3 p_a$
Δm_p	Mass content of elemental portion of porous pad
$(\Delta p)_y$	Finite pressure gradient in axial direction
Δ_r	Finite step in radial direction
Δ_t	Finite step in time
Δ_x	Finite step in x

Δ_y	Finite step in axial direction
δ	$= \Delta / \Delta_t$
Σ_{ij}^m	Error in calculation of ϕ_{ij}^m in time dependent numerical solution
η	Lubricant viscosity
θ	Angular position
Λ	Dimensionless bearing number $= 12\Phi_y r_o^2 / Hh(h^2+6\Phi_r)$
Λ_c	Dimensionless bearing number for circular step bearing $= 12k_c/\pi h^3$
λ	Constant of integration
λ_f	Friction factor
λ_n	Dimensionless parameter $= S.k_n.K^{\frac{1}{2}}$
μ	Multiplier in Roscoe technique
ν	Coefficient, defined in equation A.2.5
ξ	$= C/C_c$
ρ	Density of lubricant
ρ_m	Density of lubricant at mean pressure
σ	Perturbation about steady-state film thickness
τ	Phase angle between dimensionless pressure force vector and the film thickness vector
Φ	Viscous permeability
Φ_r	Viscous permeability in radial direction
Φ_y	Viscous permeability in axial direction
Φ_θ	Viscous permeability in angular direction

ϕ	$\overline{P}^2$
ϕ_{ij}^m	$\overline{P}^2$ at numerical grid point i, j, m
$[\phi_{ij}^m]$	Initiated value of ϕ_{ij}^m in numerical method
$[\phi_{ij}^m]_T$	True value of ϕ_{ij}^m
ϕ_r	Inertia permeability in radial direction
ϕ_y	Inertia permeability in axial direction
Ω	$= \omega / \omega_r$
ω	Frequency of oscillation
ω_n	Natural frequency
ω_r	Resonant frequency
P*	Porosity of Porous material (inter-communicative)

CHAPTER ONE

INTRODUCTION TO THE INVESTIGATION

1.1 DEFINITION OF AN EXTERNALLY PRESSURISED POROUS BEARING

An externally pressurised bearing consists of two or more surfaces, moving or stationary, between which a viscous fluid, the lubricant, is fed under pressure. The lubricant is pressurised at an external source and then fed into the clearance space between these surfaces, generally through a flow restrictor. This flow restrictor ensures that an excess lubricant flow does not occur when the bearing is unloaded i.e. when the bearing flow resistance becomes zero. The purpose of such a bearing is to support a given load with low frictional resistance, even at conditions unsuited for hydrodynamic action and/or to maintain a high resistance to displacement of the bearing surfaces. These bearings are often referred to as 'Hydrostatic bearings', or if the lubricant is air, as 'Aerostatic bearings'.

The externally pressurised porous bearing is an externally pressurised bearing in which the bearing surface containing the flow restrictor has been replaced by a surface that is partially or wholly porous. The lubricant is then fed through this porous section which acts as a flow restrictor.

Throughout this work the term 'externally pressurised' will be used rather than 'hydrostatic' or 'aerostatic'.

1.2 THE ADVANTAGE OF USING A POROUS RESTRICTOR IN AN EXTERNALLY PRESSURISED BEARING

Externally pressurised gas lubricated bearings are commonly used in industry since they exhibit exceedingly low frictional coefficients, even at slow speeds, and are readily operated from the factory airline.

Conventional capillary or orifice compensated bearings have, however, low load capacities for the high supply pressures and feed rates required and their operating range is often limited by pneumatic instability.

Consider the circular step, capillary compensated thrust bearing shown in figure 1 page 3 . Over the ported region the pressure is uniform, for a deep port configuration, and through the fluid film region decays to ambient conditions at the outer radius of the region. The load capacity of this bearing is the summation of the pressure forces acting on the bearing top plate. By increasing the port diameter as shown in figure 2 page 4 the load capacity of this bearing must also increase as the port pressure is acting over an increased area. However, by increasing this diameter the pressure gradients in the fluid film are also increased and thus the lubricant flow rate is increased. Figures 3 and 4 pages 5 and 6 show the variation with port diameter of the theoretical

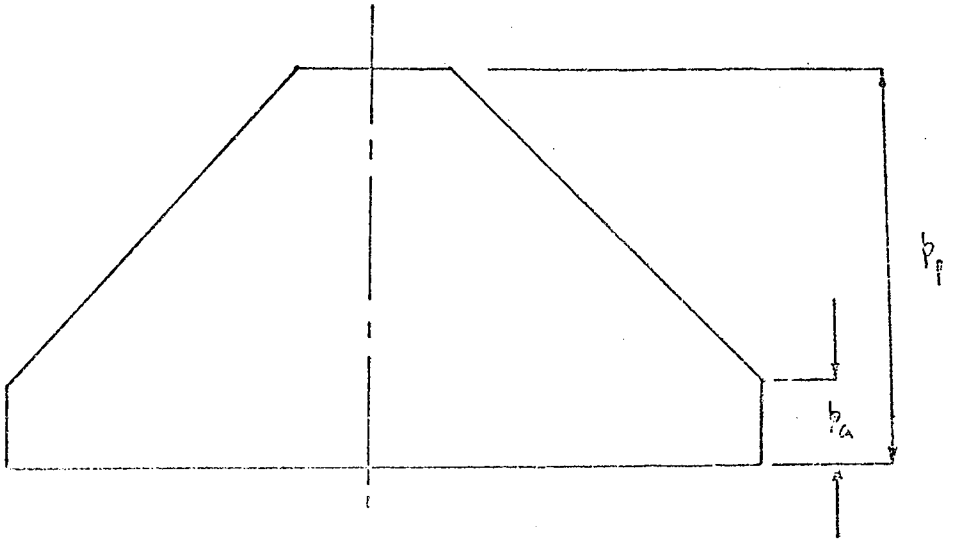

Pressure Profile (ideal)

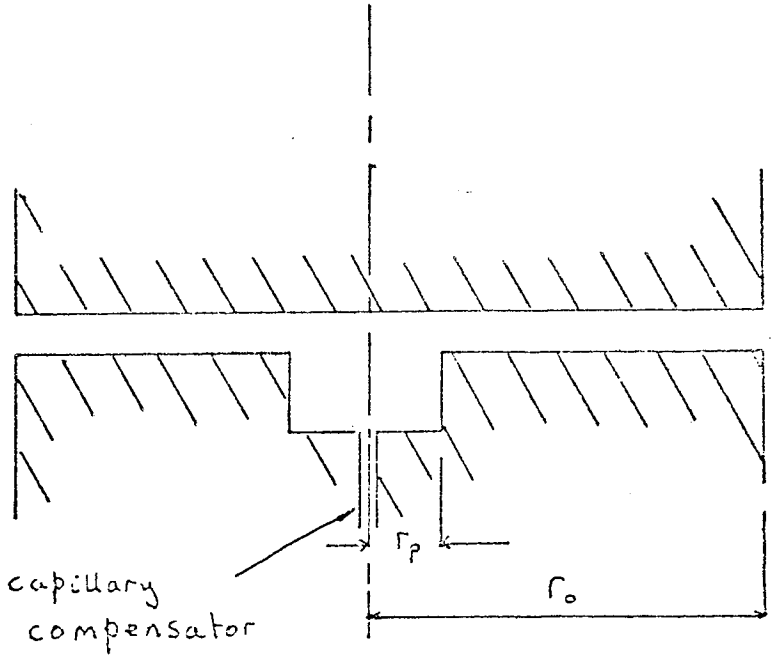

Figure 1 Circular Step Thrust Bearing
(small port)

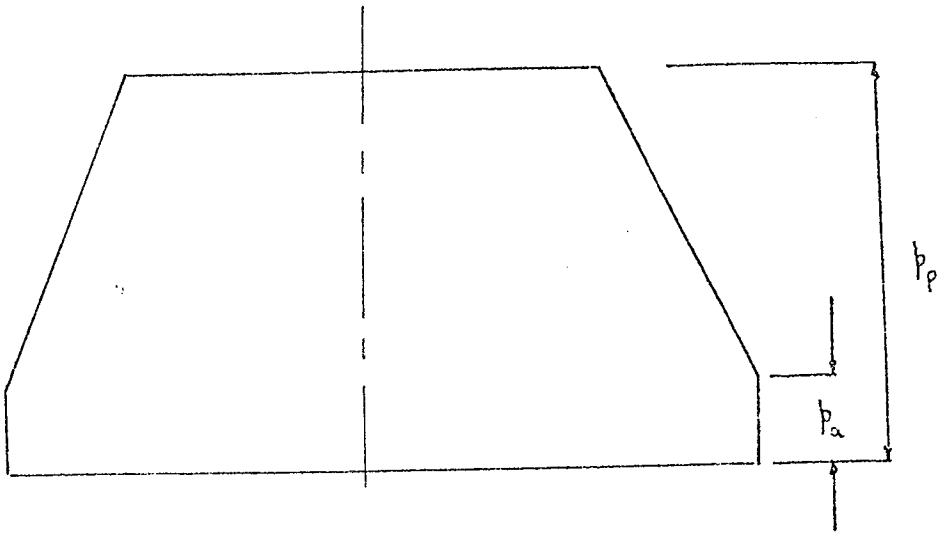

Pressure Profile (ideal)

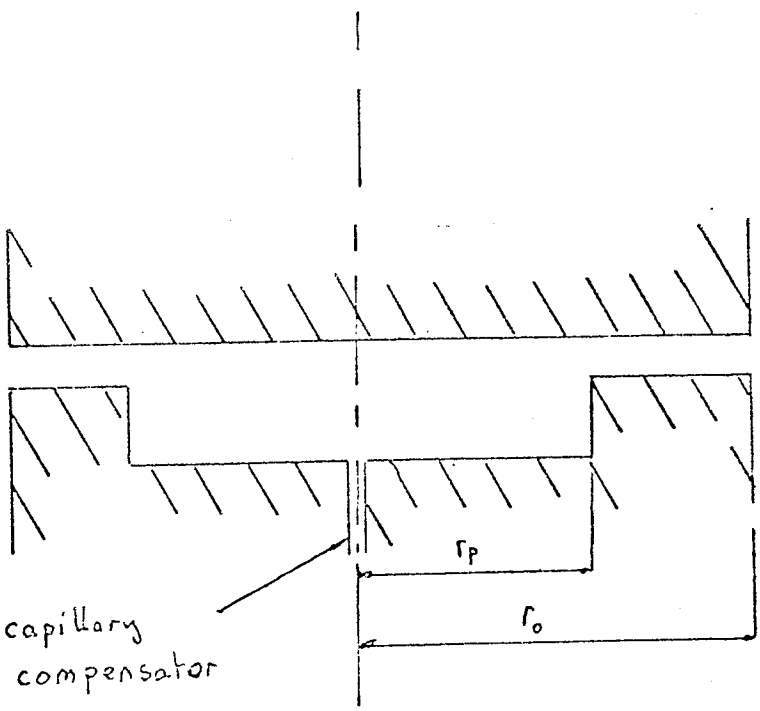

Figure 2 Circular Step Thrust Bearing
(large port)

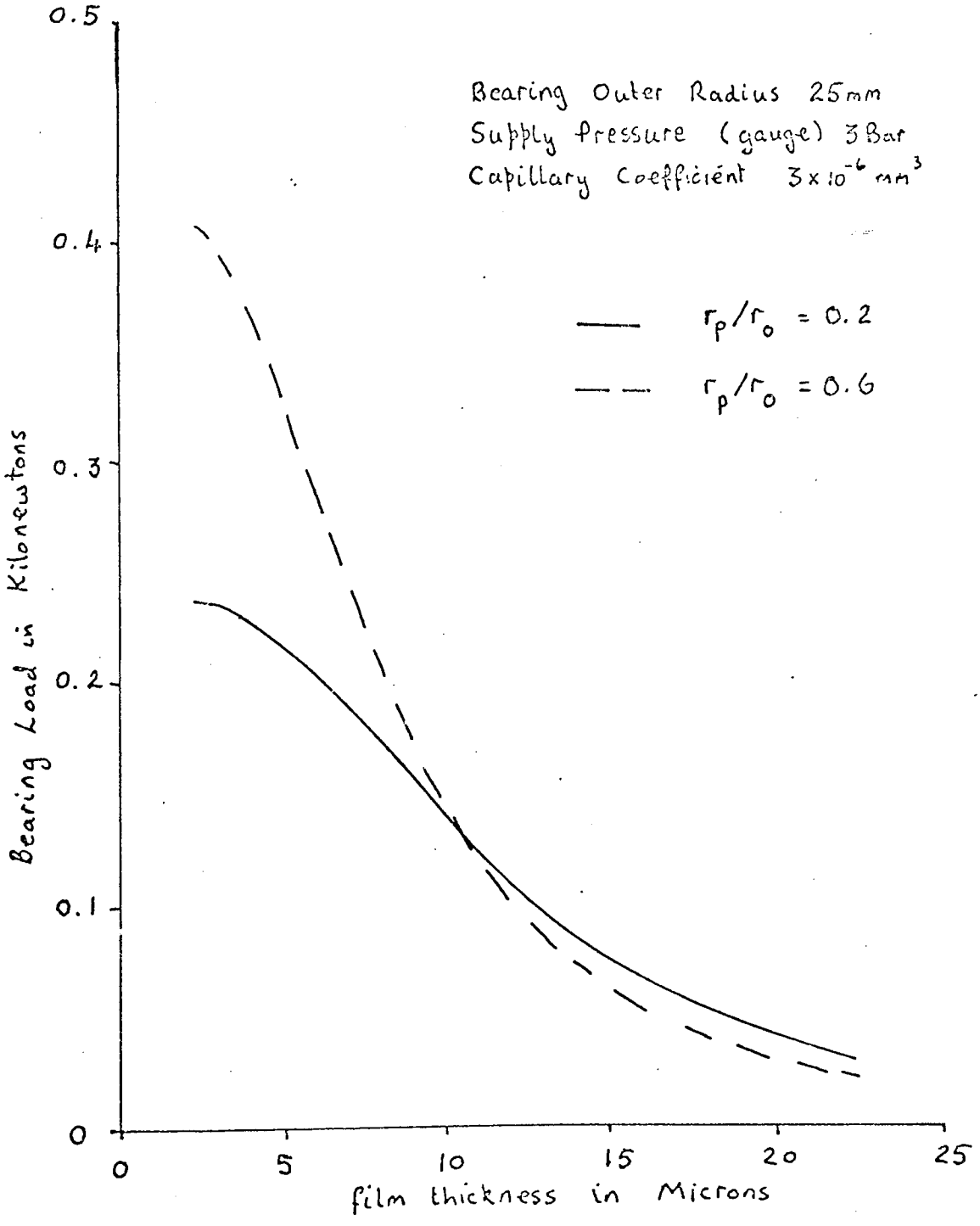

Figure 3 Variation of Bearing Load with Film Thickness for a Circular Step Thrust Bearing

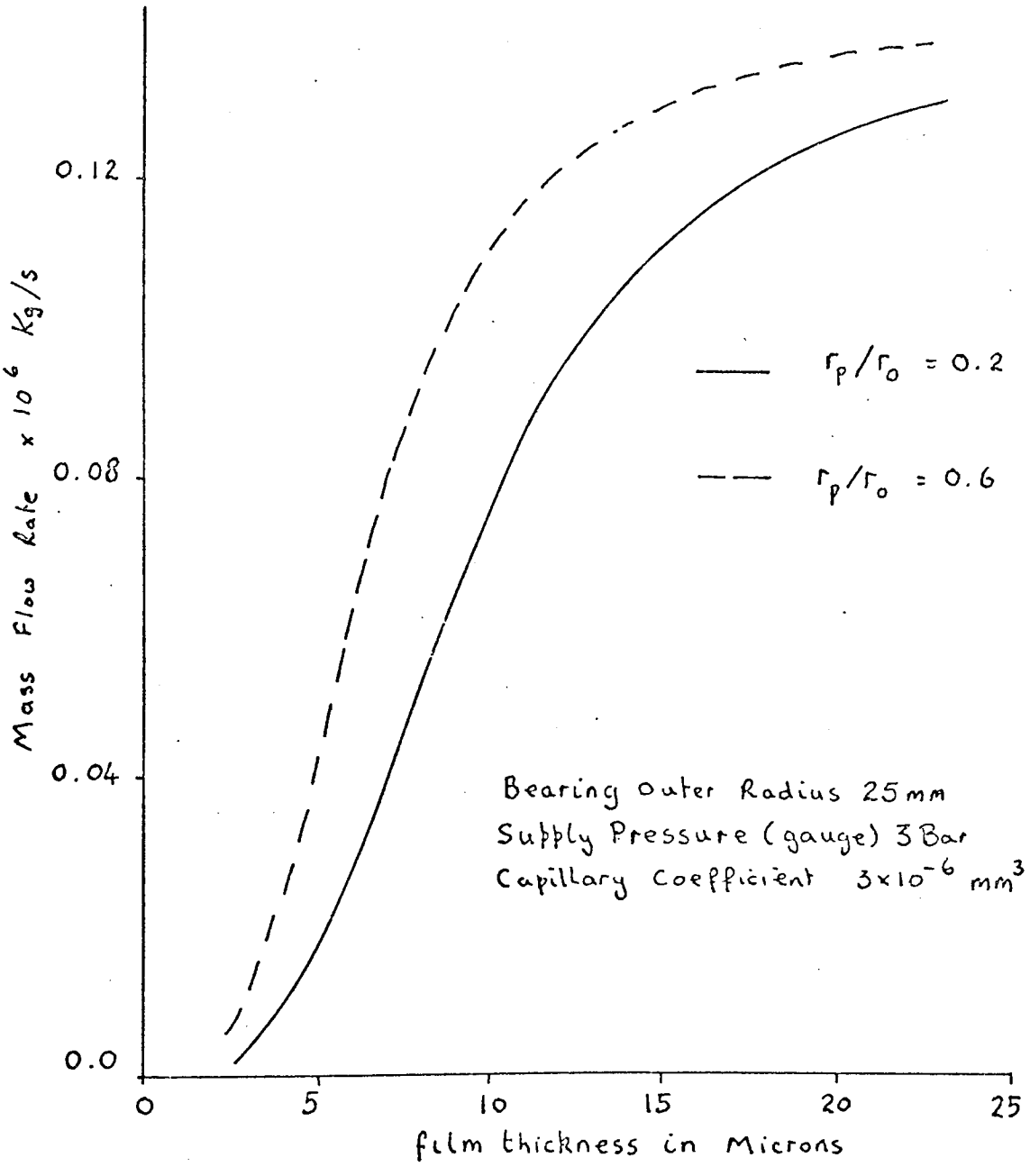

Figure 4 Variation of Mass Flow Rate with Film Thickness for a Circular Step Thrust Bearing

load capacity and lubricant mass flow rate respectively for this type of bearing when fed with air having a supply pressure of 3 Bar guage and a capillary coefficient of 300×10^{-9} mm^3 and a bearing outer radius of 25 mm for two port sizes. See appendix 1 for theory. If the load capacity is regarded as the important parameter then a large port is required and the corresponding increase in mass flow may be acceptable. There is, however, the stability of this bearing to be considered. The basic mechanism of instability can be described, Powell (1), with reference to figure 5 page 8 which shows a cross section through a circular step bearing. Under steady load conditions the mass flow through the capillary, m_1, is equal to the mass flow out of the bearing, m_2. If the upper plate is forced to execute vibrations about its equilibrium position as shown by the variation of y_1 with time, figure 5a page 8 , and if the condition $m_1 = m_2$ were to persist, then the resulting pressure change dp_p would be 180^o out of phase with y_1, as shown in figure 5c page 8 . This is analogous to a mass vibrating on a spring in the absence of damping. However, in practice two other effects are manifest which result in the flow into the pocket being possibly different to the flow out of the pocket at any instant.

Firstly the squeeze film effect influences the flow out of the pocket reducing the flow as the plate falls. The pressure changes arising from this effect

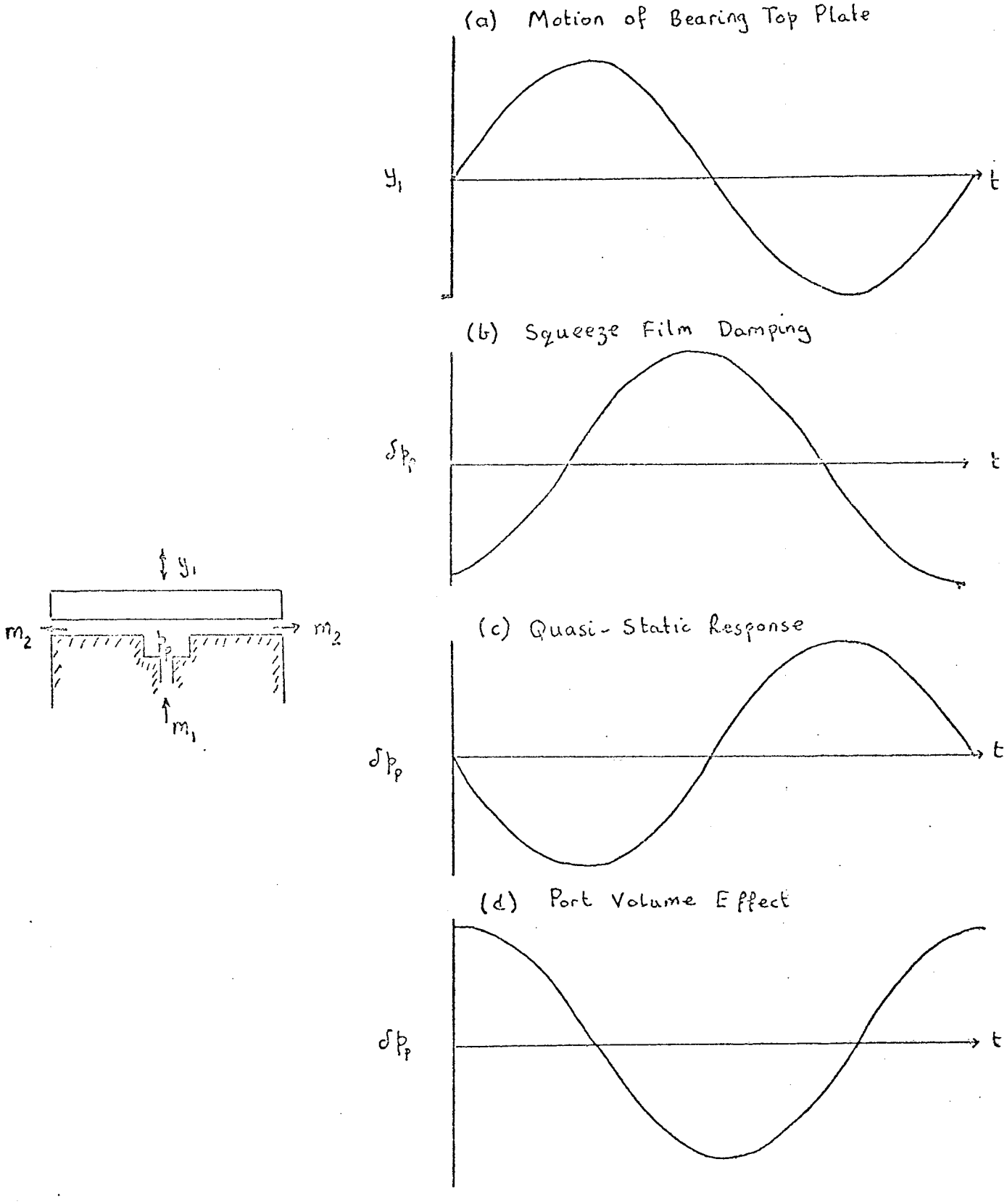

Figure 5 Pressure Effects that may lead to Pneumatic Instability in a Circular Step Thrust Bearing, (created by sinusoidal motion of the bearing top plate)

are proportional to the velocity of the upper plate and provide pure damping, as shown in figure 5b page 8

Secondly the finite volume of the pocket ensures that the pocket takes a finite time to fill and to empty. The pressure variations arising from this effect tend to lag behind the movement of the upper plate, as shown in figure 5d page 8.

If the pocket volume effect is greater than the squeeze film effect the net damping is negative and the bearing unstable. Many researchers have concerned themselves with this problem of instability, (2), (3), (4), (5), (6), (7). In summarizing the results of this previous research the following parameters or combinations of parameters should be treated as shown, in order to ensure stability: -

(a)	depth of ports	minimized
(b)	difference between supply and port pressures	
(c)	vibrating mass	
(d)	supply nozzle diameter	maximized
(e)	length (radial) of fluid-film	
(f)	area ratio of annular to port regions	

It can be seen that these recommendations tend to reduce the pocket volume effect and/or increase the squeeze film effect. The important conclusion is drawn that increasing the pocket diameter to increase the load

capacity can lead to an unstable bearing design.

How then can the port pressure be made to act over a large area without creating an unstable bearing? One method of achieving this is to fill the enlarged port, shown in figure 2 page 4 , with a porous material such that the port pressure is applied over the enlarged area and yet the volume of the port reduced. The lubricant when flowing through the porous material experiences a pressure drop due to the resistance to flow of the porous material. However, the pressure distribution in the bearing would appear to be superior to that of the stable ported bearing in that a greater pressure value is experienced at nearly all radial positions, see figure 6 page 11 . This then is the 'landed' porous pad bearing. The 'full faced' porous pad bearing is the logical extension of the design of a 'landed' porous pad bearing, achieving maximum distribution of the supply pressure.

N.B. It should be noted that as there is a resistance to flow through the porous material there is no further need for any other form of restrictor on the lubricant supply line, i.e. capillary or orifice compensation is unnecessary.

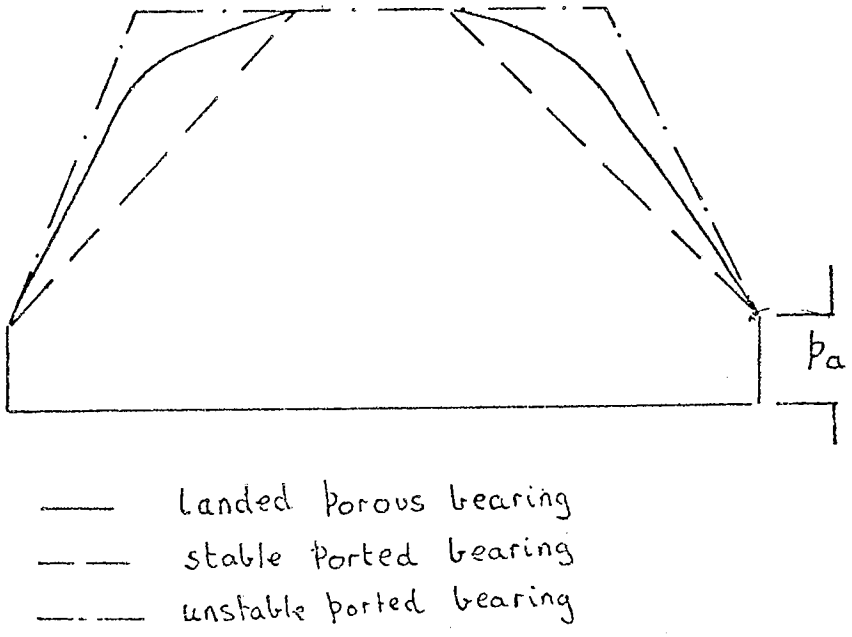

Figure 6 The Landed Porous Pad Bearing

1.3 THE PRINCIPAL OF STEADY OPERATION OF AN EXTERNALLY PRESSURISED POROUS BEARING

The principals of steady operation of an externally pressurised porous bearing can be readily understood by considering the simple case of a circular, full face, porous pad, thrust bearing as shown in figure 7, page 13 The lubricant flows from the supply source into the pressure chamber below the porous pad. The lubricant then flows axially into the porous pad over the whole of the pads lower surface and on through the porous material with a two dimensional flow pattern into the clearance space between the bearing top plate and the pad upper surface. In passing through the porous material the lubricant experiences a pressure drop due to the resistance to flow of the material. Having entered the clearance space between the pad upper surface and bearing top plate the lubricant then flows radially outwards, experiencing a further pressure drop due to the resistance to flow within this clearance space, to ambient conditions.

The load capacity of the bearing is the summation of the forces acting normal to the bearing top plate, i.e. the summation of the lubricant film pressure force and the ambient pressure force. The lubricant film pressure profile changes with load, however, a typical film pressure profile is also shown in figure 7 page 13.

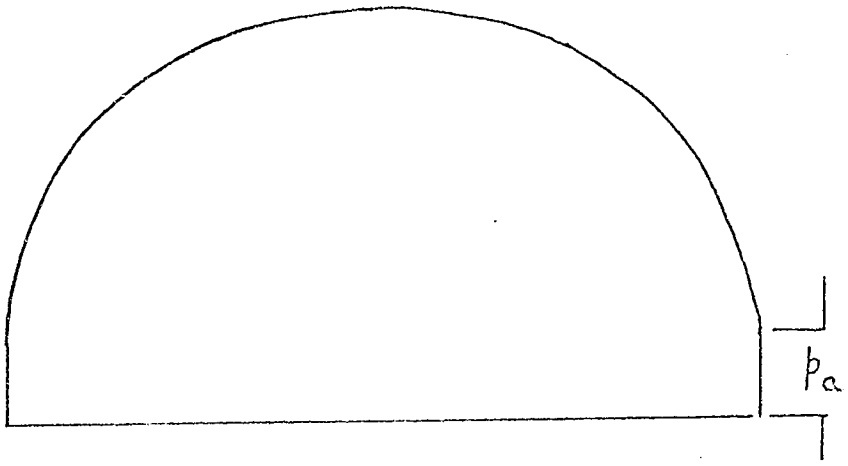

Pressure Profile

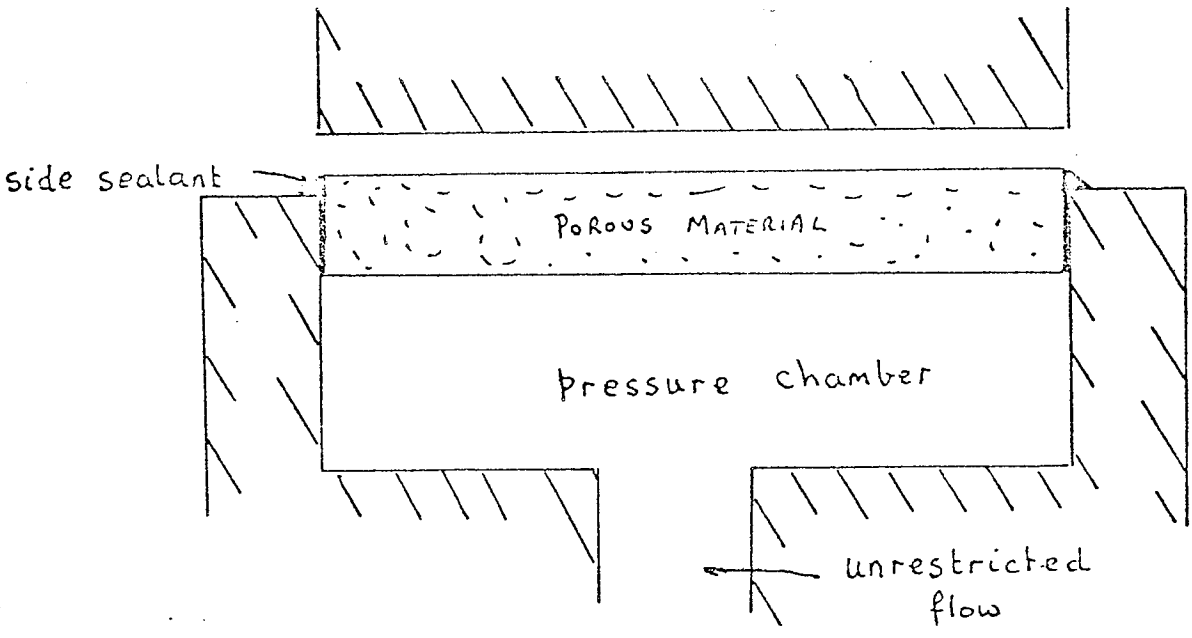

Figure 7 The Full Face Porous Pad Bearing

CHAPTER TWO

THE PROBLEM DEFINED

2.1 INTRODUCTION

The concept of an externally pressurised porous bearing is relatively new for literature has been published on this form of bearing only since 1955 whereas the externally pressurised bearing has been known since the Paris Industrial Exhibition of 1850. However, a considerable amount of literature has been published on externally pressurised porous bearings and there now arises the need for critically reviewing the information available to determine what gaps in the knowledge exist and/or if there is any conflict in this knowledge. For this reason a literature survey has been carried out and is presented in section 2.2. This survey begins with a discussion on flow through porous material.

Due to the vast amount of published literature that is available both on flow through porous material and externally pressurised bearings only a small selection of papers are reviewed. Having completed this survey of the literature the area of investigation can be determined. This is detailed in section 2.3.

2.2 A SURVEY OF THE PERTINENT LITERATURE

2.2.1 Laminar flow through porous materials

The theory of laminar flow through a homogeneous porous material is based on a classic experiment originally performed by Darcy (8), in which the pressure drop experienced by an incompressible fluid flowing through a homogeneous filter bed was studied. A schematic diagram of Darcy's apparatus is shown in figure 8 page 16 . By varying the quantities involved Darcy deduced the following relationship: -

$$Q = - \frac{k_1 . A . dh}{h_b} \qquad 2.2.1$$

where Q is the total volume of fluid flowing through the filter bed of height h_b in unit time, dh is the pressure drop across the filter bed and k_1 is a coefficient depending on the properties of the fluid and the porous material.

The original form of the Darcy law, equation 2.2.1 is rather restricted in its usefulness, in that the physical significance of the coefficient k_1 is undetermined. k_1 is obviously indicative of the permeability of a certain porous material to a particular fluid. A coefficient of the type k_1 is not very satisfactory as it would be preferred to separate the influence of the porous material

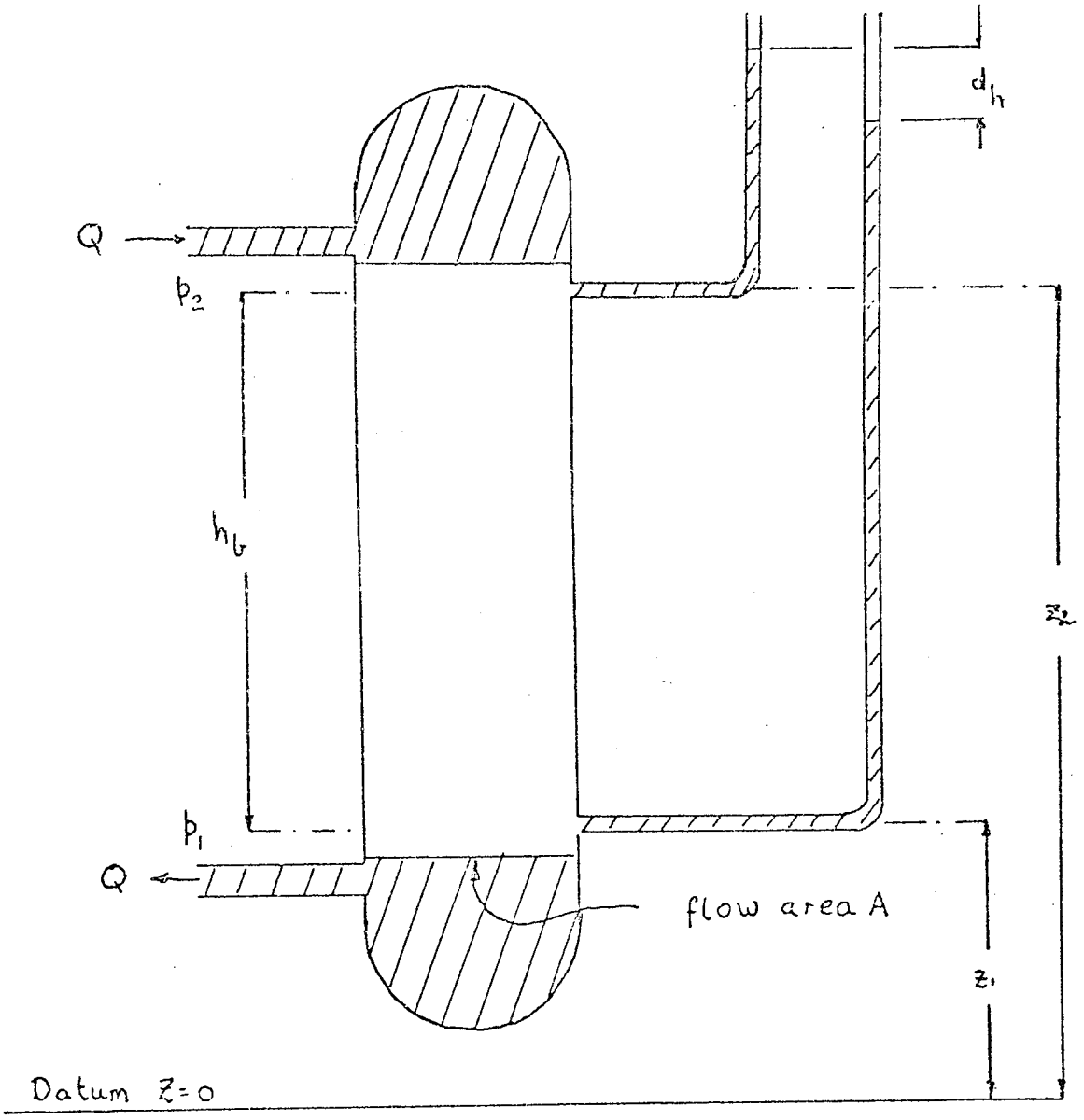

Figure 8 Schematic Diagram of Darcy's Filtration Equipment

from that of the fluid.

Nutting (9) stated that:

$$k_1 = \Phi/\eta \qquad 2.2.2$$

where η is the viscosity of the fluid and Φ the 'specific permeability' of the material. This relationship however, was not generally accepted until it was verified by Wyckoff et al (10).

The validity of Darcy's law has been tested on many occasions, e.g. Vibert (11), Iwanami (12), LeRosen (13) and Emmerich (14). However, it is known that for liquids at high velocities and for gases at very low and at very high velocities, Darcy's law becomes invalid.

2.2.2 Limitations of Darcy's Law, Excluding Inertia Flow Considerations

Deviations from Darcy's law have not only been observed at high flow rates, as would be expected by analogy with flow in pipes.

A category of such deviations is particularly found in the flow of gases. Fancher et al (15) observed that gas permeabilities were higher than liquid permeabilities in the same porous media when calculated from Darcy's law. Calhoun and Yuster (16) summarised these facts by stating that Darcy's law breaks down if the pore diameters become comparable with, or less than, the

molecular free paths of the flowing gas.

By comparing gas and liquid permeabilities for a series of porous media Calhoun (17) found that neither gas or liquid permeabilities were constant as calculated from Darcy's law. Also gas and different liquid permeabilities were not in agreement; the average for liquids was usually lower than for gas. Calhoun also found that both liquid and gas permeabilities depended upon either mean pressure or pressure gradient.

Similarly Grunberg and Nissan (18) claimed to have found that there was no correlation between the permeability of porous materials for gases and liquids. Permeabilities to gases depended mainly on the linear speed of the gas, whereas permeabilities to liquids also depended on the pore diameter and specific surface tension. A similar study to this was made by Deryagin and Krylov (19).

Explanations that have attempted to account for these anomalies have included the following theories: -

(i) A drag theory of permeability, Brinkman (20)

(ii) An absorbtion theory, Bull and Wronsky (21)

(iii) A capillary condensation theory, Carman (22)

(iv) An Ion effect, Baptist and White (23)

It should be noted that these anomalies are all at very low flow rate values.

2.2.3 Limitation of Darcy's Law due to Inertia flow

The high velocity flow phenomena occurring in porous materials can be put into mathematical terms in several ways. Without attempting to understand the mechanics of the effect, one can simply try to fit a heuristic curve or equation to the experimental data, so as to obtain a correlation between pressure drop and flow velocity. Forchheimer (24) suggested that Darcy's law should be modified for high velocities by including a second order term in velocity i.e. in one dimensional flow

$$-\frac{dp}{dy} = a_1 Q + b_1 Q^2 \qquad 2.2.3$$

and later by adding a third-order term

$$-\frac{dp}{dy} = a_2 Q + b_2 Q^2 + c_2 Q^3 \qquad 2.2.4$$

The Forchheimer equations were postulated from semi-theoretical reasoning by analogy with the phenomena occurring in pipes. The third-order term was added to make the equation fit experimental data more accurately.

The Forchheimer relation was further generalised to contain a time dependent term, Polubarinova-Kochina (25): -

$$-\frac{dp}{dy} = a_3Q + b_3Q^2 + c_3\frac{dQ}{dt} \qquad 2.2.5$$

This time dependent term, however, has been shown to be negligible, Scheidegger (26).

Another heuristic correlation has been postulated by White (27), who set:

$$-\frac{dp}{dy} = a_4Q^{1.8} \qquad 2.2.6$$

this result was derived from an analysis of dry air flow through packed towers. Missbach (28), however set: -

$$-\frac{dp}{dy} = a_5Q^{m_3} \qquad 2.2.7$$

where m_3 is indetermined but lies between the value of 1 and 2. Similar experiments were carried out by Wodnyanszky (29) and Linn (30). The exact value of the exponent, however, varied from case to case so that no universal correlation could be achieved.

It can be seen from above that heuristic techniques have failed to give universal correlation and that a different form of correlation had to be established in an attempt to obtain a universal correlation. A popular correlation that has been attempted is that between a Reynolds number and a friction factor. In order to

characterise the Darcy domain a Reynolds number of the form:

$$Re = \frac{Qd_1\rho}{\eta} \qquad 2.2.8$$

has been used. Here d_1 corresponds to a hydraulic diameter associated with the porous material. Similarly a friction factor has been expressed as:

$$\lambda_f = 2d_1 \frac{dp}{dy} \quad Q^2\rho \qquad 2.2.9$$

The number of papers proposing correlations between friction factor and Reynolds number is great. An extensive review of these correlations has been given by Romita (31). Some of the correlations that have been suggested are as follows, Uchida and Fujita (32) passed gases through beds of broken limestone and lead shot and expressed their results in the form of the equation: -

$$\frac{dp}{dy} = \rho A_b \left(\frac{Q^2}{2d_1}\right)^{r_1} . Re.^{r_2} \left(\frac{d_2}{d_1}\right)^{r_3} \qquad 2.2.10$$

where r_1 and r_3 were functions of the packing and A_b and r_2 were functions of the Reynolds number. Lindquist (33) carefully investigated the previous results and concluded that Darcy's law was valid for $Re < 4$ and postulated the

equation

$$\lambda f\ Re = b_4 Re + b_5 \quad 4 < Re < 180 \qquad 2.2.11$$

where $b_4 = 40$ and $b_5 = 2500$. Givan (34) made a similar investigation and gave an analogous result but with values of $b_4 = 34.2$ and $b_5 = 2410$.

Kling (35) obtained the result that Darcy's law held up to Re = 10 and for $10 < Re < 300$ postulated

$$\lambda f = 94/Re^{0.16} \qquad 2.2.12$$

The above listed investigations are concerned with a correlation between λf and Re given by the previous definitions only. Other investigators state that the porosity of the material should be especially significant, Chalmers et al (35), Barth and Esser (36), Happel (37).

It appears then that this form of correlation is again non-universal. The correlations are at best valid each for an application to a set of very specialised porous media.

Further researchers have attempted to approach the problem through dimensional analysis. It should be noted that the representation of friction factor and Reynolds number, discussed, above, is an outcome of dimensional considerations. The Reynolds number and friction factor

are both dimensionless groups and therefore one must be a numerical function of the other. Rose (38) made a thorough study of the possible variables that might influence the flow and the dimensionless combinations in which they might occur in a flow equation. The analysis however produced eight dimensionless groups, including a Reynolds number, all raised to unknown powers. The values of these powers had to be determined experimentally. The experimental work carried out was similar to that discussed in the fitting of heuristic curves and no additional insight into the physics of the flow phenomina was gained.

Muskat (39) has shown that when changes in elevation were neglected the Forchheimer relationship as expressed by equation 2.2.3 can be produced from dimensional considerations. In this case the constants a_1 and b_1 were

$$a_1 = \frac{a_6 \eta}{d_1^2 A} \quad , \qquad b_1 = \frac{b_4 \rho}{d_1 A} \qquad 2.2.13$$

Green and Duwez (40) considered the case of compressible flow and included in Muskat's equation a momentum term. This term, however, was found to be of negligible magnitude for the cases they considered. They further modified Muskat's equation by including the length parameter d_1 in the constants of proportionality. These new constants they named the viscous and inertia resistance coefficients. They point out that the viscous resistance coefficient is

the reciprocal of the viscous permeability as defined by Darcy's law. Since this paper's publication the reciprocal of the inertia resistance coefficient has been termed the inertia permeability. These coefficients were determined experimentally. They further achieved a correlation of Reynolds number against friction factor, the relationship they postulated being expressed by:

$$\lambda f = \frac{2}{Re} + 2 \qquad 2.2.14$$

the porous material under investigation being stainless steel.

Using a similar approach Ward (41) found that for flow through granulated beds the relationship of Reynolds number and friction factor could be expressed by: -

$$\lambda f = \frac{2}{Re} + 1.1 \qquad 2.2.15$$

It would appear that the dimensional analysis approach is just as abortive as other techniques in producing a universal correlation of Reynolds number and friction factor. The limitation of Darcy flow by this correlation has, to the author's knowledge, not yet been universally achieved and each case has to be considered in its own right.

2.2.4 Viscous and Inertia Permeabilities

In introducing the concept of viscous and inertia permeabilities (reciprocal of viscous and inertia resistance coefficients), Green and Duwez made an important contribution to the understanding of the flow through porous media. A considerable amount of investigation on these permeabilities has resulted, the best known work being that of Morgan (42). Morgan gives a technique where both viscous and inertia permeabilities can be found from one single plot of experimental results, see section 4.3.1. He also states that the inertia losses are several orders of magnitude smaller than the viscous losses if a liquid is used as the permeating fluid, while with gases both kinds of loss have to be taken into account. This sweeping statement of losses for gas flow, the author of this text has found to be in error. It may well apply for highly permeable material but not for all porous materials, see section 4.3.1.

Greenberg and Weger (43) have investigated the effect of temperature and pressure on the hitherto supposed constant values of inertia and viscous permeability. They found that the viscous permeability, while not a function of pressure, decreased significantly as the temperature of the sintered material increased. This they attributed to the slight changes in the

position or size of the smaller restriction passages plus small expansions in the surface irregularities. They also determined that the inertia permeability was neither a function of pressure or temperature. This, they explained, is due to the overall structure of the porous material, i.e. tortuosity and porosity, remaining virtually constant.

Up to this point the equation for high velocity flow has been based on Forchheimer's semi analytic heuristic equation. However, Irmay (44) has shown that this equation can be produced analytically from the Navier-Stokes equations. Similarly it is shown that for low velocity flows Darcy's law can be analytically produced.

This then completes the literature survey on flow through porous media. As was stated in the introduction of this section only a limited portion of the vast number of papers on porous material would be reviewed. If the reader wishes to investigate further into the work on porous media then the author recommends the text book written by Scheidegger (26) which he has found invaluable.

2.2.5 Gas Lubricated Porous Journal Bearings

Before reviewing published work on thrust bearings it was considered useful to describe some findings with porous journal bearings which could possibly be of use

in thrust bearing work.

Probably the first published work on porous journal bearings was that of Montgomery and Sterry (45). They demonstrated the practicability of a porous-bearing supported journal by rotating a 0.75 in. shaft at 250,000 r.p.m. in a pair of porous sleeves. Having shown the feasibility of such a bearing, Robinson and Sterry (46) proceeded with a thorough experimental study of the non-rotating performance characteristics of a porous journal bearing. They formulated an analysis of the infinitely long, non-rotating journal bearing assuming isothermal, compressible flow which was purely axial. Their experimental work was guided by the results of their simplified analysis. Its objective was to determine the corrections required to bring the approximate theory and experiments into agreement. Among the important features of the bearing which they observed experimentally were:

(a) That the viscous permeability of the porous material as defined by Darcy's law reduced as the flow rate increased, an inertia effect.

(b) That a static instability under certain operating conditions existed.

Constantinescu (47) carried out an analysis on a short bearing. This analysis assumed that the tangential pressure gradient in the Reynolds equation could be neglected. The Reynolds equation used was a modified

form of the usual Reynolds equation since it included an additional term to account for the flow through the porous wall into the clearance space.

Sneck and Elwell (48) presented a perturbation solution of the Reynolds equation for the non-rotating journal bearing, which was not restricted by the length of the bearing. The results of this analysis were in good agreement with the results of Robinson, Sterry and Constantinescu while at the same time indicating the general effect of the length to radius ratio on the bearing performance.

Sneck and Yen (49) compared the above theory with the results of an experimental investigation. They found that for small eccentricities the linear perturbation theory was sufficiently accurate to predict the load capacity of the bearing. Significantly they also found that the apparent bearing clearance was not the measured clearance but the sum of the measured clearance and the arithmetic mean roughness of the porous surface.

In all the published work discussed so far the investigators have assumed that the porous material has been pressurised over its entire length and no sealing of the outer edges of the material was attempted. Yabe (50) has investigated the effect of sealing the outer surface of the bushing at both ends, leaving only a central circumferential band open to the supply pressure, see figure 9 page 29 . This results in a

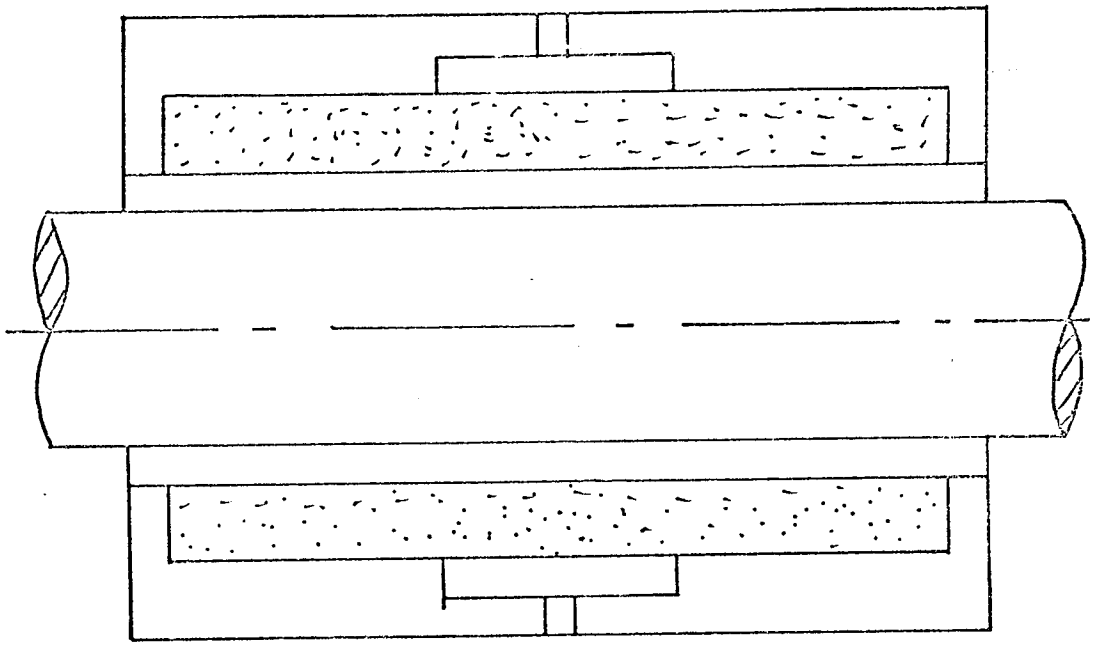

Figure 9 A Porous Wall Journal Bearing Investigated by Yabe

substantial axial flow within the porous material as well as within the lubrication film. The analysis was carried out assuming the gas to be incompressible and the flow to be strictly two-dimensional, in that no circumferential flow was assumed. To account for this two-dimensional flow the concept of an 'effective restricting thickness' was introduced. In the outer portions of the bushing, which were sealed from direct contact with the supply pressure, the axial flow in the porous material was accounted for by assigning an equivalent thickness to the bushing and treating it as an extension of the lubricant film. These effective thicknesses were determined experimentally and therefore the surface roughness effect of Sneck and Yen was inherently included. Axial pressure distributions at various circumferential positions were obtained experimentally and for small pressure differences these agreed with those predicted by the theory.

Another configuration considered by Yabe was an annular-pocket journal bearing in which the flow restrictor was a porous material. This bearing was analysed in the same way as the previous bearing though no experimental results were presented.

Barlow and Wildmann (51) theoretically analysed the case of a pressurised, hollow, non-rotating porous journal around which a flexible foil of tape moved. As the tape load was considered small it was assumed that high supply pressures were not required and the gas was considered

to be incompressible. The width of the foil was assumed small compared to the length in contact with the porous journal so that a short bearing theory was employed. For typical operating conditions this bearing was found to have a greater load capacity than a discrete restrictor fed bearing operating at the same supply pressure with the same minimum clearance and flow rate of gas.

2.2.6 Gas Lubricated Porous Thrust Bearings

Published work on porous thrust bearings appeared not long after the initial work on journal bearings. Sheinberg and Shuster (52) considered the analytic aspects of non-rotating circular thrust bearings with and without central holes for a shaft. In each case it was assumed that the edges of the porous material were sealed so that the gas was forced to flow axially through the porous material. It was also assumed that the porous material could be modelled by a large number of capillaries of uniform diameter, cf Scheidegger (26) for the inadequacies of this model. Design curves for the load capacity of both configurations were obtained from the analysis. The bearing with no central hole showed better than a two fold improvement in load capacity over a comparable non-porous pocket bearing with an orifice feed. A flow rate design curve has also been constructed from the analysis for this configuration and is given in the MTI-RPI design

of gas bearing notes (53). Experimental results of the performance of an actual bearing, however, are not given though the authors state that in actual operation the bearing with the central hole is highly resistant to vibrations. They contribute this to the permeable surface absorbing the energy of the vibrations.

A considerable amount of work on non-rotating porous thrust bearings has been done by Yabe (50) again using the equivalent clearance technique. Four thrust bearing configurations were analysed in this way. The first was a porous disc fed through a central plenum chamber. The porous material was considered to be open or sealed at the outer edge. As might be expected the bearing with the sealed outer edge carried higher loads. Experimental results correlated with an incompressible theory for small applied pressure drops, these results also showed that for this type of bearing the load capacity was a linear function of the clearance.

The second configuration considered by Yabe was an annular thrust bearing with a recessed porous disc forming a pocket and acting as a restrictor. Again comparison between theory and experiment was acceptable for small supply pressures. These results showed that the load capacity for this bearing was a non-linear function of clearance.

The other two configurations considered by Yabe were a full porous surface and a recessed ring collar

bearing. Neither of these configurations were tested so that a comparison of theory and experiment is not possible.

Mori et al (54) investigated the same configuration of Yabe's first bearing type, though considering three dimensional flow without employing the effective thickness technique. They recognised that an analysis of a porous bearing could be analytically approached as a boundary value problem, in that the Reynolds equation governing the pressure distribution in the gas film could be used as a boundary condition for the differential equation governing in the porous material. The results obtained are close to those of Yabe's simplified analysis, lending credence to the effective thickness concept.

All the analysis so far discussed have used the assumption that at the porous wall boundary of the gas film, a zero velocity component tangential to the porous surface occurs. This assumption creates a discontinuity in velocity according to Darcy's law. Ishizawa and Hori (55) questioned the validity of this assumption in their analysis of a circular thrust bearing. They concluded from a purely theoretical standpoint that there is a non-zero velocity component tangential to the porous surface and that the non-slip condition is only approached in the limiting cases of infinite film thickness, zero permeability of the porous material or small lubricant flow rates. Beavers and Joseph (56) have shown experi-

mentally that this slip velocity does occur. Their equipment was designed to measure simultaneously the flow rate through a long porous block and the flow rate through a small uniform gap above the block. The measured flow rate through the gap was larger than that predicted by the non-slip theory, total repeatability of their results was claimed.

Gargiulo and Gilmour (57) investigated the full faced porous thrust bearing. In their analysis the boundary value technique of Mori was used. However, an analytic solution for the pressure distribution was not achieved. A numerical technique suggested by Peaceman and Rachford (58), the Alternating Direction Implicit technique, was used to solve the pressure distribution. Again for this analysis the non-slip condition was assumed. The authors, however, did theoretically demonstrate that anistropic permeability effects in the porous material had little effect on the load capacity of the bearing while a large effect occurred in the flow rate. Also design curves were produced showing the effect of the aspect ratio of the bearing, i.e. ratio of bearing outer radius to porous pad thickness. A further design curve produced showed the effect of reducing the area over which the supply pressure was provided. Both effects were shown to be significant.

Experimental verification of the load capacity and

flow rate was attempted for a bearing in which the supply pressure was provided to 75% of the total pad area. For large film thicknesses a reasonable correlation was achieved. However, for small clearances the theory over-predicted the load that the bearing experimentally carried. This the authors attributed to the fact that no attempt was made to account for the surface roughness of the porous material when measuring the film thickness.

Jones et al (59), (60) analysed the same bearing and achieved an analytic solution for the pressure squared distribution in the gas film. In this analysis the slip velocity of Ishizawa and Hori was taken into account. Darcy's law it was assumed governed the flow through the porous material. Jones compared the theory of Gargiulo and Gilmour to his own and found that they predicted identical load capacities but disimilar flow rates. Jones also produced design curves for static stiffness but as Gargiulo and Gilmour had not, no comparison could be made.

Jones et al then attempted to verify this theory experimentally. No correlation between the experimental results and theoretical predictions could be achieved, in that the experimental results of load capacity were below that predicted by the theory yet the experimental results of flow were above the theoretical predictions. Jones et al assumed that this non-correlation was due to the flow through the porous material not being

governed by Darcy's law. They attempted to produce a theory in which the flow through the material was governed by Forchheimer's equation, the gas was assumed to be incompressible. A perturbation technique was used so that the first order inertia effects alone were considered. Even though this perturbation approximation simplified the equations involved, an analytic solution could not be found. They proceeded with a numerical solution of the equations formed by this perturbation technique but the final solution that was achieved could not be proved valid. It should be noted that by halving the numerical grid size used, similar solutions did not result. The solutions that were achieved showed little difference from the viscous theory and therefore experimental correlation could still not be achieved. A possible reason for this failure in theoretical solution is that in using a perturbation technique to solve this problem only an approximate solution is achieved. Therefore by attempting to solve the perturbation equations by a numerical method, another approximate technique, an approximation of an approximation was the result.

In the experimental results no attempt was made to account for the surface texture of the porous material. This then shows a severe conflict in the published literature. Two authors, using different techniques

of solution, achieve like theoretical solutions, with only one author having taken the slip condition of Ishizawa and Hori into account. One of these authors achieves experimental correlation the other cannot, yet neither of these authors have taken into account the surface finish of the porous material considered in porous journal bearings to be essential.

The literature on a steady-state stability analysis of this type of bearing is extremely scarce. Sahib (61), it is quoted by Sneck (62), found that the full faced porous thrust bearing had a narrow stability operating region and was prone to pneumatic hammer. He suggested that the stability could be improved by reducing the capacitance of the porous material through reductions in permeability or the disc thickness. Further details of this work are not known as this reference is not available.

Dah-Chen Sun (63) carried out a linear stability analysis using a perturbation technique. He assumed that the porous material was thin and therefore the flow through the material was axial. Experimental verification of this theory was not attempted. Dah-Chen Sun concluded that the lubricants compressibility is the mechanism of instability. The effect of compressibility is revealed in two forms; (a) when the film pressure is high the compressibility effect is more pronounced and

the bearing unstable. A high film pressure can be achieved by a high supply pressure or a high ratio of permeability to pad thickness. Therefore for a given bearing there exists a critical supply pressure below which instability cannot occur and for bearings of identical size the one with the larger ratio of permeability to pad thickness is more prone to pneumatic hammer; (b) the lubricants compressibility renders it impossible for the disturbances to penetrate into the entire content of the porous disc. It is also concluded that the greater the supported mass the greater the tendancy for instability and a smaller film thickness produces a greater film stiffness which would contribute to the damping of the system.

The general statement that a smaller film gives a greater film stiffness is incorrect as Jones has shown that for a constant supply pressure there is an optimum film thickness above or below which the stiffness reduces.

Donaldson and Patterson (64) have investigated the use of porous inserts in plain externally pressurised air thrust bearings using high supply pressures. The supply pressures used were as high as 3.2 MN/m^2 and bearing clearances of 2o μm were reported for a bearing load of 6KN and a bearing stiffness of 100 MN/m. They have presented many design curves showing the effects

of: -

(a) supply pressure, insert diameter and insert permeability on the bearing load/film thickness curves.

(b) supply pressure, insert diameter and insert permeability on the static bearing stiffness/film thickness curves. (Stiffness was computed from differentiating a heuristic curve that fitted the load curve).

(c) supply pressure on mass flow/film thickness curve.

They have also produced curves showing the stability regions, for a material designated as G32, on a load-supply pressure basis, and the effect of changing the insert diameter. Although these authors have not accounted for the surface finish of the porous material in their experimental results, it should be noted that as a landed bearing is used rather than a full face porous bearing the film thickness could be accurately measured in the annular region provided that these metal surfaces have been machined to fine limits.

The authors conclude that the use of porous inserts enable this form of bearing to be used with a supply pressure of more than 30 MN/m^2, power consumption is reduced by using the largest insert of high permeability and reducing the insert diameter increases the possibility

of instability.

The authors also state that the main areas of investigation left are analytic solutions including the fluid inertia in the bearing film and applications of this form of restriction in other configurations.

Gorez and Szwarcman (65) have considered the case of the use of a row of porous discs on an externally pressurised slider bearing. They assume that the row of porous discs can be replaced by an equivalent strip of porous material, they also assume that the porous material can be modelled by a system of constant diameter capillaries. No account is taken of the surface finish in their experimental results or the slip effect in the theoretical analysis. Correlation between the theoretical and analytic results shows an error which may be due to the above omissions.

An interesting point that these authors raise is that the porous pad when pressurised may not remain flat but bow like a diaphragm. Due to this consideration the porous pads are machined flat whilst pressurised. When the air pressure is shut off the pad then takes a concave shape. The authors then assume that in operation when pressurised these bearings take up the flat shape. However, it must be realised that during machining the pad is subjected to a pressure drop value of (p_s-p_a) and it is this pressure drop that creates the necessary forces

within the porous pad to form a flat upper surface. Now during operation the pad is subjected to a pressure drop of $(p_s - p_f)$ which, as $p_f > pa$, is a lower pressure drop than that which is necessary to create the desired forces within the pad and thus the pad will still be concave during operation

These authors also make no attempt to remove the pore smear that occurs due to this machining, Wheeler (66).

Two interesting practical applications are sited in this work. These are: -

(1) the standard oil bearings for the wheel spindle of a grinding machine were replaced by porous bearings. This resulted in an improvement of produced parts.

(2) a slider bearing with a circumferential set of 48 porous discs has been used in a milling/ boring machine for more than eight years.

In both cases no degradation of the performance of these bearings has been evident.

Practically no literature is available on the dynamic analysis of these bearings. Indeed the only source of information that was available was the above mentioned paper of Gorez and Szwarcman. In their analysis these authors have made no attempt to investigate the individual dynamic characteristics i.e. dynamic stiffness and damping,

but have combined these to give a dynamic flexibility. They produce for a specific bearing configuration a dynamic flexibility/frequency curve which shows that at resonance the bearing dynamic flexibility tends to zero. Their theoretical results are compared to those of an analogue computer model and good correlation is shown. However, no experimental results are available.

From this literature survey the gaps in the knowledge that exist and the conflict of evidence may be briefly summerised: -

(a) Limitations of the Darcy law assumption

(b) The case of Forchheimer flow through the porous pad

(c) Permeability determination

(d) The slip velocity component of Ishizawa and Hori

(e) Surface finish effects

(f) Dynamic analysis

(g) Steady-state stability analysis

From this it is now possible to outline the areas of investigation that need attention for a fuller understanding of the performance of porous thrust bearings.

2.3 The Area of Investigation

Before discussing the areas that need to be investigated a broad outline of the type of bearing to be studied should be made.

The type of bearing to be investigated is an externally pressurised, uniform film, air lubricated, full faced porous thrust bearing, see figure 7 page 13 . The landed bearing will not be considered.

The areas of investigation are as follows: -

(a) From the literature survey on porous materials it has been shown that there are limits to the use of the Darcy equation. Nearly all analytic approaches quoted in the porous bearing survey have assumed that Darcy's law governs the flow through the porous material. The use of this assumption requires investigation and if at all possible some form of criterion for the use of this law, for the design of these bearings, should be developed.

(b) As far as the author knows there is no solution available for the case of Forchheimer flow through the porous material when considering these bearings. A solution for this case should be developed.

(c) There appears to be two different techniques for the determination of the viscous and inertia permeabilities of porous materials, (1) Morgan and (2) Greenberg and Weger and the results are in

conflict. These techniques should be tested to find the correct method of measurement.

(d) The use of the slip velocity component, proposed by Ishizawa and Hori, by Jones and the omission of this component by Gargiulo and Gilmour to give identical non-dimensional load - non-dimensional film thickness curves needs thorough investigation. This is a serious conflict and the correct theory must be found to enable true design curves to be produced.

(e) The surface finish effect of the porous material, considered to be an essential parameter in published journal bearing literature, should be investigated for the thrust bearing. A technique of measurement of this factor needs to be developed.

(f) There seems to be little published literature on the dynamic characteristics of these bearings, i.e. dynamic spring stiffness and damping coefficient. A full analytic and experimental investigation is needed.

(g) A full stability analysis is required such that it is possible to design and use these bearings without encountering the problem of pneumatic instability.

CHAPTER THREE

THEORETICAL ANALYSIS

3.1 INTRODUCTION

This chapter is concerned with the analytic and numerical methods used to predict the steady-state and dynamic performance characteristics of full faced hydrostatic porous thrust bearings.

In order to predict the performance and hence obtain pertinent design information it is necessary to analyse the flow of the lubricating fluid in two regions: -

(a) The flow of the lubricating fluid in the porous pad.

(b) The flow of the lubricating fluid in the lubrication film.

The flow can either be analysed in both regions and the solutions matched at the porous pad/lubrication film interface or the equation governing flow in the lubrication film, a modified Reynolds equation, can be used as a boundary condition for the equation of flow in the

porous pad. This boundary condition assumption is based on the fact that the lubrication film thickness is small in comparison with the porous pad thickness, plus the basic lubrication assumption that the pressure across the lubrication film does not vary.

The first approach is relatively complex and therefore it is the second approach that is used. The choice of the latter is well precedented (67), (68), (57), (59).

The general differential equation governing the flow through the porous media and the boundary conditions are presented in section 3.2 along with the assumptions that are involved. As previously stated the steady-state solution of these equations has been presented by Jones et al (59). although they failed to achieve experimental correlation. As part of the present investigation is to find the reason for this non-correlation it was considered useful to present a precis of the analytic work of Jones (section 3.3).

An analytic solution of the dynamic equations is not possible due to the severe non-linearity of these equations. Thus in order to obtain theoretical predictions a numerical solution of the dynamic equations has been achieved (section 3.4).

3.2 THE GENERAL DIFFERENTIAL EQUATION AND BOUNDARY CONDITIONS FOR THE POROUS PAD

The coordinate system used is shown in figure 10 page 48.

3.2.1 Assumptions involved in the derivation of the general differential equation for the porous pad

(i) Darcy's law governs the flow of the lubricating fluid through the porous pad, Taylor and Lewis (69). That is, all inertia effects are assumed negligible and the fluid velocities are expressed by: -

$$u = -\frac{\Phi_r}{\eta} \cdot \frac{\partial p}{\partial r}$$

$$v = -\frac{\Phi_y}{\eta} \cdot \frac{\partial p}{\partial y}$$

$$w = -\frac{\Phi_\theta}{\eta} \cdot \frac{\partial p}{\partial \theta}$$

(ii) The flow is compressible and isothermal.

(iii) The fluid is isoviscous.

(iv) Viscous permeabilities are constant but not necessarily equal

$$\Phi_r \neq \Phi_y \neq \Phi_\theta$$

$$\Phi_r, \Phi_\theta, \Phi_y \neq f(r,y,\theta)$$

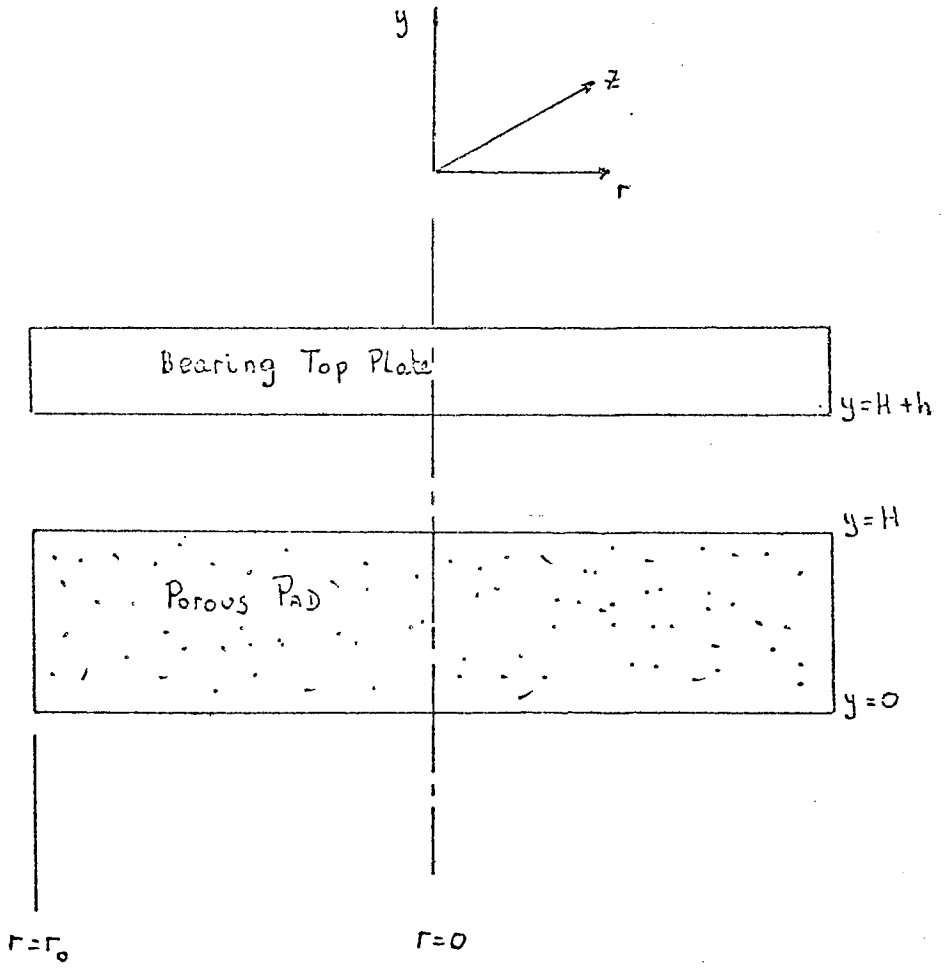

Figure10 Co-ordinate System

(v) The lubrication fluid equation of state may be written as

$$p = \rho \mathcal{R} T$$

(vi) Axisymmetry conditions prevail, i.e.

$$\frac{\partial}{\partial \theta} = 0$$

3.2.2 The Derivation of the general differential equation for flow in the porous pad

The continuity equation for flow of a fluid through a porous media may be written, (26)

$$\underline{P}^* \cdot \frac{\partial \rho}{\partial t} + \frac{1}{r} \cdot \frac{\partial}{\partial r}(\rho u r) + \frac{\partial}{\partial y}(\rho v) = 0 \qquad 3.2.1.$$

Substituting from Darcy's law (assumption (i)) for the velocity terms and from the equation of state for the density terms equation 3.2.1. becomes:

$$\underline{P}^* \frac{\partial}{\partial t}\left(\frac{p}{\mathcal{R}T}\right) = \frac{1}{r} \cdot \frac{\partial}{\partial r}\left(\frac{p}{\mathcal{R}T} \cdot r \cdot \frac{\Phi_r}{\eta} \cdot \frac{\partial p}{\partial r}\right)$$

$$+ \frac{\partial}{\partial y}\left(\frac{p}{\mathcal{R}T} \cdot \frac{\Phi_y}{\eta} \cdot \frac{\partial p}{\partial y}\right) \qquad 3.2.2.$$

Now $\mathcal{R}$ is a constant and from assumption (ii) T is a constant. Therefore both $\mathcal{R}$ and T can be taken out of the differential bracket and cancelled. From assumptions (iii) and (iv) the viscous permeability and lubricant viscosity terms may also be taken out of the differential bracket. Also remembering $2pdp = d(p^2)$ equation 3.2.2. may be written:

$$\frac{\Phi_r}{r} \cdot \frac{\partial}{\partial r}\left(r \cdot \frac{\partial}{\partial r}(p^2)\right) + \Phi_y \cdot \frac{\partial^2}{\partial y^2}(p^2) = 2\eta \underline{P}^* \frac{\partial p}{\partial t} \qquad 3.2.3.$$

Equation 3.2.3 is the general differential equation of continuity for the porous pad. The solution of this equation will give the distribution of the square of the pressure within the porous pad. This equation holds within the limits

$$0 \leqslant y \leqslant H, \quad 0 \leqslant r \leqslant r_o, \quad 0 \leqslant t \leqslant 1/\omega$$

3.2.3 The Boundary Conditions

(i) At the lower supply face of the porous pad the supply pressure is kept constant.

$$p = p_s \quad y = 0, \quad 0 \leqslant r \leqslant r_o \quad 0 \leqslant t \leqslant 1/\omega \qquad 3.2.4.$$

(ii) From the assumption (vi) the radial pressure gradient at the porous pad centre is zero.

$$\frac{\partial p}{\partial r} = 0 \qquad r = 0, \quad 0 \leqslant y \leqslant H, \quad 0 \leqslant t \leqslant 1/\omega \qquad 3.2.5.$$

(iii) As the outer edge of the porous pad is sealed, flow from the pad edge is prevented and thus the radial pressure gradient at this edge is zero.

$$\frac{\partial p}{\partial r} = 0 \qquad r = r_o, \quad 0 \leqslant y \leqslant H, \quad 0 \leqslant t \leqslant 1/\omega \qquad 3.2.6.$$

(iv) The pressure is assumed to be periodic with time.

$$p(t) = p(t + \tfrac{1}{\omega}) \qquad 0 \leqslant r \leqslant r_o, \quad 0 \leqslant y \leqslant H. \qquad 3.2.7.$$

(v) A modified Reynolds equation applies within the limits

$$0 \leqslant r \leqslant r_o, \quad y = H, \quad 0 \leqslant t \leqslant 1/\omega$$

3.2.4 The general form of the modified Reynolds equation for an externally pressurised porous thrust bearing

Further assumptions involved in deriving the modified Reynolds equation are:

(vii) All body forces, including gravity forces, are neglected.

(viii) The pressure of the lubricating fluid is constant across the thickness of the lubrication film.

(ix) The film is uniformly thick.

(x) All boundaries of the film are assumed rigid, Taylor and Lewis (70).

(xi) The flow is continuous at the surface of the porous media. By virtue of this a slip velocity occurs at this surface and is evaluated from Darcy's law.

(xii) There is no slip at the upper boundary of the lubricating film. The velocity of the lubricant layer adjacent to the bearing top plate is the same as the velocity of the bearing top plate.

(xiii) The flow through the lubrication film is isothermal, laminar and compressible.

(xiv) All velocity gradients other than $\frac{\partial u}{\partial y}$ are neglected.

By use of assumptions (vii), (xiii) and (iv) the Navier Stokes equations reduce to

$$\frac{\partial^2 u}{\partial y^2} = \frac{1}{\eta} \cdot \frac{\partial p}{\partial r} \qquad 3.2.8.$$

The continuity equation for flow through the film may be written

$$\frac{1}{r}\frac{\partial}{\partial r}(r.\rho.u) + \frac{\partial}{\partial y}(\rho.v) + \frac{\partial}{\partial t}(\rho) = 0. \qquad 3.2.9.$$

Integrating equation 3.2.8. twice with respect to y, as p is not a function of y, assumption (viii)

$$u = \frac{1}{2\eta} \cdot \frac{\partial p}{\partial r} \cdot y^2 + A_7 y + B \qquad H \leqslant y \leqslant H + h$$

Using assumption (x) and (xi) to determine the constants of integration A_7 and B yields

$$u = \frac{1}{2\eta} \cdot \frac{\partial p}{\partial r}\left(y^2 - \left(2H+h - \frac{2\Phi_r}{h}\right) y + \left(H^2 + Hh - 2\Phi_r\left(\frac{H}{h}+1\right)\right)\right)$$

$$H \leqslant y \leqslant H + h \qquad 3.2.10.$$

Integrating the continuity equation, equation 3.2.9., with respect to y between the limits H and H+h gives

$$\int_H^{H+h} \left(\frac{1}{r}\frac{\partial}{\partial r}(r.\rho.u) + \frac{\partial}{\partial y}(\rho.v) + \frac{\partial \rho}{\partial t}\right) dy = 0.$$

Replacing u by equation 3.2.10, ρ by the equation of state and using the assumption that the pressure is not a function of y yields

$$\frac{1}{\mathcal{R}T} \cdot \frac{1}{r} \cdot \frac{\partial}{\partial r} \int_{H}^{H+h} \frac{rp}{2\eta} \frac{\partial p}{\partial r} \left[y^2 - \left(2H+h- \frac{2\Phi_r}{h}\right) y \right.$$

$$\left. + H^2 + Hh - 2\Phi_r \left(\frac{H}{h}+1\right) \right] dy + \frac{1}{\mathcal{R}T} \int_{H}^{H+h} \frac{\partial p}{\partial t}\, dy$$

$$= -\frac{1}{\mathcal{R}T} \left[p \left(\frac{dh}{dt} + \frac{\Phi_y}{\eta} \left(\frac{\partial p}{\partial y} \right)_{y=H} \right) \right]$$

which upon integration and simplification yields the modified Reynolds equation for an externally pressurised porous thrust bearing lubricated by a compressible fluid

$$\frac{1}{r} \frac{\partial}{\partial r} \left(r.h.(h^2+6\Phi_r) \frac{\partial}{\partial r}(p^2) \right)$$

$$= 12\Phi_y \left[\frac{\partial}{\partial y}(p^2) \right]_{y=H} + 24\eta \frac{\partial}{\partial t}(ph) \qquad 3.2.11.$$

Equation 3.2.11. applies within the limits

$$0 \leqslant t \leqslant 1/\omega, \quad 0 \leqslant r \leqslant r_o, \quad H \leqslant y \leqslant H+h$$

3.2.5 Non-dimensional Parameters

In order to generalise the solutions obtained from the general differential equation and the boundary conditions for an externally pressurised porous thrust bearing the following non-dimensional parameters have been used.

Bearing Aspect Ratio	$S = H/r_o$
Permeability Ratio	$K = \Phi_r/\Phi_y$
Dimensionless Pressure	$\bar{P} = p/p_a$
Dimensionless Time	$\bar{T} = t.\omega/2\pi$
Radial Position	$R = r/r_o$
Axial Position	$Y = y/H$
Bearing Number	$\Lambda = 12\Phi_y r_o^2/h(h^2+6\Phi_r)H$
Frequency Factor	$\alpha = H^2\eta\underline{P}^*\omega/\Phi_y p_a$
Velocity Factor	$\gamma = 24r_o^2\eta\frac{dh}{dt}/h(h^2+6\Phi_r)p_a$
Frequency Factor	$\beta = 12r_o^2\eta\omega/(h^2+6\Phi_r)p_a$

The use of the above non-dimensional parameters transforms the general governing differential equation and the boundary conditions to:

$$\frac{S^2K}{R}\frac{\partial}{\partial R}\left(R\frac{\partial}{\partial R}(\bar{P}^2)\right) + \frac{\partial^2}{\partial Y^2}(\bar{P}^2) = \frac{\alpha}{\bar{P}}\frac{\partial}{\partial \bar{T}}(\bar{P}^2)$$

$$0 \leq R \leq 1, \quad 0 \leq Y \leq 1, \quad 0 \leq \bar{T} \leq 1 \qquad 3.2.12.$$

$$\bar{P} = \bar{P}_s \qquad Y = 0, \quad 0 \leq R \leq 1, \quad 0 \leq \bar{T} \leq 1 \qquad 3.2.13.$$

$$\frac{\partial}{\partial R}(\overline{P}) = 0 \qquad R = 0, \quad 0 \leqslant Y \leqslant 1, \quad 0 \leqslant \overline{T} \leqslant 1 \qquad 3.2.14.$$

$$\frac{\partial}{\partial R}(\overline{P}) = 0 \qquad R = 1, \quad 0 \leqslant Y \leqslant 1, \quad 0 \leqslant \overline{T} \leqslant 1 \qquad 3.2.15.$$

$$\overline{P}(\overline{T}) = \overline{P}(\overline{T}+1) \qquad 0 \leqslant Y \leqslant 1, \quad 0 \leqslant R \leqslant 1 \qquad 3.2.16.$$

$$\frac{1}{R}\frac{\partial}{\partial R}\left[R\,\frac{\partial}{\partial R}(\overline{P}^2)\right] = \Lambda\left[\frac{\partial}{\partial Y}(\overline{P}^2)\right]_{Y=1} + \frac{\beta}{\overline{P}} \cdot \frac{\partial}{\partial \overline{T}}(\overline{P}^2) + \gamma\overline{P}$$

$$Y = 1, \quad 0 \leqslant R \leqslant 1, \quad 0 \leqslant \overline{T} \leqslant 1 \qquad 3.2.17.$$

3.3 THE STEADY-STATE SOLUTION

Equations 3.2.12 to 3.2.17 are the time dependant equations; for the steady-state case these equations simplify as the dimensionless parameters α, β, γ equal zero as ω equals zero. Thus the steady-state form of equations 3.2.12 to 3.2.17 may be written:

$$\frac{S^2K}{R}\frac{\partial}{\partial R}\left[R\,\frac{\partial}{\partial R}(\overline{P}^2)\right] + \frac{\partial^2}{\partial Y^2}(\overline{P}^2) = 0$$

$$0 \leqslant R \leqslant 1, \quad 0 \leqslant Y \leqslant 1 \qquad 3.3.1.$$

$$\overline{P} = \overline{P}_s \qquad 0 \leqslant R \leqslant 1, \quad Y = 0 \qquad 3.3.2.$$

$$\frac{\partial}{\partial R}(\overline{P}) = 0 \qquad R = 0, \quad 0 \leqslant Y \leqslant 1 \qquad 3.3.3.$$

$$\frac{\partial}{\partial R}(\overline{P}) = 0 \qquad R = 1, \quad 0 \leqslant Y \leqslant 1 \qquad 3.3.4.$$

$$\frac{1}{R}\frac{\partial}{\partial R}\left[R\frac{\partial}{\partial R}(\overline{P}^2)\right] = \Lambda\left[\frac{\partial}{\partial Y}(\overline{P}^2)\right]_{Y=1}$$

$$0 \leqslant R \leqslant 1, \quad Y = 1 \qquad 3.3.5.$$

Jones et al (59) used the method of decomposition in order to show that the solution of equation 3.3.1 may be written

$$\overline{P}^2 = [A_1 J_0(kR) + A_2 K_0(kR)][B_1 \cosh(\lambda Y) + B_2 \sinh(\lambda Y)] \qquad 3.3.6.$$

By using the boundary condition expressed in equation 3.3.2., 3.3.3., 3.3.4 it was further deduced that

$$\overline{P}^2 = \overline{P}^2_s + C_2 Y + \sum_{n=2}^{\infty} Cn_2 J_0(k_n R) \sinh(\lambda_n Y)$$

$$0 \leqslant R \leqslant 1, \quad 0 \leqslant Y \leqslant 1 \qquad 3.3.7.$$

After differentiating equation 3.3.7. and evaluating the result at Y = 1 Jones substituted the result into the modified Reynolds equation, equation 3.3.5., the last boundary condition. Upon integration of the result and evaluation of the constants of integration it was determined that

$$\overline{P}^2 = \left[1 + \frac{\Lambda C_2 (R^2 - 1)}{4} + \Lambda \sum_{n=2}^{\infty} \frac{\lambda_n C_{n2} (J_o(k_n) - J_o(k_n R)) \cosh\lambda_n}{k_n^2} \right]^{\frac{1}{2}}$$

$$Y = 1, \quad 0 \leq R \leq 1 \qquad 3.3.8.$$

By equating equation 3.3.8. to equation 3.3.7., evaluated at Y = 1, and by using various properties of the Bessel functions it can be shown that

$$C_{n2} = \frac{\Lambda C_2}{J_o(k_n)(k_n^2 \sinh(\lambda_n) + \Lambda\lambda_n \cosh(\lambda_n))} \qquad 3.3.9.$$

$$C_2 = \frac{(\overline{P}_s^2 - 1)}{\left(\Lambda^2 \sum_{n=2}^{\infty} E_n - \Lambda/8 - 1\right)} \qquad 3.3.10.$$

$$E_n = \frac{\lambda_n}{[\Lambda\lambda_n + k_n^2 \tanh(\lambda_n)]k_n^2} \qquad 3.3.11.$$

where

$$n = (2, 3, 4, \ldots..)$$

Equations 3.3.8., 3.3.9., 3.3.10., and 3.3.11 give the pressure distribution in the lubricating film.

Having obtained an analytic solution for the pressure distribution in the lubrication film the bearing load capacity and lubricant mass flow rate may now be determined. The bearing load capacity is found as the sum of pressure forces acting normal to the bearing surface

$$W = \int_0^{2\pi} \int_0^{r_o} (P-p_a)\, r \, dr d\theta$$

In dimensionless form

$$\overline{W} = \frac{W}{\pi r_o^2 (p_s - p_a)} = \frac{2}{(\overline{P}_s - 1)} \int_0^1 (\overline{P}-1)\, R \, dR \qquad 3.3.12.$$

The lubricant mass flow rate may be calculated from the lubricant velocity crossing from the porous media into the lubrication film

$$M = 2\pi \int_0^{r_o} (\rho v)_{y=H} \cdot r \cdot dr$$

Substituting for v from equation 3.2.10., integrating and re-arranging gives, in dimensionless form

$$\overline{M} = \frac{2M\eta RTH}{\pi r_o^2 (p_s^2 - p_a^2) \Phi_y} = - \frac{C_2}{(\overline{P}_s^2 - 1)} \qquad 3.3.13.$$

The static stiffness of the bearing is

$$X = - \frac{dW}{dh_o} = - \frac{d\overline{W}}{d\Lambda} \cdot \frac{d\Lambda}{dh_o} \cdot \frac{dW}{d\overline{W}}$$

Substitution of the above differentials gives, in dimensionless form

$$\overline{X} = \frac{Xh_o(h_o^2 + 6\Phi_r)}{\pi r_o^2 (p_s - p_a)(h_o^2 + 2\Phi_r)} = \frac{6\Lambda}{(\overline{P}_s - 1)} \int_0^1 \frac{\partial \overline{P}}{\partial \Lambda} R.dR$$

3.3.14.

Differentiating equation 3.3.8. gives

$$\frac{dP}{d\Lambda} = \frac{1}{2\bar{P}}\left[\frac{(R^2-1)}{4}\left(C_2+\Lambda\frac{dC_2}{d\Lambda}\right)\right.$$

$$\left. + \sum_{n=2}^{\infty} \frac{\lambda_n[J_o(k_n)-J_o(k_nR)]\cosh\lambda_n(\Lambda\frac{dC_{n2}}{d\Lambda}+C_{n2})}{k_n^2}\right]$$

3.3.15.

where

$$\frac{dC_2}{d\Lambda} = -\frac{C_2^2}{(\bar{P}_s^2-1)}\cdot\left[2\Lambda\sum_{n=2}^{\infty}E_n + \Lambda^2\sum_{n=2}^{\infty}\frac{dE_n}{d\Lambda} - \frac{1}{8}\right]$$

3.3.16.

$$\frac{dE_n}{d\Lambda} = -E_n^2k_n^2$$

3.3.17.

$$\frac{dC_{n2}}{d_\Lambda} = C_{n2}\left[\frac{1}{\Lambda}+\frac{1}{C_2}\cdot\frac{dC_2}{d\Lambda} - \frac{\lambda_n}{(k_n^2\tanh(\lambda_n)+\Lambda\lambda_n)}\right]$$

3.3.18.

Substituting equations 3.3.15 into equation 3.3.14. gives

$$\overline{X} = \frac{3\Lambda}{(\overline{P}_s{}^2-1)} \int_0^1 \left[\frac{(R^2-1)}{4} \left(C_2 + \Lambda \frac{\partial C_2}{\partial \Lambda} \right) \right.$$

$$\left. + \sum_{n=2}^{\infty} \frac{\lambda_n [J_o(k_n) - J_o(k_n R)] \cosh \lambda_n \left(\Lambda \frac{dC_{n2}}{d\Lambda} + C_{n2} \right)}{k_n{}^2 \overline{P}} \right] R dR$$

3.3.18.

Now as $\overline{M} = - \frac{C2}{(\overline{P}_s{}^2-1)}$ equation 3.3.13., it can be seen from equation 3.3.10. that $\overline{M}$ is not a function of $\overline{P}_s$. Hence

$$\overline{W} = f_1 (\overline{P}_s, \Lambda, S)$$

$$\overline{M} = f_2 (\Lambda, S)$$

$$\overline{X} = f_3 (\overline{P}_s, \Lambda, S)$$

For a given bearing design either the aspect ratio of the porous media will be limited by the space available or the lubricant supply pressure will be the limiting factor. Hence performance curves are plotted as functions of Λ for a specific value of S and varying $\overline{P}_s$, except in the case of $\overline{M}$ which is not a function of $\overline{P}_s$, and a specific value of $\overline{P}_s$ and varying S. These performance curves are shown in figures 76 to 80 pages 264 to 268.

The expressions for $\overline{W}$ and $\overline{X}$ contain infinite series and are therefore difficult to evaluate exactly and so numerical integration (Simpson's Rule) has been used to

enable these performance curves to be drawn.

The computer programme used to evaluate these parameters is given in appendix 7.

3.4 THE TIME DEPENDENCE SOLUTIONS

3.4.1 Introduction

An analytic solution of the time dependence system of equations cannot be achieved. Thus a numerical method is used to solve this system of equations, equations 3.2.12. to 3.2.17. which is a composite method comprising:

(i) A semi-analytic technique used to discretise the differential equations, the 'Roscoe' technique (71) see appendix 2.

(ii) The 'Alternating Direction Implicit' technique (A.D.I.) devised by Peaceman and Rachford (58).

(iii) An 'Extrapolated Leibmann Relaxation Parameter'.

As the 'Roscoe' technique is relatively new, it is desirable to show that it gives valid results for the mathematical model of this study.

In order to validate this technique a comparison was made between the analytic solution and the respective numerical solution for a steady-state pressure distribution in the gas film of a porous thrust bearing.

The computation involved and a typical result for comparison are given in appendix 3. Good agreement is seen to be achieved.

The formulation and solution of the difference equations for the time dependence system of differential equations is mathematically long and tedious. For this reason the difference equations are directly quoted in this section and the solution assumed. The full derivation and solution of these are given in appendix 4.

One of the most common problems when dealing with numerical solutions of time dependence problems is that of numerical instability. For example when using a simple explicit technique to solve a time dependence problem it can be shown quite easily that the process stability is governed by

$$\Delta_t \leq (\Delta_r)^2 / 4$$

see figure 11, page 65 for nomenclature. It is therefore advisable before using a complex numerical analysis to ensure that either the process is inherently stable or the maximum value of Δ_t to ensure a stable process is not exceeded. By virtue of this an error analysis of the numerical process used in the time dependence case has been completed. Again the mathematics involved are long and tedious and therefore are presented in appendix 5

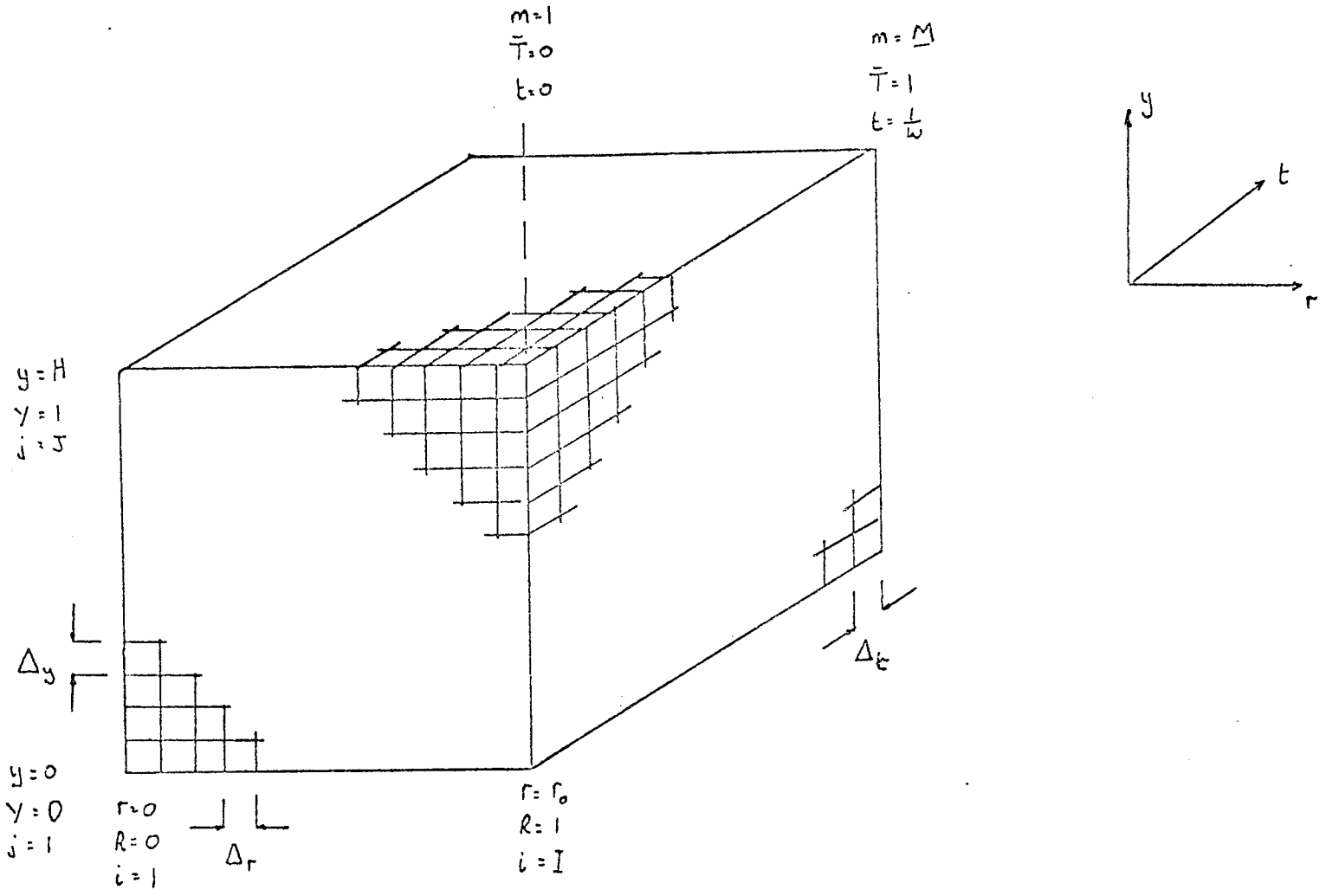

Figure 11 The Three Dimension Finite Grid used in the Numerical Solution of the Time Dependence Equations

rather than in the main text. It is found from this analysis that the process is inherently stable for all values of Δ_t. The limit then of Δ_t is therefore no longer governed by numerical instability, but accuracy of computation and time to reach a converged solution.

Although the numerical process has been shown to be inherently stable the rate of convergence of the process may be slow. If this is the case the process of over-relaxation can be used to increase this convergence rate. The rate of convergence of this process has been investigated and the results of this investigation are given in appendix6.

3.4.2 Solution of the Pressure Distribution in the Gas Film

The numerical process requires two forms of the discretised differential equations. These are written, see appendix 4, firstly implicitely in the R-direction only

$$\left[\frac{\phi_{ij}^{2m+1}-\phi_{ij}^{2m}}{\Delta_t}\right]\frac{\alpha}{(\phi_{ij}^{2m+1})^{\frac{1}{2}}} = \frac{S^2K}{(i-1)\left(1-e^{-\frac{1}{i-1}}\right)} \quad \ldots\ldots$$

$$\left[\frac{\phi_{i+1}^{2m+1} - \phi_{ij}^{2m+1}\left(1+e^{-\frac{1}{i-1}}\right) + \phi_{i-1j}^{2n+1}\, e^{-\frac{1}{i-1}}}{(\Delta_r)^2}\right]$$

$$+ \frac{\phi_{ij+1}^{2n} - 2\phi_{ij}^{2m} + \phi_{i,j-1}^{2m}}{(\Delta_y)^2} \qquad 3.4.1.$$

secondly implicitely in the Y-direction only

$$\left(\frac{\phi_{ij}^{2m+2} - \phi_{ij}^{2m+1}}{\Delta_t} \right) \frac{\alpha}{(\phi_{ij}^{2m+2})^{\frac{1}{2}}} = \frac{S^2 K}{(i-1)(1-e^{-\frac{1}{i-1}})} \quad \ldots\ldots$$

$$\left[\frac{\phi_{i+ij}^{2m+1} - \phi_{ij}^{2m+1}(1+e^{-\frac{1}{i-1}}) + \phi_{i-ij}^{2m+1} e^{-\frac{1}{i-1}}}{(\Delta_r)^2} \right]$$

$$+ \frac{\phi_{ij+1}^{2m+2} - 2\phi_{ij}^{2m+2} + \phi_{ij-1}^{2m+2}}{(\Delta_y)^2} \qquad 3.4.2.$$

The computer solution of equation 3.4.1. and equation 3.4.2. are in the form of a three dimensional array. Each array element is a dimensionless pressure squared value for each nodal point on the numeric grid. As the object of this analysis is to determine the dynamic stiffness and damping ratio values for the porous bearing, only the gas film pressures are of interest, as it is these values that determine the dynamic parameters. Thus only the gas film pressure values are further analysed, i.e. the values of

$$\phi_{ij}^{m} \quad \text{for } 1 \leqslant i \leqslant I, \quad 1 \leqslant m \leqslant \underline{M} \qquad 3.4.3.$$

3.4.3 Harmonic Analysis

One of the boundary conditions of the time dependence system of equations is that the pressure is periodic with time. For a first approximation assume that the gas bearing exhibits linear dynamic characteristics, i.e. constant spring stiffness and damping coefficients. This means that the mass supported by the bearing will have a motion that is not only periodic but sinusoidal as well, such that it may be written:

$$h = h_o + \sigma \sin \bar{T} \qquad 3.4.4.$$

By virtue of this the film pressure will also be periodic and sinusoidal with time but there will be a phase difference between the pressure vector and the film thickness vector such that it may be written:

$$\bar{P} = \bar{P}_o + \bar{P}' \sin (\bar{T} + \tau) \qquad 3.4.5.$$

Now the gas film pressures solved by the numerical method are in the form of $\underline{M}$ equally spaced discrete values of dimensionless pressure for the time range of one cycle for each radial position. This series of discrete values must now be converted, by harmonic analysis, such that for each radial position the dimensionless pressure distribution with respect to time can be expressed in

the form of equation 3.4.5. Thus assume that the gas film dimensionless pressure distribution with time for a given radial position can be expressed as:

$$\bar{P} = \tfrac{1}{2} a_o + \sum_{n=1}^{\infty} (a_n \cos(n\bar{T}) + b_n \sin(n\bar{T})) \qquad 3.4.6.$$

where

$$\left.\begin{aligned} a_o &= \frac{1}{\pi}\int_o^{2\pi} \bar{P}\, d\bar{T} \simeq \frac{2}{M} \sum_{m=2}^{M} \bar{P}_m \\ a_n &= \frac{1}{\pi}\int_o^{2\pi} \bar{P} \cos(n\bar{T})\, d\bar{T} \simeq \frac{2}{M} \sum_{m=2}^{M} \bar{P}_m \cos(n\bar{T}) \\ b_n &= \frac{1}{\pi}\int_o^{2\pi} \bar{P} \sin(n\bar{T})\, d\bar{T} \simeq \frac{2}{M} \sum_{m=2}^{M} \bar{P}_m \sin(n\bar{T}) \end{aligned}\right\} \qquad 3.4.7.$$

As it has been assumed that the gas bearing will exhibit linear dynamic characteristics and thus the pressure will be sinusoidal with respect to time equation 3.4.6. reduces to

$$\bar{P} = \tfrac{1}{2} a_o + a_1 \cos(\bar{T}) + b_1 \sin(\bar{T}) \qquad 3.4.8.$$

Expanding equation 3.4.5. gives

$$\overline{P} = \overline{P}_o + \overline{P}' \sin(\overline{T}) \cos(\tau) + \overline{P}' \cos(\overline{T}) \sin(\tau) \qquad 3.4.9.$$

comparing equation 3.4.8. to equation 3.4.9. gives

$$\tau = \tan^{-1}(a_1/b_1) \qquad 3.4.10.$$

$$\overline{P}' = a_1/\sin(\tau) = b_1/\cos(\tau) \qquad 3.4.11.$$

$$\overline{P}_o = \tfrac{1}{2}a_o \qquad 3.4.12.$$

3.4.4 Dynamic Characteristics

Having determined the dimensionless pressure perturbation $\overline{P}'$ and the phase angle τ the dynamic stiffness and damping forces can now be calculated. Figure 12, page 71 shows a free body diagram of the bearing top plate with all forces imposed. Figure 13, page 71 shows a vector diagram of the dynamic forces acting on the bearing top plate. The magnitude of the dynamic pressure force vector p_f is given by:

$$p_f = 2\pi \int_0^{r_o} p' r \, dr \qquad 3.4.13.$$

which in dimensionless form may be expressed as

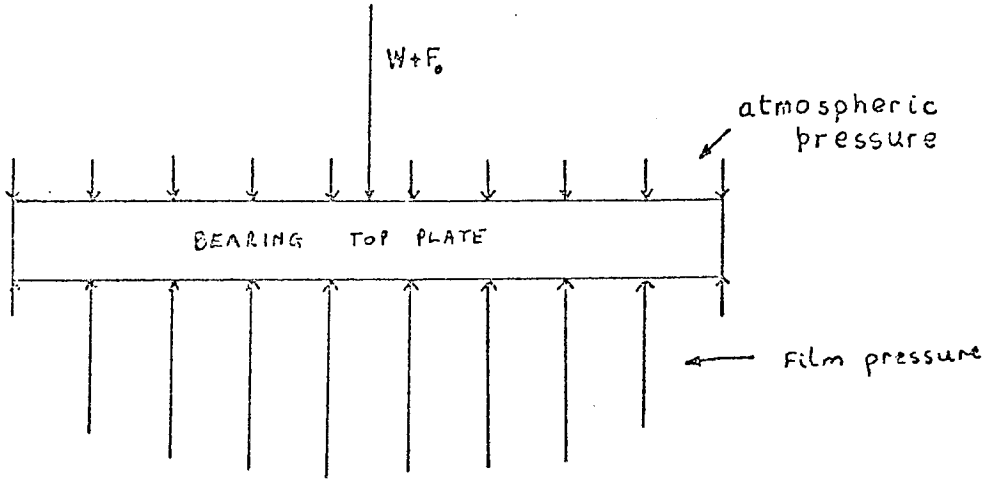

Figure 12 Free Body Diagram of Bearing Top Plate

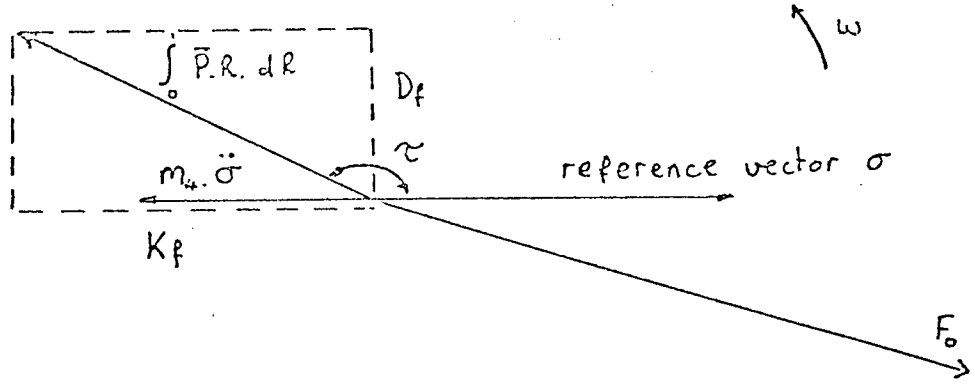

Figure 13 Dynamic Forces acting on Bearing Top Plate, shown in Vector form

$$\bar{P}_f = \frac{p_f}{\pi r_o p_a} = 2 \int_0^1 \bar{P}' \; R \; dR \qquad 3.4.14.$$

It can be seen from figure 13 that the dynamic pressure force vector can be split into two components. These components are:

(i) 90^o out of phase with film thickness vector. This component is in phase with the velocity vector and may be made analogous to the damping force vector for a linear dynamic system.

(ii) 180^o out of phase with the film thickness vector. This may be made analogous to the spring force of a linear dynamic stiffness. Normally in a linear system the spring force is in phase with the displacement vector; however, in this case the 180^o phase shift is due to the minus sign involved with bearing stiffnesses i.e.

$$\text{Static stiffness} = - \, {}^{dW}/_{dh}$$

The dimensionless dynamic spring force is given by

$$K_f = 2 \int_0^1 \bar{P}' \sin(\tau) \, . R \, . dR \qquad 3.4.15.$$

the dimensionless dynamic damping force by

$$D_f = 2 \int_0^2 \bar{P}' \cos(\tau) \, . R \, . dR \qquad 3.4.16.$$

For a linear dynamic system a plot of damping force against velocity and spring force against displacement both result in a straight line graph. As it has been assumed that the bearing will exhibit linear characteristics then this type of graphical representation will demonstrate the accuracy of this approximation.

Upon inspection of the non-dimensional parameters it can be seen that there are three dynamic parametric groups of which γ is a velocity factor. Thus the non-dimensional damping force is plotted against γ. Also γ/β gives a ratio of film thickness perturbation to mean film thickness, i.e. a displacement factor. Thus the non-dimensional spring force is plotted against γ/β. Both of these design curves are plotted for a constant value of α the third dynamic parametric group. These design curves are shown in figures 90 to 97, pages 278 to 285.

CHAPTER FOUR

STEADY-STATE EXPERIMENTAL TECHNIQUES

4.1 INTRODUCTION

The objective of this portion of the experimental work is to provide experimental verification of the steady-state theoretical analysis of Chapter 3. As the theoretical analysis deals only with the idealised situation, the significant practical effects that, when accounted for, will lead to a good correlation between experimental results and theoretical predictions need to be discovered and understood.

This part of the experimental work can be conveniently sub-divided. The first section (section 4.3) is concerned with the measurement of the porous pad permeability, an exact value of which is required for accurate performance prediction. The second section (section 4.4) concerns the measurement of the bearing characteristics, as represented by load capacity, mass flow rate and film thickness. However, before discussing the experimental work the design of the steady-state experimental rig is outlined in section 4.2.

4.2 THE STEADY-STATE EXPERIMENTAL RIG

In all cases a circular, uniform section, stationary, porous pad thrust bearing is to be examined.

It was required to relate non-dimensional load capacity and non-dimensional mass flow rate with a non-dimensional bearing number incorporating the parameters known to influence performance. In particular it was required to determine the individual effects on the bearing performance of the following indpendent variables

(i) Viscous permeability of the porous pad

(ii) Pad aspect ratio.

In order to evaluate the non-dimensional load, non-dimensional mass flow rate and non-dimensional bearing number for each given bearing configuration, provision must be made to measure

(i) Viscous permeability of the porous pad

(ii) Pad aspect ratio

(iii) Air film thickness

(iv) Air temperature for air viscosity

(v) Air supply pressure

(vi) Air flow rate

(vii) Bearing load.

4.2.1 Design of the Permeability Measurement Rig

The basic experimental rig is shown in figure 14 page 76 . The rig is so designed that, upon removal

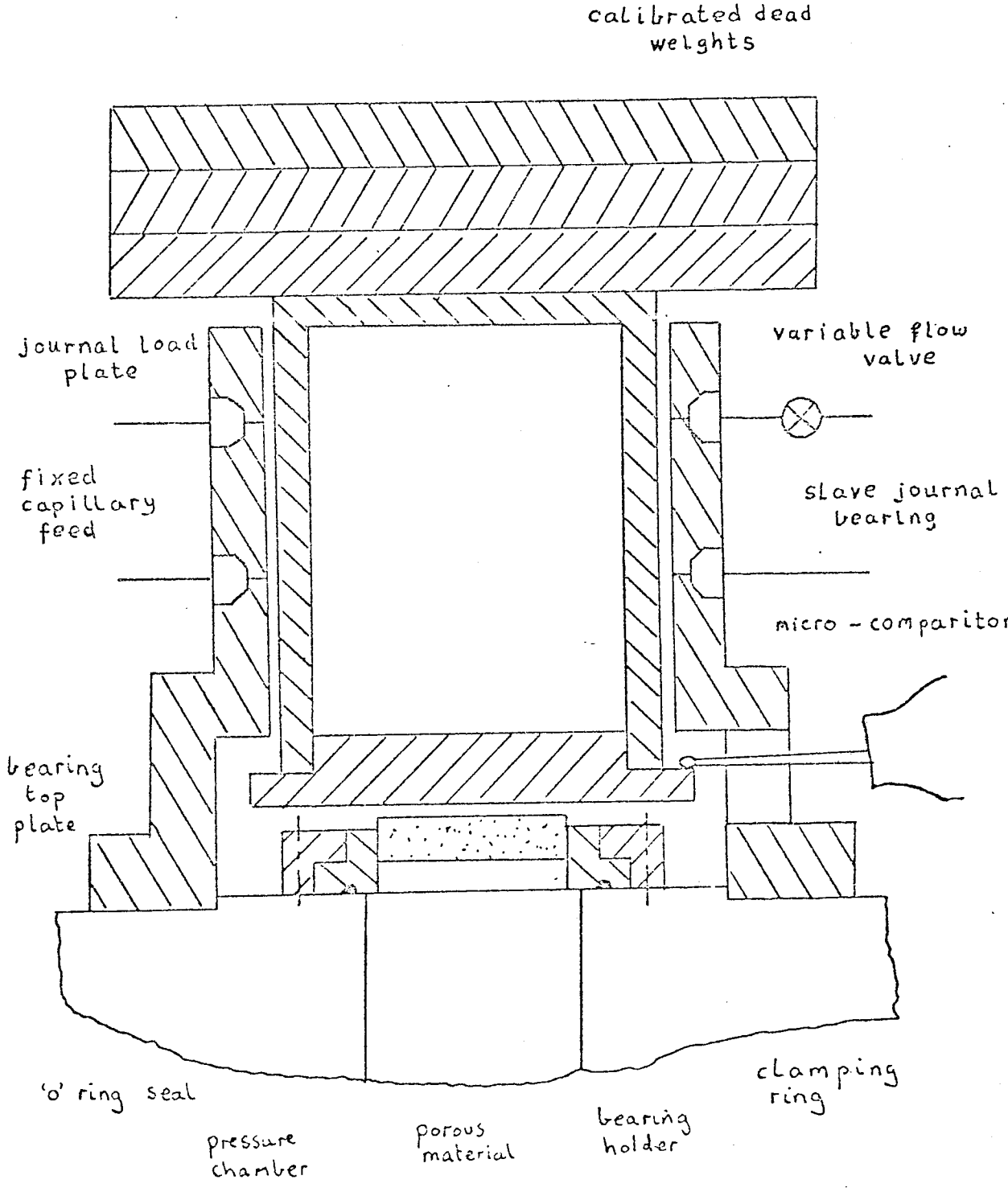

Figure 14 The Steady-State Experimental Rig, used to determine the Porous Thrust Bearing Characteristics

of both the slave journal bearing and thrust bearing top plate, the remaining portion of the rig, see figure 15, page 78 , and plate 1 page 79 , may be used to determine the porous pad permeabilities.

In designing this portion of the rig to measure the porous pad permeabilities certain conditions must be considered, these conditions are: -

(i) As the permeabilities are directional properties it must be ensured that all direction factors involved in their measurements are also uni-directional, e.g. pressure gradient.

(ii) The flow area through the porous pad must be accurately determinable.

To comply with condition (i) the flow through the porous pad must be uni-directional, i.e. the porous material must only have two opposing faces open to air flow and the remaining faces must be sealed to prevent air flow across them. As the pad is circular the circumferential edge may be sealed. Then by applying a pressure drop across the end faces the axial permeability may be determined.

One of the difficulties inherent in this task is that, due to the 'wettability' of porous materials, most sealing compounds placed on their surfaces will permeate to the interior of the material, thus inducing anistropic permeability effects. Greenberg and Weger (43) were

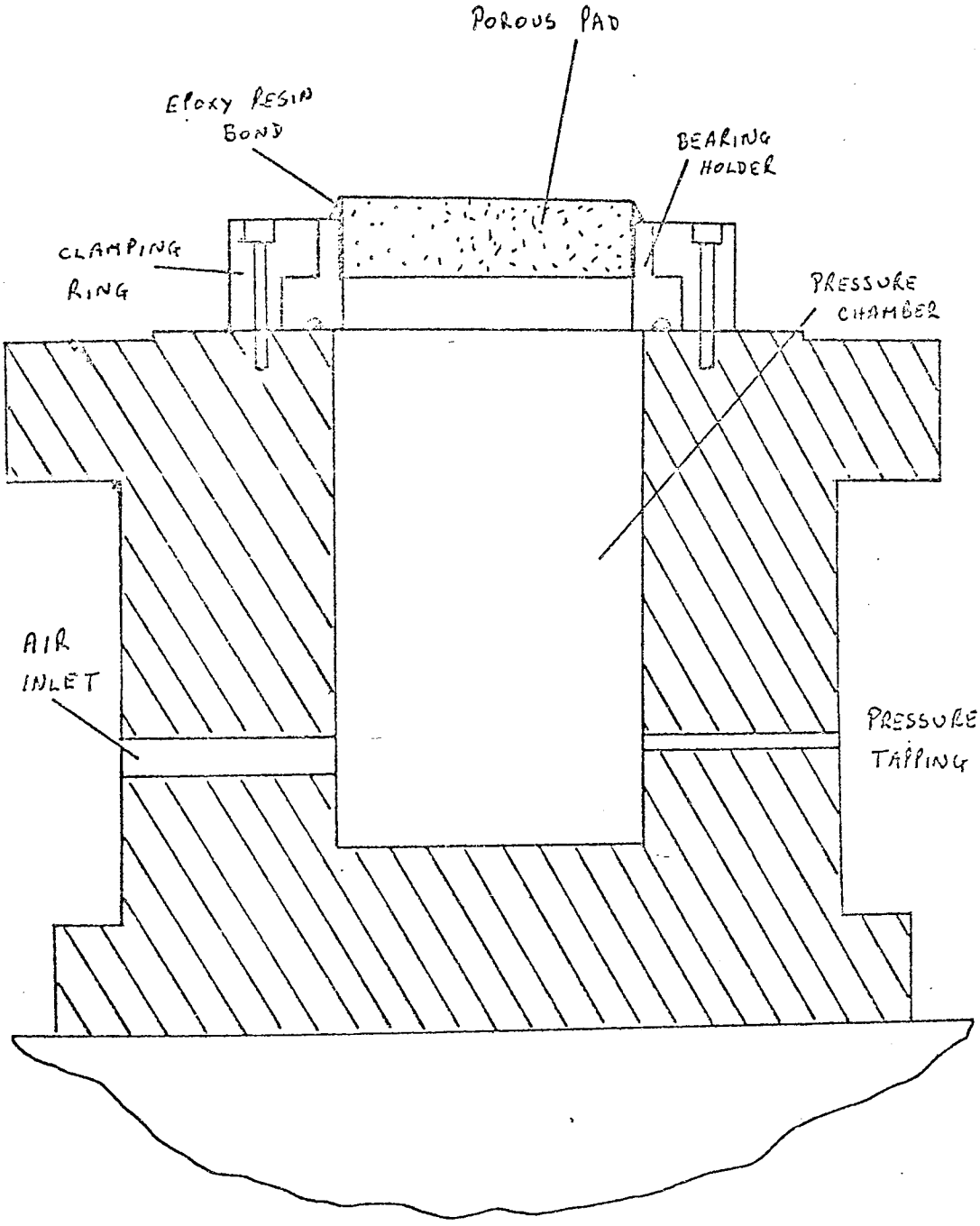

Figure 15 Experimental Rig used to determine Porous Pad Permeability values

Experimental Rig used to determine
Porous Pad Permeability Values

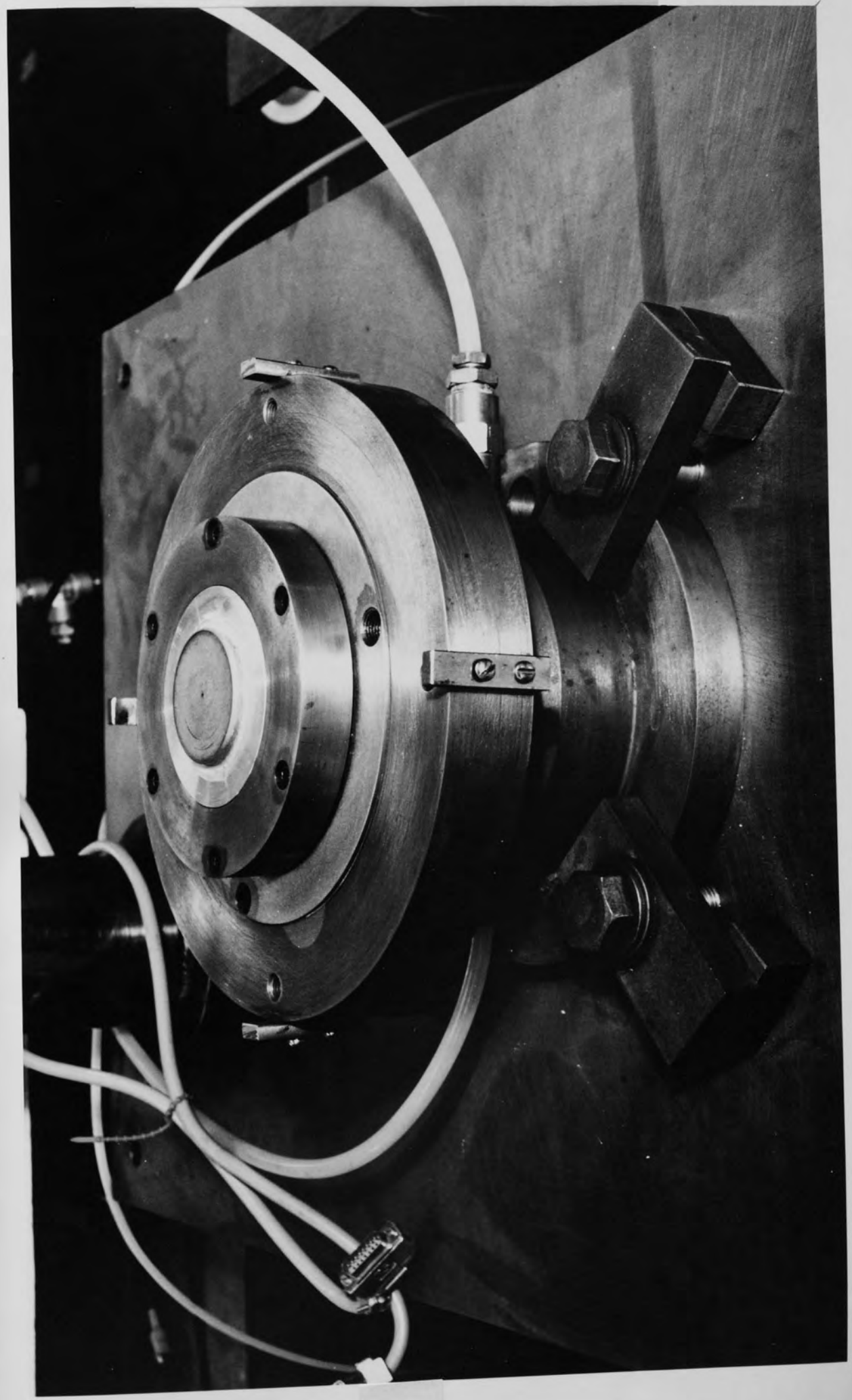

faced with this problem and recommended the use of an aluminium putty. Jones et al (60) also recommended the use of an aluminium putty, a propriety brand 'Devcon F', which consisted of 80% aluminium and 20% epoxy platic. Jones et al considered that penetration should be prevented due to the grain size of the aluminum. As the porous blanks used are machined down to size on the circumferential edge pore smear occurs, Wheeler (66), thus the possiblity of penetration is further restricted.

To comply with condition (ii), the need to easily determine the flow area, a uniform section of porous material was chosen. The section chosen by Jones et al was non-uniform and by virtue of this one directional flow through the porous pad could not have occurred, Morgan (42). However, in choosing a uniform section of material a holding problem occurs in that a circumferential shoulder, as given in the section chosen by Jones et al does not exist and therefore solid location cannot be achieved. In order to obliviate this problem the porous pad, having had the circumferential edge sealed, is cemented, using an epoxy resin, into a bearing holder, see figure 15, page 78.

The bearing holder is secured to the pressure chamber with a clamping ring, shown in figure 15, page 78. An air tight seal between the bearing holder and the pressure chamber is ensured by an 'O' ring seal.

4.2.2 Measurements involved in Permeability Determination

Before sealing the circumferential edge of a porous pad, the pad thickness and outer diameter are measured using a micrometer. After sealing and cementing the porous pad into a pad holder the excess sealant and epoxy resin on the outer diameter of the pad that protrudes out of the bearing holder is chamfered such that the outer diameter of the bearing upper face is equal to the measured diameter seeplate 2, page 82.

It can be seen in figure 15, page 78 that the upper face of the porous pad is vented to atmosphere giving a uniform and constant pressure on this face. The use of a pressure chamber ensures that the lower face is also subjected to a uniform and constant pressure thus complying with the requirements of uni-directional flow. The pressure drop across the pad is measured by measuring the gauge pressure in the pressure chamber using a mercury manometer for gauge pressures less than 2 Bars and a standard Bourdon test gauge for higher pressures.

The air volumetric flow rate is measured upstream of the porous pad using standard variable orifice flow meters calibrated for air at standard temperature and pressure. Conversion to true values of volumetric flow is achieved by using the manufacturers conversion graphs.

Three stages in the construction of
a Porous Thrust Bearing

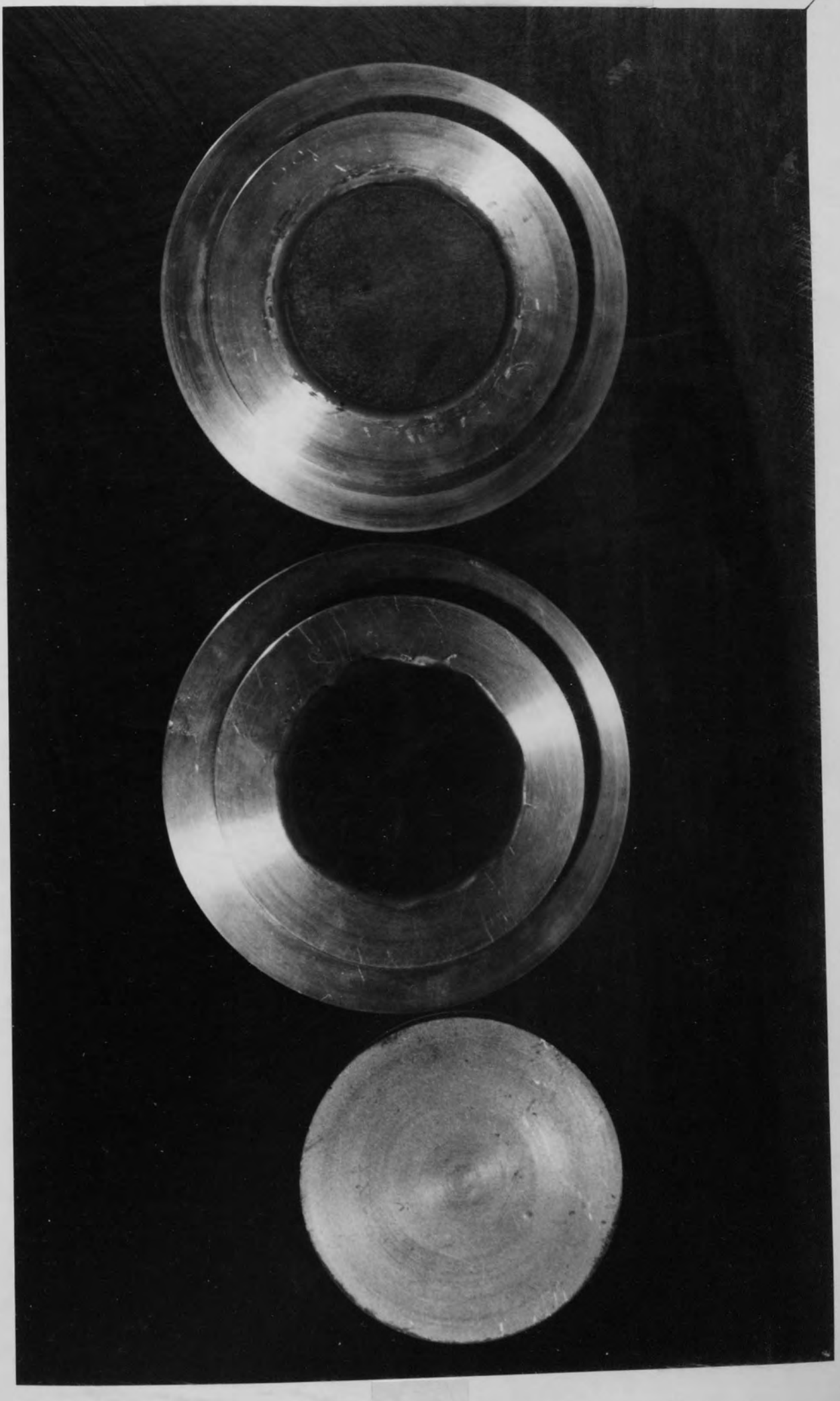

4.2.3 Design of the Bearing Characteristic Measurement Rig

With the slave journal bearing and thrust bearing top plate in position on the permeability measurement rig, as shown in figure 14, page 76 , the thrust bearing formed can be investigated. The slave journal bearing is symmetrically positioned above the porous thrust bearing via a spigot on the pressure chamber. This ensures that the thrust bearing top plate is held centrally over the thrust bearing so that the bearing load is symmetrically applied. Subsidiary air is fed to the journal housing on two admission planes through six equispaced orifices in each plane. In line with the orifices in the upper admission plane are fine adjustment flow valves. The inclusion of these variable flow valves enables bearing tilt to be eliminated and hence the formation of a uniform film for the porous thrust bearing.

The thrust bearing top plate is fitted with pressure transducers to enable air film pressure measurements to be made. The pressure transducers must be flush mounted in the top plate to avoid pockets and hence avoid their possible effects on pneumatic instability. To achieve this, small adaptors were made to the specification given in figure 16, page 84 . Tri-diameter holes were then drilled into the bearing top plate, see figure 17, page 84. The transducer adaptors were inserted into the top plate and locked up to the shoulder, formed by the two smaller

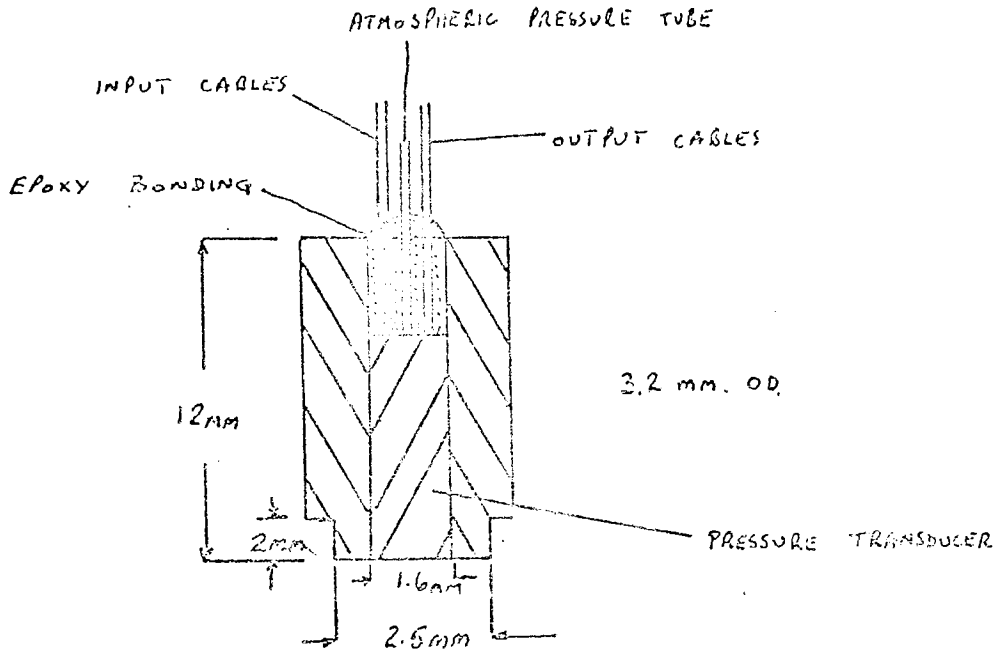

Figure 16 Pressure Transducer Adapter

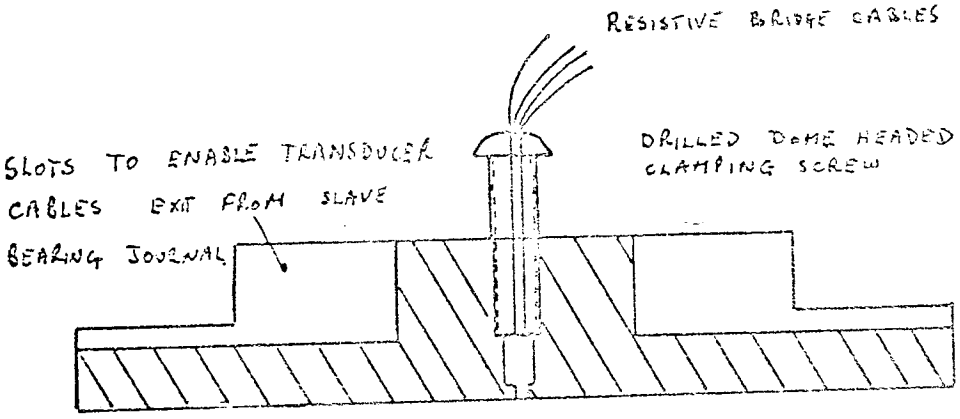

Figure 17 Sectional View of Bearing Top Plate, showing Transducer Adapter hole and clamping screw

diameter holes, by small flat bottom screws. The bearing top plate assembly was then lapped flat. The adaptors were removed and a pressure transducer was cemented into each adaptor using an epoxy resin. Care was taken to note which adaptor fitted which radially positioned hole. To ensure that the transducers were flush to the adaptor face the adaptors were placed on a ground glass surface and the transducers pushed through the adaptors up to this surface. After cementation the adaptors, now with the pressure transducers in position, were refitted into the bearing top plate in their respective positions see plate 3, page 86 . To ensure air tight seal a silicon rubber solution was used to seal the back face of these mountings. This system not only ensures a flush mounting of the transducers, giving a continuous surface to the bearing top plate, but also enables the transducers to be removed should they be damaged or required for use elsewhere.

4.2.4 Measurements involved in Bearing Characteristic Determination

Bearing lift off is monitored by three micro comparitors, equispaced about the thrust bearing, which sense the vertical movement of the bearing top plate.

In addition to the inherent load the thrust bearing can be loaded by means of calibrated dead weights through the load plate, which is attached to the journal of the slave bearing.

Bearing Top Plate showing pressure transducers in position

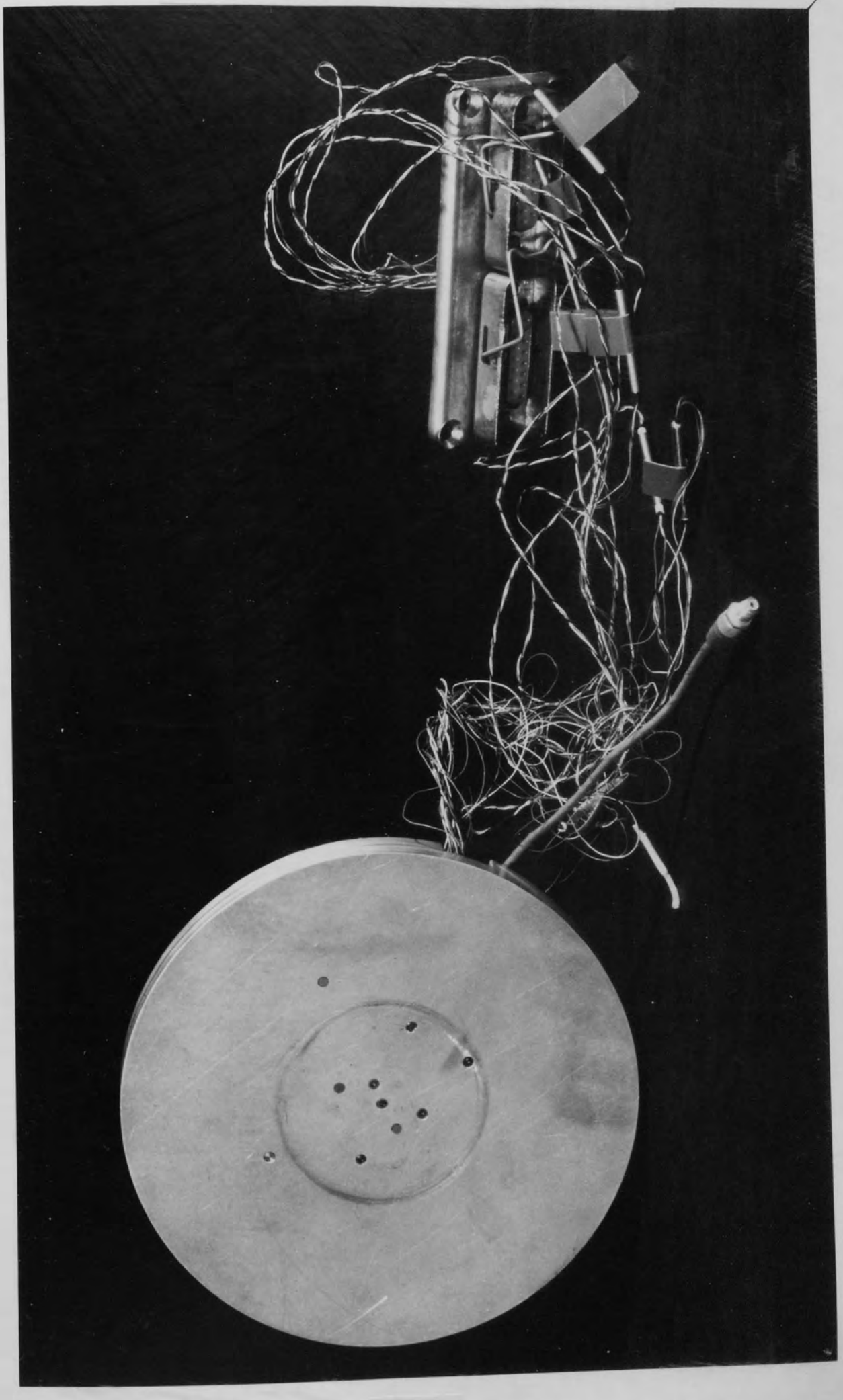

The lubricant flow rate and lubricant supply pressure are monitored in the same way as for a permeability test.

As stated in the above section the bearing top plate is fitted with pressure transducers. The need for these pressure measurements are discussed in section 4.4.
It was initially envisaged that film pressure measurements would be carried out by different means for steady-state and dynamic experiments. The steady-state film pressures were to be measured using standard pressure guages whereas the dynamic film pressures were to be measured by means of pressure transducers. The reason for using pressure transducers for the dynamic measurement was that the pressure gauges require a large sample volume.

The type of pressure transducer chosen was a miniature resistive bridge element transducer, manufactured by Kulite. The major reason for the selection of these transducers stems from their small size, i.e. small external diameter of 1.6mm. Because of their small external diameter it is possible to fit transducers at non-dimensional radial positions of 0.0, 0.2, 0.4, 0.6, 0.8 and 0.9 for a 51mm diameter bearing.

As the pressure sensitive area, 0.07mm in diameter, is small, local pressures can be assessed accurately uninfluenced by any pressure gradients even in the regions of high pressure gradient.

A benefit of these resistive bridge transducers is that both static and dynamic pressures can be measured for,

unlike the piezo-electric crystal transducers, these transducers do not suffer from the charge leakage problem.

However, due to their high cost it was decided to reduce the ancillary equipment, in that only one amplifier and one digital voltmeter would be used to record all transducer outputs. This can be achieved by the use of a high quality multi-channel switch selected to ensure that there is little or no differential voltage drop across the channels.

There are, however, problems involved in this technique. Due to the miniature size of these transducers only a nominal sensitivity is given and a zero balance for each transducer may be as high as $\pm$ 6% full scale deflection. In the case of individual amplification and measurement this presents no problem. In the case of single amplification and measurement of a group of transducer outputs a method must be devised to enable all transducers to be zeroed. This has been achieved by designing a resistive circuit as shown in figure 18, page 89 . Having achieved a zero match the transducers were then calibrated. The calibration curves for these transducers are shown in figures 31 to 32, page 217 to 218.

4.3 PERMEABILITY OF A POROUS MATERIAL

4.3.1 Nature of the Flow Through Porous Materials

Many investigators of porous bearings assume that the flow through the porous material is predominantly viscous

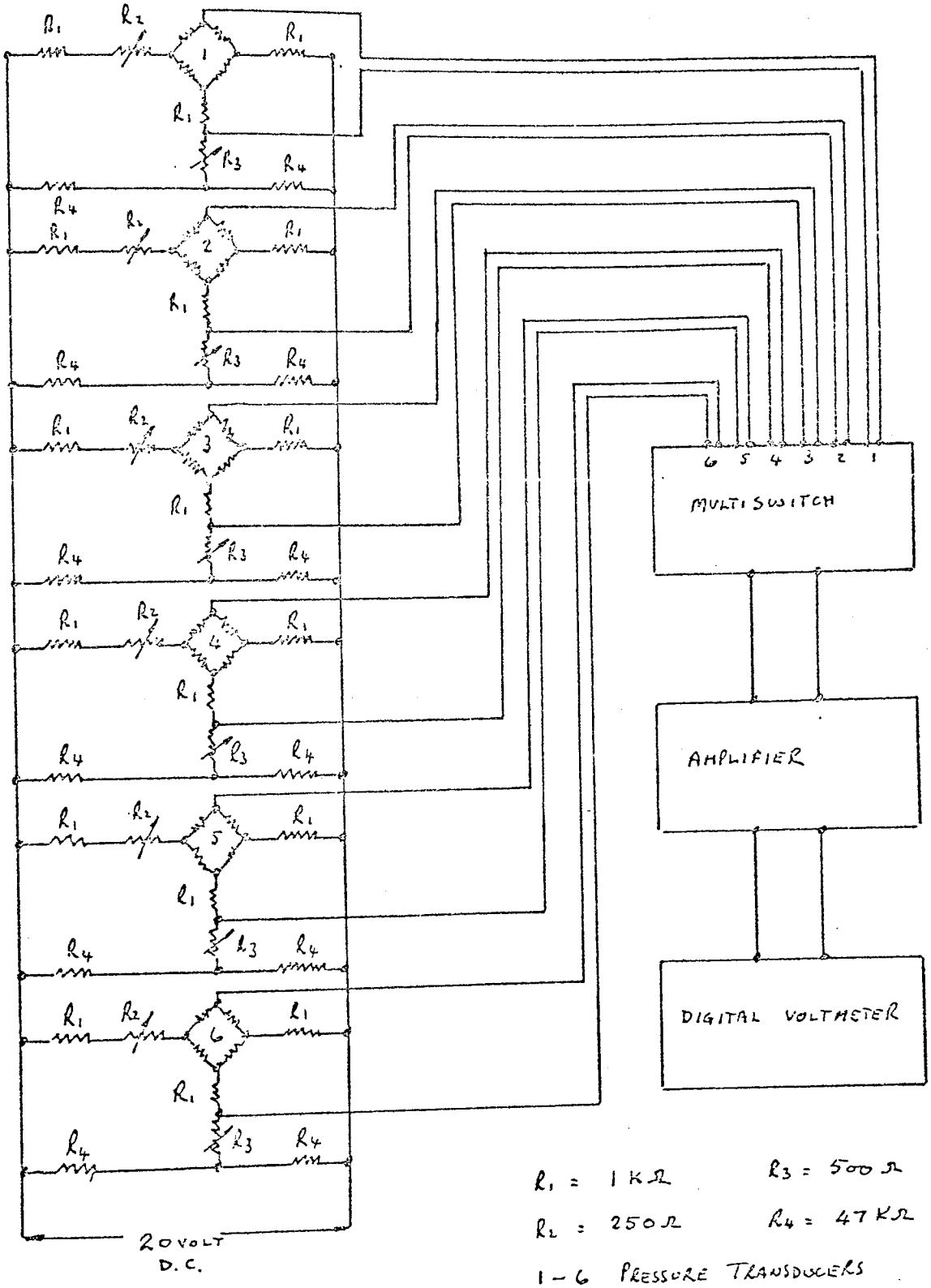

Figure 18 Resistive Balancing Circuit used on Pressure Transducer Outputs

and governed by the Darcy law, i.e. in one-dimensional flow

$$-\frac{dp}{dy} = \frac{\eta}{\Phi_y} v \qquad 4.3.1.$$

Here the viscous permeability of the material is taken as constant for all flow rates. Sterry and Robinson (46) in an investigation of a porous journal bearing found that as the flow rate through the porous media is increased, this viscous permeability as defined by Darcy's law decreases. To overcome this problem other authors, Morgan (42), Greenberg and Weger (43) have used an equation suggested by Forchheimer (24) which introduces the concept of an inertia permeability, such that the governing equation for the flow through the porous material is written, again considering one-dimensional flow, to include an inertia term.

$$-\frac{dp}{dy} = \frac{\eta}{\Phi_y} .v + \frac{\rho}{\phi_y} .v^2 \qquad 4.3.2.$$

Morgan re-wrote equation 4.3.2. in the form

$$\frac{(\Delta p)_y}{H} = \frac{\eta}{\Phi_y} \cdot \frac{Q_m}{A} + \frac{\rho_m}{\phi_y} \frac{Q_m^2}{A^2} \qquad 4.3.3.$$

and re-arranged to give

$$\frac{(\Delta p)_y \cdot A}{Q_m \cdot \eta \cdot H} = \frac{1}{\Phi_y} + \frac{Q_m \cdot \rho_m}{A \cdot \eta} \cdot \frac{1}{\phi_y} \qquad 4.3.4.$$

Equation 4.3.4. suggests that by presenting the experimental results of flow through a porous pad in graphical form by plotting $(\Delta p)_y \cdot A/Q_m \cdot \eta \cdot H$. against $Q_m \cdot \rho_m / A \cdot \eta$, it should be possible to relate them by a single straight line for the whole range of experimental flow rates. The equation thus implies that both viscous and inertia terms are significant at all flow rates. However, clearly from equation 4.3.2. when v is small, v^2 is negligible and it is expected that the inertia term involving v^2 becomes insignificant. Similarly when v is large, v is negligible in comparison to v^2 and therefore the viscous term becomes insignificant. It is considered that as in the case of flow through pipes, so for, porous media two distinct types of flow can be recognised i.e. viscous-dominated flow and inertia-dominated flow with a transition between these regions. Each region is governed by a unique law, i.e. in one-dimensional flow

Viscous region

$$-\frac{dp}{dy} = \frac{\eta}{\Phi} \cdot v \qquad 4.3.5.$$

Inertia region

$$-\frac{dp}{dy} = \frac{\rho}{\phi} \cdot v^2 \qquad 4.3.6.$$

Transition

$$-\frac{dp}{dy} = \frac{\eta}{\Phi} \cdot v + \frac{\rho}{\phi} \cdot v^2 \qquad 4.3.7.$$

Writing equations 4.3.5. to 4.3.7. in the same form as Morgan, gives respectively

$$\frac{(\Delta p)_y \cdot A}{Q_m \cdot \eta \cdot H} = \frac{1}{\Phi_y} \qquad 4.3.8.$$

$$\frac{(\Delta p)_y \cdot A}{Q_m \cdot \eta \cdot H} = \frac{Q_m \rho_m}{A \cdot \eta} \cdot \frac{1}{\phi_y} \qquad 4.3.9.$$

$$\frac{(\Delta p)_y \cdot A}{Q_m \cdot \eta \cdot H} = \frac{1}{\Phi_y} + \frac{Q_m \rho_m}{A \cdot \eta} \cdot \frac{1}{\phi_y} \qquad 4.3.10.$$

Considering the case where full inertial flow is not attained, then presenting experimental results of flow through a porous pad in graphical form by plotting $(\Delta p)_y \cdot A/Q_m \cdot \eta \cdot H.$ against $Q_m \cdot \rho_m / A \cdot \eta$ should exhibit the two regions expressed by equation 4.3.8 and 4.3.10. Figure 19, page 93 shows the results of passing air through a porous bronze specimen. It can be clearly seen that these two regions are in evidence.

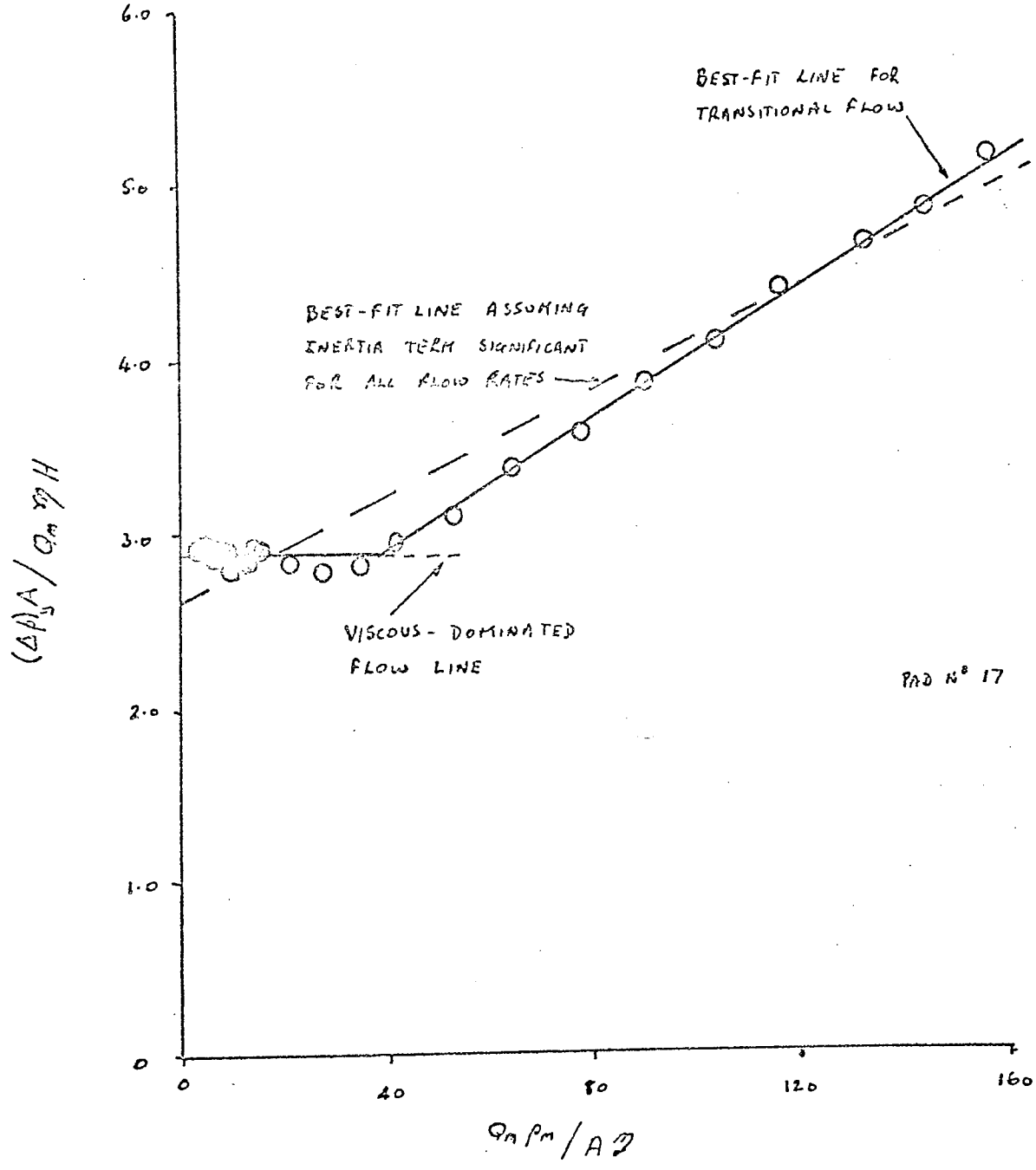

Figure 19 Experimental Results of Flow through a Porous Bronze Pad presented in the form described by Morgan

4.3.2 Determination of the Permeability Values

Using the horizontal 'viscous' line in figure 19, page 93 in conjunction with equation 4.3.8. would yield a value for the viscous permeability. However, due to experimental scatter, the value would be subject to a wide tolerance.

A technique then for accurately determining the viscous permeability is required. Equation 4.3.5. in finite form may be written

$$(\Delta p)_y = \frac{H.\eta}{\Phi_y A} \cdot Q_m$$

or

$$l_{1o}(\Delta p)_y = l_{1o}\left(\frac{H\eta}{\Phi_y A}\right) + l_{1o}Q_m \qquad 4.3.11$$

Thus plotting $l_{1o}(\Delta p)_y$ against $l_{1o}Q_m$ will result in a straight line of unity gradient. The intercept of this line with the y axis, at $l_{1o}Q_m$ equal to zero, would give the value of $l_{1o}(H\eta/\Phi_y A)$. Now $l_{1o}Q_m$ can never equal zero, however, by use of a mathematical method, the least squares technique, a value of this intercept can be established. The viscous permeability can then be determined from this value. The advantage of this form of graphical representation is that when transitional flow is encountered the experimental points will break

away from the unity gradient line, therefore establishing at what pressure drop the Darcy law assumption no longer holds true. Figure 20, page 96 shows the previously mentioned results plotted on $l_{10}(\Delta p)_y - l_{10}Q_m$ basis and it can be clearly seen where the Darcy region ends and the transitional region begins.

Having now determined the viscous permeability of the specimen the inertia permeability must be evaluated. Now the transitional region is emphasized by the log-log graph and for this type of flow equation 4.3.10. holds true. Using the same technique as Morgan and using only the experimental values in the transition region allows the inertia permeability value to be determined. It should be noted that the intercept value given by this method does not give the reciprocal value of the viscous permeability, as can be seen in figure 19, page 93.

All porous material permeability values for this work have been determined using these improved techniques, i.e. the $l_{10}(\Delta p)_y - l_{10}Q_m$ plot and modified Morgan plot.

Figures 33 to 49, pages 219 to 275 are the experimental results of permeability tests for a selection of stainless steel porous pads.

4.4. THE MEASUREMENT OF THE STEADY-STATE BEARING CHARACTERISTICS

The steady-state bearing characteristics to be examined are the variation of the load capacity, lubricant

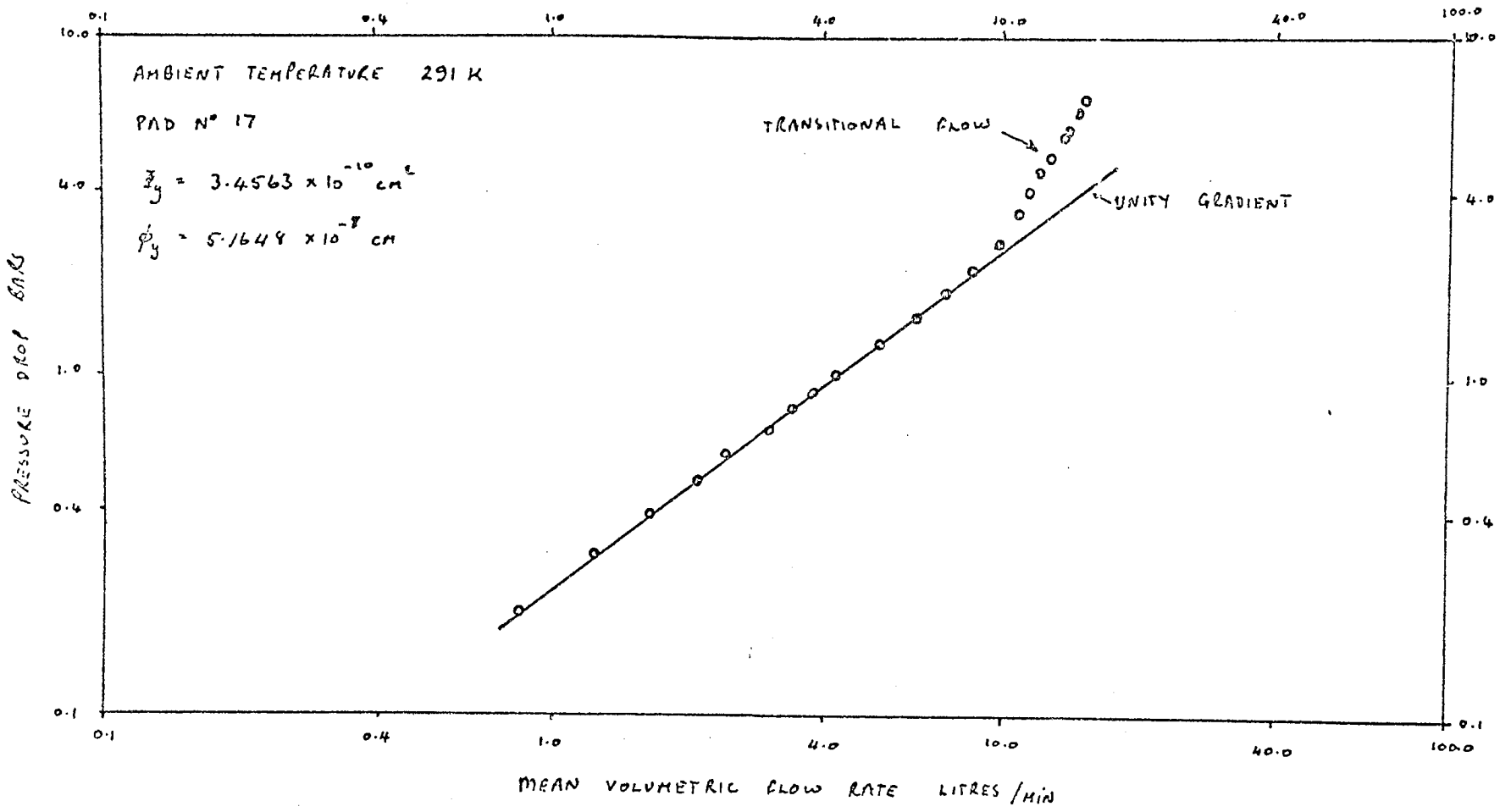

Figure 20 Variation of Mean Volumetric Flow Rate through a Porous Bronze Pad with the Pressure Drop across the Pad

flow rate and static spring stiffness with film thickness. In gas bearings film thicknesses of less than 2 micron may be encountered and hence it must be ensured that:

(a) The two surfaces forming the bearing are flat.

(b) The film is uniform.

(c) True evaluation of the film size is obtained.

In order to satisfy condition (a) both surfaces must be finely machined. The bearing top plate of aluminium presents no problem as conventional machining techniques can be used, i.e. fine grinding and lapping. The porous blanks, however, are more difficult to machine. These blanks are produced by a sintering process. During this process powdered metal is heated and compacted in specially made presses and a certain amount of elastic deformation of the powder takes place. When the presses are removed the deformed metal 'springs back' to its natural shape so that, even though flat plates are used to compact the metal, the product is not perfectly flat. Conventional machining to eliminate this spring back cannot be used due to the pore smearing problem, Wheeler (66). Wheeler suggests that the porous material to be machined should first be immersed in oxalic acid. The acid should then be heated to its melting point and allowed to impregnate the metal. After cooling, the metal may be machined as a solid face, the acid supporting the porous metal so that no smearing of the pores takes place. Jones (60) attempted this process,

using a porous material which had the sides sealed with the aluminium putty 'Devcon F', and found that the temperature required to melt the oxalic acid caused the putty to peal away from the porous pad. Jones then used a freeze lapping process, also suggested by Wheeler. In this process the porous material was impregnated with water and then placed in liquid nitrogen thus freezing the water. The porous material was then lapped on a lapping plate which was kept at a temperature of -78C by placing in a mixture of dry ice and acetone. However, this freeze lapping technique could not be used here due to the design of the bearing. It may be recalled that the porous pad, after having sealed the radial edge with aluminium putty, was cemented into a bearing holder. The coefficient of expansion of the porous material differed from that of the material of the bearing holder, thus, upon freezing the epoxy bond was damaged. If freeze lapping was attempted before cementing the pad into the bearing holder two problems are encountered, these being: -

(i) the lapped face may be contaminated with epoxy resin during cementation

(ii) the pad may not be truely aligned i.e. the upper face of the pad may not be parallel to the lower face of the pad holder.

Due to these problems a new technique of machining the porous material had to be devised. Various methods were attempted, Taylor (72), before a solution was achieved. The process of machining eventually used is as follows:-

(i) Cement the porous pad into the bearing holder.

(ii) Machine grind the top face.

(iii) Clamp the bearing holder to the pressure chamber.

(iv) Connect air supply.

(v) Acid etch using a mild solution of Nitric acid.

(vi) Clean pad using water.

(vii) Leave pad to dry by continuing to blow air through the material.

In grinding the upper face of the bearing the pores are smeared over and the flow of air through the pad is severely limited. The acid etching solution is then wiped over the machined surface while the pad remains pressurised. The effect of pressurising the porous material is that the etching proceeds until the pores are unsmeared. Upon clearing the pores the flow of air drastically increases resulting in the prevention of acid penetration of the pad and further etching of the unsmeared pore.

Now it must be ensured that the air film is uniform, condition b. Non-uniformity of the air film can be created in two possible ways, the first being that of bearing tilt. This problem has already been discussed

in section 4.2.3 . dealing with the design of the steady-state rig. The second possible cause is due to structural flexure of the porous pad.

The porous pad may be made analogous to a diaphragm rigidly held at the outer edges. If the elastic properties of the porous material are inadequate flexure of the porous pad will occur. It should be noted that these elastic properties are inferior to the parent material due to the discontinuities within the porous structure. Should the porous pad bow a non-uniform film will be created causing a change in the pressure distribution in the film, Taylor and Lewis (70) appendix 8. It must, therefore, be ensured that a negligible pad flexure occures. This is achieved by measuring any deflection of the centre of the pad relative to the circumferential edge during pressurisation of the pad. Figure 21, page 101 shows the method employed for checking pad flexure.

Having now ensured that the two surfaces forming the bearing are flat and the air film is uniform, conditions (a) and (b) the true evaluation of the film thickness must be considered. As previously mentioned small thickness values may be encountered and the surface finish, due to acid etching of the porous pad and indeed the pores themselves, may be of the same order of magnitude as the film thickness. It is a fairly well established fact that the mean roughness of a porous surface has to be taken into

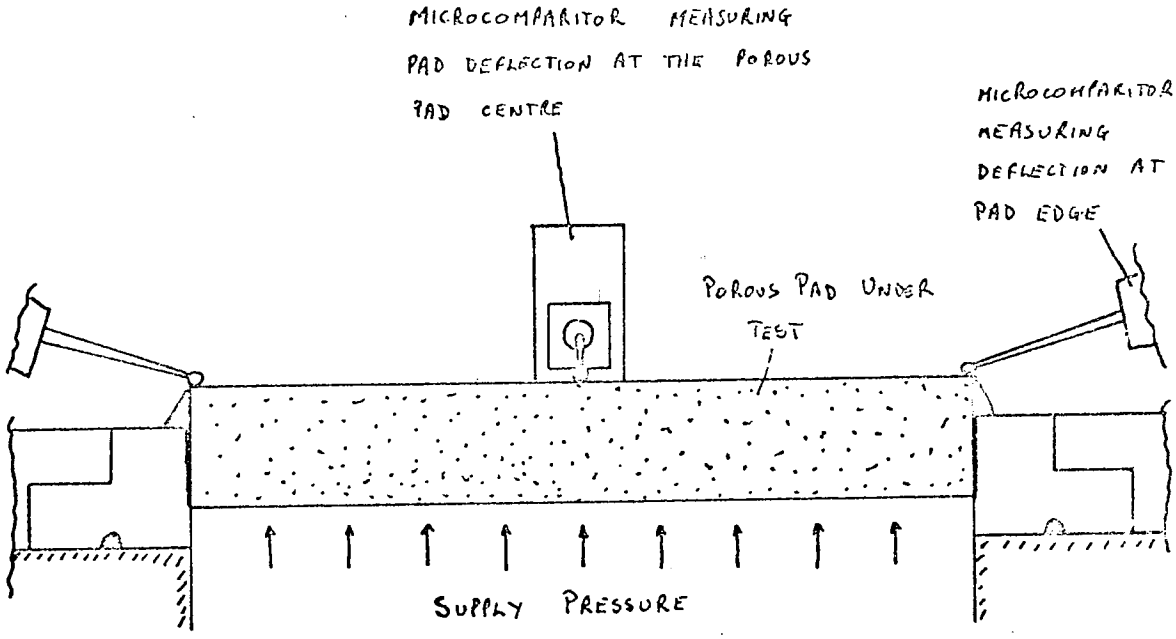

Figure 21 Checking for Porous Pad Flexure when Pad subjected to Supply Pressure Loading, by varying Supply Pressure Shear deflection of Pad Bonding can be Calibrated

account when assessing the bearing clearance, Sneck and Elwell (48), Garguilo and Gilmour (57), Yabe (50). The problem is how to relate this mean roughness to the film thickness. The 'Centre Line Average' technique assesses the roughness over a very small area and in itself is not a measure of mean roughness over the whole bearing. One technique would be to draw a graph of the surface along a diameter of the pad under consideration, using a Rank Taylor Hobson Tallylin machine. The maximum and minimum metal lines could then be drawn and a mean roughness determined. This process is subjective in that it depends upon the skill of drawing the maximum and minimum metal lines. A considerable number of these graphs would have to be produced and statistical methods employed to evaluate a mean roughness value that may be considered valid.

A far simpler technique has been devised and is as follows. Figures 22 and 23, page 103 show the ideal and real air film respectively. It can be shown that for the ideal air film the volumetric flow at any radial position can be expressed by

$$Q_r = 2\pi r \int_0^{h_o} U \, dy \qquad 4.4.1.$$

Substitution of equation 4.3.1 for u gives upon integration

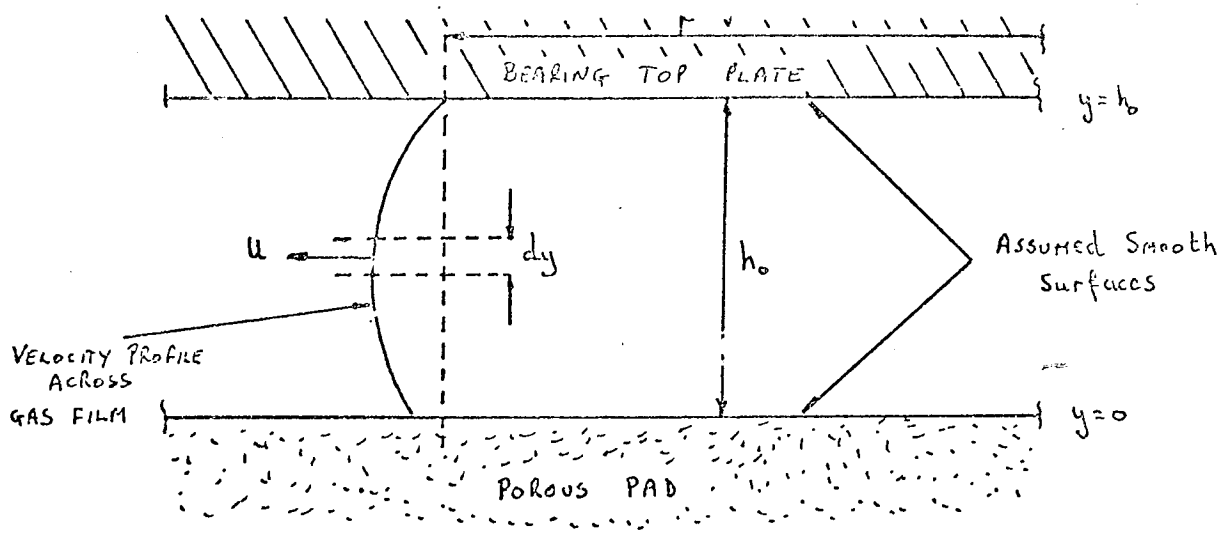

Figure 22 Ideal Air Film assumed in Theoretical Analysis

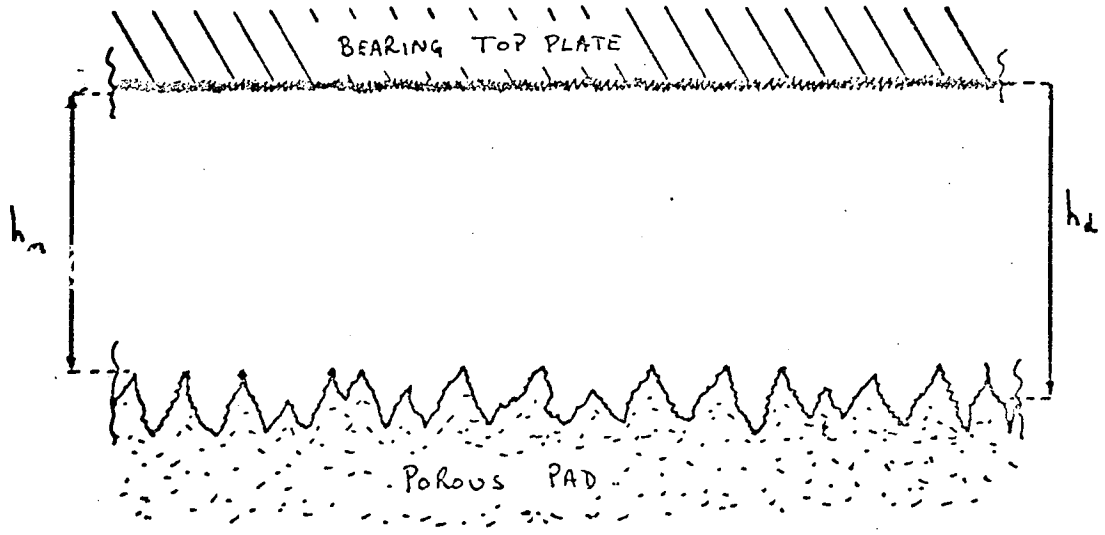

Figure 23 Real Air Film showing Surface Finish Problem

$$Q_R = - \frac{2\pi r_o^2 \Phi_y R}{\eta . H . \Lambda} \left[\frac{\partial p}{\partial R}\right]_R \qquad 4.4.2.$$

Now in a porous thrust bearing the air filters into the air film over the whole of the bearing. Therefore the only radial position in the film at which the gas mass flow rate is known is at the outer radius, where it equals the measured mass flow rate to the bearing, i.e. at R = 1.0 .

At R = 1.0 equation 4.4.2. may be written

$$Q_{R=1} = - \frac{2\pi r_o^2 \Phi_y}{\eta H \Lambda} \cdot \left[\frac{\partial p}{\partial R}\right]_{R=1} \qquad 4.4.3.$$

or

$$\Lambda = - \frac{2\pi r_o^2 \Phi_y}{\eta . H . Q_{R=1}} \cdot \left[\frac{\partial p}{\partial R}\right]_{R=1} \qquad 4.4.4.$$

The gas film thickness is contained in the bearing number Λ.

For the real case an equivalent ideal film thickness h_d, is postulated for theoretical analysis. It is considered to be the addition of the measured lift of the

bearing h_m and an equivalent pneumatic clearance SF, such that

$$h_d = h_m + SF \qquad 4.4.5.$$

If the volumetric flow rate and pressure gradient at the outer radius of the bearing can be determined then the bearing number and hence the film thickness h_d can be determined through equation 4.4.4. The volumetric flow rate at the outer edge can easily be computed from the mass flow rate, which is known. In order to evaluate the pressure gradient at the outer edge, pressure transducers were placed into the bearing top plate at various radial positions and the pressure gradient computed using a polynomial regression technique. If equation 4.4.5. is true then by plotting the derived film thickness h_d, which has been computed from equation 4.4.4., against the measured lift h_m a straight line of unity gradient should be obtained, the intercept of this straight line with the h_d axis giving the value of SF. Figure 24, page 106 shows the results of a series of load tests on bearing number 1. It can be seen from this that a unity gradient is achieved. This unity gradient has been achieved by taking into account any movement of the porous pad due to shear deflection of the porous pad epoxy bond.

Calibration of this shear deflection before the bearing load test is achieved by relating pad movement

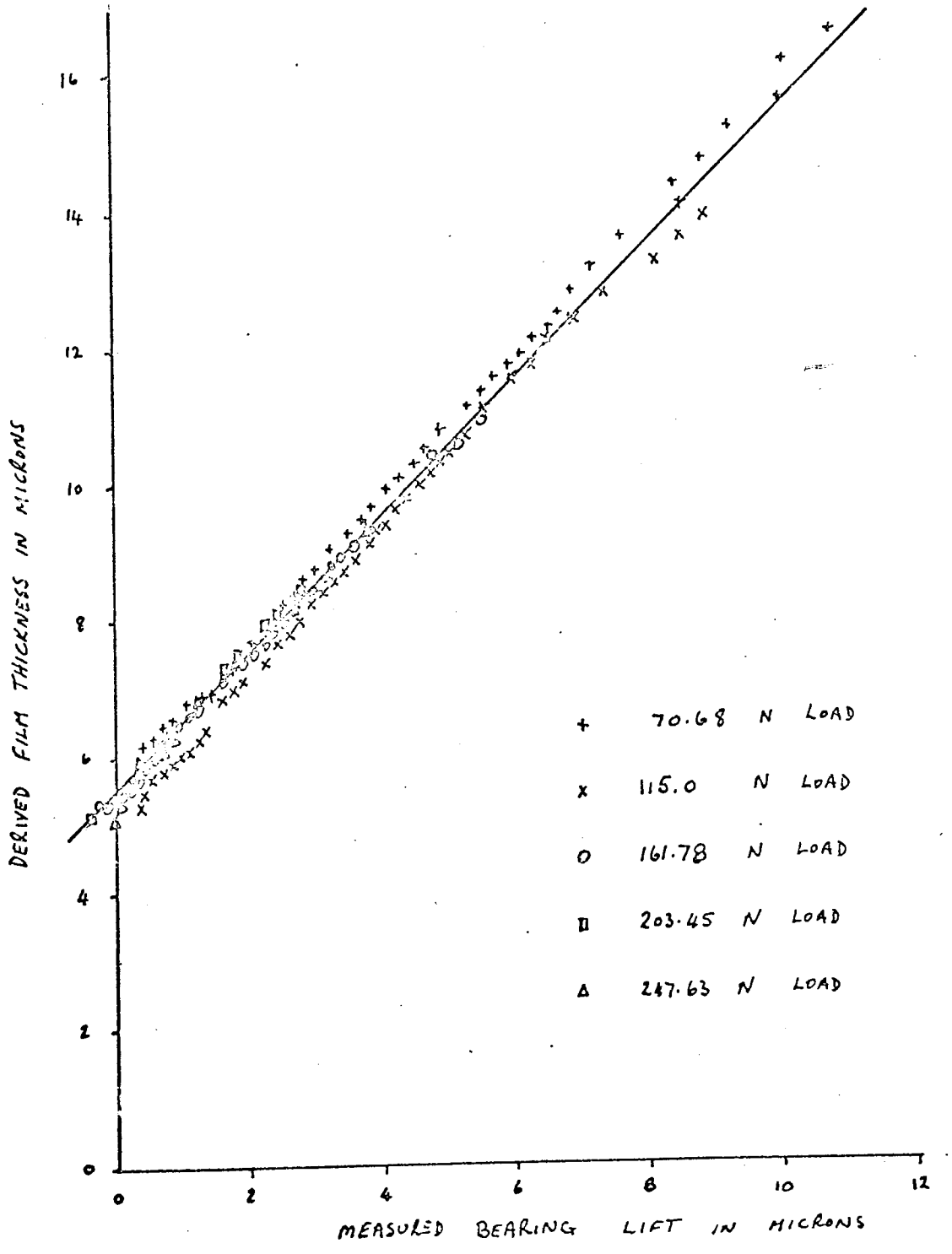

Figure 24 Variation of Derived Film Thickness with Measured Bearing Lift for Bearing Pad Number 1

to the mean applied pressure. In the load test itself the mean applied pressure is taken to be the supply pressure less the mean film pressure w/A.

This pressure gradient technique has been used to measure bearing clearances for all steady-state experiments. However, to ensure a uniform lift off of the bearing load the mitronic comparators were used.

Having now ensured that the gas film thickness can be correctly assessed the experimental verification of the design curves can be attempted. There are two possible ways in which the bearing film thickness may be altered, these two methods being:

(i) Keep the air supply pressure constant and vary the actual bearing load.

(ii) Keep the actual bearing load constant and vary the air supply pressure.

In using the first method great care must be employed in loading and unloading the bearing. The loads must be placed symmetrically on the bearing load plate so that uncontrollably large bearing tilts do not occur.

Care must also be taken to ensure that the bearing is not rotated or suddenly loaded as the delicate mitronic comparators may be disturbed.

The second method does not require the bearing rig to be disturbed. By altering the air supply pressure practically no bearing disturbance of the type described

above occurs and only small bearing tilts have been experienced, these being easily removed by use of the variable flow valves. However, in using this method of testing the design curves of load capacity and spring stiffness shown in figures 76 to 80, pages 264 to 268 , cannot be checked directly as both load and stiffness have been shown to be functions of supply pressure. It is therefore necessary to draw a design curve in which the actual bearing load is constant and the supply pressure changes. As this simply entails a small amount of additional computation the saving in experimental accuracy was considered more beneficial and therefore mathod (ii) has been used to change the bearing film thickness in all steady-state experiments.

Figures 54 to 75, pages 240 to 263 , show experimental results of these tests in comparison with the theoretical predictions.

It should be noted that although transitional flow through the porous pad was achieved in the permeability tests the inherent load of the steady state rig and the upper pressure limitation of the equipment prevent transition flow being encountered during bearing tests.

Before reading the section dealing with the dynamic experimental analysis the reader may wish to refer directly to the discussion of the steady-state results. This discussion can be found in Chapter 6, sections 2, 3 and 4.

CHAPTER FIVE

EXPERIMENTAL TECHNIQUES OF THE FORCED VIBRATION TESTS

5.1 INTRODUCTION

The objectives of this portion of the experimental work are: -

(1) To provide experimental verification of the time dependent theoretical analysis of Chapter 3.

(2) As the theoretical analysis of the time dependent equations considers the bearing film to possess linear characteristics the practical limitations of this linear theory must be determined.

This Chapter has been conveniently sub-divided into two sections. The first section, section 5.2. is concerned with the design of the forced vibration rig. The second section is concerned with the experimental approach that has been used to determine the dynamic characteristics of these bearings.

5.2 THE FORCED VIBRATION EXPERIMENTAL RIG

5.2.1 Rig Design Specification

In designing a forced vibration rig to enable the dynamic characteristics of these bearings to be determined certain basic design conditions must be adhered to, these conditions are:

(i) The bearing rig must be shielded from any extraneous vibrations.

(ii) The forced vibrations must be applied in the vertical plane only, all other degrees of freedom must be suppressed.

(iii) The vibration force must be centrally applied to the test bearing.

The main reasons for these conditions are:

(a) Due to the relatively small film thickness the amplitude of any applied vibration will also be small, i.e. only a small input force will be applied. Any extraneous vibration force may result in a severe influence on the experimental results and/or bottoming of the bearing may occur causing damage to the instrumentation.

(b) No measurement of the extraneous motion or force could be made.

(c) Experimentation must be carried out under conditions as similar to the theoretical model as is practical, the

theory assumes only one degree of freedom.

(d) By applying an offset vibration force bearing tilt would ensue.

The following rig specification was used in order that the design allowed for these conditions.

(i) The rig was to be mounted on a large seismic mass such that extraneous vibrations would be damped out by this large mass.

(ii) The rig was to be isolated from the earth via vibration isolation pads.

(iii) The vibrator was to be de-coupled from the bearing rig, in that the vibrator body was to be isolated from the test rig and only the vibrator shaft directly connected to the rig.

(iv) The vibrator must be centrally positioned over the bearing rig.

(v) Motion of the bearing top plate was to be constrained to vertical motion only. This constraint, however, must induce little or no frictional drag on vertical motion as only small input forces are to be applied during testing.

In compliance with this rig specification the design shown in figure 25, page 113 and plate 4, page 114 was used. It can be seen that the steady-state bearing rig has been clamped onto a large seismic mass. The seismic mass consists of a large block of concrete on which a large bed plate of steel has been cemented via a vibration

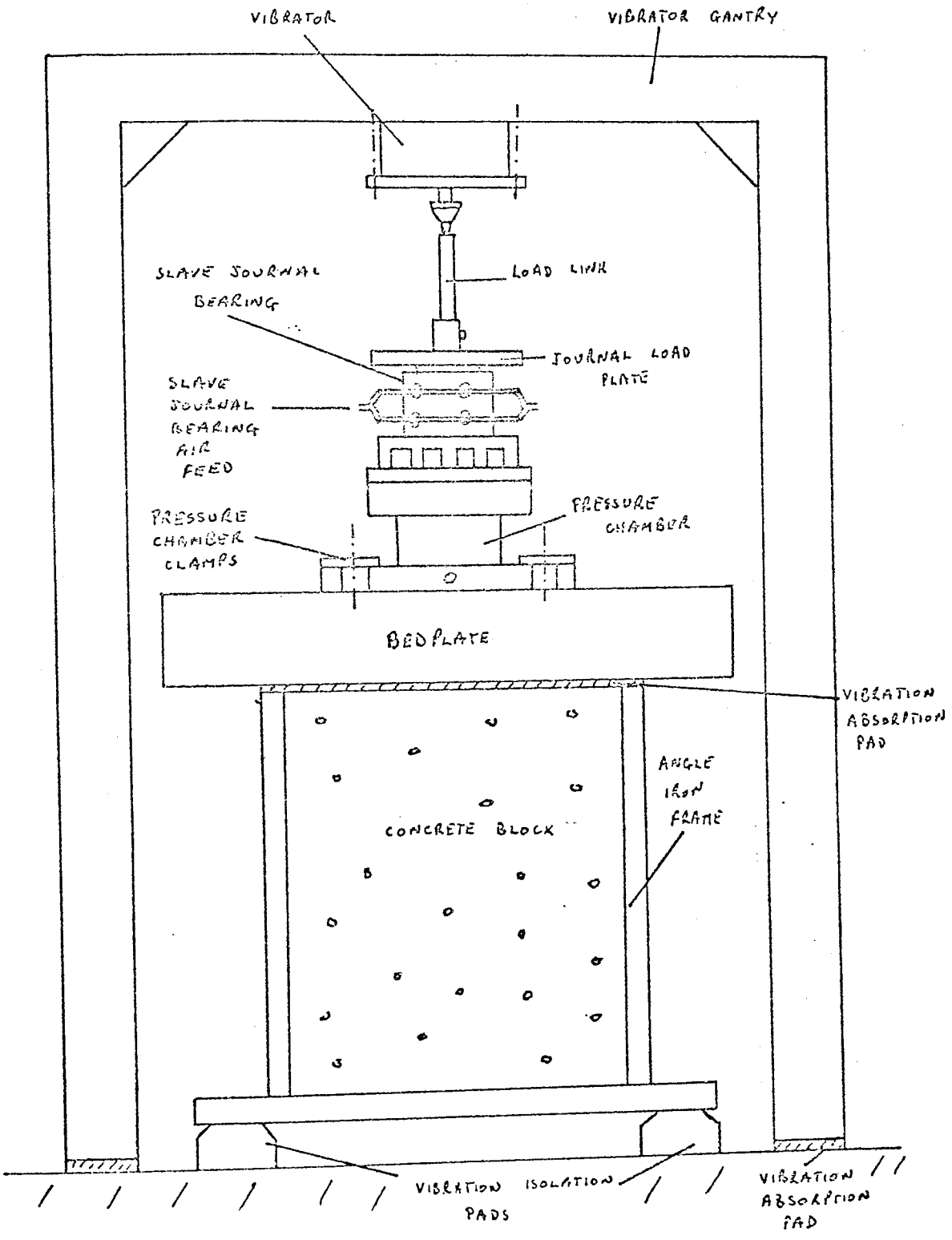

Figure 25 Experimental Rig used in Forced Vibration Tests

Experimental Rig used in the Forced Vibration Tests

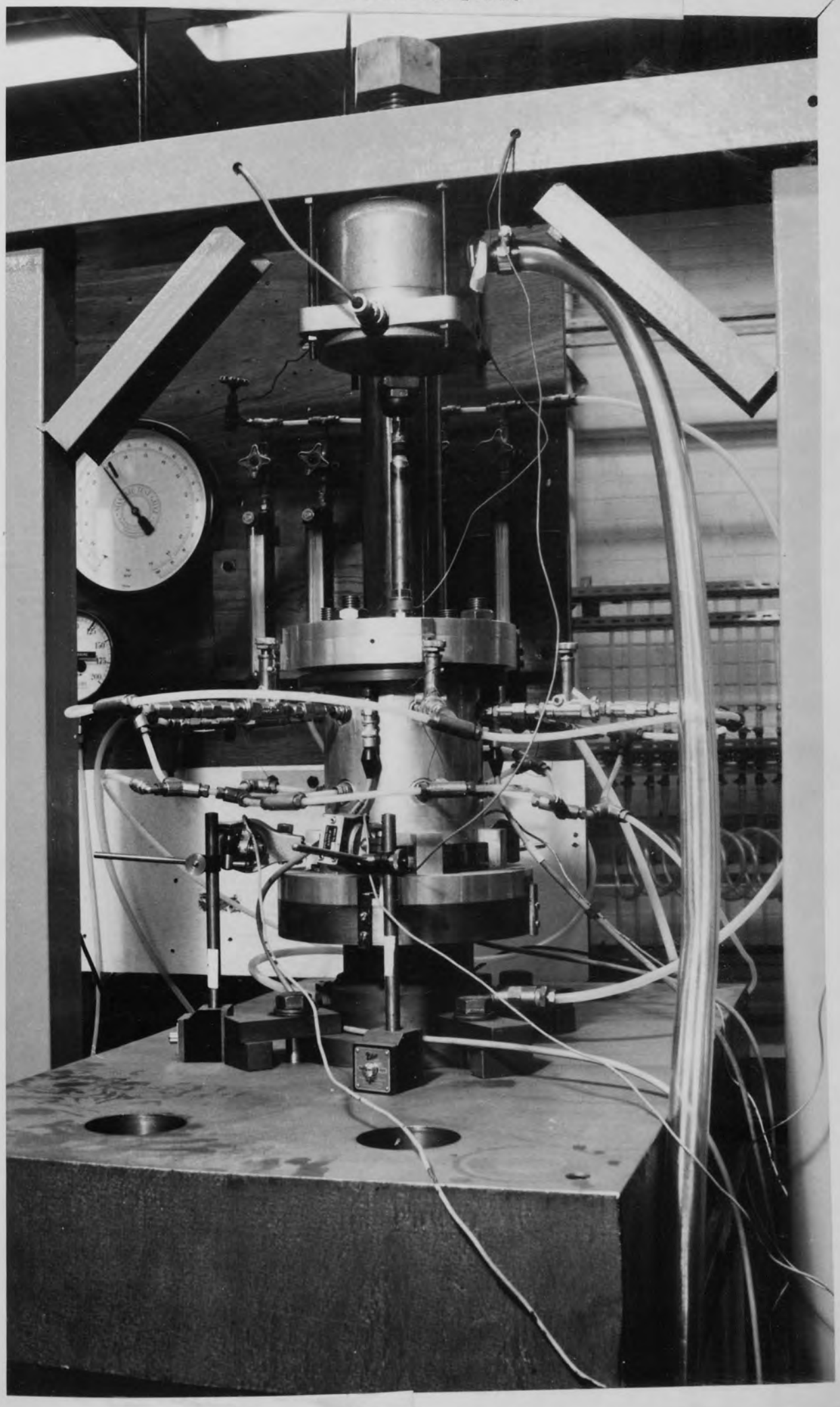

absorption pad. The concrete mass has been cast in an angle iron frame which enables four vibration isolation pads to be mounted at each corner.

The vibrator has been mounted to a bridging gantry that spans the seismic mass. This structure has also been isolated from the floor via vibration absorption pads. The gantry was positioned centrally about the seismic mass. The vibrator body is held to the gantry by four 'all thread' studs which pass through four location lugs on the vibrator body and screw into the gantry top beam.

The vibrator shaft is connected to the load plate, secured to the journal of the slave bearing, by a specially designed load link. This load link can be split into three sections. These sections are: -

(a) apiezo electric load cell which records the imposed vibration force.

(b) a double hemisphere ball joint, to overcome any slight misalignment of the vibrator and steady-state rig.

(c) a connection bar.

Details of this load link are shown in figure 26, page 116 and plate 5, page 117.

The steady-state bearing rig design provides the necessary restraining mechanism to ensure that only the vertical mode of vibration is permitted. The restraint

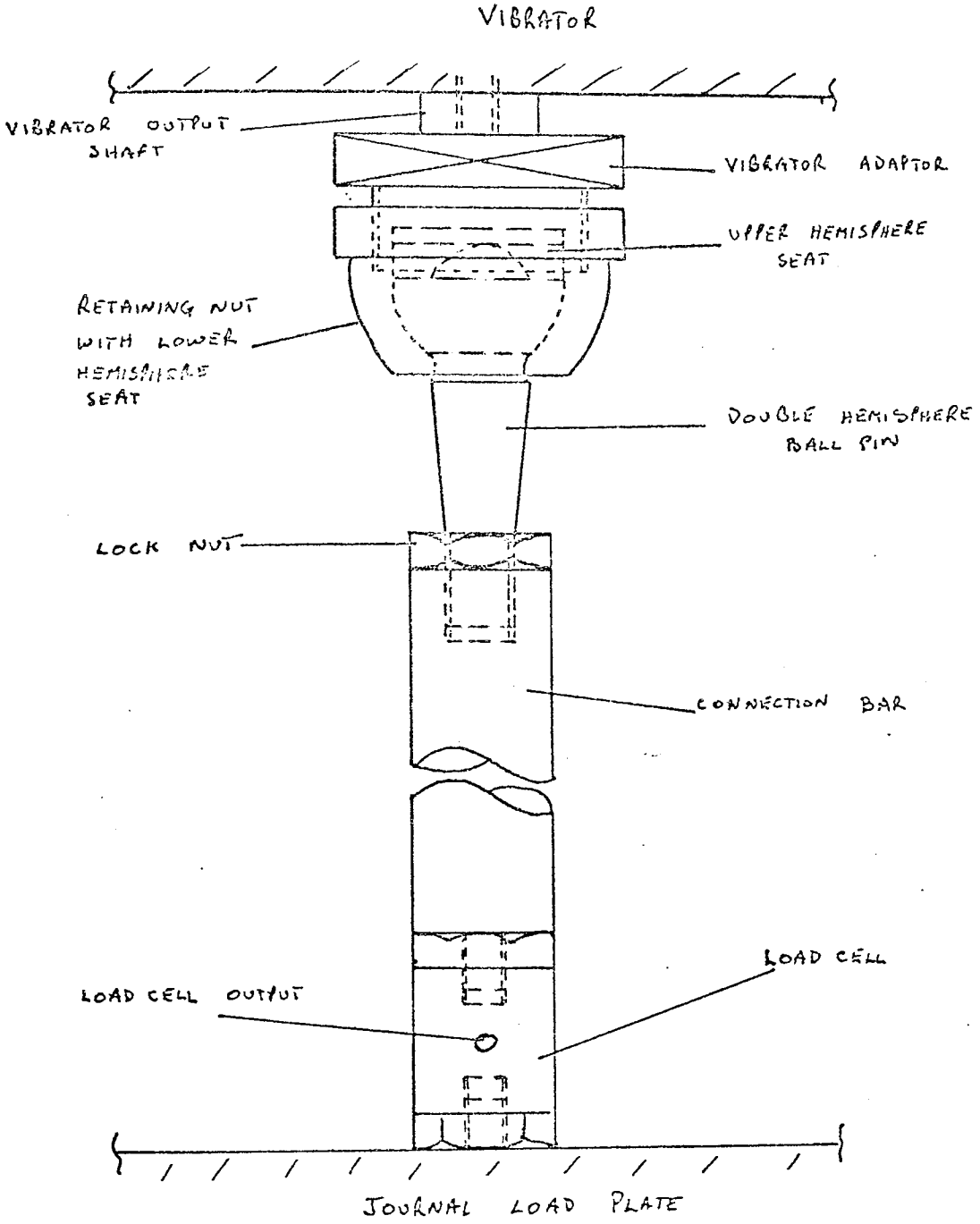

Figure 26 Load Link connecting Vibrator Output Shaft to the Journal Load Plate

Load Link connecting Vibrator Output
Shaft to the Journal Load Plate

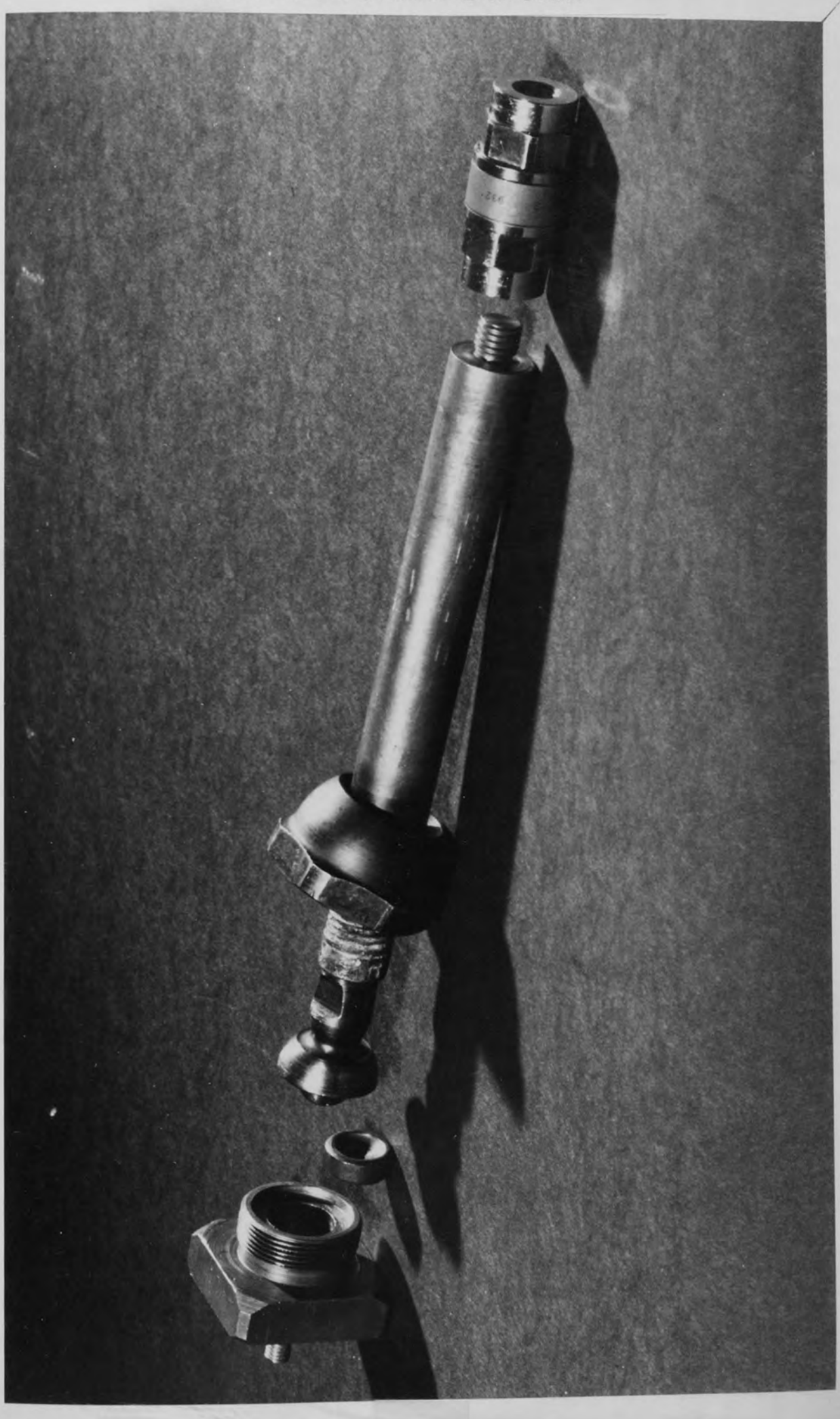

properties of this rig are inherent in the slave journal bearing which was originally designed to centralise the dead load on the thrust bearing and enable bearing tilt to be eliminated. This journal bearing restrains all degrees of freedom except vertical vibration and rotation about the vertical axis. As the journal of the slave bearing is rigidly attached to the vibrator this rotational mode is eliminated. The use of an air bearing as the restraint mechanism is approaching the ideal design as the only friction drag force experienced by the vibrating portion of the rig is due to the shearing of the air film.

5.2.2 Rig Alignment

As has been stated the vibrator gantry has been centrally positioned about the seismic mass of the rig. To ensure that the vibrator is concenttrically positioned over the thrust bearing under test the following procedure was used: -

Air was supplied to the pressure chamber and journal bearing of the steady-state rig causing the thrust bearing top plate to lift off. As the load link between the vibrator and the slave journal bearing was not connected the journal of the slave bearing could be rotated. A dial test indicator (D.T.I.), graduated in steps of 0.0001", with a magnetic base was positioned on

the load plate secured to the journal bearing, such that it indicated, upon rotation of the journal, the eccentricity of the steady-state rig in relation to the vibrator output shaft. The clamps securing the pressure chamber of the steady-state rig to the bed plate were released such that by gently tapping the pressure chamber base, with a nylon headed hammer, it could be repositioned. By rotating the journal of the slave bearing and gently tapping the pressure chamber vase the eccentricity of the steady-state rig in relation to the vibrator, indicated by the D.T.I., was removed. The pressure chamber was reclamped to the bed plate and a check on eccentricity was made to ensure the pressure chamber had not moved during clamping.

The air supply was switched off. The mitronic microcomparitors were positioned about the thrust bearing and the load link was connected. If any tilting of the thrust bearing top plate was indicated, by the micro-comparitors, due to connection, the above procedure was repeated until a successful connection was achieved.

5.2.3. Vibration Measurement Techniques

The dynamic rig design incorporates a number of bolted sections. To ensure that the bolts were tightly fastened and remained tightly fastened during the test the acceleration of the two extremities of the moving portion of the rig were monitored throughout any test.

The two extremities were (a) the thrust bearing top plate and (b) the load plate secured to the journal of the slave bearing. The acceleration of these two points were measured using accelerometers, see figure 27, page 121 . By checking that these two signals were identical confidence in the tightness of these bolted sections was validated. Had any of these bolted sections been loose, the two wave forms would not have been identical in that one wave form would have been distorted such that harmonics would have been imposed on this wave form.

The accelerometers used were piezo-electric crystal accelerometers, the outputs of which were passed through a dual-channel charge amplifier to a dual-channel oscilloscope. By using dual channel instruments any phase shift of the signals due to the instrumentation should be identical. This identical phase shifting property of the instruments involved was, however, checked by inputing to the dual channels of the charge amplifier two outputs from a single signal source and the outputs from the charge amplifier to the oscilloscope were superimposed on each other. If a non-identical phaseshift had occurred these two signals could not have been superimposed on each other.

Now, as the output from the charge amplifier is a voltage output a single output can be converted into a number of outputs by use of a parallel circuit system, see figure 28, page 122 , without altering the magnitude

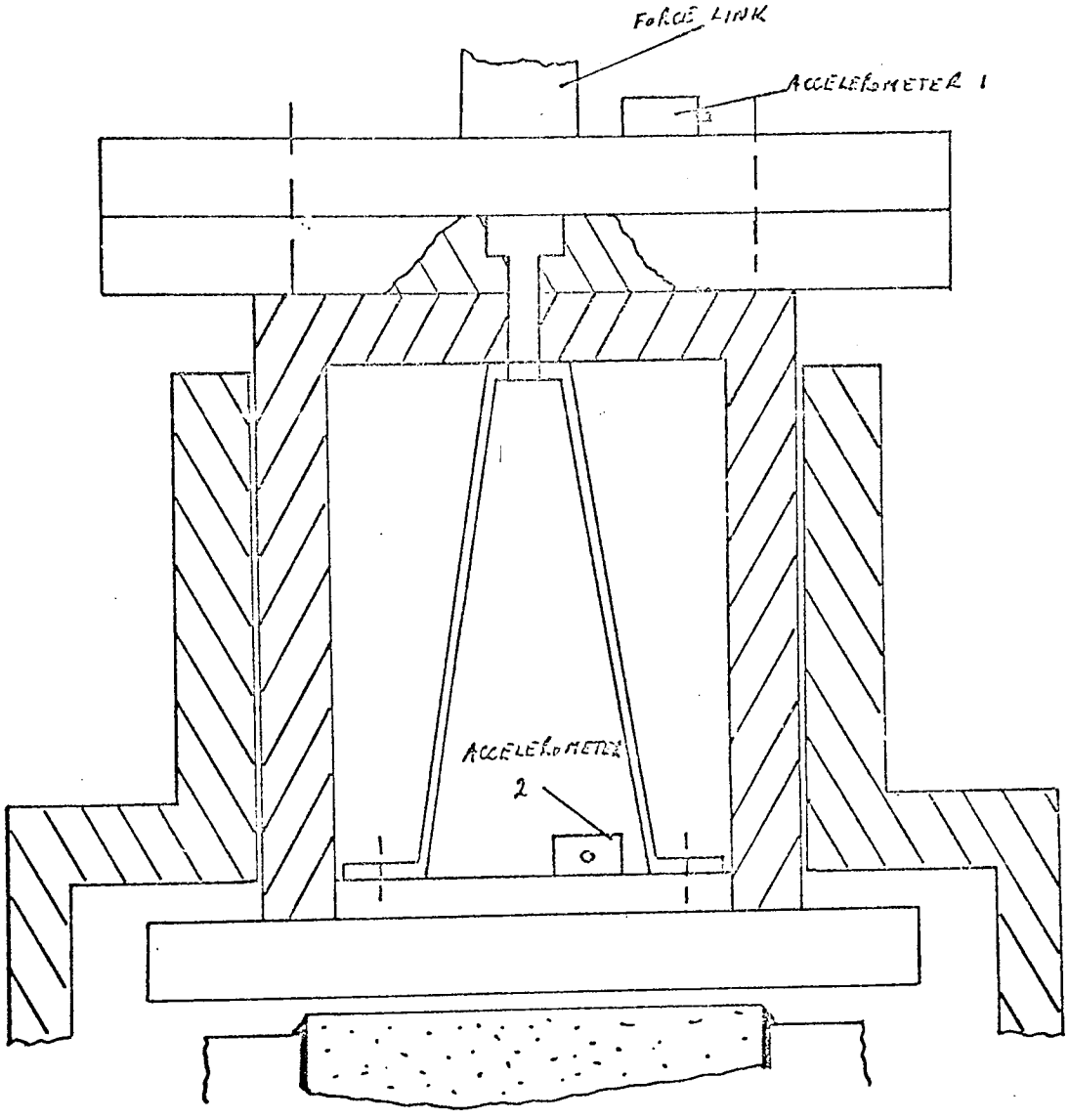

Figure 27 Section of Slave Bearing showing Bolting involved in Rig Assembly and positions of the Accelerometers

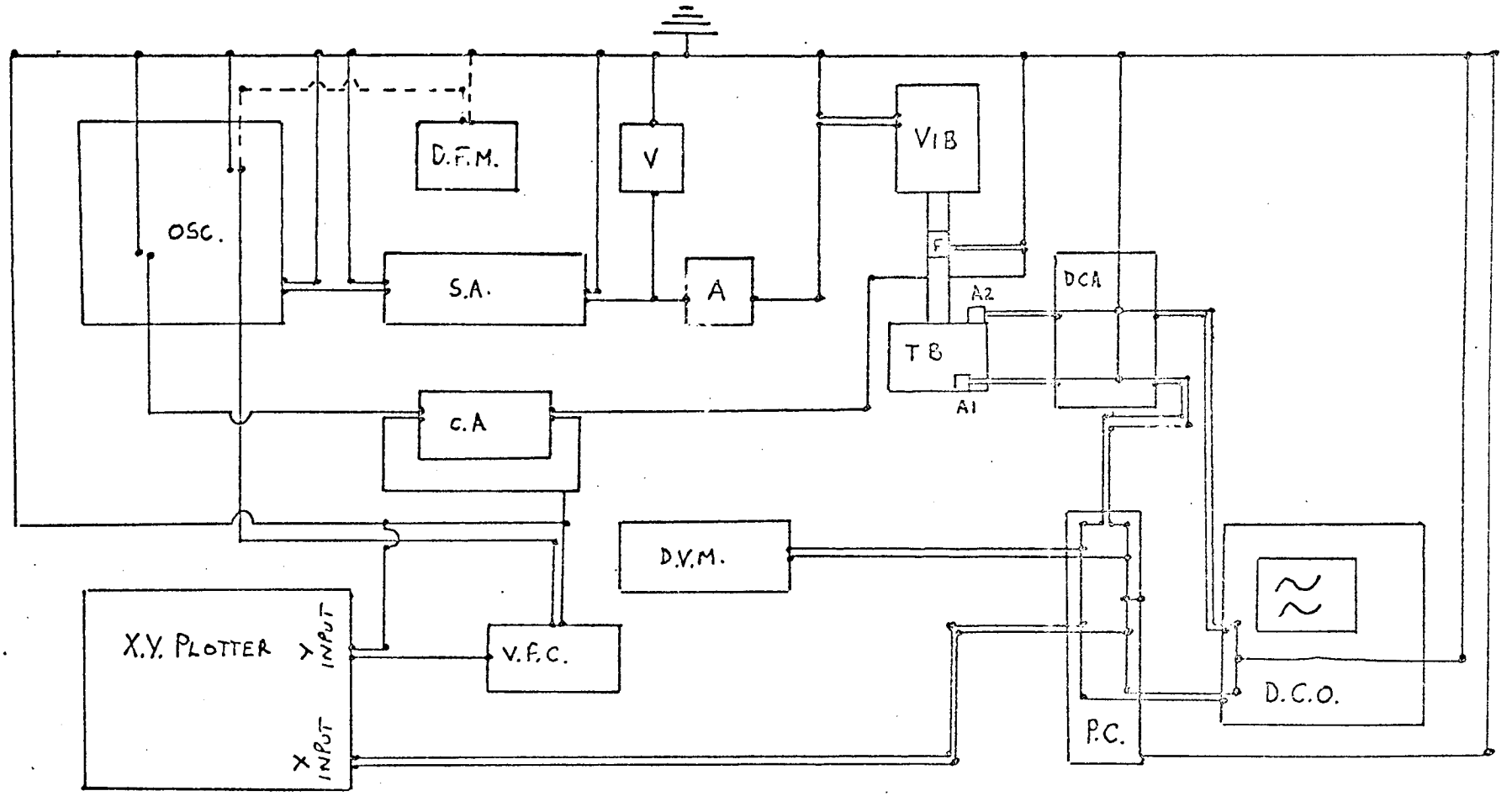

Figure 28 Schematic Diagram showing the Circuits of , and Instrumentation used in a Sweep Frequency Test

KEY TO FIGURE 28

OSC.	Beat Sweep Frequency Oscillator
S.A.	Signal Amplifier
D.F.M.	Digital Frequency Meter
V.	Voltmeter } monitoring signal to vibrator
A.	Ammeter } monitoring signal to vibrator
VIB.	Vibrator
F.	Force transducer
A1, A2	Accelerometers
D.C.A.	Dual Channel Charge Amplifier
C.A.	Charge Amplifier
T.B.	Test Bearing
D.C.O.	Dual Channel Oscilloscope
P.C.	Parallel Circuit
D.V.M.	Digital Voltmeter
V.F.C.	Voltage/Frequency Converter
------	Signifies connection before test i.e. in setting sweep frequency limits.

of this signal. By splitting the voltage signal not only can the signal be monitored on the oscilloscope but the voltage value of the signal can be measured by a voltmeter of some form and the signal can be used to drive any voltage driven recording machine. As a sweep frequency test has been used to determine the dynamic characteristics of the bearing under test, see section 5.3, the output from the accelerometer on the bearing top plate was split into three like signals by using such a series circuit.

The first signal was fed to the oscilloscope to ensure bolt tightness, see above, the second signal was used to drive the y-axis servo-motor system of an X-Y plotter, see section 5.3.2., and the third signal was fed to a digital voltmeter (D.V.M.) to determine the R.M.S. value of the signal at a given frequency.

As has been stated, the sweep frequency test has been used and in order to set the limits of this frequency sweep accurately, the output signal from the oscillator was initially fed to a digital frequency meter (D.F.M.) which had the facility of measuring the periodic time of a signal input.

The vibrator used throughout these tests was a Goodman V 50 Mk2. This vibrator has a maximum current input of 2 amps R.M.S., if no external cooling is provided. To ensure this limit was not exceeded the current input to this vibrator was monitored by a standard R.M.S. ammeter in series with the vibrator.

The imposed vibration force was measured using a piezo-electric load cell fitted to the load link which connects the vibrator to the load plate secured to the journal of the slave bearing.

Besides all the above measurements the measurements for a steady-state test were also taken.

5.3. FORCED VIBRATION EXPERIMENTAL APPROACH

5.3.1 Spring Stiffness and Viscous Damping Coefficient Determination for a Linear System

It is well known that by applying a constant amplitude force to a spring-mass viscous damper system with linear characteristics that the resulting amplitude of the mass acceleration for forced damped vibrations is related to the forcing frequency by the equation:

$$\hat{a} = -\left(\omega/\omega_n\right)^2 \frac{f_o}{m_4} \Big/ \left(\left(1-(\omega/\omega_n)^2\right)^2 + 4\xi^2 (\omega/\omega_n)^2 \right)$$

5.3.1.

By plotting the amplitude of this mass acceleration against the forcing frequency a resonance curve of the form shown in figure 29, page 126 can be produced.

It is also well known that the frequency ω_r, at which the peak acceleration amplitude, $\hat{a}_r$, occurs is related to the natural frequency, ω_n, of the system by the equation

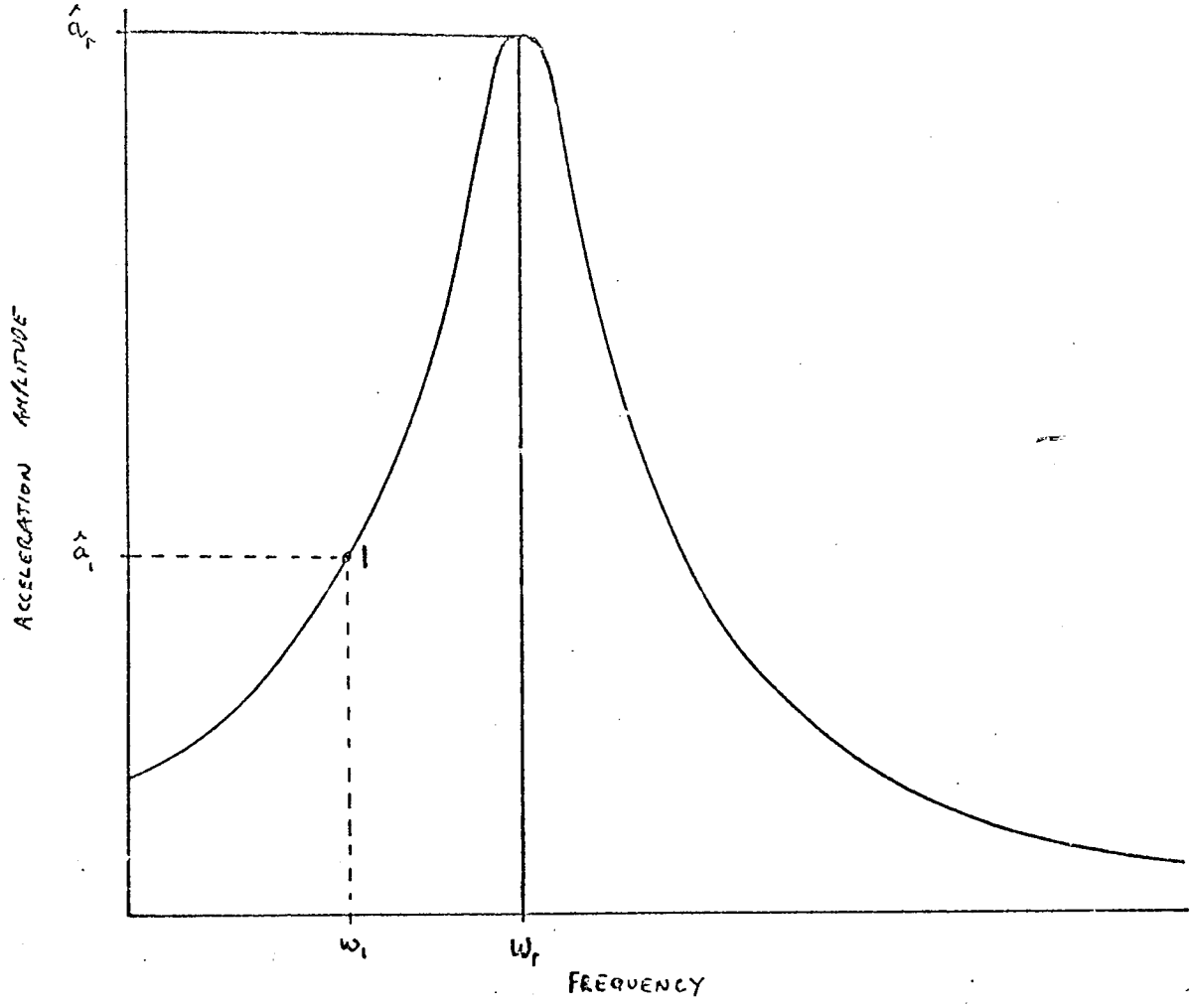

Figure 29 Resonance Curve for a Spring-Mass-Viscous Damper System with Linear Coefficents

$$\omega_r = \omega_n \; / \; (1-2\xi^2)^{\frac{1}{2}} \qquad 5.3.2.$$

Substituting equation 5.3.2. into equation 5.3.1 gives

$$\hat{a}_r = f_o/m_4 \; / \; 2\xi(1-\xi^2)^{\frac{1}{2}} \qquad 5.3.3.$$

Also ω_n may be replaced by $\omega_r(1-\xi^2)^{\frac{1}{2}}$ in equation 5.3.1 giving

$$\hat{a} = -\Omega^2 \; f_o/m_4 \; / \; ((1-2\xi^2-\Omega^2)^2 + 4\xi^2(1-2\xi^2)\Omega^2) \qquad 5.3.4.$$

where

$$\Omega = \omega/\omega_r$$

Consider now the acceleration amplitude shown at point 1 in figure 29, page 126 , and let the relationship between this acceleration amplitude and the resonant accleration amplitude be:

$$\frac{\hat{a}_1}{\hat{a}_r} = P \qquad 5.3.5.$$

Substituting equations 5.3.3. and 5.3.4. into equation 5.3.5. yields

$$\xi = \left[\frac{1}{2}\left\{1 \pm \left(1 - \frac{P^2(1-2\Omega_1^2+\Omega_1^4)}{\Omega_1^4-P^2(2\Omega_1-1)}\right)^{\frac{1}{2}}\right\}\right]^{\frac{1}{2}} \qquad 5.3.6.$$

It can easily be shown that the spring stiffness, k_3 of the system is given by

$$k_3 = m_4\omega_r^2(1-2\xi^2) \qquad 5.3.7.$$

and the viscous damping coefficient, C is given by:

$$C = 2m_4\omega_r(1-2\xi^2)^{\frac{1}{2}}\xi \qquad 5.3.8.$$

Thus for a constant force test if an acceleration resonance curve can be produced experimentally then the value of the spring stiffness and viscous damping coefficient can be found from equations 5.3.6., 5.3.7., and 5.3.8., by determining from this resonance curve (1) the ratio of the acceleration amplitude at any frequency and the resonant acceleration amplitude (2) the ratio of the frequency at which the above ratio was taken and the rsonant frequency.

5.3.2 Bearing Dynamic Characteristics

In order to test the validity of the time dependent theoretical analysis of Chapter 3, which assumed that the bearing could be satisfactorily modeled by a linear system, the equivalent experimental linear characteristics of the bearing under test should be determined. This technique

of determining the dynamic characteristics requires the acceleration amplitude resonance curve to be drawn. There are two possible ways of drawing this resonance curve, these being: -

(1) Manual Drawing. By selecting specific values of frequency and manually setting at each frequency the input power to the vibrator, such that the vibration force remains constant, measure the acceleration amplitude for each frequency. Having sufficient values allows the resonance curve to be drawn.

(2) Sweep Frequency Test using an X-Y plotter. By using an oscillator with feed back control circuitry to enable the input power to the vibrator to be altered, such that the vibrator output force remains constant and with the added facility of frequency sweeping, the resonance curve can be drawn automatically. This automatic drawing of the resonance curve is achieved by feeding an accelerometer output direct to the Y-axis servomotor system of an X-Y plotter while the X-axis servomotor system is fed with a signal proportional to the frequency of the oscillating force.

The manual drawing technique is tedious and inaccurate as the true resonance frequency may not be measured. By

virtue of this the sweep frequency test method was used to perform all dynamic experiments.

The oscillator used was a 'beat sweep frequency' oscillator with the requisite control circuitry 'built-in', this control circuitry enables the oscillator to vary the input power to the vibrator such that the force vibrating the bearing under test remained constant. This oscillator also gave a secondary output signal of constant voltage with a frequency equal to the primary output signal. Thus by feeding this secondary signal to the X-axis servometer system of the X-Y plotter via a frequency to d.c. voltage converter the correct drive of the X-axis was achieved. A schematic diagram of this equipment is shown in figure 28, page 122 . Plate 6, page 131 shows the actual equipment used.

As has been stated in sub-section 5.2.3. the accelerometer signal was split into three signals of equal voltage and one of these signals was directly connected to the X-Y plotter via the Y-axis servometer system inputs. It should be noted that the X-Y plotter had the facility to accept d.c. voltage or a.c. voltage.

Having automatically drawn the desired resonance curve the determination of the dynamic characteristics could be simply achieved by measuring the ratios mentioned in sub-section 5.3.1.

By measuring the acceleration amplitude at any given frequency during the sweep frequency test and noting the

Vibration Instrumentation

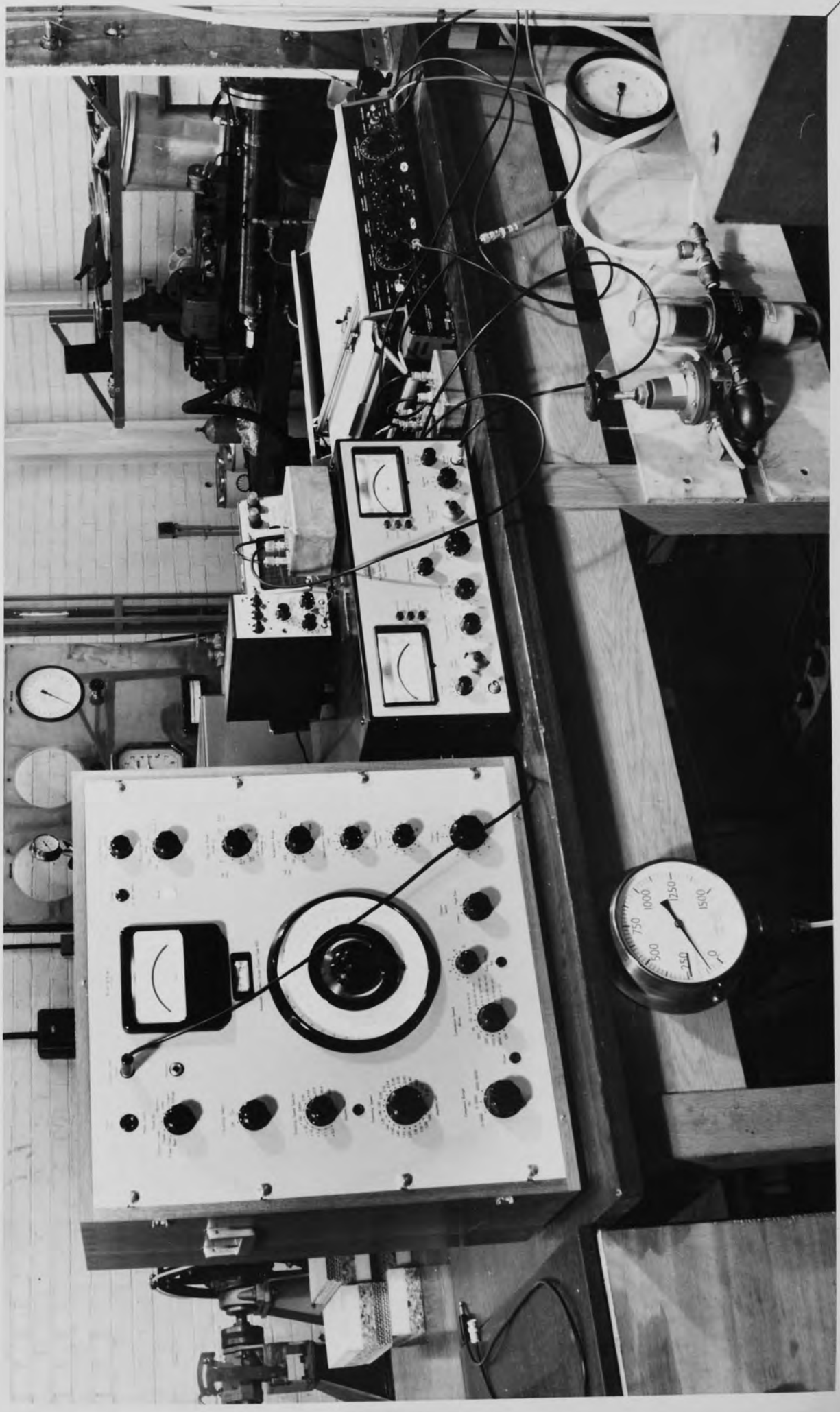

frequency at which the acceleration was measured the resonance curve was automatically calibrated. Knowing the value of the acceleration at any particular frequency enabled the velocity and displacement to be calculated. The dynamic characteristic results are shown in figure 102, to 109 pages 290 to 297.

5.3.3. Porous Pad Porosity Measurement

A porous material may be defined as a solid body containing void spaces that are either interconnected or non-interconnected. The porosity of a porous material may be defined as the ratio of the voidage volume to the bulk volume. If the voidage volume used in this ratio is the total voidage volume including the non-interconnected spacial voidage this ratio is known as the overall porosity. If the voidage volume used is only the interconnected voidage volume then the ratio is termed the intercommunicative or effective porosity. It is the effective porosity that is of interest in this case and therefore where the term porosity is used it should be noted that reference is made to the effective porosity and not the overall porosity.

The technique used to measure the porosity of the materials tested was the 'gas expansion technique', cf Scheidegger (26). Fundamentally this method is the direct measurement of the volume of air contained in the

interconnected pores of the material, the equipment used is shown in figure 30, page 134 . The porous material to be tested is sealed in container A, valves 1 and 2 being closed, valve 3 being open. Valve 1 is then opened to allow air under pressure into container A. Once the desired pressure is obtained, measured by the mercury manometer, valve 1 is re-closed. At this point valve 3 is also closed. Valve 2 is then opened and the pressure in containers A and B is allowed to equalise, container B having an original pressure equal to the atmospheric pressure. Once the pressure in containers A and B has equalised the value of that pressure is measured using the mercury manometer. The system is then exhausted to atmosphere by opening valve 3. This process is repeated for various initial pressures in container A.

By use of the ideal gas laws, Boyle-Mariotte assuming an isothermal expansion, the volume of gas that was contained within the porous media can be calculated, if the volume of containers A and B and the specimen volume is known, i.e.

$$p_1(V_A - V_S + V_p) + p_a V_B = p_2(V_A + V_B - V_S + V_p)$$

i.e.

$$V_p = \frac{(p_2 - p_a)}{(p_1 - p_2)} \cdot V_B + V_S - V_A$$

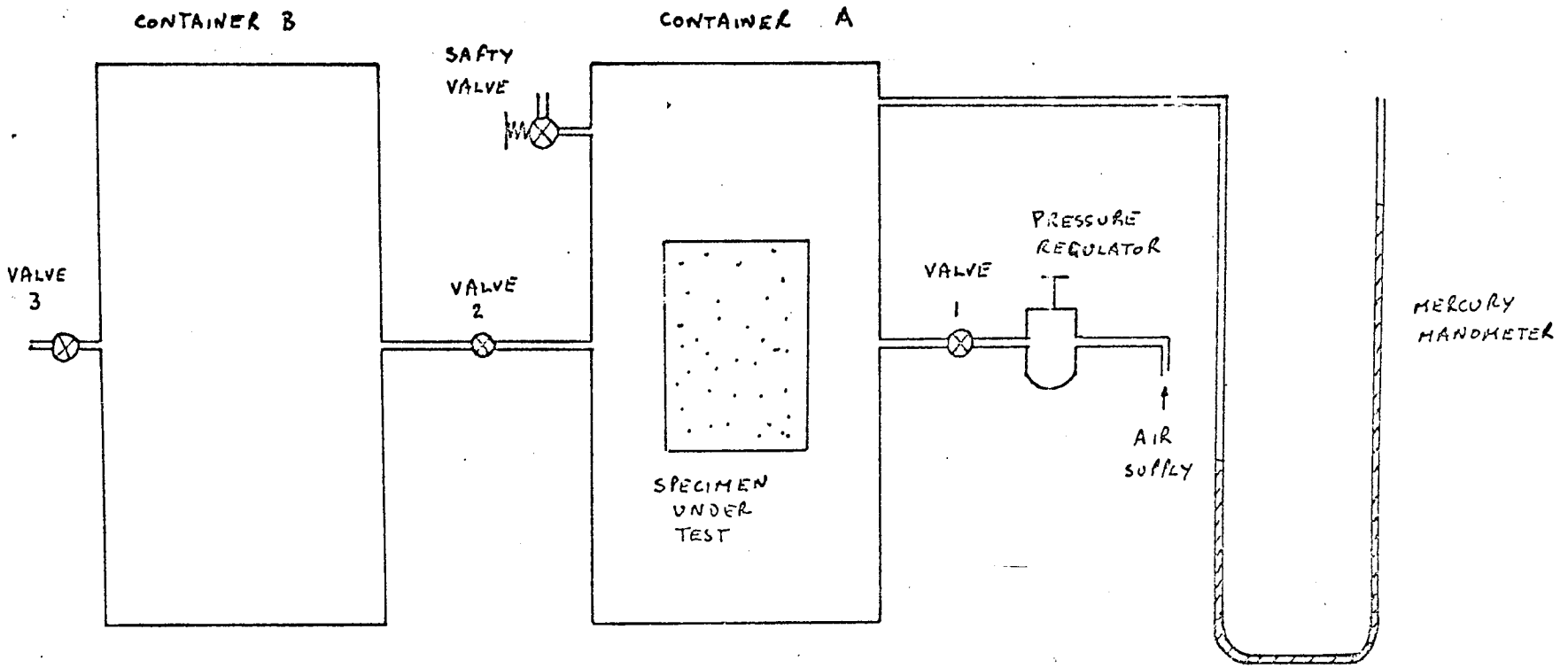

Figure 30 Experimental Test Rig used to determine Specimen Porosity

The volume of container B was measured by the following method: -

(1) Weigh container empty.

(2) Fill container with water.

(3) Re-weigh container.

Knowing the density of water the volume of container B can be simply deduced. Knowing the volume of container B enables the volume of container A to be determined by the gas expansion method, thus calibrating the rig.

CHAPTER SIX

DISCUSSION OF RESULTS

6.1 INTRODUCTION

Due to the diversity of results accumulated over the three year period of this research programme, this section has been conveniently sub-divided into the following sub-sections. Each sub-section deals with its listed subject.

Sub-section Number	Subject
6.2	Permeability measurement
6.3	Comparison of steady-state theory and experimental results
6.4	Theoretical steady-state performance
6.5	Theoretical dynamic performance characteristics
6.6	Comparison of dynamic theory and experimental results

6.2 PERMEABILITY MEASUREMENT

It was shown in section 4.3 that the empirical technique of determining the viscous and inertia permeabilities of a porous material outlined by Morgan (42) cannot be used to measure these permeability values in the case of a porous material with a high resistance to flow. A new experimental technique involving a logrithmic plot of pressure drop and mean volumetric flow rate as outlined in section 4.3.1 enables the viscous permeability of such a material to be determined accurately. This logrithmic plot also identifies the experimental points to be plotted subsequently on a modified Morgan plot to enable the inertia permeability to be determined. It was also stated in section 4.3.2. that both permeability values would be determined by the combined use of this logrithmic plot and the modified Morgan plot.

It has been found, however, that for the range of pressure drops used in this research, departure from pure viscous flow occurred for only two of the seventeen specimens tested. Consequently the log plot of the experimental results revealed sufficient points to enable a modified Morgan plot to be drawn in these two cases only.

The experimental results, plotted on this logrithmic basis, of sixteen of these porous specimens are given in figures 33 to 48, pages 219 to 235 . The results of the seventeenth specimen plotted on a logrithmic basis

has already been given in figure 20, page 96 . The lines drawn through these experimental points have been obtained by using a well known statistical regression analysis technique i.e. 'Least Squares Method'. The results of all of these permeability tests are reasonably correlative to a unity gradient line in the Darcy region of flow. There are, however, two major causes of the experimental scatter manifest in these graphs, these being: -

(a) The measurements of the volumetric flow rates for these tests were made using standard variable orifice flowmeters that were calibrated at ambient conditions. This calibration is guaranteed to $\pm$ 2% of the maximum measureable flow rate for the meter if metering is carried out in the upper two thirds of the meterable range of the flowmeter. In order to determine the value of the mean volumetric flow rate at conditions other than ambient, i.e. higher pressure and temperature, the manufacturers conversion charts were used. These conversion charts, basically a Reynolds number - coefficient of discharge plot, are only available for a limited number of flowmeter readings and thus interpolation has to be used in order to obtain correction factors for values of flowmeter readings other than the plotted values.

(b) In most tests several different flowmeters had to be used to measure volumetric flow rates, as the range of flowrates throughout a test exceeded the working

range of some of the flowmeters. As these flowmeters all had different working ranges the calibration tolerance mentioned above differed for each meter. This gives a discontinuity of the results as a change in flowmeter occurs. A typical example of this is specimen number 7 figure 39, page 225 . In this example, three flowmeters were used to cover the flowrate range of the test. It can be seen that at pressure drops of 1 Bar and 2 Bar the discontinuity is in evidence.

However, it can be generally stated that the majority of the experimental results are within the manufacturers calibration tolerances.

The two specimens, already referred to, that exhibit the transitional mode of flow are: -

(a) Pad number 16. This pad was made from a porous stainless steel material. The pad dimensioned 50.8mm in diameter and 12.7 mm in thickness.

(b) Pad number 17. This pad was made from a porous bronze material. The pad dimensioned 76.2 mm in diameter and 12.7 mm in thickness.

The logrithmic plots of the experimental results of these pads are shown in figures 48 and 20, pages 234 and 96 respectively. All experimental points for these two specimens have also been plotted using the technique of Morgan. These plots are shown in figures 49 and 19 pages 235 and 93 for pads 16 and 17 respectively. It can

be seen that for pad 17, both the viscous and transitional modes of flow are clearly in evidence. However, for pad number 16 the two modes of flow are not so easily recognised. This is because the viscous region, as demonstrated in this graph by a line parallel to the X-axis, is small and due to experimental scatter this region is hidden. This scattering effect is inherent in the Morgan technique. Consider the parametric groups plotted on this graph, i.e.

$$(\Delta p)_y \; A/Q_m \; \eta H \qquad \text{and} \qquad Q_m \rho_m / A\eta$$

Both variables p and Q_m are included or implied in both parametric groups. In the ordinate group the volumetric flow rate appears in the denominator whereas in the abscissa group the volumetric flow rate appears in the numerator. In the ordinate group the pressure appears in the numerator as in the pressure drop term whereas in the abscissa group it appears in the numerator as the mean density term. Clearly the experimental tolerance of these quantities is enhanced by the method of presentation in the Morgan technique. To demonstrate this scattering effect the results for pad number 10 were plotted using the Morgan technique, see figure 50, page 236 . It is known that as all these experimental results are in the viscous region, as confirmed by figure 42, page 228 which shows a straight line with a unity gradient, these experimenta

points should form a line parallel to the X-axis on the Morgan plot. By using regression analysis it should be found that the inertia permeability is infinite i.e. the slope of this line is zero. However, it was found that these results give a negative slope, i.e. a negative inertia permeability, which is meaningless as this denotes a decrease in resistance by increasing the flowrate, i.e. negative inertia losses.

Use of the new technique outlined in section 4.3.1. enables the true values of both viscous and inertia permeabilities for specimens 16 and 17 to be found. The values given by the Morgan technique were also determined. These values are listed below along with the percentage error that occurs in the determination of these values using the Morgan technique.

Technique of Measurement	Pad Number	Permeability		Error	
		Viscous x 10^{10}cm^2	Inertia x 10^8 cm	Viscous	Inertia
Log + Mod.Morgan	16	3.0228	4.7270		
Morgan	16	3.1697	4.8754	4.86%	3.14%
Log + Mod.Morgan	17	3.4563	5.1648		
Morgan	17	3.8158	5.6503	10.4%	9.4%

It is suggested from this tabulation that as the resistance to flow of the porous material increases then the values determined by the Morgan technique become more erroneous. An explanation of this is that as the inertia resistance

to flow of the material increases then the slope of the Morgan graph increases. Since the Morgan technique incorrectly assumes that a continuous line passes through all the experimental values, the intercept of this line with the Y axis is further removed from the true value as the slope of the line becomes greater. Similarly the larger the viscous region the more erroneous the slope becomes in assuming a continuous line.

It has been shown then that the combined logrithmic and modified Morgan plot technique is a simple and accurate method of determining the viscous and inertia permeabilities of porous materials. Not only is the true value of the viscous permeability of a porous specimen found from the logrithmic plot, essential for accurate performance prediction of a porous bearing, but the upper limit of pressure drop across the porous material for which Darcy's law is valid can be found.

Now for pad numbers 1 to 15 the inertia permeability has not been determined. A possible technique for determining this permeability value was thought to be available. This is because Green and Duwez (40) found that for porous stainless steel, the material used to manufacture these pads, there existed a friction factor/Reynolds number relationship, for all flow rate, in the form:

$$\lambda_f = \frac{2}{Re} + 2 \qquad 6.2.1.$$

The experimental results for pad number 16 was plotted using the definitions of Green and Duwez and were found to correlate with this relationship, see figure 51, page 237. Therefore, it was considered that through their definitions of friction factor and Reynolds number the value of the inertia permeability may be found even though the experimental range was limited to the viscous flow region for these pads. However, upon inspection of this relationship it was found that this could not be achieved, i.e.

Since

$$\lambda_f = \frac{2}{Re} + 2$$

where

$$Re = \frac{\rho_m Q_m \Phi_y}{\eta A \phi_y} \quad , \qquad \lambda_f = \frac{2(\Delta p)_y A^2 \phi_y}{H \rho_m (Q_m)^2}$$

Now in the viscous flow region

$$Re \ll 1$$

thus

$$\frac{2}{Re} \gg 2$$

Hence it may be written that in the viscous flow region

$$\lambda_f = 2/Re$$

i.e.

$$\frac{(\Delta p)_y \cdot A^2 \cdot \phi_y}{H \rho_m (Q_m)^2} = \frac{\eta A \phi_y}{\rho_m \Phi_y Q_m}$$

from which it can be seen that the inertia permeability cancels as it is common to both numerators. Therefore the evaluation of the inertia permeability by this method is not possible. Thus the transitional mode of flow must be encountered, to enable a modified Morgan plot to be drawn, in order that values of the inertia permeability may be determined.

Although the inertia permeabilities of pad numbers 1 to 15 have not been determined this is not detrimental to the assessment of the porous thrust bearings that can be formed by these pads. The analytic approach assumes that the flow through the porous material is governed by Darcy's law and by virtue of the fact that transitional flow has not been encountered for the applied pressure drops then this assumption is validated for these pads, for these applied pressure drop values.

Not all of the porous pads that have been subjected to a permeability test have been used as porous thrust bearings. As the Morgan technique for permeability determination has been rejected there was a need to amass experimental evidence that the logrithmic approach used was an exact method of viscous permeability evaluation. By virtue of the fact that all seventeen speciments tested exhibited the unity gradient property on a logrithmic plot of pressure drop and mean volumetric flow rate sufficient confidence now exists in this method of viscous permeability evaluation.

6.3 EXPERIMENTAL VERIFICATION OF THE STEADY-STATE THEORY

6.3.1 Introduction

The theoretical analysis of the steady-state equations made in Chapter 3 is only valid within the bounds of the assumptions made within that analysis and as such is of no value until it can be shown that the results given by this analysis accurately predict the real situation. The theoretical predictions made by this analysis must be experimentally verified so that the engineer may then have confidence in the use of these predictions to design a porous bearing.

In order to investigate the validity of these theoretical predictions, steady-state tests were performed on five bearing configurations. The five bearings chosen were: -

Bearing Number	Outer Radius mm	Porous Pad Thickness mm	Aspect Ratio	Material Viscous Permeability x 10^{11} cm^2
1	25.4	12.7	0.5	1.3594
2	25.4	12.7	0.5	1.7799
3	25.4	12.7	0.5	2.4283
4	25.4	19.05	0.75	1.8302
5.	25.4	25.4	1.0	1.9662

All of these bearings were prepared by the acid etching process detailed in section 4.4.

It can be seen from the bearing specification tabulation above that (1) three bearings have the same aspect ratio but different viscous permeabilities, bearings 1, 2 and 3; (2) three bearings have differing aspect ratios and viscous permeabilities, bearings 1, 4 and 5.

The steady-state tests performed on these bearings were within the following limitations: -

Test Number	Bearing Number	Actual Bearing load N	Supply Pressure Bars		Figure No.	
			Maximum	Minimum	$\bar{W}$	$\bar{M}$
1	1	70.7	6	0.7	54	55
2	1	115	6	0.9	56	57
3	1	162	5	1.0	58	59
4	2	70.7	4.5	0.5	60	61
5	3	70.7	4.0	0.5	62	63
6	4	70.7	4.8	0.7	64	65
7	4	115	4.8	0.9	66	67
8	4	159	5.0	0.9	68	69
9	5	70.7	5.0	1.0	70	71
10	5	90.2	5.0	1.0	72	73
11	5	115	4.5	1.5	74	75

It can be seen from the test limitation tabulation that bearings 1, 3 and 4 were tested for three different actual bearing loads.

Thus from the two tabulations above it can be seen that the experimental tests enable the effect of bearing aspect ratio, material viscous permeability, supply pressure and

actual bearing load to be investigated in turn. The results of these tests are shown in figures 54 to 75, page 240 to 263 . For each test the bearing non-dimensional load and mass flow rate variation with bearing number has been checked against the theoretical prediction. However, before discussing the comparison of these test results with the theoretical predictions the technique of film thickness measurement, and hence bearing number determination, will be discussed.

6.3.2. The Film Thickness Determination and Porous Pad Axial Shift Problem

A new technique of film thickness determination, the pressure gradient technique, has been detailed in section 4.4. This technique enables a mean pneumatic clearance to be determined to account for the surface irregularities on both the porous specimen and bearing top plate surfaces. The need to take this mean penumatic clearance into account when measuring the film thickness has been shown to be of great importance, (49). The pressure gradient technique entails the determination of the pressure gradient at the outer radius of the porous bearing. This pressure gradient value has been obtained by differentiating a heuristic curve fitted to the experimentally determined pressure/radius values. The order of this heuristic curve was empirically obtained by fitting several curves through

the experimental points and identifying the curve that smoothly passed through these points. To increase the fitting accuracy of the curve two boundary conditions were imposed on the film equation. These boundary conditions were: -

(a) at the centre of the bearing the radial pressure gradient was made to be zero, i.e. axisymmetrical conditions;

(b) at the bearing outer radius the pressure was equated to atmosphere and the curve was forced through this point.

The imposition of these bearing conditions were achieved by the following modifications to the general heuristic curve equation: -

the general equation may be written

$$p = \sum_{n=0}^{N} e_n r^n \qquad 6.3.1.$$

Boundary condition (a) at

$$r = 0 \qquad \frac{\partial p}{\partial r} = 0$$

Differentiating equation 6.3.1. and equating to zero at r=0 gives $e_1 = 0$ thus

$$p = e_0 + \sum_{n=2}^{N} e_n r^n \qquad 6.3.2.$$

boundary condition (b) at

$$r = r_o \qquad p = p_a$$

substitution of this boundary condition into equation 6.3.2. yields

$$e_o = p_a - \sum_{n=2}^{N} e_n r_o^n \qquad 6.3.3.$$

substitution of equation 6.3.3. into equation 6.3.2. gives the equation for the curve as

$$p = p_a + \sum_{n=2}^{N} e_n (r^n - r_o^n) \qquad 6.3.4.$$

Equation 6.3.4. then is the equation used to fit the heuristic curve through the experimental pressure/radius points. The regression analysis technique of the Least Squares method was also used to reduce the experimental scatter effects.

In order to validate the axisymmetrical condition, the boundary condition used at the bearing centre, the following experimental procedure was used. A uniform film was formed and pressure values taken within the film. The bearing top plate was rotated through a given angle and the film was re-adjusted to ensure uniformity. Film pressures were again measured. This was repeated for various angular positions and no appreciable difference in the measured pressure values occurred at any angular position.

In order to show that the gradient technique gives valid film thickness measurements the film thickness derived from this technique can be plotted against the experimentally determined bearing lift. This plot, it is pointed out in section 4.4., should result in a straight line of unity gradient. A plot of the derived film thickness against measured bearing lift for bearing number 1 has already been given in figure 24, page 106 . It can be seen from this graph that the pressure gradient technique not only gives valid results but enables minute film thickness variation, sub-micron variations, to be measured accurately.

In plotting the results shown in figure 24 any axial deflection of the porous pad epoxy bond has been taken into account. This axial shift of the porous pad was calibrated using the technique given in section 4.4. Figure 52, page 238 shows the derived film thickness results for one load test plotted against the measured bearing lift before and after any account of bearing shift. It can be seen in this figure that the effect of bearing shift is to reduce the gradient of this plot. This is due to the fact that before accounting for the bearing shift the measured bearing lift is greater than the actual bearing lift. To explain this consider performing a load test on the bearing by the following method. Load the bearing before applying the air supply. Zero the bearing lift measuring

devices. Connect the supply pressure to the bearing and measure the bearing lift. In applying the load to the bearing without any supply pressure an unbalanced downward force is applied to the porous pad. This force creates a downward axial shift of the porous pad until the downward force is balanced by the shear forces in the epoxy bond. This deflected position of the porous pad is taken to be the zero position for the measuring devices. Upon connecting the supply pressure to the bearing the air flows through the porous pad and supports the load at a given film thickness, the bearing lift off being measured by the mitronic measuring devices. Now the integral of the film pressure forces equals the load applied to the bearing. Thus the same downward force is applied to the pad. If no other forces were present the porous pad would remain in its downward deflected position. However, there is another force now being applied to the porous pad. This force is the upward acting force of the supply pressure, thus the pad moves axially upwards. Now the mitronic devices have measured the upward lift of the bearing top plate and thus no account is made of the porous pad zero shift. Hence the measured upward lift of the top plate is greater than the actual bearing lift. By knowing the applied supply pressure the actual bearing lift can be determined by subtracting the upward bearing shift from the measured bearing lift, the upward bearing shift having been found from the calibration previously

mentioned.

Now having discussed the technique of film thickness measurement and the method of taking axial shift into account, it is possible to produce individual graphs of derived film thickness against measured bearing lift for each bearing tested. This leads to numerous graphs. There is, however, a method by which all the above mentioned graphs can be plotted on one non-dimensional graph. Consider the equation of this derived film thickness/ measured bearing lift graph, i.e. equation 4.4.5.

$$h_d = h_m + SF$$

By dividing through by the mean pneumatic clearance SF the equation becomes:

$$\frac{h_d}{SF} = 1 + \frac{h_m}{SF} \qquad 6.3.5.$$

As each bearing tested will have a different mean pneumatic clearance value, as the surface irregularities of each bearing will be different, the use of equation 6.3.5. correlates all the derived film thickness/measured bearing lift graphs on to one non-dimensional graph. The results of the five bearings tested have been presented this way, see figure 53, page 239 . It can be seen that good experimental confirmation is achieved. Clearly the mean pneumatic clearance SF is dependant on surface finish

only. It is constant for a given pad independent of loading. The actual lift off h_m can be corrected by adding SF to obtain an equivalent ideal film thickness h_d in order that the performance of real bearings may be successfully predicted.

6.3.3. The Load and Flow Test Results

The results of the steady-state tests are shown in figures 54 to 75, pages 240 to 263 . These results show that by correctly evaluating the viscous permeability of the porous material, by accounting for the porous pad surface finish and axial shift, and by ensuring that the flow through the porous material is within the Darcy law region, it is now possible to obtain good correlation of observed performance and theoretical prediction.

There is, however, one anomaly that must be discussed. In all the steady-state test results at moderately high bearing numbers the bearings appear to be unpredictably stiff. This is in fact due to touch down of the bearing on roughness peaks. A continuous air film is no longer being maintained. As stated before, the porous pad is not smooth and the peaks of the two surfaces now contact, the gas film no longer fully supports the load, as the load is transmitted through the peaks. This can be seen by examining the results for any of the bearings tested. Consider the results for bearing number 1. The unpredictable

bearing stiffness occurs at a bearing number of approximately 2.5 independent of the load supported by the bearing. In using the mean pneumatic clearance figure to calculate a bearing number the result is a bearing number of 7.7. Now in order to obtain a film thickness of the mean pneumatic clearance value, some of the material in the roughness peaks would have to be displaced into the material roughness troughs. This obviously cannot be achieved. Therefore, bearing touchdown must occur at a bearing number below the value of the bearing number obtained by using the mean pneumatic clearance as the film thickness. This is also shown in the flow data in that the flow rate is lower than predicted. If contact of the surfaces occurs then the film flow area is reduced.

No measurement of the bearing stiffness has been made. However, as good correlation between the experimental and theoretical values of the bearing non-dimensional load/bearing number has been achieved and as the non-dimensional static stiffness is defined as the rate of change of the non-dimensional bearing load with respect to the bearing number multiplied by three times the bearing number, it can be stated that at low bearing numbers the theoretical non-dimensional static stiffness values can be used to design porous bearings.

At high bearing numbers the bearing, it has been stated, is unpredictably stiff due to bearing touchdown. It is therefore, necessary to operate these bearings at

a bearing number below the touchdown bearing number in order that the steady-state theoretical curves can be used in designing the bearing. Insufficient data has been accumulated in order to determine a relationship between the value of the bearing touchdown point and other bearing properties. Indeed this relationship may be extremely complex as the touchdown point will be directly related to the mean pneumatic clearance value. The mean pneumatic clearance value will be a function of the etching time, grain size of the material, viscous permeability and possibly other properties of the material and may even be related to the surface roughness as determined on a Tallysurf. It may be that this touchdown value can only be determined empirically. In order that bearing touchdown does not occur the overall film thickness must be large in comparison to the mean pneumatic clearance value. This large film thickness may mean that the optimum bearing static stiffness bearing number may not be attained. As the engineer may wish to design a bearing at the optimum static stiffness the bearing number at which the optimum static stiffness occurs can be reduced by increasing the supply pressure, increasing the viscous permeability of the material and reducing the bearing aspect ratio, as discussed in the following section.

6.4 THEORETICAL STEADY-STATE BEARING PEFORMANCE

6.4.1 Introduction and Definitions

The steady-state analysis of Chapter 3 enables theoretical design curves of non-dimensional load capacity, $\overline{W}$, non-dimensional mass flow rate, $\overline{M}$, and non-dimensional static stiffness, $\overline{X}$, against a parametric group defined as the bearing number, Λ, to be drawn. However, before discussing these design curves an explanatory note on the meaning of these parametric groups is required.

The non-dimensional load capacity is the ratio of the actual load the bearing area can support at a given film thickness to the maximum possible load the bearing area can support, i.e. at zero film thickness, for the same supply pressure. In itself it is basically an efficiency figure giving the efficiency value of the bearing, i.e. how effectively the bearing utilises the available pressure energy.

The non-dimensional mass flow rate is the ratio of the actual mass flow rate through the bearing to the maximum possible flow rate through the porous pad given certain conditions. It is basically an inverse efficiency figure for the higher the mass flow rate the higher the ratio of the available pressure drop used to create this mass flow rate through the pad to the overall available

pressure drop. Clearly it is desirable to minimise this non-dimensional group.

The non-dimensional static stiffness is the ratio of the force required to bottom the bearing top plate from its operating position if the operational static stiffness of the bearing was to remain constant to the maximum load the bearing can support, i.e. stiffness x film thickness/ maximum load.

The bearing number is a parametric group containing the bearing outer radius, the pad thickness, the pad viscous permeability and the film thickness. For a given aspect ratio and pad viscous permeability this parametric group is basically the film thickness design parameter. In designing a bearing the engineer is liable to be limited by available space, thus fixing the bearing outer radius and pad thickness. This group enables the engineer to determine at what film thickness the bearing will operate for a given viscous permeability.

In designing a porous thrust bearing the engineer will obviously desire a highly effective use of the pressure energy available, i.e. designing for a high $\overline{W}$ and low $\overline{M}$. However, the engineer's design may require the bearing to have large resistance to positional fluctuations, i.e. a large stiffness. This may be in conflict with the efficient use of pressure energy for high load capacity. In designing a bearing the engineer must decide which of these parameters is the most desirable and use the design curves to determine the optimum bearing parameters to suit the working conditions.

The steady-state design curves are shown in figures 76 to 80, pages 264 to 268 , and depict:

(a) the effect of the bearing aspect ratio on the variation of the non-dimensional load capacity, non-dimensional mass flow rate and non-dimensional static stiffness with the bearing number, see figures 76 to 78, pages 264 to 266 ;

(b) the effect of the supply pressure on the variation of the non-dimensional load capacity and non-dimensional static stiffness with bearing number, see figures 79 and 80, pages 267 and 268 .

The non-dimensional mass flow rate has been shown not to be a function of supply pressure, see section 3.3.

The effect of the viscous permeability of the porous material cannot be shown on the non-dimensional curves mentioned above, as this effect is hidden by an ensuing film thickness effect, (section 6.4.5.). By virtue of this the permeability effect is shown in the dimensional plots of load capacity, mass flow rate and static stiffness against film thickness curves, see figures 81 to 83, pages 269 to 271 .

6.4.2. The General Shape of the Steady-state Design Curves

Before discussing the individual effects mentioned above let us first consider the general shape of the

non-dimensional curves. In order to show clearly what occurs these curves have been plotted on a logrithmic/linear basis, the bearing number being plotted on the logrithmic scale while the bearing parameters, i.e. $\overline{W}$, $\overline{M}$, or $\overline{X}$ are plotted on the linear scale. The need to plot the bearing number on a logrithmic scale exists because this parameter can vary from a near zero value for a very large film thickness to an infinite value for a zero film thickness.

In the case of the non-dimensional load capacity and the non-dimensional mass flow rate curves it can be seen that the design curves are asymptotic to zero and unity values of the bearing parameters. At high bearing numbers, i.e. small film thickness, one approaches bearing 'touch-down'. The film resistance to flow increases, thus decreasing the mass flow through the bearing. As the mass flow through the bearing is reduced the pressure drop through the porous material reduces, leading to higher film pressures and hence a higher load capacity. In the limiting case i.e. zero film thickness, the mass flow rate through the bearing is zero and the load capacity is unity. However, the bearing number becomes infinitely large and therefore cannot be expressed in graphical form. This then leads to an asymptote at high bearing numbers for both non-dimensional load capacity, which approaches unity, and non-dimensional mass flow rate, which approaches zero.

At low bearing numbers, i.e. large film thickness, the film pressure becomes close to the atmospheric pressure yet, theoretically, the film pressures cannot be equal to the atmospheric pressure unless there exists an infinite film, i.e. the bearing top plate is removed. For an infinite film thickness the mass flow through the porous pad is a maximum as all the available pressure energy is used in creating this mass flow. This gives a unity value to the non-dimensional mass flow rate and a zero value to the non-dimensional load capacity. However, an infinite film thickness gives a zero bearing number which cannot be represented on a logrithmic scale. This then leads to an asymptote at low bearing numbers for both the non-dimensional load capacity, approaching zero, and non-dimensional mass flow rate approaching unity.

In the case of the non-dimensional static stiffness the design curve shows that at high and low bearing numbers this parameter is asymptotic to a zero value, with an optimum value at some intermediate bearing number. The reason for this shape is appreciated by referring to the definition of non-dimensional static stiffness. It is defined as the negative value of the rate of change of the non-dimensional load capacity with respect to the bearing number, multiplied by the bearing number. As the non-dimensional load capacity curve is asymptotic at both high and low bearing numbers the non-dimensional static

stiffness must also be asymptotic to zero at high and low bearing numbers as the rate of change of the non-dimensional load capacity approaches zero. However, the rate of change of non-dimensional load capacity with bearing number does maximise through the transferance from one asymptote to the other and therefore there is a bearing number at which the non-dimensional static stiffness obtains an optimum value.

6.4.3. The Effect of the Bearing Aspect Ratio on the Bearing Performance

Let us now consider the individual effects mentioned previously. Firstly consider the effect of the bearing aspect ratio, S, on the variation of the non-dimensional bearing parameters with bearing number, see figures 76 to 78, pages 264 to 266 . The bearing aspect ratio is defined as the ratio of the pad thickness to the bearing outer radius; there are therefore three ways of altering this ratio. It must be shown that, no matter which pad parameter is altered to alter the aspect ratio a similar effect on performance occurs.

Suppose there is an increase in the aspect ratio due to an increase in pad thickness. The effect is to increase the porous pad's overall resistance to flow. This increase causes the air passing through the pad to experience a greater pressure drop. The increased pressure drop gives, for a constant supply pressure, a reduction in the film

pressures, hence reducing the load capacity. This can be described as a reduction in the efficient use of the available pressure energy as more pressure energy has had to be used in overcoming the increased resistance to flow of the porous pad. If it can be shown that reducing the pad outer radius also reduces the efficiency (load capacity) of the bearing then it will have been shown that altering either of these pad parameters has a similar effect on the bearing.

In order to demonstrate that a smaller diameter bearing is not as efficient in using pressure energy as a large diameter bearing, compare a bearing that has an outer radius of 2 units to a bearing having an outer radius of 1 unit. Consider that these bearings are supplied with air at the same supply pressure, operate at the same film thickness and that the bearing pads are the same thickness and have the same viscous permeability.

As the pad thickness and viscous permeability are identical in these bearings the axial resistance to flow through the pads will be identical. As the bearings are operating at the same film thickness the film resistance to flow per unit length will also be identical. A reduction in the outer radius will mean that the film resistance must be reduced and thus the smaller bearing will have a smaller overall resistance to flow. As the same supply pressure is available to these bearings the mass flow rate through the smaller bearing must be greater

due to the reduction in overall flow resistance. To create a greater mass flow rate through the bearing pad a greater proportion of the pressure energy available must be utilised. This then means that the available pressure energy to support the load must be reduced and therefore the smaller bearing operates at a lower efficiency in comparison to the larger bearing.

Now consider the design curves shown in figures 76 to 78, pages 264 to 266 . It can be seen that this reduction in the efficient use of the available pressure energy by an increase in the bearing aspect ratio distorts the non-dimensional load capacity curve. This affects the non-dimensional static stiffness of the bearing for not only has the optimum stiffness been reduced in value but its occurance relative to the bearing number has also been altered. This increase in bearing number for the occurance of optimum non-dimensional static stiffness may seem trivial, but it has been shown in the previous section that high bearing numbers, i.e. small film thicknesses, may not be attainable due to the surface roughness of the bearing pads. This means then that an engineer may find that an increase in the bearing aspect ratio will prevent the designing of a bearing at the optimum non-dimensional static stiffness condition as the requisite film thickness may be less then the mean pneumatic clearance value.

This reduction in non-dimensional static stiffness can be seen in the non-dimensional load curves in that the rate of change of non-dimensional load with respect to bearing number for a high aspect ratio is less than for a low aspect ratio, i.e. a large range of bearing number is required to transgress from one non-dimensional load to another. This explains the interlacement of the non-dimensional static stiffness curves that occurs at high bearing numbers. In the case of the low aspect ratio bearing the non-dimensional load capacity curve has tended to the asymptote before the high aspect ratio bearing curve. By virtue of this the rate of change of the low aspect ratio bearing tends to zero at a lower bearing number than the high aspect ratio bearing.

Upon inspection of the non-dimensional mass flow rate curves, see figure 77, page 265 , it can be seen that an increase in bearing aspect ratio also distorts these curves. This also requires explanation for in increasing the aspect ratio of the bearing by increasing the pad thickness results in a reduction of the actual mass flow rate through the bearing. However, in increasing the pad thickness the maximum possible mass flow rate through the porous pad is also reduced, given the same operating conditions. As the efficiency of the bearing is reduced by increasing the aspect ratio, a greater proportion of the pressure energy is used is creating mass flow through the porous pad. Now in the maximum mass flow conditions all the available

pressure energy is used in creating mass flow. Therefore, this increase in proportion of pressure energy used to create mass flow for a high aspect ratio bearing, as compared to a low aspect ratio bearing, means that at a given bearing number the ratio of pressure energy used to create mass flow through the porous pad to total pressure energy available is higher for the larger aspect ratio bearing, resulting in a higher non-dimensional mass flow rate.

It can be stated then that the smaller the bearing aspect ratio the greater the effective use of the available pressure energy. However, it must be realised that a decrease in the bearing aspect ratio may result in the porous pad having insufficient strength to withstand the pressure load across it, this pressure load being due to the difference in film pressures to supply pressures. This lack of strength may cause the pad to bow like a diaphragm, creating a non-uniform film. This has detrimental effects on the load capacity and mass flow rates, Taylor and Lewis (70). The designer must be aware of this problem and ensure that, if the design of his bearing is based on the uniform film theoretical design curves, that a uniform film exists.

6.4.4. The Effect of the Supply Pressure on the Bearing Performance

Consider now the curves showing the effect of the supply pressure on the variation of the non-dimensional load capacity and non-dimensional static stiffness with the bearing number as shown in figures 79 and 80, pages 267 and 268 respectively.

These curves show that an increase in the supply pressure causes a decrease in the bearing number such that the design curves move the left without any distortion of the curve occurring. This is explained by the reasoning that an increase in the supply pressure has no effect on the efficiency of the bearing, this is assuming that Darcy's law still governs within the porous pad. As there is no change in bearing efficiency the ratio of pressure energy to support the bearing load to the overall pressure energy available remains constant. However, the actual pressure energy available is increased giving rise to higher film thicknesses. This means that the non-dimensional load capacity is unaffected but the bearing number decreases. Thus the curves are moved to the left.

Because there is no distortion of the non-dimensional load capacity curve the rate of change of these curves with respect to the bearing number is unaffected. This means that the non-dimensional static stiffness curves are unaltered in shape or magnitude but simply shifted to the left.

Although it has been shown mathematically that the non-dimensional mass flow rate is not a function of supply pressure a physical explanation of this phenomina should be given. Consider the case of a bearing operating with a given load at a given film thickness for a given supply pressure. By increasing this supply pressure, there is a resulting increase in the film thickness. Now increase the bearing load such that the original film thickness is obtained, thus the overall resistance to flow of the bearing remains unaltered. Due to the increase in supply pressure there is now more pressure energy available. This increase in pressure energy is absorbed in two ways:

(a) a portion of this extra energy enables a greater load to be supported at a given film thickness;

(b) the remaining extra energy creates a higher actual mass flow through the bearing.

Now in increasing the supply pressure the maximum possible mass flow rate through the porous pad is also increased. As the increase in supply pressure has not altered the efficiency of the bearing, the ratio of pressure energy used to create mass flow to the overall available pressure energy remains unaltered and therefore the non-dimensional mass flow rate remains unaltered. As the same film thickness is maintained the bearing number must remain unaltered. Hence it is immaterial what supply pressure is used for only one non-dimensional mass flow

rate/bearing number curve can be produced.

In actual terms an increase in supply pressure means that for a given film thickness there is a resulting increase in actual bearing load, actual mass flow rate and actual static stiffness. Also the film thickness at which the optimum static stiffness occurs is increased. As previously mentioned the bearing surface finish effect affects the possibility of attaining high bearing numbers. Thus if the bearing number at which this optimum stiffness occurs can be reduced there is a greater possibility of designing a practical bearing that can operate under optimum stiffness conditions.

6.4.5. The Effect of the Porous Material Viscous Permeability on the Steady-state Performance

It has been stated that the effect of varying the viscous permeability of the porous pad cannot be demonstrated on the non-dimensional plots. For this reason this effect has been shown on dimensional plots of load capacity, mass flow rate and static stiffness against film thickness, see figures 81 to 83, pages 269 to 271.

The viscous permeability of a porous material is, in effect, a measure of the viscous conductivity to flow of that material. Hence by decreasing the viscous permeability the resistance to flow of a material is increased.

Consider two bearings having the same basic dimensions operating at the same film thickness fed with the same

supply pressure but having different viscous permeabilities. The bearing with the higher viscous permeability, lower resistance to flow, uses less of the available pressure energy in overcoming the resistance to flow of the porous material. Therefore the air passing through this porous pad experiences a smaller pressure drop. This gives higher film pressures and thus a higher load capacity at this film thickness. This can readily be seen in figure 81, page 269 .

Because these two bearings are operating at the same film thicknesses the film resistance to flow is identical. The driving force for the mass flow through the film is the pressure gradient within the film. Because the film pressure profiles are of the same form, the pressure gradients in the bearing with the lower viscous permeability will be lower due to smaller film pressures. This means that the driving force for the mass flow rate is smaller for the bearing with the lower viscous permeability resulting in lower mass flow rates. This can readily be seen in figure 82, page 270.

The static stiffness of these two bearings does not fall into a lower or higher category as the load and mass flow rate. It depends on what film thickness these bearings operate at which of these bearings has the superior value of stiffness. At these bearings have the same operational area and are fed with the same supply pressure the maximum load capacity of these bearings will

be identical. It has been shown that, for the bearing with the lower viscous permeability, the film thicknesses experienced will be lower than the film thicknesses for the bearing with the higher viscous permeability. Therefore, the bearing with the lower viscous permeability must have a greater rate of change of load capacity with film thickness in comparison with the bearing with the higher viscous permeability. However, it should be remebered that in order to obtain a zero load capacity there must exist within the bearing an infinitely large film thickness. This means that the load/film thickness curve will be asymptotic at high film thicknesses. The bearing with the lower viscous permeability has a load/film thickness curve that approaches this asymptotic line more rapidly than the bearing with the higher viscous permeability. Hence at high film thicknesses the bearing with the higher viscous permeability will have a greater rate of change of the load with respect to film thickness than the bearing with the low viscous permeability. This gives rise to the high viscous permeability bearing having a superior static stiffness at high film thicknesses.

This phenomina can readily be seen in figure 83, page 271 . It should also be noted that the film thickness at which the optimum stiffness occurs reduces as the viscous permeability reduces. This as has already been mentioned may lead to problems, see discussions on surface finish effects in sub-section 6.3.

6.4.6 The Effect on the Design Curves of Neglecting the 'Slip Factor' of Ishizawa and Hori

It was mentioned in section 2 that two authors have produced identical design curves yet one of the authors had neglected the slip flow effect of Ishizawa and Hori. There is an obvious need to determine why this occurred and also to determine the effect of neglecting this slip flow.

The bearing number has been defined as

$$\Lambda = \frac{12\Phi_y r_o^2}{h_o(h_o^2+6\Phi_r)H} = \frac{12\Phi_y r_o^2}{h_o^3(1+6\Phi_r/h_o^2)H} \qquad 6.4.1.$$

the term $6\Phi_r/h_o^2$ is a slip factor accounting for the slip flow of Ishizawa and Hori. Let

$$\mu = 6\Phi_r/h_o^2 \qquad 6.4.2.$$

$$\therefore \quad \Lambda = \frac{2\mu r_o^2}{Hh_o(1+\mu)K} \qquad 6.4.3.$$

If the slip factor is neglected

$$\Lambda_R = \frac{2\mu r_o^2}{h_o HK} = (1+\mu)\Lambda \qquad 6.4.4.$$

where Λ_n is the bearing number calculated without the slip factor.

Curves showing the effect of neglecting this slip factor are shown in figures 84 to 86, pages 272 to 274 It can be seen from these curves that at a given film thickness neglection of the slip factors causes an erroneous value of non-dimensional load capacity, non-dimensional mass flow rate, non-dimensional static stiffness and the bearing number at which the optimum static stiffness occurs. An engineer using a design curve which neglects this slip factor to design a porous bearing under optimum stiffness conditions will find that the actual load capacity is insufficient, the mass flow rate for which he designed for is below the actual mass flow rate and the static stiffness is below the optimum value, all of which lead to bearing failure. It is obvious then that the slip factor is of great importance.

Now the curves depicted in figures 84 to 86, pages 272 to 274 have been drawn assuming a constant slip factor value for changing bearing number. This in practice cannot happen, for in order to obtain a constant slip factor value for changing bearing number, and hence changing film thickness, the viscous permeability must also vary. In practice the viscous permeability is fixed. This means that at relatively high film thicknesses the slip factor will be small thus the neglection of this factor will have a negligible effect in this region in

comparison to the effect the neglection of this factor has at relatively low film thicknesses. From this it can be seen that a practical line crosses the iso-slip factor lines shown on these design plots and eventually at a high bearing number, the value of the bearing number depending on the permeability, blend to the true theoretical curve.

In the case of the low permeability material the slip factor is small, thus the effect of neglecting the slip factor may not be evident. This then is the reason why in comparing the curves of Garguilo and Gilmour (57) to those of Jones et al (60) there was no appreciable difference. The material viscous permeability used by Garguilo and Gilmour was 1.68×10^{-11} in^2. The lowest film thickness encountered was 2×10^{-4}in. This gives a maximum slip factor of 2.52×10^{-3}.

The slip factor then can only be neglected at very high film thicknesses and for very low viscous permeability materials. However, it is not advisable to neglect this factor as designing from curves which neglect this factor may result in under designing of a bearing leading to bearing failure.

6.4.7. Comparison of a Porous Bearing with a Capillary Compensated Bearing

A considerable amount of discussion has been presented on the effects on the steady performance of a porous thrust

bearing by the variation of certain bearing parameters without actually showing that a porous thrust bearing performance is an improvement on the more standard form of thrust bearing. In this section a comparison has been made between a porous thrust bearing and a standard capillary compensated thrust bearing, both air lubricated, in order to determine if the porous bearing characteristics are superior to the capillary bearing.

In order to compare these bearings it was decided to equalise the resistance to flow through the bearing restrictors. This means that, for a given supply pressure, the mass flow through the capillary of the capillary compensated bearing, when vented to atmosphere, equals the mass flow through the porous pad of the porous bearing, when vented to atmosphere. In order that this is so the Darcy law must be equated to the Hagen-Poiseuille law, i.e.

$$m = \frac{(p_s^2 - p_a^2) A . \Phi_y}{2HRTn} \qquad \text{Darcy law} \qquad 6.4.5.$$

$$m = \frac{k_c (p_s^2 - p_a^2)}{2nRT} \qquad \text{Hagen-Poiseuille law} \qquad 6.4.6.$$

$$\therefore \quad \frac{(p_s^2 - p_a^2) A . \Phi_y}{2HRTn} \equiv \frac{k_c (p_s^2 - p_a^2)}{2nRT} \qquad 6.4.7.$$

leading to

$$\frac{A\Phi_y}{H} = k_c \qquad 6.4.8.$$

Figures 87 to 89, pages 275 to 277 , show the load capacity, mass flow rate and static stiffness variation with film thickness curves for a porous thrust bearing and a capillary compensated bearing which (a) is inherently compensated, (b) has a port radius to outer radius ratio of 0.2 and (c) has a port radius to outer radius ratio of 0.6. The outer radius of these bearings has also been equated such that the maximum load of these bearings is identical.

The load capacity curves, shown in figure 87, page 275 show that at high film thicknesses, 15 micron or above, all forms of the capillary compensated bearing will support a higher load than the porous thrust bearing. However, the magnitude of the load at this film thickness is very small and the bearings are operating in a region of very low efficiency. As the film thickness is reduced to 4 micron or less, the general operating region of an air bearing, the porous bearing load capacity is shown to be superior to all forms of the capillary compensated bearing. The reason for this is for the capillary compensated bearing there are two basic regions in which pressure forces are applied to the bearing top plate (a) the port area and (b) the film area. As the film thickness

decreases the port pressure can rise to practically the supply pressure due to direct connection to the pressure chamber via the capillary. However, the film pressures cannot approach supply pressure value until the bearing has practically shut down as there is no direct connection to the pressure chamber. In the case of the porous bearing the whole of the film region can approach the supply pressure value more easily due to the direct connection via the porous pad to the supply chamber.

This more even spreading of the supply pressure in the porous bearing gives a superior pressure profile at small film thicknesses, and hence a higher load capacity.

For a given film thickness the pressure gradient at the outer radius of a porous bearing is higher than the pressure gradient for a capillary bearing. As it is this pressure gradient that is the driving force for mass flow out of the bearing film, the mass flow through a porous bearing is greater than the capillary bearing, see figure 88, page 276. This then is the disadvantage of a porous bearing in comparison to a capillary bearing. However, generally the designer of a bearing is concerned more with load capacity and stiffness of a bearing than mass flow rate through the bearing.

The static stiffness of the porous bearing is never less than the capillary bearing, for the condition of equal resistance to flow, as can be seen in figure 89, page 277 . It can also be seen that the rate of change

of the static stiffness from its optimum value of the porous bearing as the film thickness is reduced is not as high as that of the capillary bearing.

Consider the case of an engineer designing a bearing to operate at its optimum stiffness. In comparing the porous bearing and capillary compensated bearing having a port radius to outer radius ratio of 0.6 in which flow resistance has been equalised it would be found that:

Using the capillary bearing as a base the porous bearing would give 18.75% more load capacity, 34.38% more static stiffness yet requiring only 32.8% more mass flow.

Not only are the steady performance figures of the porous bearing superior to the comparable capillary bearing but the porous bearing is less liable to pneumatic hammer effects, due to the smaller volume content of the bearing (2), (63) and is cheaper to manufacture as the complicated machining of the bottom bearing plate is un-necessary, (66), (69).

6.5 THEORETICAL DYNAMIC BEARING CHARACTERISTICS

6.5.1 Introduction and Definition

For the case of forced vibration of these bearings, i.e. a time dependent situation, it was stated in section 3.4, the section dealing with the time dependent analysis,

that a truely analytic solution could not be achieved due to the complexity of the equations involved. It was therefore necessary to resort to a numerical method of solution in order to obtain the theoretical predictions of bearing performance. The numerical method used in itself is not a simple one, numerical instability was encountered by using a standard central difference method and in order to eliminate this instability excessive computational storage and time was required. The numerical method employed is a combination of the Roscoe technique, the Alternating Direction Implicit technique and a relaxation process, see section 3.4. Even though this sophisticated numerical process of solution was employed the computational time involved was still high and therefore solutions proved to be prohibitively expensive. Due to this the dynamic characteristic curves have been limited to one bearing configuration. The dynamic characteristic curves produced, however, are thought to exhibit the general trends involved.

The theoretical analysis performed was in two sections, these sections were:

(a) A constant displacement analysis. This analysis was to determine if the air film dynamic spring force was a linear function of displacement.

(b) A constant velocity analysis. This analysis was to determine if the air film damping force was a linear function of velocity.

Before discussing the results of the above theoretical analysis an explantory note on the meaning of the parametric groups involved is necessary.

The frequency factor, α, is a parametric group containing the following indpendent variables: -

the porous pad thickness, porosity and viscous permeability,
the lubricant viscosity,
the frequency of oscillation,
the atmospheric pressure.

For a given bearing configuration with air lubrication this parameter is basically a measure of the frequency of oscillation.

The velocity factor, γ, is a parametric group containing the following variables: -

the bearing outer radius and film thickness,
the porous pad viscous permeability,
the lubricant viscosity,
the velocity of bearing top plate due to the forced vibration.

For a given bearing configuration with air lubrication this parameter is basically a measure of the velocity of oscillation.

The frequency factor, β, is a parametric group which although prevalent in the analysis, is not an independent variable, i.e. it is not considered to be a design factor

in its own right. This parametric group is combined with the velocity factor parametric group to give a displacement factor. By dividing the velocity factor by this frequency factor, the result is a ratio of the amplitude of vibration of the bearing to the mean film thickness.

The non-dimensional dynamic spring force is the ratio of the in-phase component of the pressure perturbation integral vector to the atmospheric pressure force experienced by the bearing.

The non-dimensional damping force is the ratio of the quadrature component of the pressure perturbation integral vector to the atmospheric pressure force experienced by the bearing.

6.5.2 Constant Displacement Factor Analysis

The theoretical results of the constant displacement analysis are shown in figures 90 to 93, pages 278 to 281 Figure 90, page 278 shows the non-dimensional dynamic spring force variation with the displacement factor $\frac{\gamma}{\beta}$ for a series of frequency factor values, α values. It can be seen from this family of curves that for a given frequency factor, α value, the non-dimensional dynamic spring force is a linear function of the displacement factor, $\frac{\gamma}{\beta}$. Now this linear relationship could be due to: (see figure 13, page 71)

(a) a linear increase in the pressure perturbation integral

vector without any change in the phase angle τ between this vector and the film thickness vector;

(b) an increase in the phase angle τ between the pressure perturbation integral vector and the reference vector without any change in the magnitude of the pressure perturbation integral vector;

(c) a combination of (a) and (b).

One technique of determining which of the above three variations give rise to this linear relationship between the non-dimensional dynamic spring force and the displacement factor is to inspect the relationship between the non-dimensional damping force and the displacement factor. If (a) is the cause of this linear relationship then the relationship between the displacement factor and the non-dimensional damping force will also be linear, in that as the displacement factor increases the non-dimensional damping force will increase. If, however, (b) is the cause then there will still be a linear relationship between the non-dimensional damping force and the displacement factor but in this case as the displacement factor increases the non-dimensional damping force will decrease. If (c) is the reason for the linear relationship between the non-dimensional dynamic spring force and the displacement factor the relationship between the

non-dimensional damping force and the displacement factor will be a non-linear relationship. Figure 91, page 279 shows the variation of the non-dimensional damping force with the displacement factor $\frac{\gamma}{\beta}$. It can be seen that a non-linear relationship exists between the non-dimensional damping force and the displacement factor. Thus it can be stated that as the displacement factor is increased the magnitude of the pressure perturbation integral vector increases and there is a resulting change in the phase angle τ between this vector and the reference vector.

The question now to be answered is why does the phase angle between these vectors alter with displacement factor? An explanation of this can be given by considering the pressure changes that take place during vibration, in the same way as the pneumatic instability problem of the ported bearing was explained in section 1.2. In forcibly vibrating the porous bearing three pressure change effects are manifest. These effects are:-

(a) The quasi-static film pressure effect.

(b) The squeeze film effect.

(c) The porous pad content effect, analogous to the ported bearing port content effect.

Consider the quasi-static film effect. In this case, if the mass inflow equals the mass outflow, by increasing the displacement factor the pressure force on the bearing top plate would increase linearly and the phase angle

between the pressure perturbation integral vector and the reference vector would remain constant, analogous to a spring-mass system with the absence of damping. The squeeze film effect, for a given frequency, increases in an $(1-e^{-1_4})$ form for an increase in the amplitude of vibration, C.H.T. Pan (73). By increasing the amplitude of vibration, without increasing the frequency, the squeeze film effect would give rise to an $(1-e^{-1_4})$ increase in the damping of this bearing and a resulting decrease in the phase angle τ.

However, by increasing the amplitude of vibration, without increasing the frequency, the film pressures, on an upward stroke will decrease to a lower value than previously. This decrease will result in a greater exhausting of the porous pad content. This could have been explained by the fact that an increase in the amplitude of vibration for a given frequency gives an increase in velocity of vibration. This increase in the velocity of the bearing top plate creates a greater suction effect on the porous pad. Now on a downward stroke the lubricants compressibility renders it impossible for the pad pressure to be increased throughout the pad from the film. Instead the disturbances are squeezed within a thin layer adjacent to the porous pad/gas film interface, Dah-Chen Sun (63). The porous pad then can only have its content filled from the pressure chamber. This porous pad exhaustion effect

gives rise to negative damping and a resulting increase in the phase angle τ. The increase in the negative damping is an $(1-e^{-l_2})$ increase due to the exponent form of exhausting from the pad, Peaceman and Rachford (74), though of a different rate of change than the squeeze film effect.

The addition then of the squeeze film effect and the porous pad content effect is the addition of two $(1-e^{-l})$ effects. This then gives rise to the change in phase angle and the resulting non-linear relationship between the non-dimensional damping force and the displacement factor. The squeeze film effect appears, from the results obtained, to be initially the dominent effect with the porous pad content effect becoming more effective as the displacement factor values increase.

Now from figures 90 and 91, pages 278 and 279 it can be seen that both the non-dimensional dynamic spring force and the non-dimensional damping force relationship to the displacement factor is also dependent upon the frequency factor α. To examine these relationships figures 92 and 93, pages 280 and 281 have been drawn. Figure 92, page 280 shows the variation of the non-dimensional spring force with the frequency factor α for a series of displacement factors while figure 93, page 281 shows the variation of the non-dimensional damping force with the frequency factor α for a series of displacement factors.

It can be seen from figure 92, page 280 that by increasing the frequency and hence increasing the frequency factor α whilst the displacement factor remains constant, that the non-dimensional spring force decays in an exponential form, eventually becoming asymptotic to some value, this value being dependent upon the value of the displacement factor. This decrease in the value of the non-dimensional dynamic stiffness force may be explained by an inertia effect. By increasing the value of the frequency, the time available for pressure changes is reduced. In a quasi-static situation there is ample time for the full pressure change relevant to the displacement to occur. However, as the time of change reduces then the full pressure change will not be manifest due to the inertia of the gas molecules. There will, however, be a minimum pressure change that can occur for a given displacement.

It can be seen in figure 93, page 281 that by increasing the frequency and hence increasing the frequency factor, whilst the displacement factor remains constant, that the non-dimensional damping force initially increases, reaches a maximum value and then decreases, eventually leading to a negative damping force. In increasing the frequency of oscillation the squeeze film effect will initially increase but eventually will optimise at a given frequency and will remain at this optimum value for any further

increase in the frequency, C.H.T. Pan (73). However, in increasing the frequency and keeping the amplitude of vibration constant the velocity of vibration increases. In increasing the velocity the porous pad experiences a greater suction effect on the upward stroke, as previously mentioned. This increase in the velocity of the bearing top plate causes an increased porous pad content effect, i.e. increased negative damping effect. Again from the results obtained it can be seen that the squeeze film effect is the initial dominating effect with the porous pad content effect becoming more effective as the frequency factor increases. At high frequency factors the porous pad content effect dominates with a resulting negative damping for high displacement factor values.

6.5.3 Constant Velocity Factor Analysis

The theoretical results of the constant velocity analysis are shown in figures 94 to 97, pages 282 to 285 Figures 94 and 95, pages 282 and 283 show the non-dimensional dynamic spring force variation with the velocity factor γ and the non-dimensional damping force with the velocity factor γ respectively for a series of frequency factor values. For a given frequency factor value an increase in the velocity factor can only be achieved by an increase in the amplitude of vibration, for a given bearing configuration. Now an increase in the amplitude

of vibration gives an increase in the displacement factor. Thus these curves must exhibit identical relationships to those shown by an increase in the displacement factor, see figures 90 and 91, pages 278 and 279 . It can be seen that this is so and therefore these relationships shown in these families of curves require no explanation.

The relationships between the non-dimensional dynamic spring force and the non-dimensional damping force with the frequency factor α for a series of given velocity factors are shown in figures 96 and 97, pages 284 and 285 respectively and it is these relationships that are more informative in this analysis. The variation of the non-dimensional dynamic spring force with the frequency factor α for a given value of velocity factor is shown in figure 96, page 284 . It can be seen from this family of curves that as the frequency factor increases there is an initial sharp decline in the non-dimensional dynamic stiffness which eventually becomes asymptotic at high values of the frequency factor, the asymptotic value being dependent upon the velocity factor value. The explanation of this behaviour can be given by referring to the family of curves showing the relationship for a given displacement factor of the non-dimensional dynamic spring stiffness with the frequency factor α , figure 93, page 281 . It can be seen in figure 93 that for a constant displacement factor the initial reduction of

the non-dimensional dynamic spring force is far less than that for a constant velocity factor. For a given bearing configuration in order to keep the velocity factor constant for an increase in the frequency factor the amplitude of vibration must reduce. The relationship between frequency factor and displacement factor for a constant velocity factor is shown in figure 98, page 286 . It can be seen that initially the variation of the amplitude is high eventually becoming asymptotic to zero. This then explains the initial sharp decline in the velocity factor curves and asymptotic behaviour at high frequency factor values. Thus a superimposition of the velocity factor family of curves on the displacement factor family of curves would show that a given velocity factor curve would transgress from one displacement factor curve to another for a given increase in the frequency factor α , see figure 99, page 287 .

A similar explanation of the relationship of the non-dimensional damping force to the frequency factor α for a constant velocity factor can be given A superimposition of the velocity factor family of curves on the displacement factor family of curves is shown in figure 100, page 288 . The results of these two analysis then show that: -

(a) the non-dimensional dynamic spring force has a linear relationship with the displacement factor $\frac{\gamma}{\beta}$.

(b) the non-dimensional dynamic spring force has a non-linear relationship with the frequency factor α .

(c) The non-dimensional damping force has a non-linear relationship with both the velocity factor γ and the frequency factor α . An optimum value of the damping force occurs within this relationship.

6.5.4 The Use of the Dynamic Characteristic Curves in the Design of a Porous Bearing

In designing a gas bearing the engineer requires information on the dynamic characteristics of the type of bearing to be designed, for during the operational life of the bearing it may well be that the bearing will be subjected to vibrational forces, as in the case of a machine tool situation. The engineer needs to design the bearing such that when it is subjected to these vibrational forces, stable operation of the bearing will continue. This means then that the design of the bearing should be such that positive damping of the vibrational forces will ensue from the gas film forces.

Consider the case where an engineer requires to design an air lubricated porous thrust bearing for use within a machine tool under the optimum static stiffness condition. Having designed the bearing for steady operation from the steady-state design curves presented

previously, the engineer must ensure that stable conditions will continue for dynamic operation. In designing the bearing for steady operation the designer will have found the operating bearing number. Generally in machine tool design the space available for bearings is severely limited and by virtue of this the designer will have little or no choice on the outer radius of the bearing and porous pad thickness.

In designing a bearing for use within a machine tool the engineer should have details of the operational speeds of the machine tool, these speeds will be the values of the primary frequencies of the vibrational loads. Consider that the engineer has a limited choice of porous material and that he is limited to a given porosity. By knowing the porous pad thickness, porosity and viscous permeability and the range of forcing frequencies the engineer can determine the range of the frequency factor α. By use of the design curve showing the dimensionless damping force variation with the frequency factor α for a series of displacement factor values the engineer can determine which displacement factor is desirable to give positive damping throughout the known frequency factor range.

In knowing this displacement factor the engineer can then determine the range of the dimensionless dynamic spring force and hence the dynamic spring stiffness of the bearing. This will allow the computation of the range of natural frequencies the bearing will have for a given supported mass. If it is found that these natural

frequencies are within the operating frequencies of the machine tool then the engineer should choose a different displacement factor, such that the new range of natural frequencies are out of the operating range of the machine tool speeds. If this procedure is not followed, natural vibration of the bearing may occur.

Having determined the displacement factor that gives the desired damping and dynamic stiffness the engineer may then decide the maximum amplitude of vibration the design will allow. In knowing this he can compute the requisite steady operational film thickness to give the required displacement factor. By knowing the steady operational film thickness he can then compute the necessary porous pad viscous permeability from the operating bearing number. If this permeability value does not agree with the value used in computing the range of the frequency factor α the engineer must either reiterate the above procedure until agreement is reached or determine if the static stiffness of the bearing for the new bearing number is adequate.

6.6 THE FORCED VIBRATION EXPERIMENTAL RESULTS

It was stated in section 5.3.2. that the experimental approach used in the forced vibration tests would be the sweep frequency test in which the applied force amplitude would be held constant. This form of test enables the

acceleration/frequency of oscillation resonance curve to be automatically drawn by a system of monitoring equipment as described in section 5.3.2. It was also shown in section 5.3.1. that the dynamic spring stiffness and damping coefficient of the vibrating system could be determined from this acceleration amplitude/frequency of oscillation resonance curve.

Consider then a sweep frequency test on a porous bearing which is operating under a given set of steady conditions, i.e. bearing load, supply pressure, film thickness etc. Before the sweep frequency test begins a force amplitude value is set at the lower limit of the frequency range of the frequency test. This force amplitude gives a corresponding value of displacement, velocity and acceleration of the bearing top plate. Upon initiation of the sweep frequency test the frequency of oscillation is increased and, assuming the lower frequency level is below the resonance frequency, approaches the resonant frequency. In approaching the resonant condition the displacement, velocity and acceleration of the bearing top plate increase. Upon attaining the resonant frequency a further increase in frequency gives a decrease in the displacement, velocity and acceleration of the bearing top plate.

It can be seen then from this description of a sweep frequency test that for a given set of steady operating conditions and a given force amplitude that the displacement factor $\frac{\gamma}{\beta}$ and the velocity factor γ vary. Thus it

can be seen that a sweep frequency test gives a range of displacement, frequency and velocity factor values. By changing the amplitude of the applied vibrational force a different range of displacement factor and velocity factor values can be obtained, for the same steady operating conditions and frequency factor values. There is obviously an upper and lower limit to the range of forces that can be applied to this bearing. The upper limit of the force is the force value that will cause, at resonance, the amplitude of vibration to equal the steady film thickness. The lower limit of the force is the force value that can overcome the inertia of the system.

Further ranges of velocity and displacement factor values can, however, be obtained by changing the steady film thickness value. By altering this value no alteration is made to the frequency factor α and thus a new range of forces will give new ranges of displacement and velocity factor values. By obtaining these various ranges of displacement and velocity factor values for a given range of frequency factor values enables a series of non-dimensional dynamic spring force/displacement factor and non-dimensional damping force/velocity factor values to be determined for discreet values of the frequency factor α. This means that a comparison between the theoretical predictions and experimental results can be made.

Now consider a resonance curve produced by a sweep frequency test on a linear system. For such a system it

is immaterial at what frequency, other than resonance, the ratio of acceleration amplitude to resonance acceleration amplitude and ratio of frequency to resonance frequency are taken the same value of dynamic stiffness and damping coefficient should be determined. This means that as resonance is approached the dynamic spring force and damping force should increase as the displacement and velocity increase respectively. These two forces should maximise at the frequencies the displacement and velocity maximise and then decrease as the frequency increases. This linear system should also retain the same resonant frequency value no matter what the value of applied force.

In performing the sweep frequency tests on the porous bearings it has been found that these bearings do not always exhibit linear characteristics. Indeed great difficulty has been experienced in obtaining linear vibrations of these bearings and in order to do so the range of the displacement factor of the bearing top plate is severely limited. When larger values of this displacement factor were encountered, i.e. by either increasing the amplitude of the applied force or as resonance was approached, the motion of the bearing top plate was no longer sinusoidal. The motion encountered was a distorted sinusoidal motion, the distortion was caused by harmonics. This distortion of the motion is a characteristic of non-linear vibrations.

This meant then that at the beginning of a sweep frequency test for a small applied force sinusoidal motion of the bearing top plate occurred, but as resonance was approached it was possible that non-linear vibrations of the bearing ensued. Upon passing the resonance point it was possible that linear vibration of the system occurred again. Another indication that the bearing was vibrating in a non-linear fashion was shown by comparing the resonant frequencies of various tests for the same steady film thickness. As the value of the applied force amplitude was increased the resonant frequency also increased. A typical family of resonance curves for a given set of steady operating conditions are shown in figure 101, page 289 . It can be seen from this family of curves that for the smaller force amplitude the resonance curve appears to show linear characteristics, in that a smooth resonance curve has been produced. As the force magnitude and hence displacement increases the resonance curve becomes severly distorted at the resonant frequency. The sharp cut off form of distortion exhibited in these curves is a common indication of a vibrating system with a hardening spring stiffness (75). This increase in spring stiffness will give rise to a greater increase in spring force than would be encountered if the bearing had linear characteristics.

Now as a considerable proportion of the time available for this research programme had been employed in determining

the relevant practical factors involved in the steady-state analysis of these bearings it was decided that even though non-linear vibrations were encountered in the majority of the frequency sweep tests, the acceleration amplitude/ frequency of oscillation resonance curves should be drawn for these sweep frequency tests. From these resonance curves the equivalent linear characteristics should be determined such that a first approximation of the dynamic characteristics of these bearings could be achieved.

A typical sample of the comparison of the theoretical predictions and experimental results are shown in figures 102 to 109, pages 290 to 297 . It can be seen from these figures that for all values of the frequency factor α the theoretical predictions of the non-dimensional spring force at moderate to high values of displacement factor seriously under-estimate the real value of the non-dimensional spring force. At low values of displacement factor the theoretical predictions, although still under-estimating the real non-dimensional spring force, do not show such a serious under-estimation. This is the hardening spring stiffness effect. The experimental results show that as the displacement factor increases there is a distinct upward curving in the value of the non-dimensional spring force the result of an increasing value of the spring stiffness.

In the case of the non-dimensional damping force the theory over predicts the non-dimensional damping force

available for low values of the frequency factor α. As the frequency factor is increased the theory correctly predicts the non-dimensional damping force available but eventually under predicts the non-dimensional damping force.

These results then show that for the bearing tested in this series of tests the linear characteristics assumption in the theoretical analysis is invalid. This means that the theoretical analysis in itself does not truely describe the real situation of this research programme. However, the statement that this theory is invalid for all forms of vibration is unfair as this theory has not been tested for truely linear vibrations of these bearings.

Thus two statements can be made from the above discussion. The first statement is that the theoretical analysis presented in Chapter 3 is invalid if the vibrations of the porous bearing are non-linear and a new theory must be produced, see section 7. The second statement is that the experimental tests performed on these bearings do not fully invalidate the linear dynamic theory as the range of the experiments are outside the domains of the theoretical assumptions. Further tests in the linear vibration mode must be performed in order to check this theory.

6.7 CONCLUSIONS

A new and accurate technique of measurement of the viscous and inertia permeabilities of a porous material has been specified. This technique not only enables accurate measurement of these properties but also enables a designer to determine the pressure drop limitation of the Darcy law of flow through the porous material.

The effect of surface finish on effective film thickness can be accounted for by a new method of film thickness measurement based on a knowledge of film pressure distribution.

The slip velocity term of Ishizawa and Hori has been found to be of great importance in the construction of the non-dimensional steady-state design curves.

Good agreement between theoretically predicted and actual performance of a full faced porous thrust bearing is possible provided account is taken of several practical influences. Those considered are elastic deflection of the porous pad, shear distortion of the pad bond, surface finish of the pad and the nature of gas flow through it.

A linear vibration analysis of full faced porous bearings has been presented. Experimental verification of this analysis has not been achieved.

High amplitudes of vibration of these bearings result in the bearing having non-linear vibrational characteristics.

CHAPTER SEVEN

FURTHER WORK

7.1 INTRODUCTION

Even though this research programme has enabled a considerable amount of work to be carried out in analysing and understanding the performance of the full faced porous thrust bearing a complete analysis of the mechanisms involved in these bearings is still not available. Some of the work areas listed in the area of investigation, see section 2.3, have not been analysed either theoretically or experimentally due to the limited time available. The author of this text, however, has considered some of the problems involved in these areas and it is hoped that the following ideas of analysis shown below may be of some use to future workers in this field.

The basic fields of analysis together with experimental verification still to be investigated are: -

(a) The case where the Forchheimer law governs the flow through the porous material.

(b) A steady-state stability analysis

(c) A non-linear theoretical analysis of the time dependent situation.

7.2 FORCHHEIMER FLOW THROUGH THE POROUS MATERIAL

7.2.1 Governing Differential Equation

For this form of flow through the porous material the law governing the flow may be written as, considering one dimensional flow

$$-\frac{dp}{dy} = \frac{\eta v}{\Phi_y} + \frac{\rho v^2}{\phi_y} \qquad 7.2.1.$$

solving equation 7.2.1. for v gives:

$$v = -\frac{\phi_y \eta}{2\rho\Phi_y}\left[1 - \left(1 - \frac{4\rho\Phi_y^2}{\phi_y\eta^2}\frac{dp}{dy}\right)^{\frac{1}{2}}\right] \qquad 7.2.2.$$

Substitution of equation 7.2.2. into the continuity equation for flow of a fluid through a porous media, equation 3.2.1. gives

$$\frac{P^*}{RT}\frac{\partial p}{\partial t} + \frac{1}{r}\frac{\partial}{\partial r}\left(\frac{r.\phi_r\eta}{2\Phi_r}\left[1 - \left(1 - \frac{2\Phi_r^2}{\phi_r\eta^2 RT}\frac{\partial(p^2)}{\partial r}\right)^{\frac{1}{2}}\right]\right)$$

$$+ \frac{\partial}{\partial y}\left(\frac{\phi_y\eta}{2\Phi_y}\left[1 - \left(1 - \frac{2\Phi_y^2}{\phi_y\eta^2 RT}\frac{\partial(p^2)}{\partial y}\right)^{\frac{1}{2}}\right]\right) = 0 \qquad 7.2.3.$$

which upon non-dimensionalisation gives

$$\frac{\alpha_1}{\overline{P}} \frac{\partial(\overline{P}^2)}{\partial \overline{T}} + \frac{K_2 S}{KR} \frac{\partial}{\partial R}\left[1 - \left(1 - \alpha_2 \frac{\partial(\overline{P}^2)}{\partial R}\right)^{\frac{1}{2}}\right]$$

$$+ \frac{\partial}{\partial Y}\left[1 - \left(1 - \frac{\alpha_2 K_2}{K^2 S} \frac{\partial(\overline{P}^2)}{\partial Y}\right)^{\frac{1}{2}}\right] = 0 \qquad 7.2.4.$$

where

$$\alpha_1 = \frac{2H\Phi_y P^* \omega p_a}{\phi_y \eta R T}$$

$$K_2 = \phi_r / \phi_y$$

$$\alpha_2 = \frac{2\Phi_r^2 p_a^2}{\phi_r \eta^2 R T r_o}$$

7.2.2. Boundary Equations for Forchheimer Flow

At three of the boundaries similar conditions prevail, i.e.

$$\overline{P} = \overline{P}_s \qquad 0 \leqslant R \leqslant 1, \quad Y = 0$$

$$\frac{\partial}{\partial R}(\overline{P}^2) = 0 \qquad R = 0, \quad 0 \leqslant Y \leqslant 1$$

$$\frac{\partial}{\partial R}(\overline{P}^2) = 0 \qquad R = 1, \quad 0 \leqslant Y \leqslant 1$$

Now at the fourth boundary the Reynolds equation holds. However, as this equation contains the slip velocity term the equation must be modified to take into account Forchheimer flow.

Integrating equation 3.2.8. and evaluating the constants of integration A, and B with the boundary conditions of:

$$y = H + h \quad U = 0$$

$$y = H \quad U = U_o = -\frac{\phi_r \eta}{2\rho\Phi_r}\left[1 - \left(1 - \frac{4\rho\Phi_r^2}{\phi_r \eta^2}\frac{\partial p}{\partial r}\right)^{\frac{1}{2}}\right]$$

yields

$$U = \frac{1}{2\eta}\frac{\partial p}{\partial r}(y^2 - (2H+h)y + H^2 + Hh) + U_o\left(1 + \frac{H}{h} - \frac{y}{h}\right) \qquad 7.2.5.$$

Integrating the continuity equation, equation 3.2.9. with respect to y between the limits H and (H + h) gives

$$\int_H^{H+h} \left(\frac{1}{r}\frac{\partial}{\partial r}(r\rho u) + \frac{\partial}{\partial y}(\rho v) + \frac{\partial \rho}{\partial t}\right) dy = 0$$

Replacing u by equation 7.2.5., ρ by the equation of state and using the assumption that the pressure is not a function of y yields upon integration and simplification:

$$\frac{1}{r}\frac{\partial}{\partial r}\left(rh\left[\frac{h^2}{2}\frac{\partial}{\partial r}(p^2) - 6p\eta u_o\right]\right)$$

$$+ 12\eta p v_o\Big|_{y=H} = 12\eta \frac{\partial}{\partial t}(ph)$$

7.2.6.

Equation 7.2.6. is the modified Reynolds equation which upon non-dimensionalising becomes:

$$\frac{1}{R}\frac{\partial}{\partial R}\left[R\left(\frac{\partial}{\partial R}(\overline{P}^2) + \alpha_3\left(1 - \left(1-\alpha_2\frac{\partial}{\partial R}(\overline{P}^2)\right)^{\frac{1}{2}}\right)\right)\right] =$$

$$\alpha_4\left[1 - \left(1 - \frac{\alpha_2 K_2}{K^2 S}\frac{\partial}{\partial Y}[\overline{P}^2]_{y=1}\right)^{\frac{1}{2}}\right] + \frac{\beta_1}{\overline{P}}\frac{\partial}{\partial \overline{T}}(\overline{P}^2) + \gamma_1 \overline{P}$$

7.2.7.

where

$$\alpha_3 = 6r_o\eta^2\phi_r RT \;/\; h^2\Phi_r p_a^2$$

$$\alpha_4 = 2r_o K\alpha_3 \;/\; hK_1$$

$$\beta_1 = 12r_o^2\eta\omega \;/\; h^2 p_a$$

$$\gamma_1 = 24r_o^2\eta\frac{\partial h}{\partial t} \;/\; h^3 p_a$$

7.2.3 Equation Systems for both Steady-State and Time Dependent Cases

The steady-state system of equations to be solved for the case of Forchheimer flow may be written:

$$\frac{K_2 S}{KR}\frac{\partial}{\partial R}\left[1-\left(1-\alpha_2\frac{\partial}{\partial R}\left(\bar{P}^2\right)\right)^{\frac{1}{2}}\right]+\frac{\partial}{\partial Y}\left[1-\left(1-\frac{\alpha_2 K_2}{K^2 S}\cdots\right.\right.$$

$$\left.\left.\cdots\frac{\partial}{\partial Y}\left(\bar{P}^2\right)\right)^{\frac{1}{2}}\right]$$

$$0 \leqslant Y \leqslant 1, \quad 0 \leqslant R \leqslant 1 \qquad 7.2.8.$$

$$\bar{P} = \bar{P}_s \quad 0 \leqslant R \leqslant 1, \quad Y = 0 \qquad 7.2.9.$$

$$\frac{\partial}{\partial R}\left(\bar{P}^2\right) = 0 \quad R = 0, \quad 0 \leqslant Y \leqslant 1 \qquad 7.2.10.$$

$$\frac{\partial}{\partial R}\left(\bar{P}^2\right) = 0 \quad R = 1, \quad 0 \leqslant Y \leqslant 1 \qquad 7.2.11.$$

$$\frac{1}{R}\frac{\partial}{\partial R}\left[R\left(\frac{\partial}{\partial R}\left(\bar{P}^2\right)+\alpha_3\left(1-\left(1-\alpha_2\frac{\partial}{\partial R}\left(\bar{P}^2\right)\right)^{\frac{1}{2}}\right)\right)\right]$$

$$=\alpha_4\left[1-\left(1-\frac{\alpha_2 K_2}{K^2 S}\frac{\partial}{\partial Y}\left(\bar{P}^2\right)\right)^{\frac{1}{2}}\right]$$

$$0 \leqslant R \leqslant 1, \quad Y = 1 \qquad 7.2.12$$

The time dependent system of equations to be solved for the case of Forchheimer flow may be written -

$$\frac{\alpha_1}{\bar{P}} \frac{\partial(\bar{P}^2)}{\partial \bar{T}} + \frac{K_2 S}{KR} \frac{\partial}{\partial R}\left[1 - \left(1 - \alpha_2 \frac{\partial}{\partial R}\left(\bar{P}^2\right)\right)^{\frac{1}{2}}\right]$$

$$+ \frac{\partial}{\partial Y}\left[1 - \left(1 - \frac{\alpha_2 K_2}{K^2 S} \frac{\partial}{\partial Y}\left(\bar{P}^2\right)\right)^{\frac{1}{2}}\right]$$

$$0 \leqslant R \leqslant 1, \quad 0 \leqslant Y \leqslant 1, \quad 0 \leqslant \bar{T} \leqslant 1 \qquad 7.2.4.$$

$$\bar{P} = \bar{P}_s \quad 0 \leqslant R \leqslant 1, \quad 0 \leqslant \bar{T} \leqslant 1, \quad Y = 0 \qquad 7.2.13$$

$$\frac{\partial}{\partial R}(\bar{P}^2) = 0 \quad R = 0, \quad 0 \leqslant Y \leqslant 1, \quad 0 \leqslant \bar{T} \leqslant 1 \qquad 7.2.14$$

$$\frac{\partial}{\partial R}(\bar{P}^2) = 0 \quad R = 1, \quad 0 \leqslant Y \leqslant 1, \quad 0 \leqslant \bar{T} \leqslant 1 \qquad 7.2.15$$

$$\bar{P}(\bar{T}) = \bar{P}(\bar{T} + 1) \qquad 0 \leqslant R \leqslant 1, \quad 0 \leqslant Y \leqslant 1 \qquad 7.2.16$$

$$\frac{1}{R} \frac{\partial}{\partial R}\left[R\left(\frac{\partial}{\partial R}\left(\bar{P}^2\right) + \alpha_3\left(1 - \left(1 - \alpha_2 \frac{\partial(\bar{P}^2)}{\partial R}\right)^{\frac{1}{2}}\right)\right)\right]$$

$$= \alpha_4\left[1 - \left(1 - \frac{\alpha_2 K_2}{K^2 S}\left(\frac{\partial(\bar{P}^2)}{\partial Y}\right)_{Y=1}\right)^{\frac{1}{2}}\right] + \frac{\beta_1}{\bar{P}} \frac{\partial}{\partial \bar{T}}\left(\bar{P}^2\right) + \gamma_1 \bar{P}$$

$$0 \leqslant R \leqslant 1, \quad 0 \leqslant \bar{T} \leqslant 1, \quad Y = 1 \qquad 7.2.7$$

A truely analytic solution of the two sets of equations given above is thought to be improbable due to their severe non-linearity. Solution then must be made by a numerical process. The author considers that the A.D.I. scheme of Peaceman and Rachford should be used to solve

both the time dependence and steady-state cases. In the case of the time dependence equations either a linear or non-linear analysis can be made.

7.3 STABILITY ANALYSIS

The problem of pneumatic instability can still be encountered for porous bearings, indeed some of the bearings manufactured during this research programme were found to be prone to this form of instability. The following analysis was compiled by the author as it was hoped that during this research programme this problem could be investigated. However, insufficient time was available and this analysis has not been proven by experimental correlation.

The analysis itself is based on the classical work of Licht, Fuller and Sternlicht. It has been assumed that the flow through the porous media was governed by Darcy's law. However, a like analysis could be made for the case of Forchheimer flow.

7.3.1 Mass Content within the Bearing

7.3.1A Mass Content of Porous Pad

It is known from the steady-state analysis made in section 3.3 that the pressure distribution within the porous pad is given by -

$$\overline{P}_{pad} = \left[\overline{P}_s + C_2 Y + \sum_{n=2}^{\infty} C_{n2} \sinh(\lambda_n Y) J_o(k_n R)\right]^{\frac{1}{2}} \qquad 7.3.1.$$

The mass content held in an elemental volume of the porous pad is given by -

$$\Delta m_p = 2P^*.\pi.r\rho.dr.dy \qquad 7.3.2.$$

The total mass content contained in the porous pad is given by -

$$m_p = \int_o^{r_o}\int_o^{H} 2P^*.\pi.r.\rho.dr.dy \qquad 7.3.3.$$

Substituting for ρ by the equation of state gives

$$m_p = \int_o^{r_o}\int_o^{H} P^* \frac{P_{pad}}{RT} 2\pi r \, dr.dy \qquad 7.3.4.$$

which may be written as

$$m_p = 2\pi \int_o^1 \int_o^1 \frac{H\, p_a P^* r_o^2}{RT} \overline{P}_{pad} R.dR.dY \qquad 7.3.5.$$

now if $\overline{P}$ is expressed in this double integral by equation 7.3.1. the double integration cannot be performed. Let the pressure distribution in the porous pad be described by:

$$\overline{P}_{pad} = \overline{P}_s + (\overline{P}_{film} - \overline{P}_s) \sum_{n=0}^{\infty} C_n Y^n \qquad 7.3.6.$$

Now at Y = 0 $\overline{P} = \overline{P}_s$ thus evaluating 7.3.6. at Y = 0 gives

$$\overline{P}_s = \hat{\overline{P}}_s + (\overline{P}_{film} - \overline{P}_s)C_o \qquad 7.3.7.$$

thus $C_o = 0$ which gives

$$\overline{P}_{pad} = \overline{P}_s + (\overline{P}_{film} - \overline{P}_s) \sum_{n=1}^{\infty} C_n Y^n \qquad 7.3.8.$$

Substituting equation 7.3.8. into equation 7.3.5. gives

$$m_p = \frac{2\pi r_o^2 HP^* p_a}{RT} \int_o^1 \int_o^1 \left[\overline{P}_s + (\overline{P}_{film} - \overline{P}_s) \sum_{n=1}^{\infty} C_n Y^n \right] R.dR.dY$$

7.3.9.

now as the pressure function expressed by equation 7.3.8. is a continuous function the double integration of equation 7.3.9. can be performed in two sections yielding, i.e. firstly integrating with respect to y

$$m_p = \frac{2\pi r_o^2 HP^* p_a}{RT} \int_o^1 \left(\overline{P}_s + (\overline{P}_{film} - \overline{P}_s) \sum_{n=1}^{\infty} C_n/n+1 \right) R \, dR$$

7.3.10.

now integrating with respect to R gives

$$m_p = \frac{2\pi r_o^2 HP^* p_a}{RT}\left[\frac{\bar{P}_s}{2}\left(1 - \sum_{n=1}^{\infty}\frac{c_n}{n+1}\right) + \sum_{n=1}^{\infty}\frac{c_n}{n+1}\int_o^1 \bar{P}_{film}\, R\, dR\right]$$

7.3.11

now let

$$\left.\begin{aligned} \bar{P}_{film} &= \bar{P}_{f_o} + \bar{P}f' \\ \int_o^1 \bar{P}f'\, R\, dR &= A' \\ \int_o^1 \bar{P}f_o\, R\, dR &= A_o \end{aligned}\right\}$$

7.3.12

also

thus

$$m_p = \frac{2\pi r_o^2 HP^* p_a}{RT}\left[\frac{\bar{P}_s}{2}\left(1 - \sum_{n=1}^{\infty}\frac{c_n}{n+1}\right) + \sum_{n=1}^{\infty}\frac{c_n}{n+1}(A_o + A'\right]$$

7.3.13

7.3.1B <u>Mass Content of Gas Film</u>

Total mass contained in the gas film is given by, as the gas film pressure is not a function of y see section 3.3.

$$m_f = \int_o^{r_o} 2\pi r h \rho\, dr$$

7.3.14

Substituting for ρ from the equation of state gives

$$m_f = \frac{2\pi r_o^2 h\, p_a}{RT}\int_o^1 \bar{P}f\, R\, dR$$

7.3.15

i.e.

$$m_f = \frac{2\pi r_o^2 h\, p_a}{RT} \left(A_o + A'\right) \qquad 7.3.16$$

7.3.1C Time Rate of Change of Mass Content of Bearing

Hence total mass content of the bearing is given by the addition of equation 7.3.13 and 7.3.16

$$m_b = \frac{2\pi r_o^2 p_a}{RT} \left[\frac{\bar{P}_s HP^* \left(1 + \sum_{n=1}^{\infty} \frac{c_n}{n+1}\right)}{2} + \left(h + HP^* \sum_{n=1}^{\infty} \frac{c_n}{n+1}\right) \cdots \right.$$

$$\left. \cdots \left(A_o + A'\right) \right] \qquad 7.3.17$$

The time rate of change of the mass content of the bearing is given by, differentiating equation 7.3.17 with respect to time

$$\dot{m}_b = \frac{2\pi r_o^2 p_a}{RT} \left[\left(A_o + A'\right) \frac{dh}{dt} + \left(h + HP^* \sum_{n=1}^{\infty} \frac{c_n}{n+1}\right) \frac{\partial A'}{\partial t} \right]$$

7.3.18

7.3.2 Mass Outflow From the Bearing

In the film the mass flow through an annular gap is

$$\dot{m}f_r = 2\pi \int_o^h \rho_r U_r\, r\, dy \qquad 7.3.19$$

$$U_r = \frac{1}{\eta}\frac{\partial}{\partial r}(P_{film})\ (\frac{y^2}{2} - h_y - \frac{\Phi_r y}{h}) \qquad 7.3.20$$

hence

$$\dot{m}f_r = \frac{2\pi r\rho r}{\eta}\frac{\partial}{\partial r}(P_{film})\int_o^h (\frac{y^2}{2} - h_y - \frac{\Phi_r y}{h})\,dy \qquad 7.3.21$$

giving

$$\dot{m}f_r = -\frac{\pi r h(h^2+6\Phi_r)}{12\eta_V RT}\frac{\partial}{\partial r}(p^2_{film})$$

after substitution for $\frac{\partial}{\partial r}(p^2_{film})$ from equation 3.3.8, equation 7.3.21 may be written as

$$\dot{m}f_R = -\frac{\pi h(h^2+6\Phi_r)\,p_a{}^2\Lambda}{12\eta_V RT}\left[C_2 R + \sum_{n=2}^{\infty}\frac{\lambda_n C_n{}^2 R J_1(k_n R)\cosh\lambda_n}{k_n}\right] \qquad 7.3.22$$

evaluating equation 7.3.22 at R = 1.0 gives

$$m_{out} = -\frac{\pi h(h^2+6\Phi_r)\,p_a{}^2\Lambda C_2}{24\eta_V RT}$$

now

$$\Lambda = 12\Phi_y r_o{}^2 \;/\; Hh(h^2+6\Phi_r)$$

hence

$$m_{out} = - \frac{\pi p_a^2 \Phi_y r_o^2 C_2}{2\eta RTH} \qquad 7.3.23$$

7.3.3 Mass Inflow to the Bearing

$$m_{in} = 2\pi \int_o^{r_o} (\rho v)_{y=0} \, r \, dr \qquad 7.3.24$$

substituting for ρ by the equation of state and for v from Darcy's law gives

$$m_{in} = - 2\pi \int_o^{r_o} \frac{p_s}{RT} \frac{\Phi_y}{\eta} \left[\frac{\partial}{\partial y} (p_{pad}) \right]_{y=0} r \, dr$$

i.e.

$$m_{in} = - \frac{2\pi r_o^2 p_a^2 \Phi_y \overline{P}_s}{RTH\eta} \int_o^1 \frac{\partial}{\partial Y} (\overline{P}_{pad})_{Y=0} R \, dR$$

substituting for $\frac{\partial}{\partial y}(\overline{P}_{pad})$ by differentiating equation 7.3.6 and evaluating Y = 0 gives upon completing the integration: -

$$m_{in} = - \frac{2\pi r_o^2 \overline{P}_s p_a \Phi_y C_1}{RTH\eta} \left[A_o + A' - \frac{\overline{P}_s}{2} \right] \qquad 7.3.25$$

7.3.4 Mass Continuity

The time rate of change of the mass content of the bearing must equal the difference of mass inflow and mass outflow changes.

$$\text{Change of mass inflow} = -\frac{2\pi r_o^2 \bar{P}_s p_a^2 \Phi_y C_1 A'}{RTH\eta}$$

$$\text{Change of mass outflow} = -\frac{\pi p_a^2 \Phi_y r_o^2}{2\eta RTH} \cdot \frac{\partial C_2}{\partial \Lambda} \cdot \frac{\partial \Lambda}{\partial h} \cdot dh$$

time rate of change of bearing mass content is given by equation 7.3.18. Thus from mass continuity

$$\frac{\pi p_a^2 \Phi_y r_o^2}{2\eta RTH} \cdot \frac{\partial C_2}{\partial \Lambda} \cdot \frac{\partial \Lambda}{\partial h} \cdot dh - \frac{2\pi r_o^2 \bar{P}_s p_a^2 \Phi_y C_1 A'}{RTH\eta}$$

$$= \frac{2\pi r_o^2 p_a}{RT}\left[(A_o + A')\frac{dh}{dt} + \left(h + HP^* \sum_{n=1}^{\infty} \frac{C_n}{n+1}\right)\frac{\partial A'}{\partial t}\right] \qquad 7.3.26$$

now the equation of motion of the bearing may be written

$$m_4 \ddot{h}' = 2\pi \int_o^{r_o} p_f' \, r \, dr = 2\pi r_o^2 p_a \int_o^1 \bar{P}_f' \, R \, dr$$

where

$$h = h_o + h'$$

hence

hence

$$m_4 \ddot{h}' = 2\pi r_o p_a A'$$

thus

$$m_4 \dddot{h}' = 2\pi r_o p_a \frac{\partial A'}{\partial t} \qquad 7.3.27$$

substituting from equation 7.3.27 into equation 7.3.26 gives

$$\frac{\pi p_a^2 \Phi_y r_o^2}{2\eta H} \cdot \frac{\partial C_2}{\partial \Lambda} \cdot \frac{\partial \Lambda}{\partial h} \cdot h' - \frac{\bar{P}_s p_a \Phi_y C_1 m_4}{H\eta} \ddot{h}'$$

$$= 2\pi r_o^2 p_a A_o \dot{h}' + \left(h_o + HP^* \sum_{n=1}^{\infty} \frac{C_n}{n+1}\right) m_4 \dddot{h}' \qquad 7.3.28$$

Now let

$$Z_1 = \left(h_o + HP^* \sum_{n=1}^{\infty} \frac{C_n}{n+1}\right) m_4$$

$$Z_2 = \frac{m_4 p_s \Phi_y C_1}{H\eta}$$

$$Z_3 = 2\pi p_a r_o^2 A_o$$

$$Z_4 = -\frac{\pi p_a^2 \Phi_y r_o^2}{2H\eta} \frac{\partial C_2}{\partial \Lambda} \cdot \frac{\partial \Lambda}{\partial h} \qquad 7.3.29$$

Therefore equation 7.2.28 may be written

$$Z_1 \dddot{h}' + Z_2 \ddot{h}' + Z_3 \dot{h}' + Z_4 h' = 0$$

Using the Routh-Hurwitz stability criteria

$$\begin{vmatrix} Z_2 & Z_1 \\ Z_4 & Z_3 \end{vmatrix} > 0 \quad \text{and} \quad Z_1 > 0$$

Thus the porous bearing will be stable if

$$Z_3 Z_2 > Z_4 Z_1 \quad \text{and} \quad Z_1 > 0$$

7.4. NON-LINEAR THEORETICAL ANALYSIS OF THE TIME DEPENDENT EQUATIONS

In the time dependent experimental analysis carried out in this research programme it was found that porous bearings may execute non-linear vibrations when forced to vibrate. In order to theoretically predict the non-dimensional spring force and non-dimensional damping force of the gas film when the bearing oscillates in a non-linear fashion it is necessary to determine the harmonic distortion of the sinusoidal motion. Having determined the form this distortion will take, a slight modification to the computer program for the linear analysis will give a non-linear analysis.

Consider that the motion of the bearing can be described by the following equation:

$$h = h_0 + \sigma \sum_{n=1}^{3} f_n \sin(n\bar{T}) \qquad 7.4.1$$

i.e. the fundamental frequency with two imposed harmonics.

By changing the program line which contains the motion description, the pressure variation for a non-linear vibration will be found. The pressure variation will be of a form

$$\bar{P} = \bar{P}_0 + \bar{P}' \sum_{n=1}^{3} g_n \sin(n\bar{T} + \tau) \qquad 7.4.2$$

Thus the harmonic analysis section of the computer program will require changing to suit the order of harmonics. Having now determined the values of $\bar{P}'$ and g_n the non-dimensional damping and non-dimensional dynamic spring forces can be calculated.

The non-dimensional dynamic spring force will be given by:

K_f = vector addition of three spring forces

and the non-dimensional damping force will be given by:

D_f = vector addition of three damping forces.

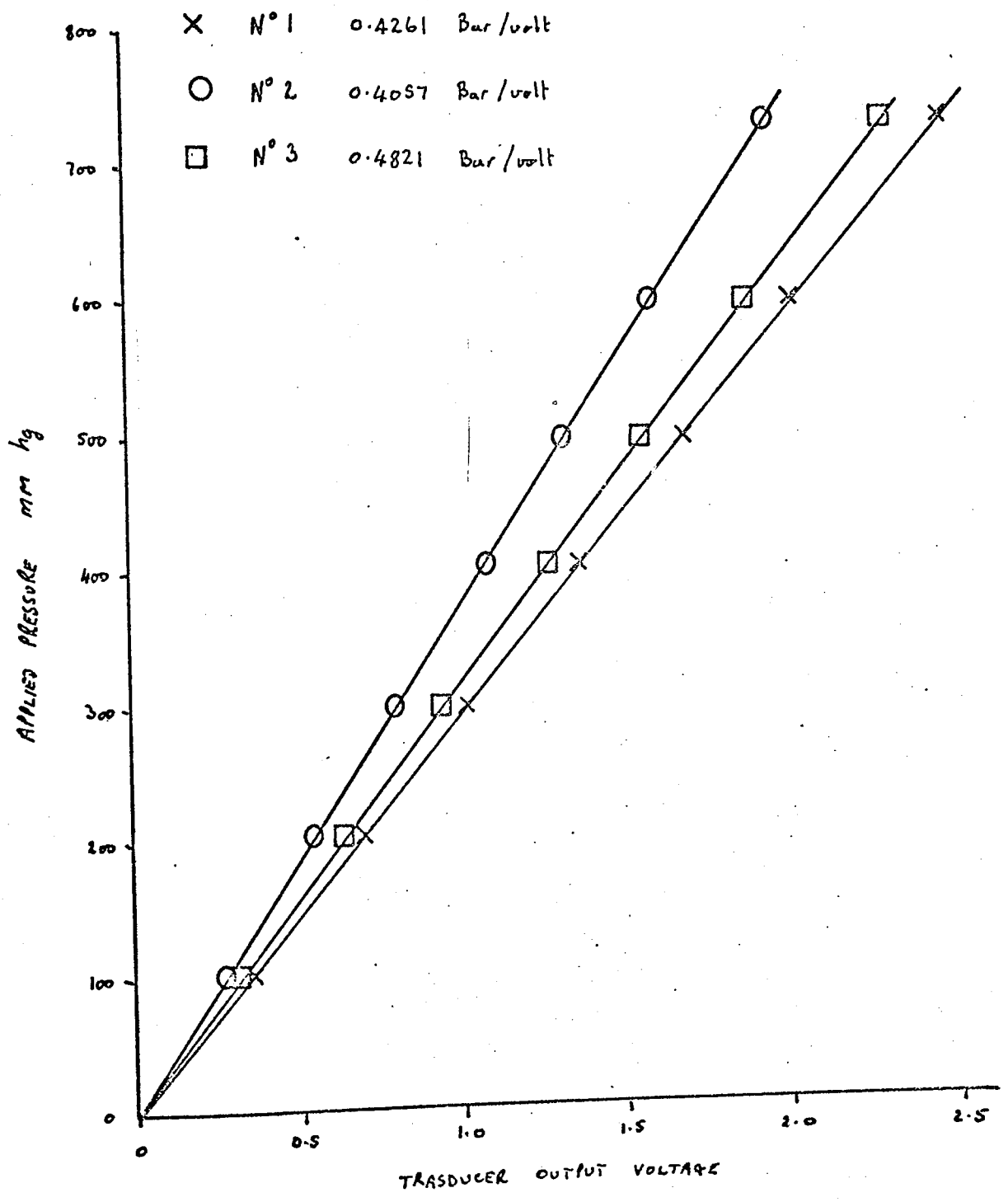

Figure 31 Calibration Curves for Pressure Transducers Numbers 1, 2 and 3

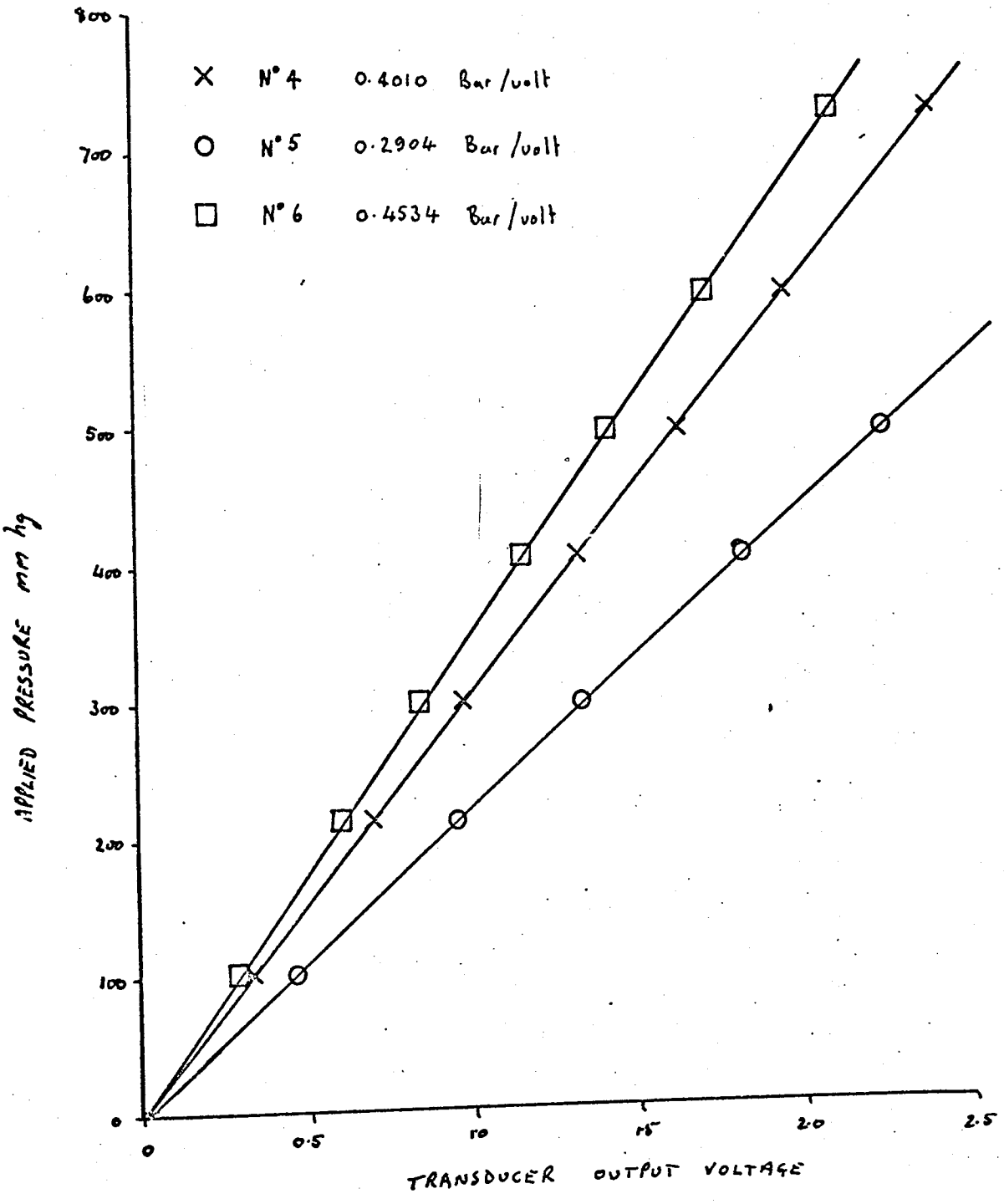

Figure 32 Calibration Curves for Pressure Transducers Numbers 4, 5 and 6

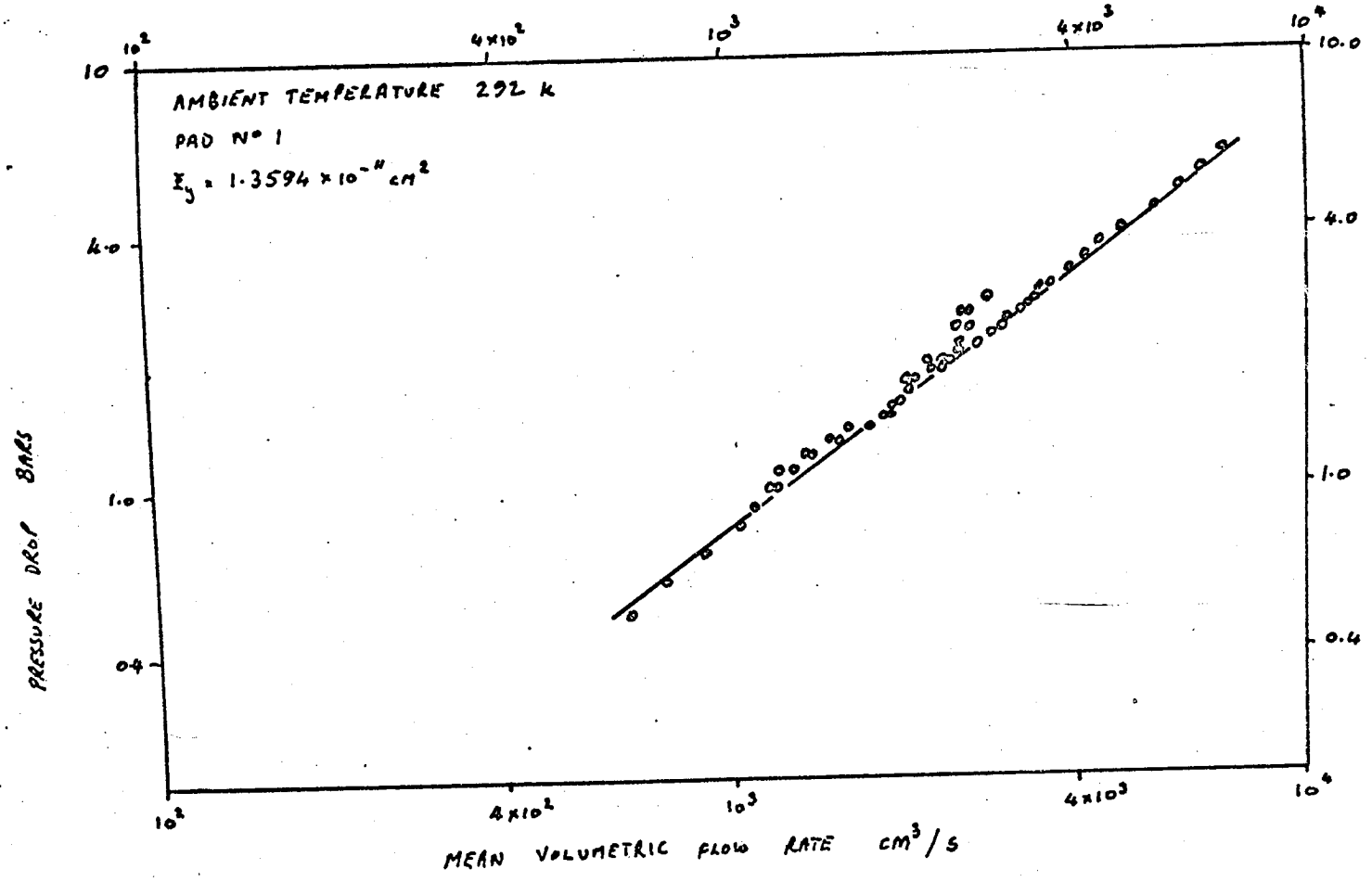

Figure 33 Variation of Mean Volumetric Flow Rate through Pad Number 1 with the Pressure Drop across the Pad

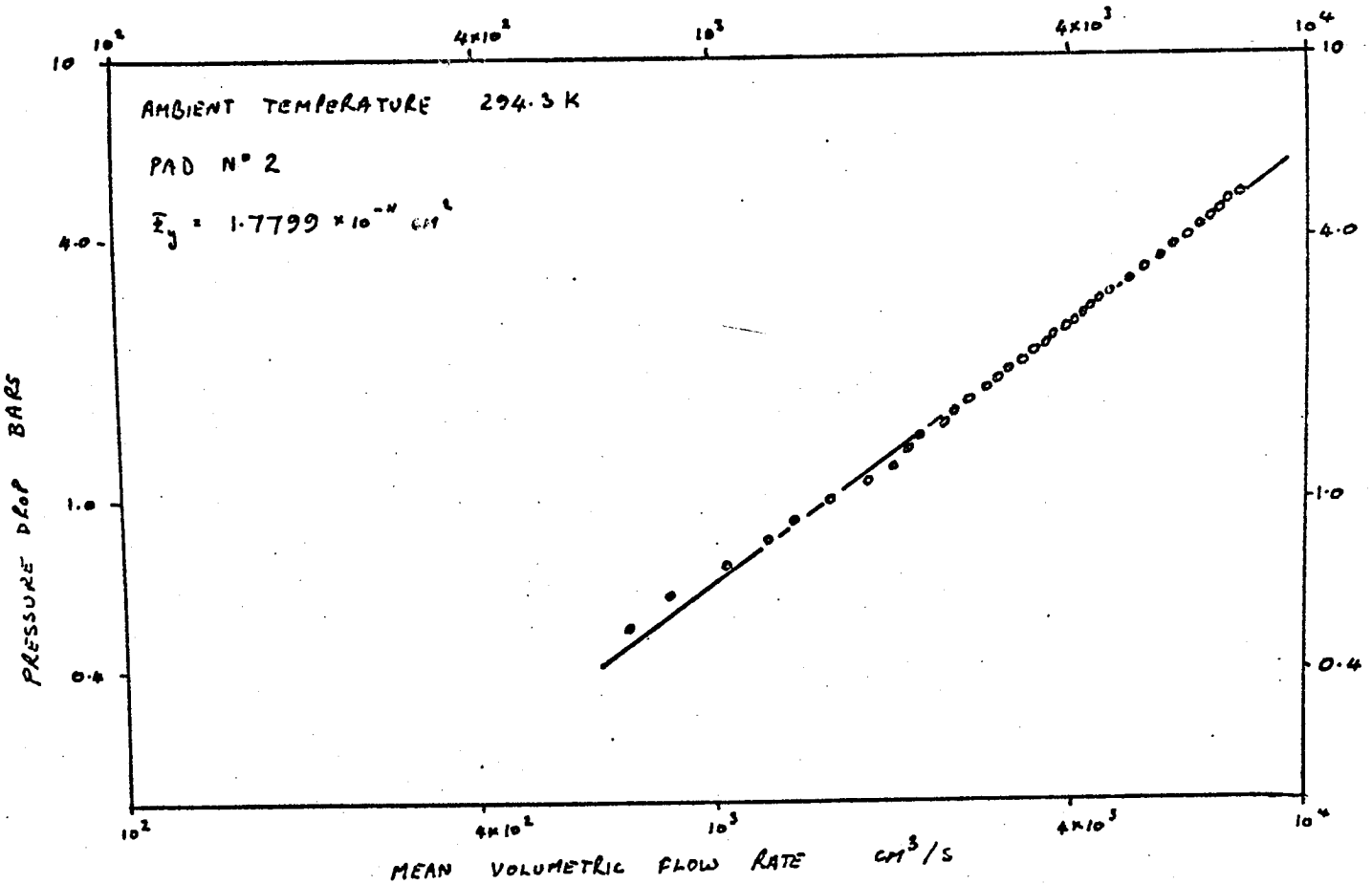

Figure 34 Variation of Mean Volumetric Flow Rate through Pad Number 2 with the Pressure Drop across the Pad

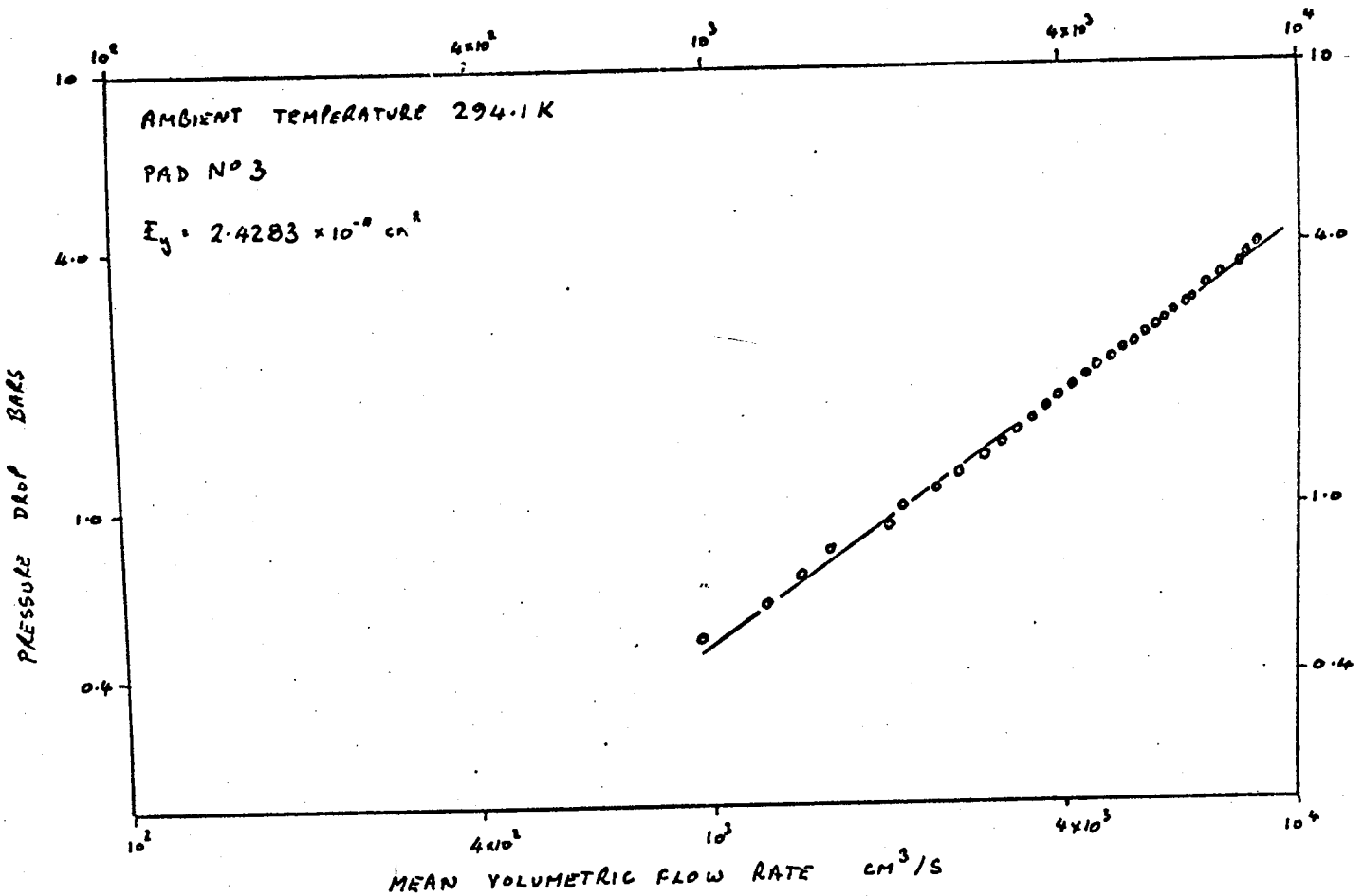

Figure 35 Variation of Mean Volumetric Flow Rate through Pad Number 3 with the Pressure Drop across the Pad

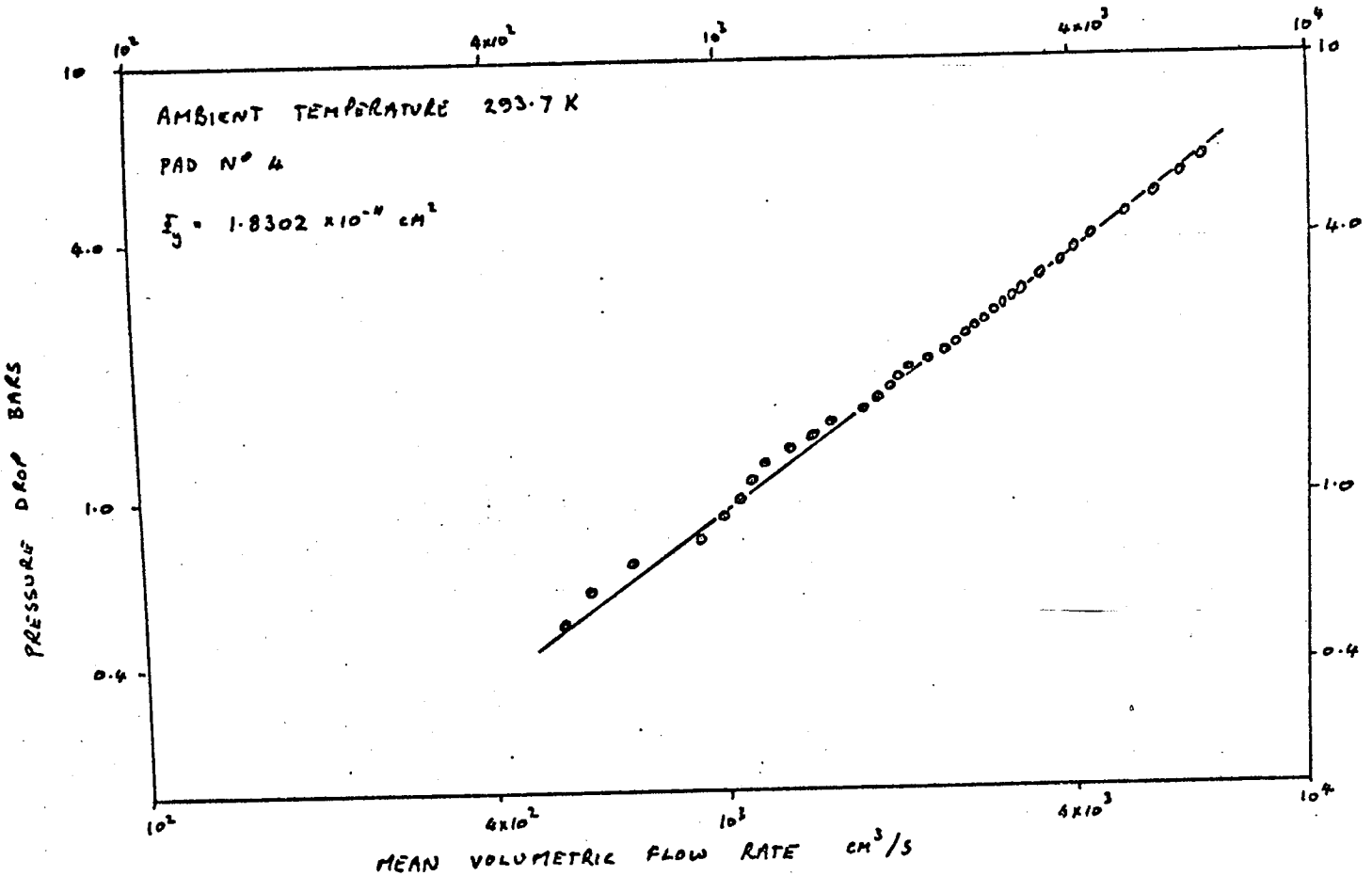

Figure 36 Variation of Mean Volumetric Flow Rate through Pad Number 4 with the Pressure Drop across the Pad

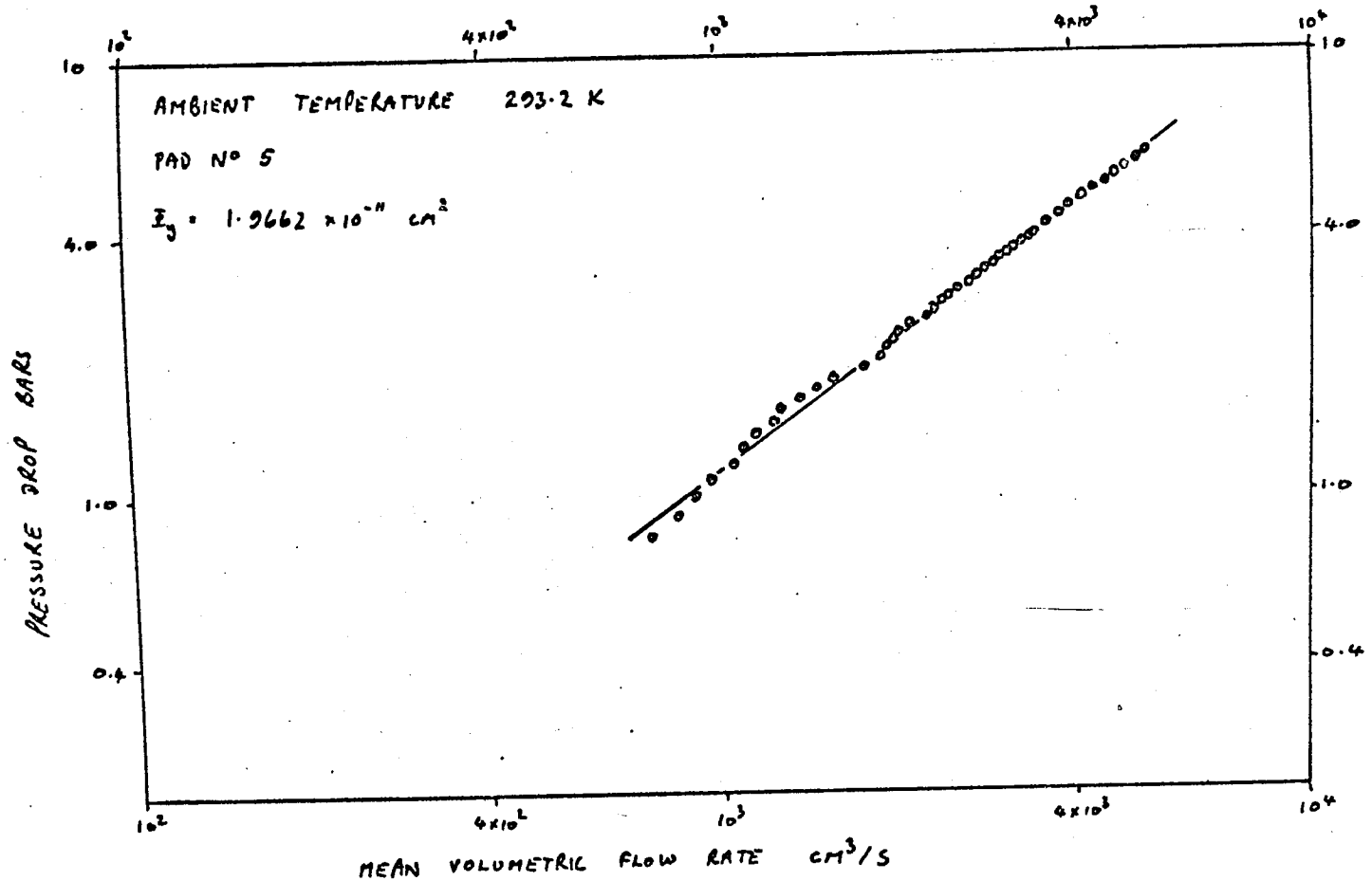

Figure 37 Variation of Mean Volumetric Flow Rate through Pad Number 5 with the Pressure Drop across the Pad

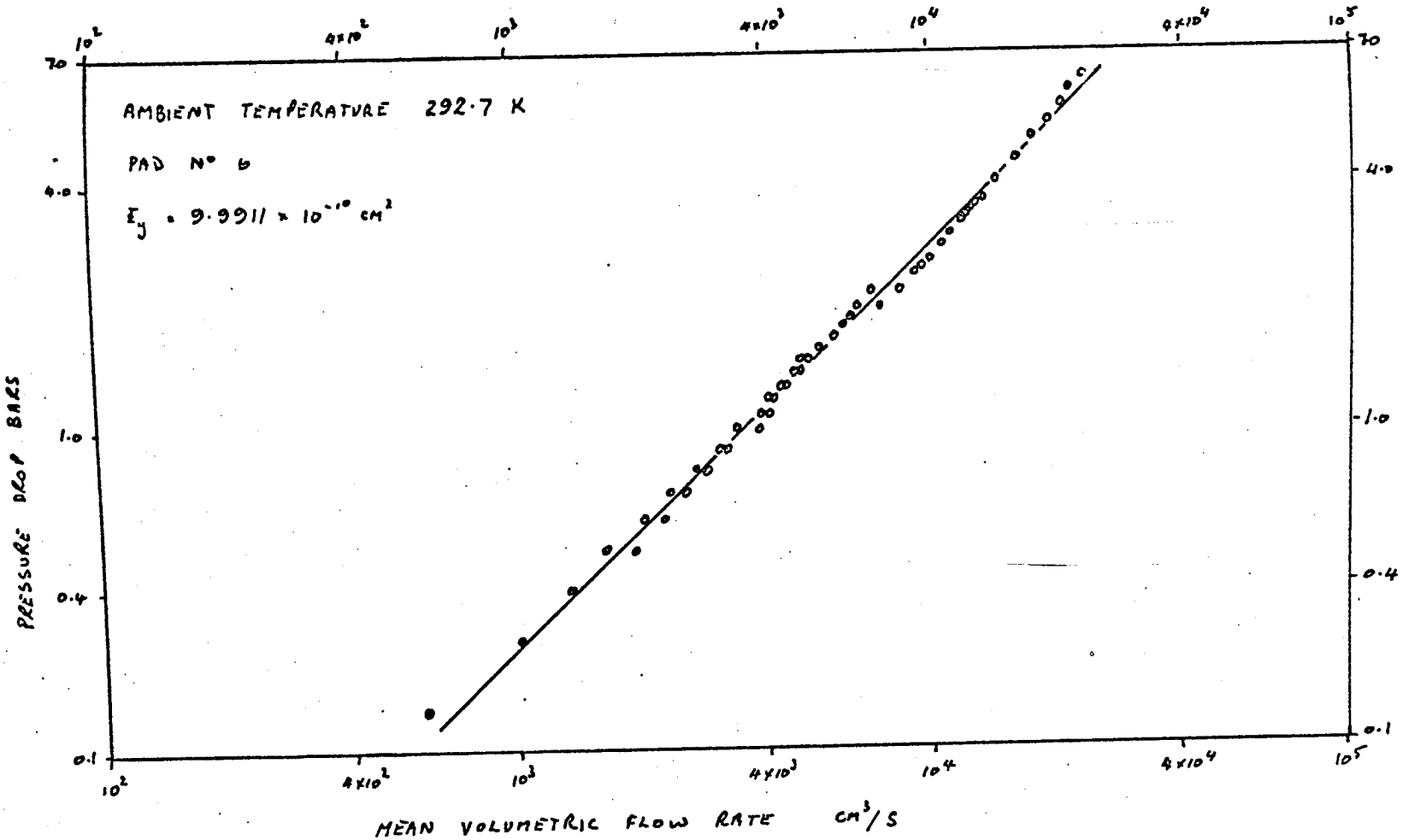

Figure 38 Variation of Mean Volumetric Flow Rate through Pad Number 6 with the Pressure Drop across the Pad

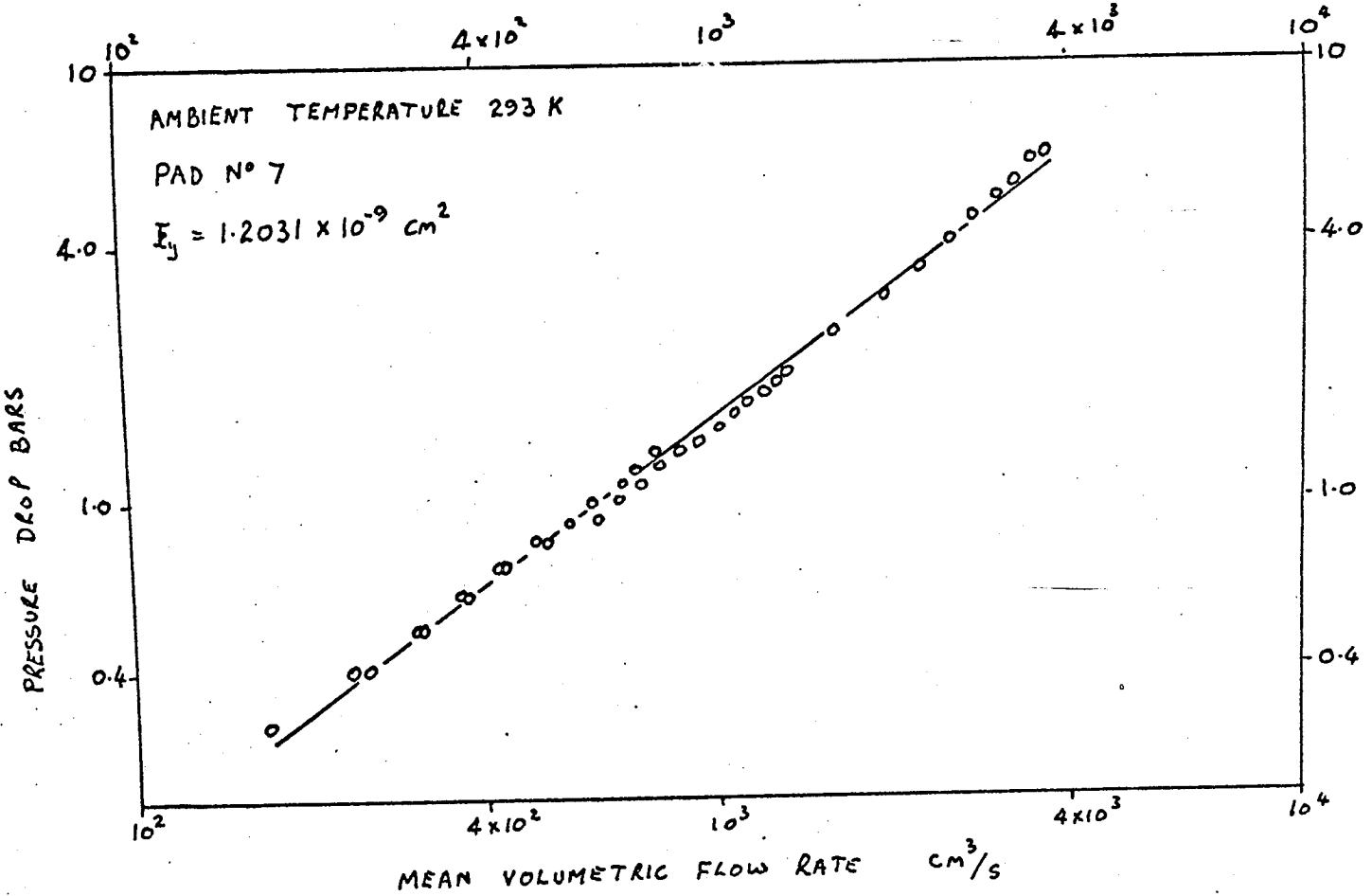

Figure 39 Variation of Mean Volumetric Flow Rate through Pad Number 7 with the Pressure Drop across the Pad

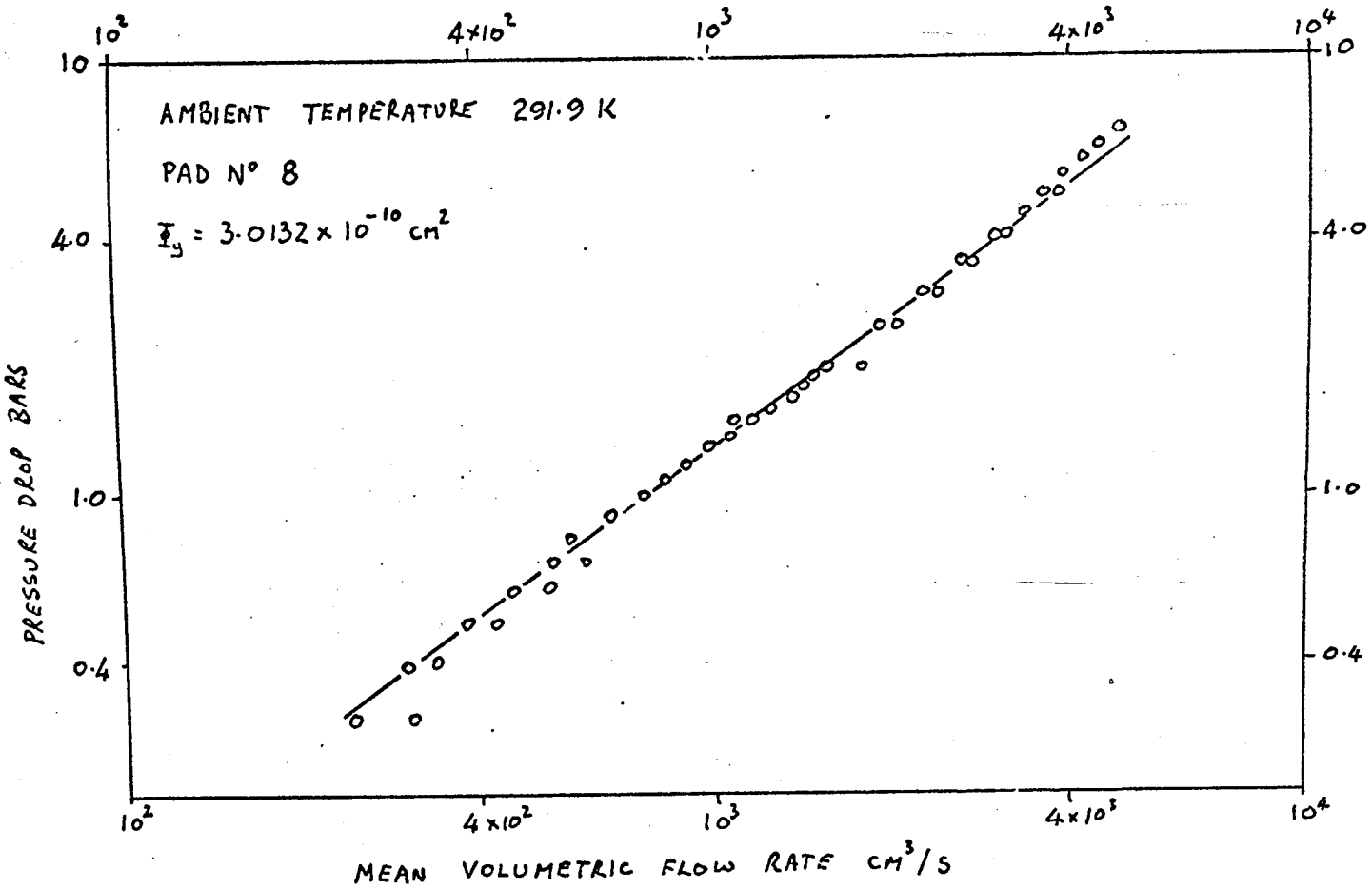

Figure 40 Variation of Mean Volumetric Flow Rate through Pad Number 8 with the Pressure Drop across the Pad

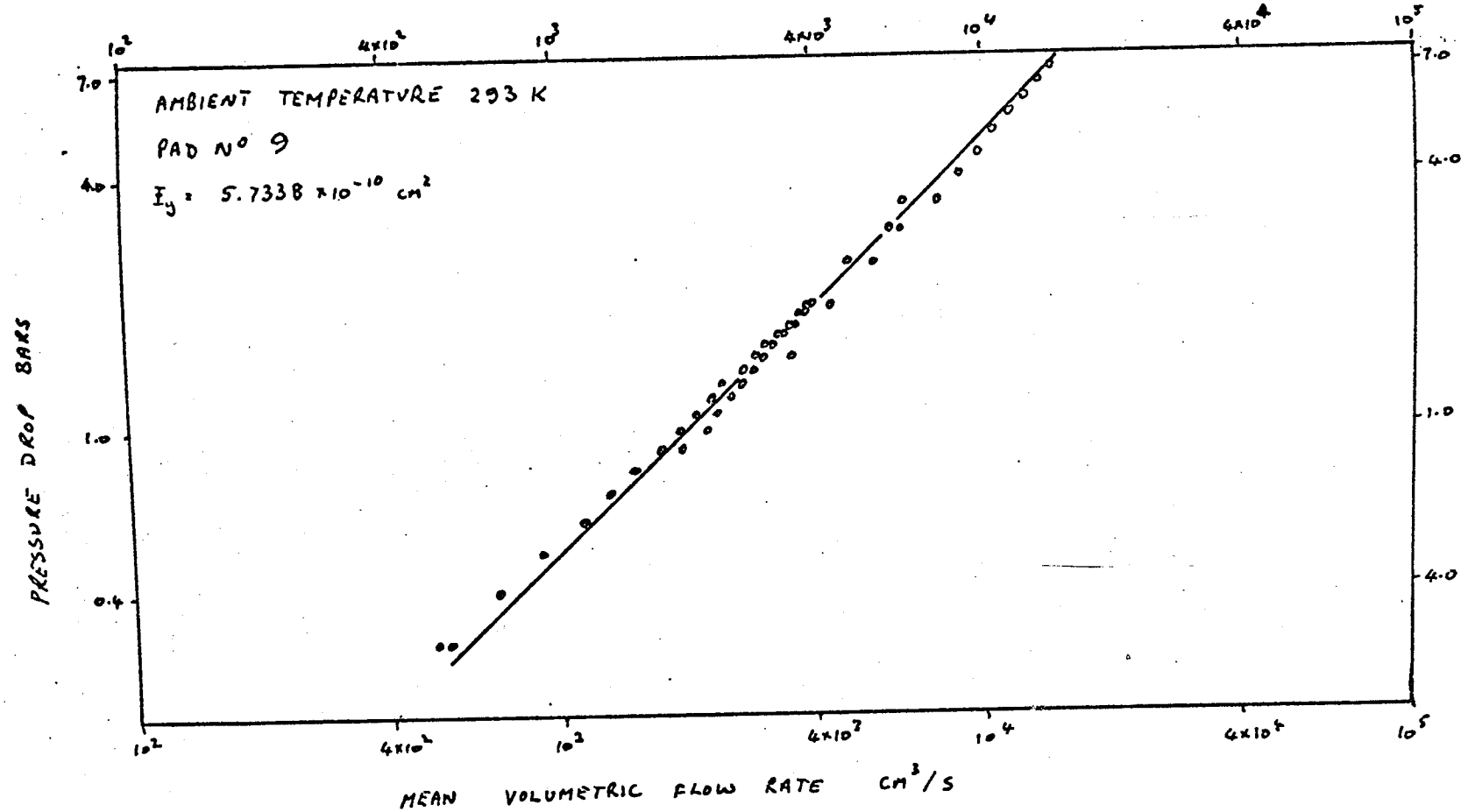

Figure 41 Variation of Mean Volumetric Flow Rate through Pad Number 9 with the Pressure Drop across the Pad

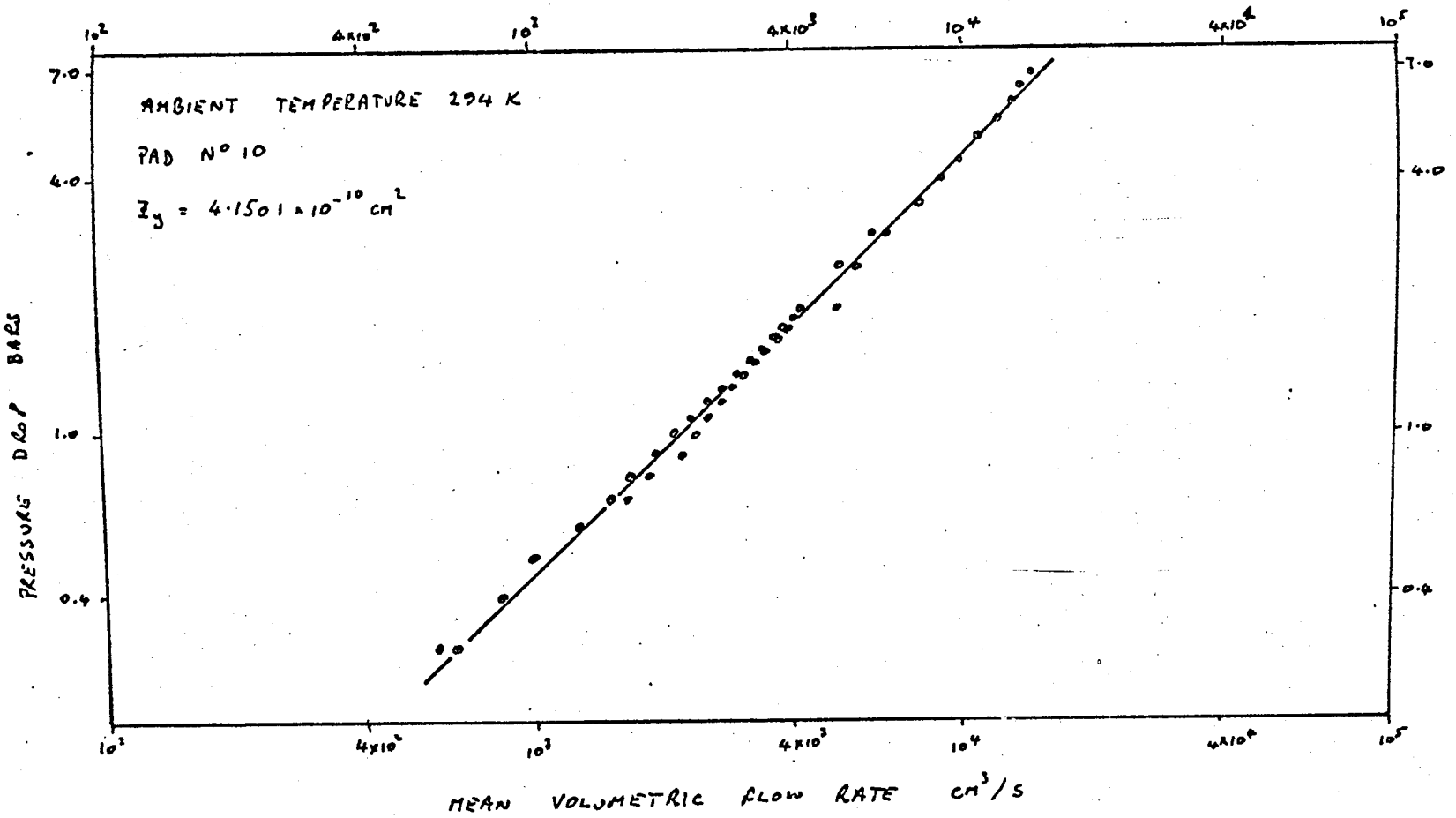

Figure 42 Variation of Mean Volumetric Flow Rate through Pad Number 10 with the Pressure Drop across the Pad

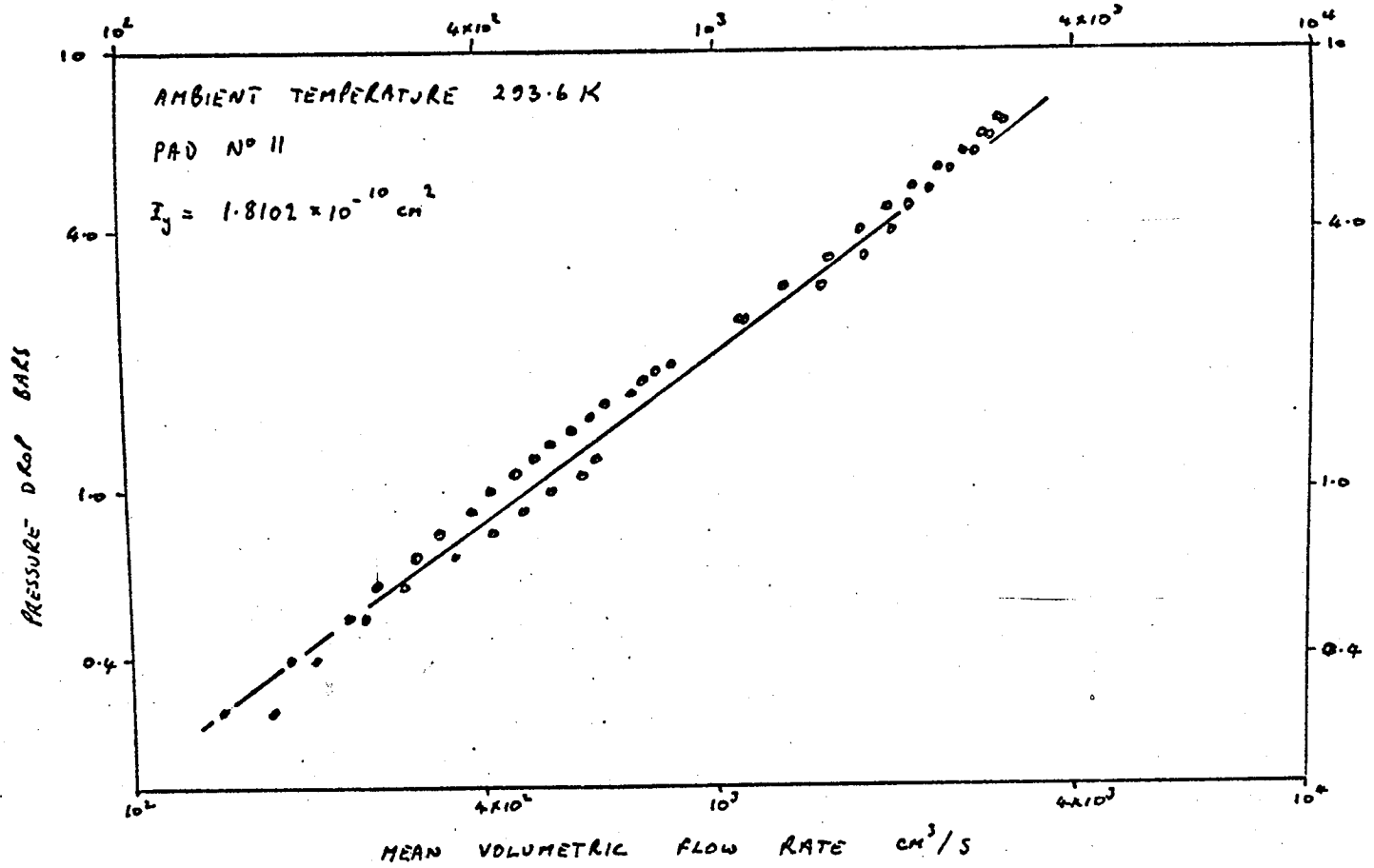

Figure 43 Variation of Mean Volumetric Flow Rate through Pad Number 11 with the Pressure Drop across the Pad

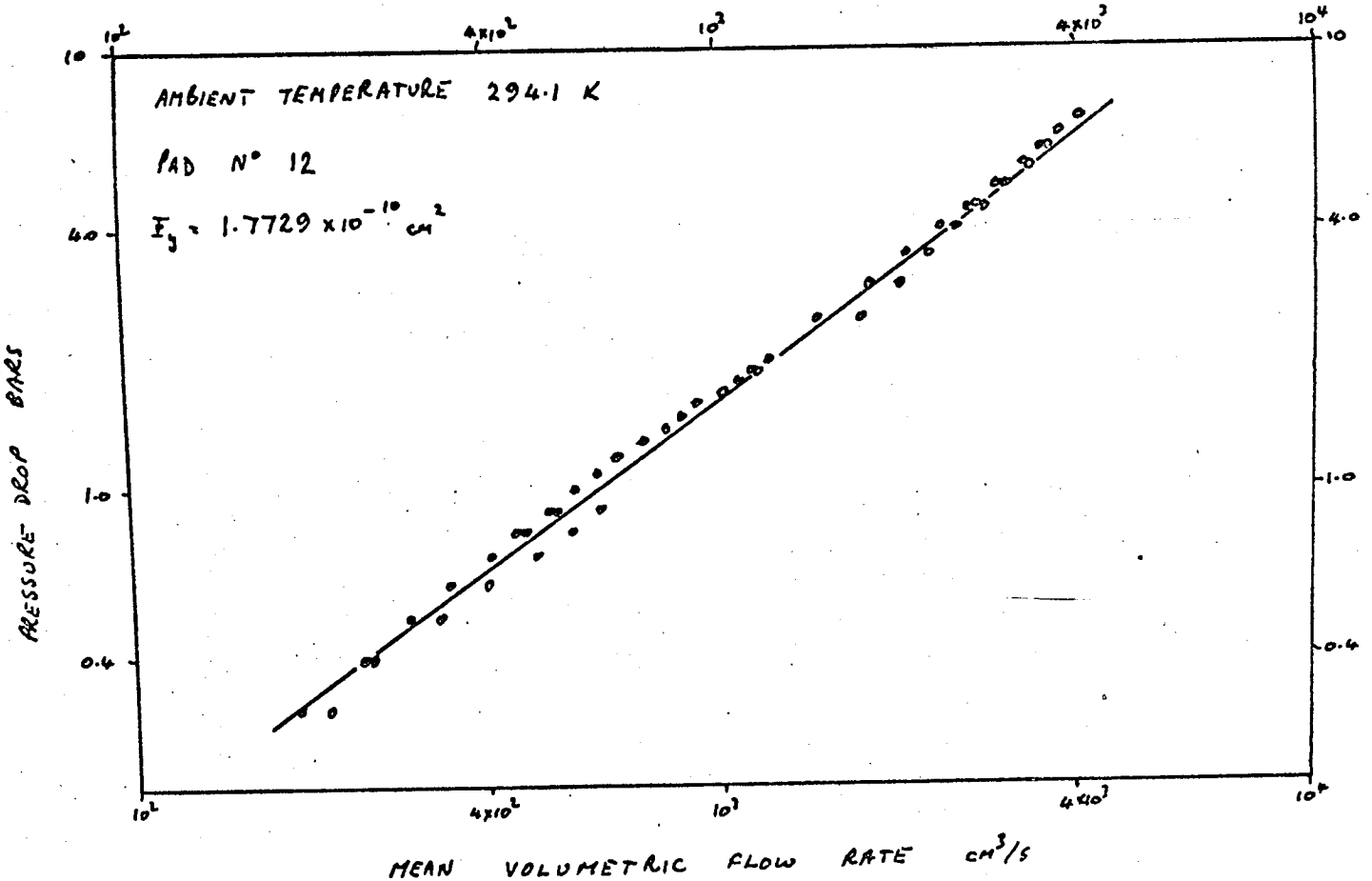

Figure 44 Variation of Mean Volumetric Flow Rate through Pa
Number 12 with the Pressure Drop across the Pad

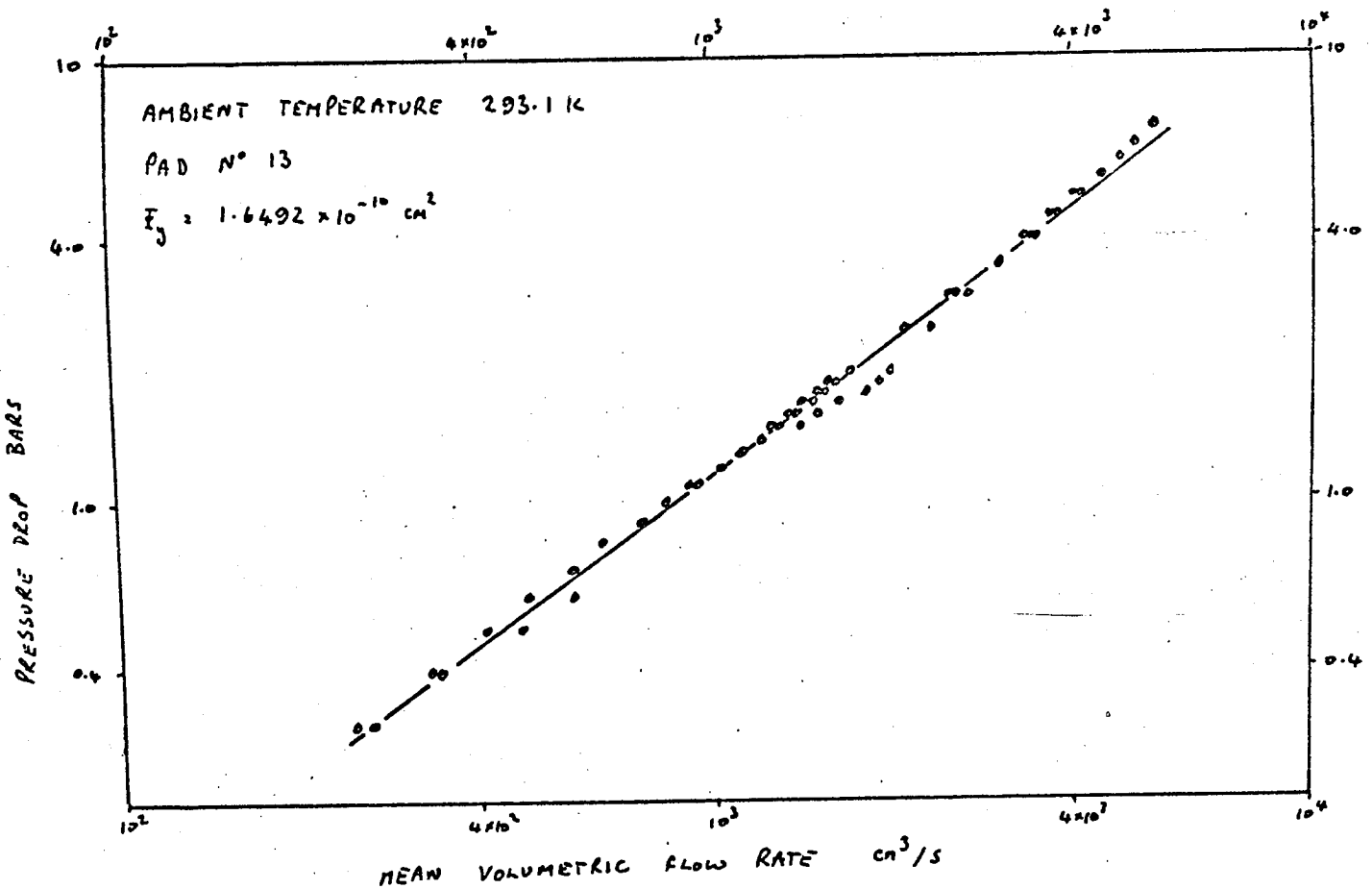

Figure 45 Variation of Mean Volumetric Flow Rate through Pad Number 13 with the Pressure Drop across the Pad

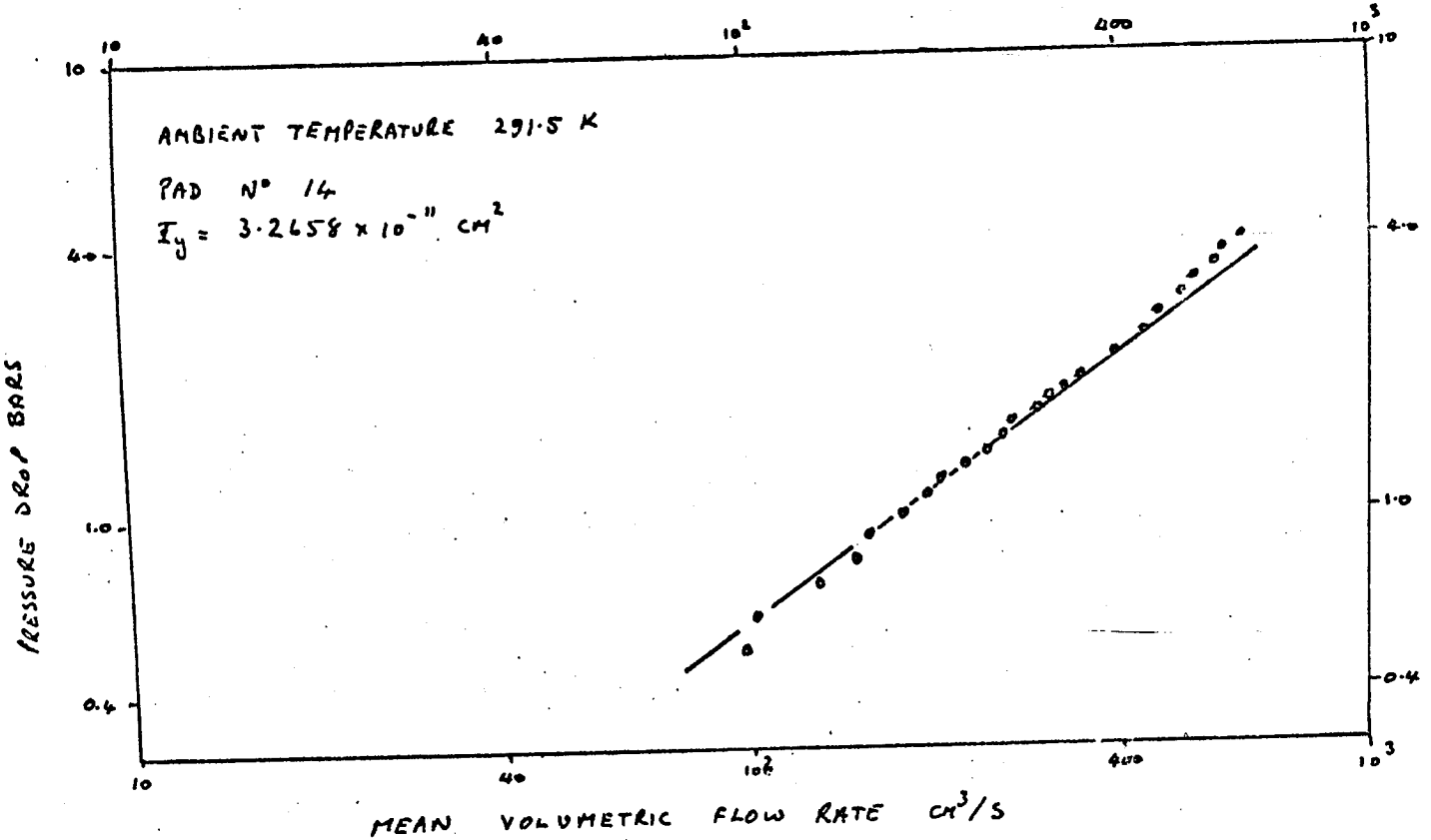

Figure 46 Variation of Mean Volumetric Flow Rate through Pad Number 14 with the Pressure Drop across the Pad

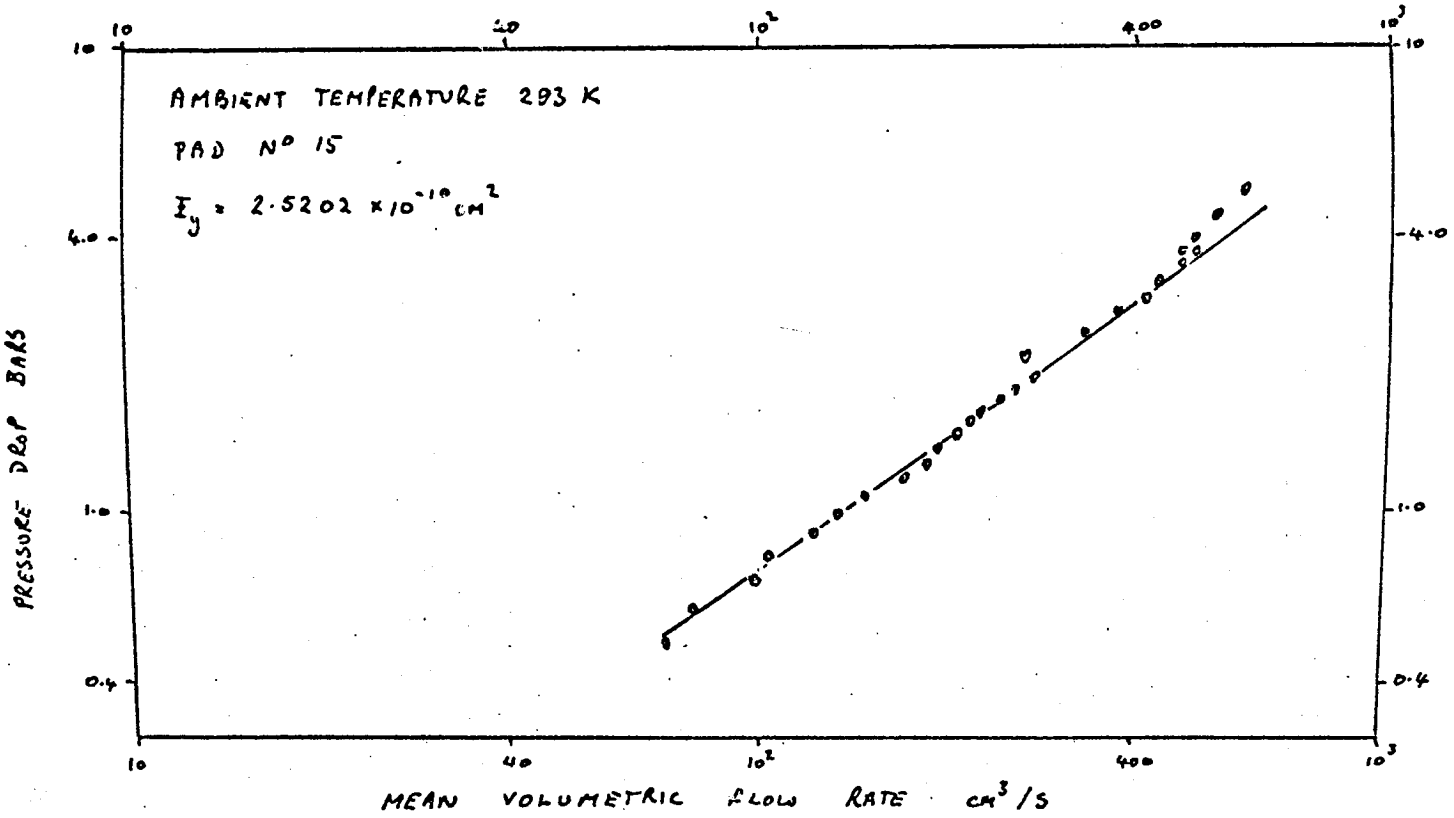

Figure 47 Variation of Mean Volumetric Flow Rate through Pad Number 15 with the Pressure Drop across the Pad

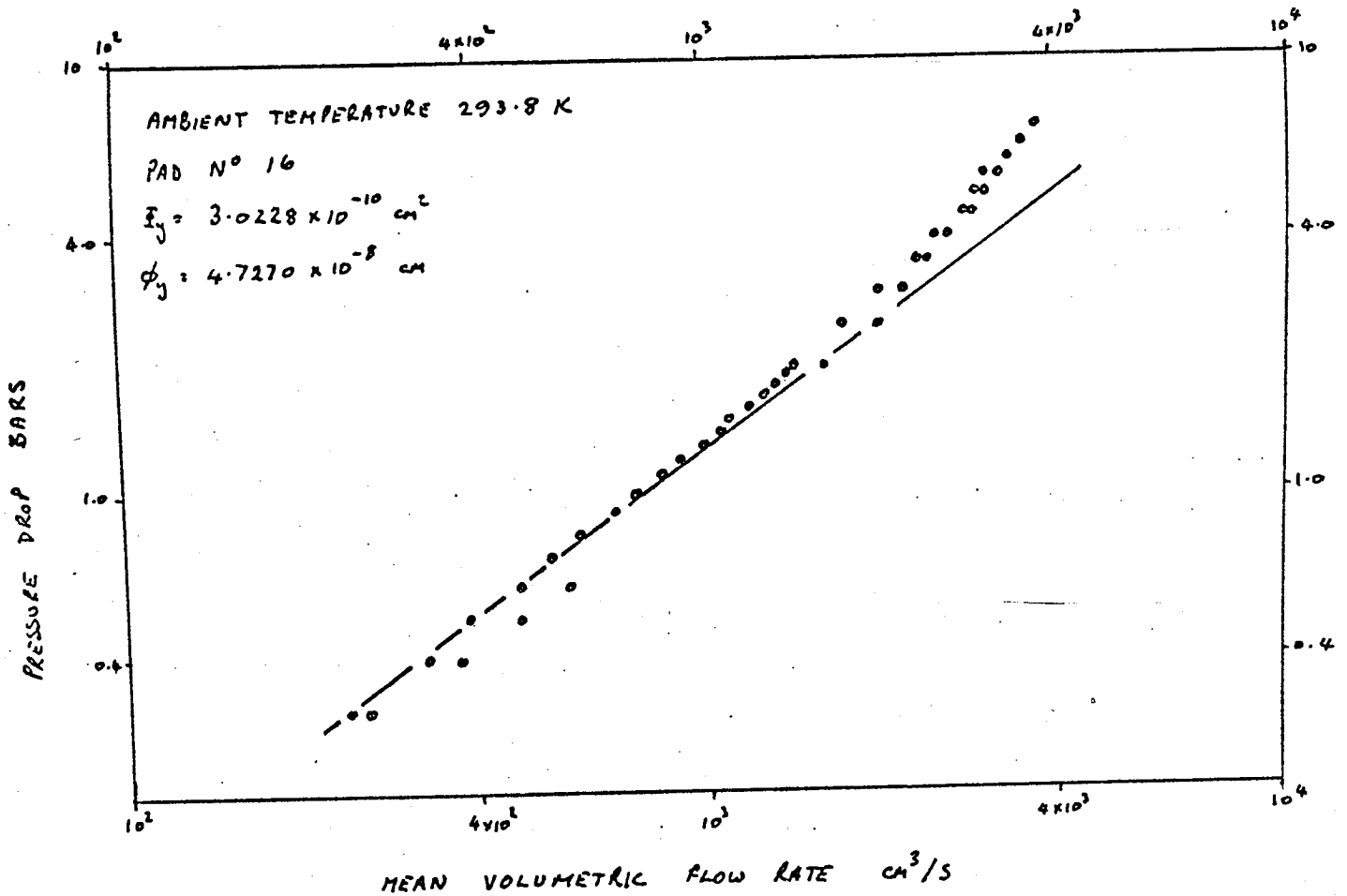

Figure 48 Variation of Mean Volumetric Flow Rate through Pad Number 16 with the Pressure Drop across the Pad

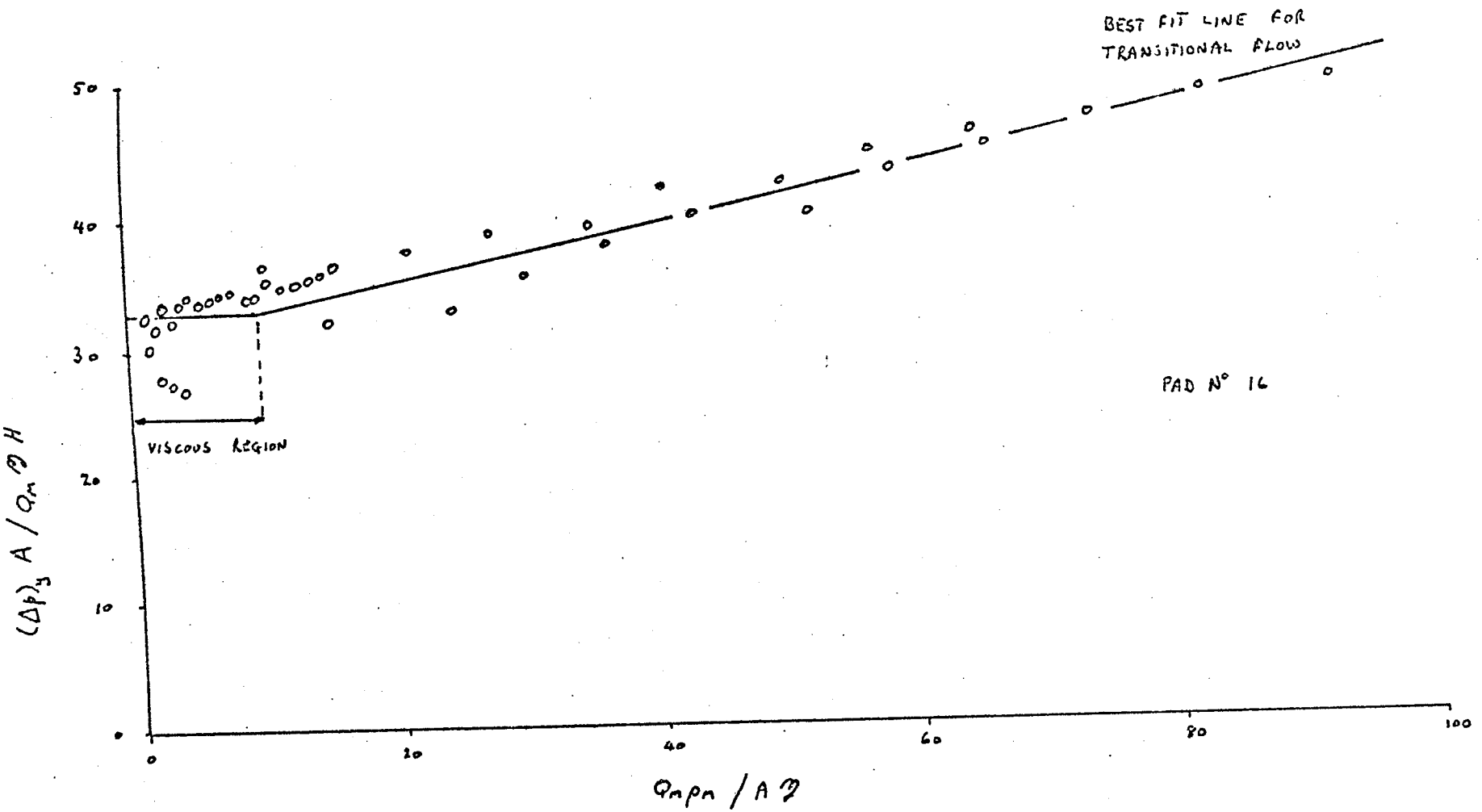

Figure 49 Experimental Results of Flow through Pad Number 16 presented in the form described by Morgan

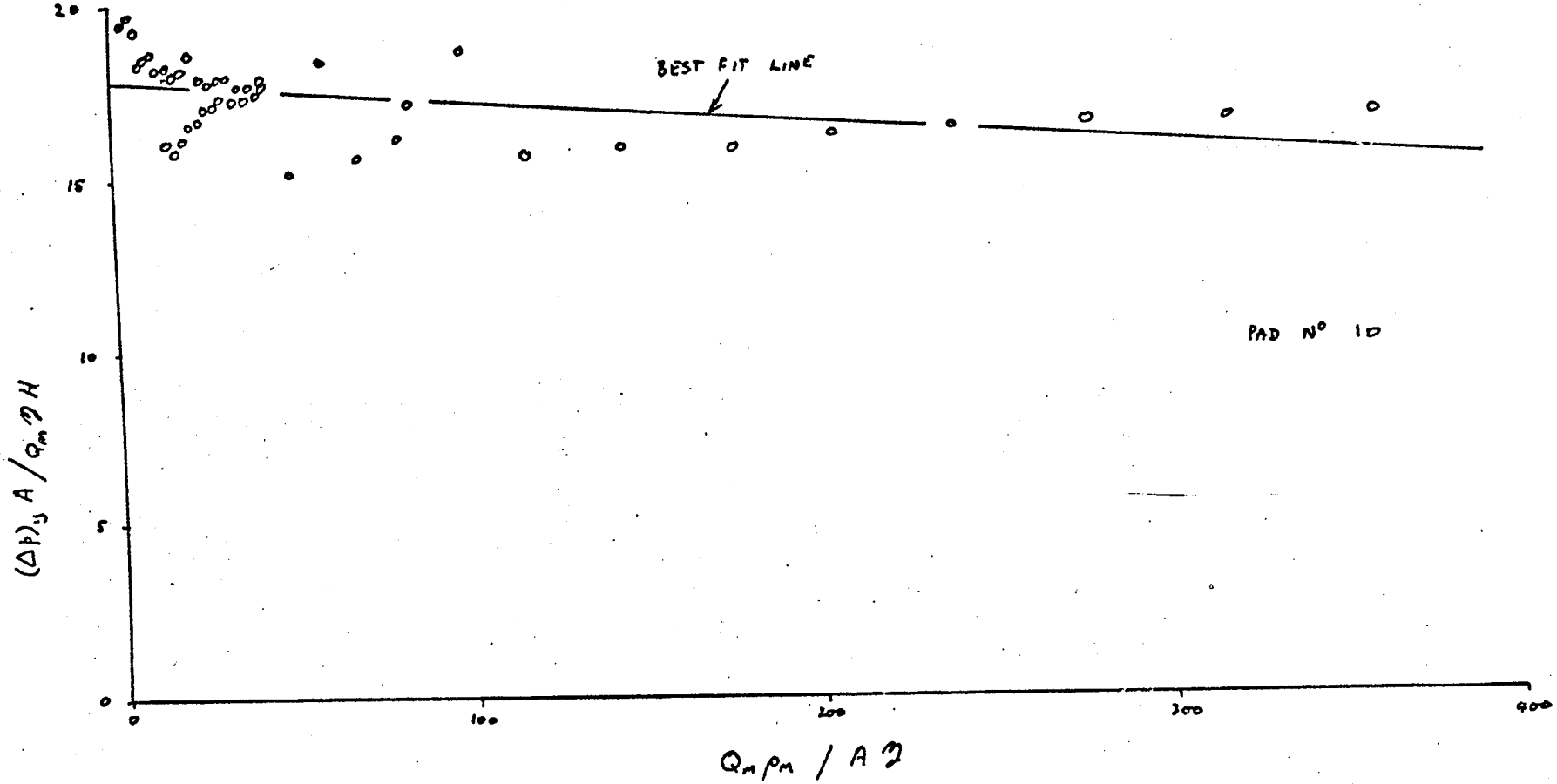

Figure 50 Experimental Results of Flow through Pad Number 10 presented in the form described by Morgan

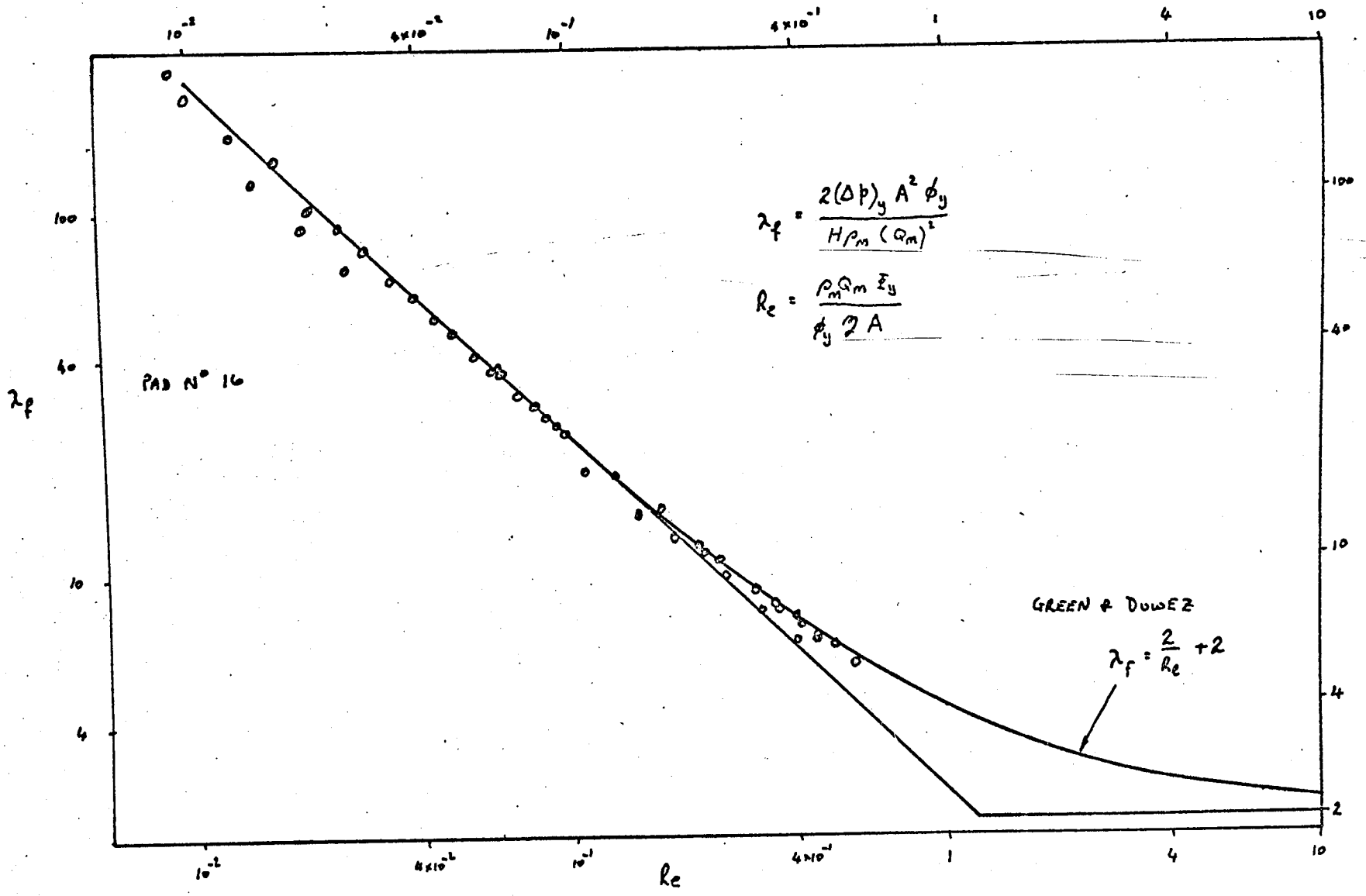

Figure 51 A Friction Factor / Reynolds Number Plot for Pad Number 16 using the definitions of Green & Duwez

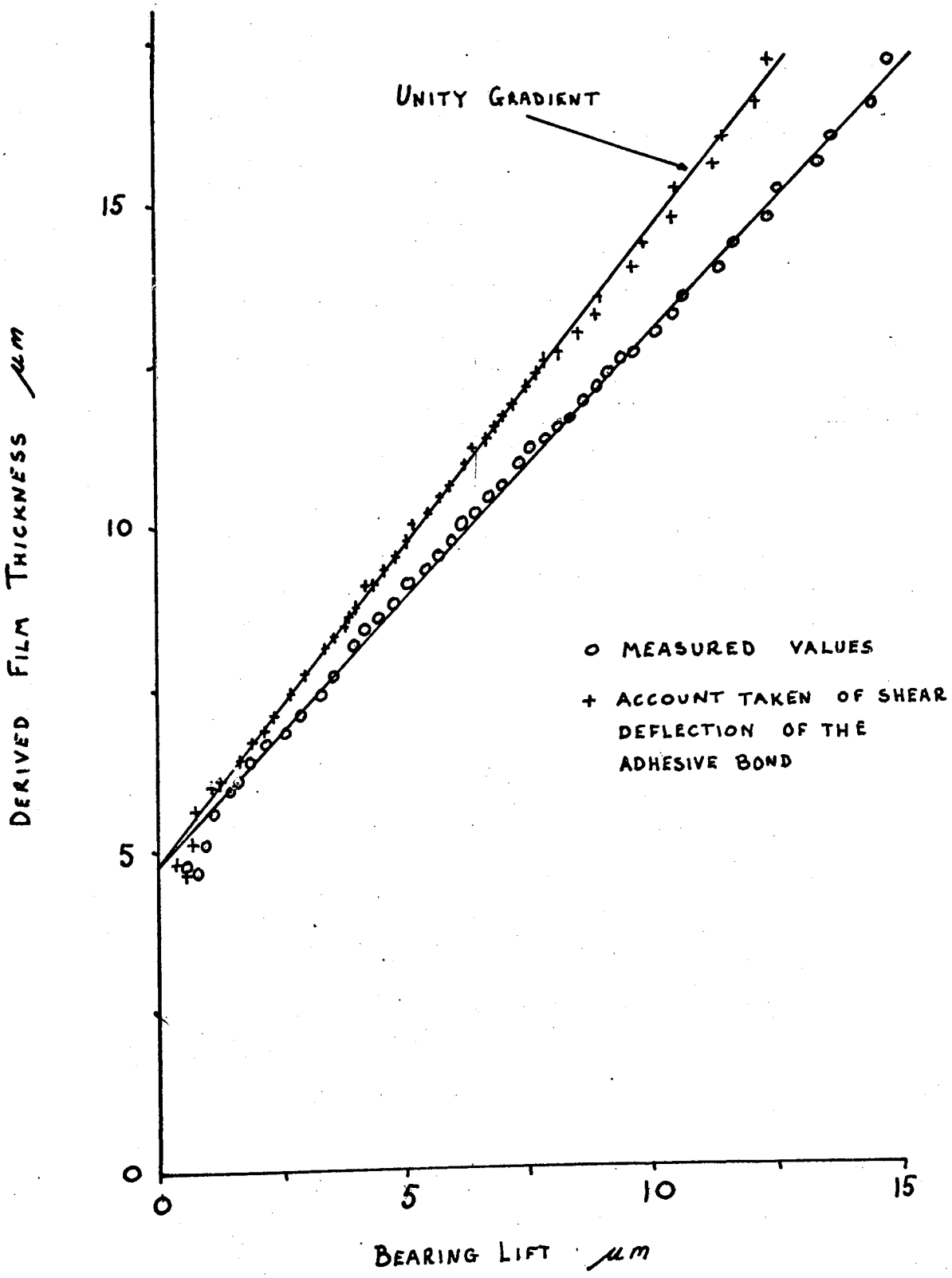

Figure 52 Variation of Derived Film Thickness with Measured Bearing Lift for Bearing Pad Number 1

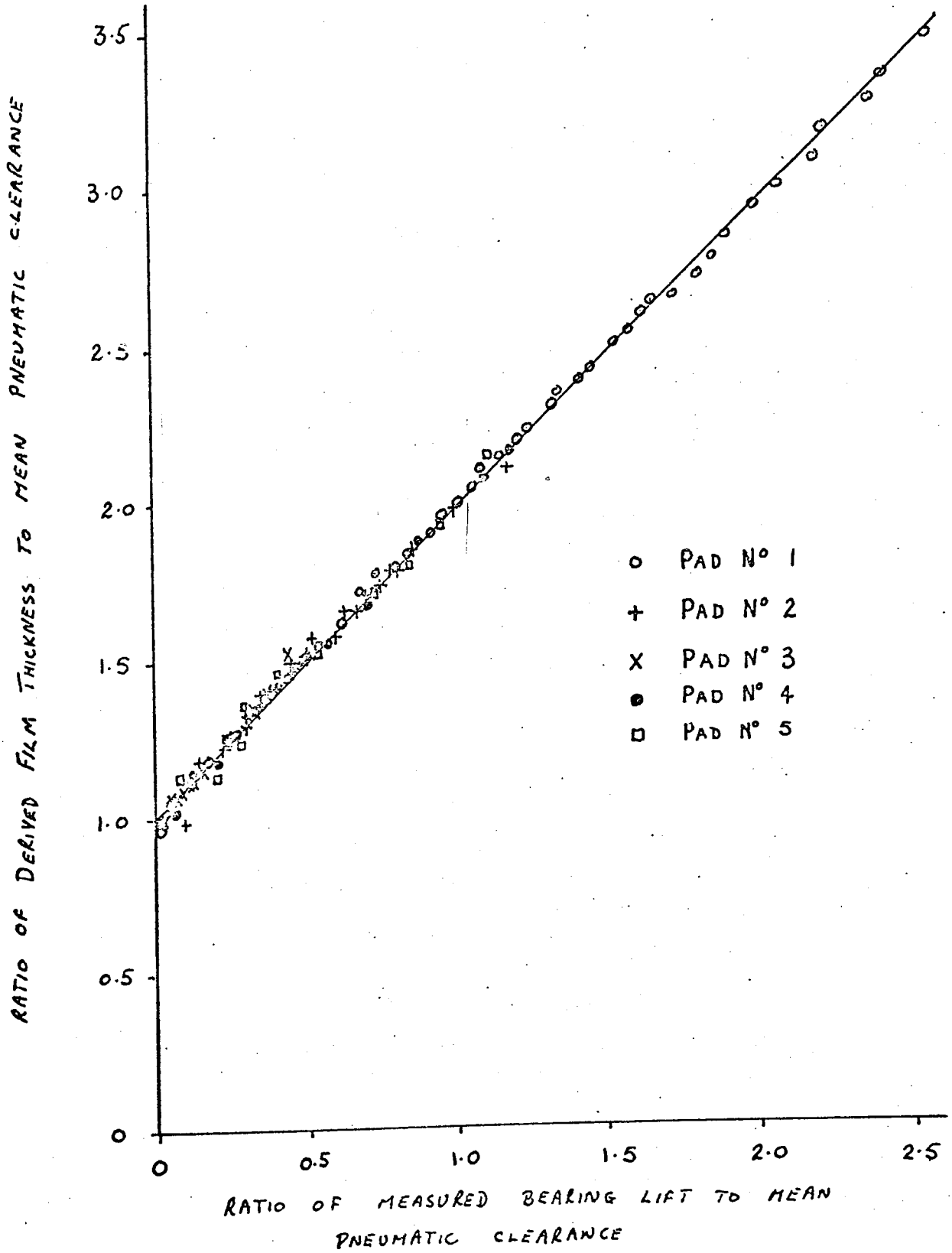

Figure 53 Variation of the Ratio of Derived Film Thickness to Mean Pneumatic Clearance with the Ratio of Measured Bearing to Mean Pneumatic Clearance for various Bearing Pads

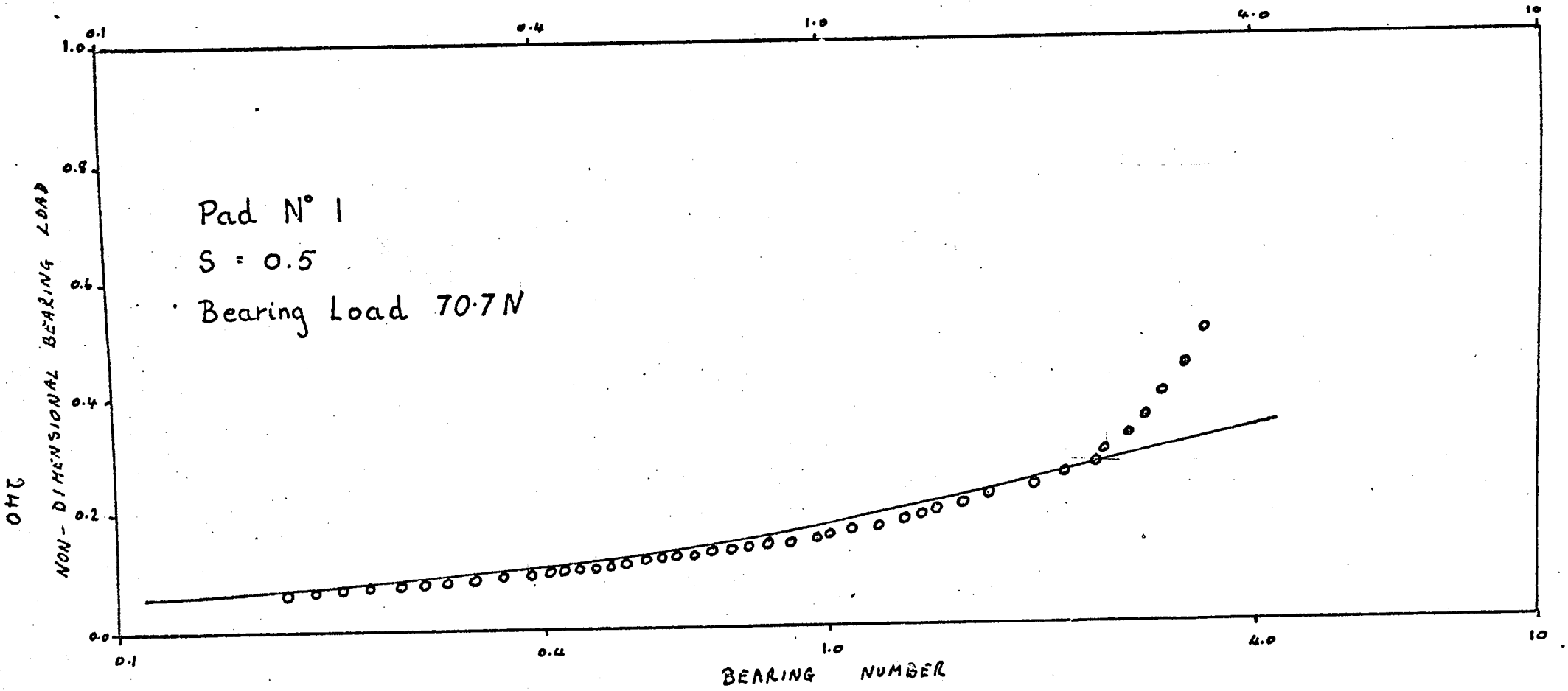

Figure 54 Comparison of the Experimentally determined and Theoretically predicted variation of Non-Dimensional Bearing Load with Bearing Number

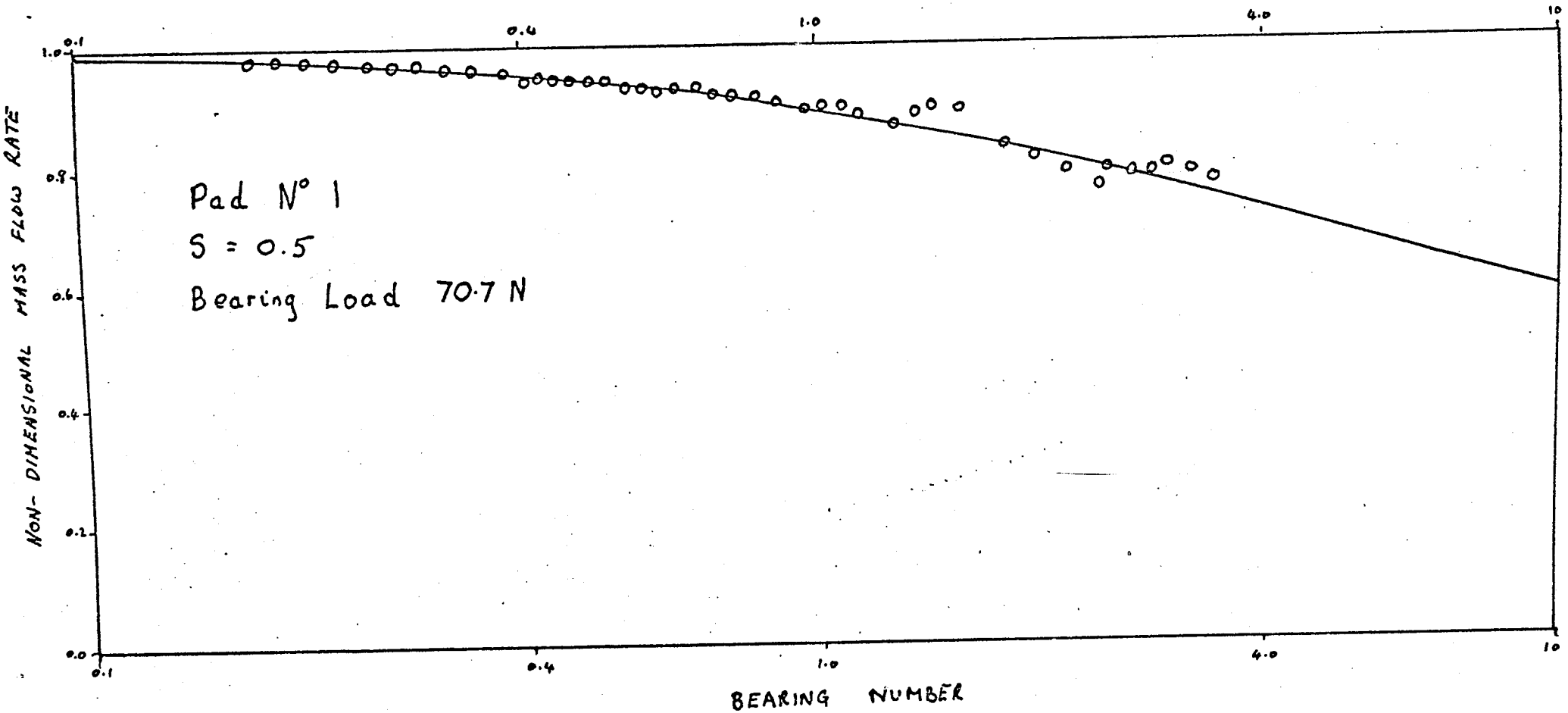

Figure 55 Comparison of the Experimentally determined and Theoretically predicted variation of Non-Dimensional Mass Flow Rate with Bearing Number

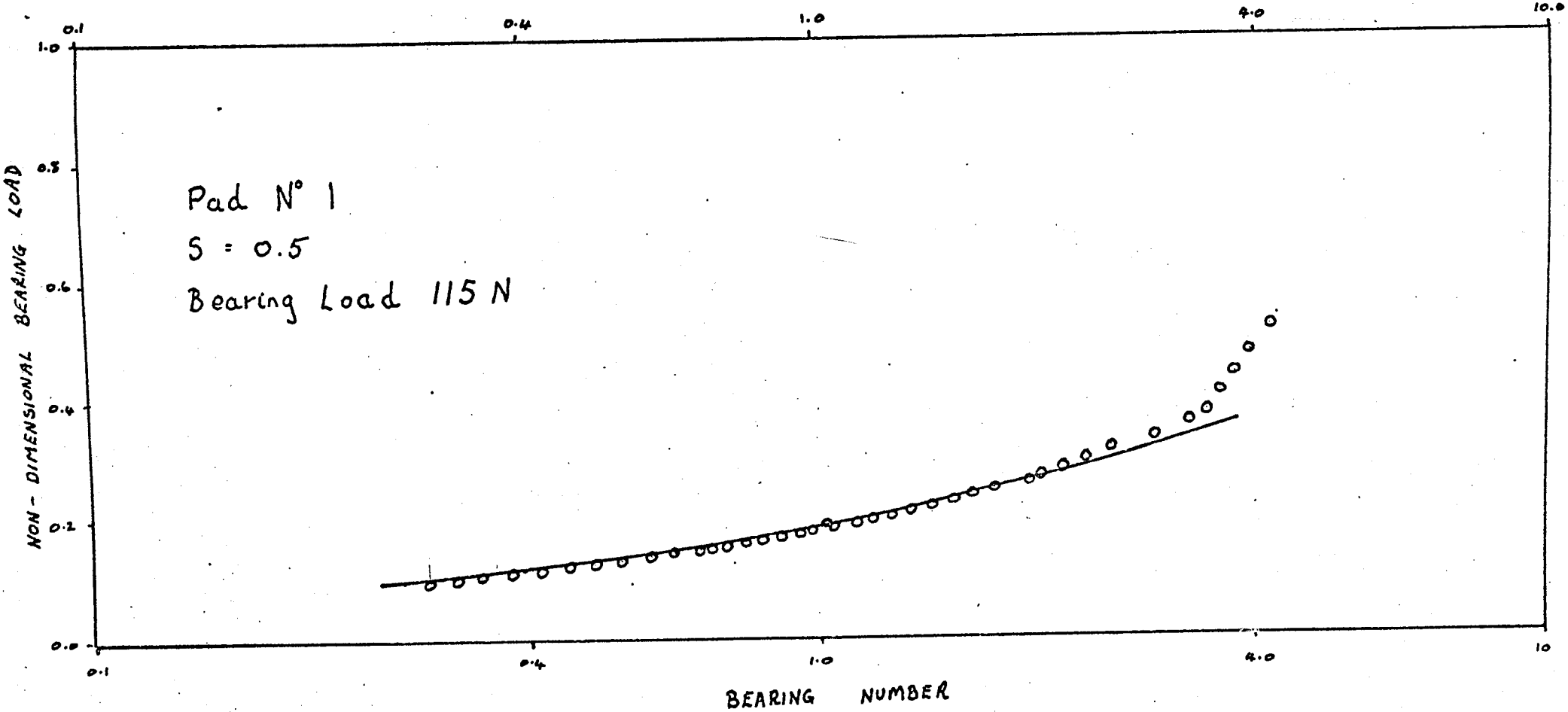

Figure 56 Comparison of the Experimentally determined and Theoretically predicted variation of Non-Dimensional Bearing Load with Bearing Number

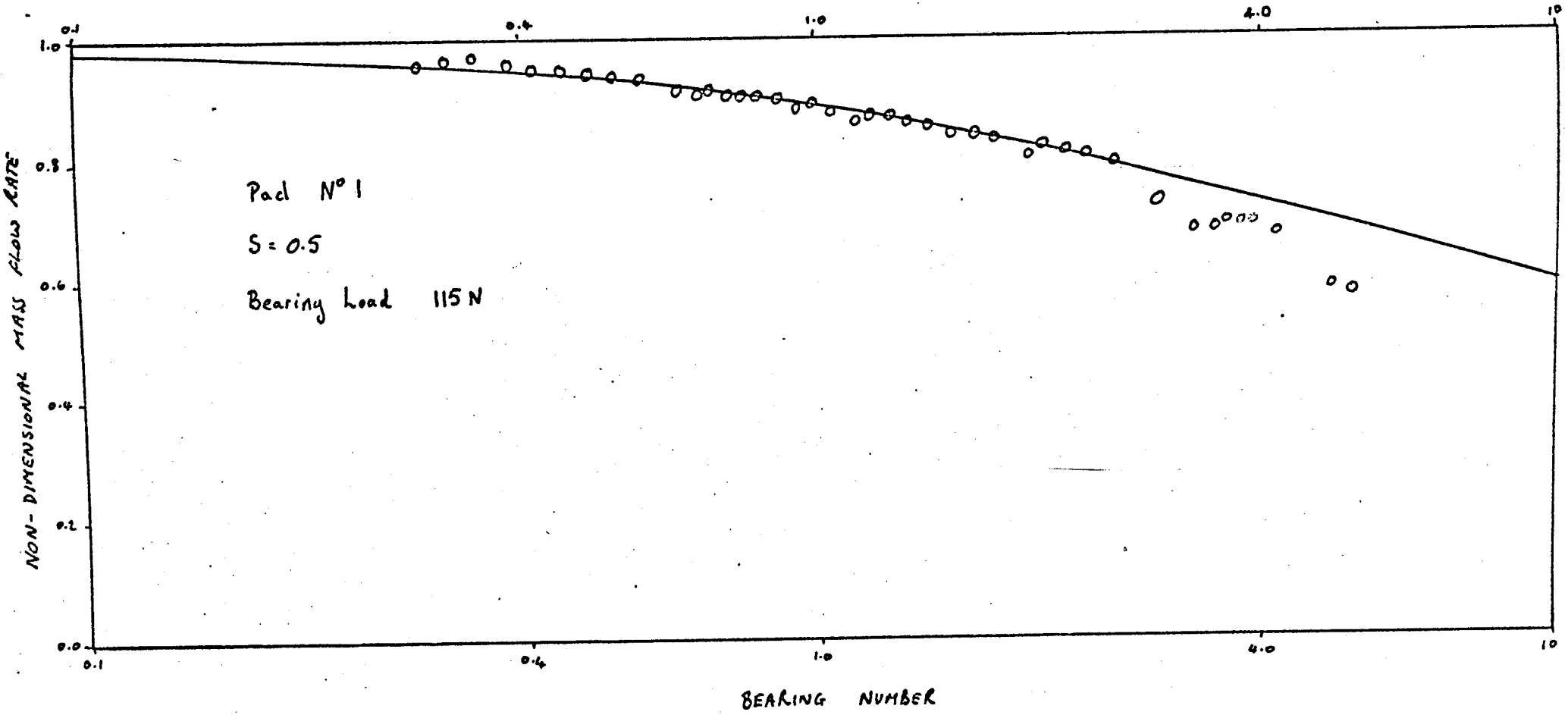

Figure 57 Comparison of the Experimentally determined and Theoretically predicted variation of the Non-Dimensional Mass Flow Rate with Bearing Number

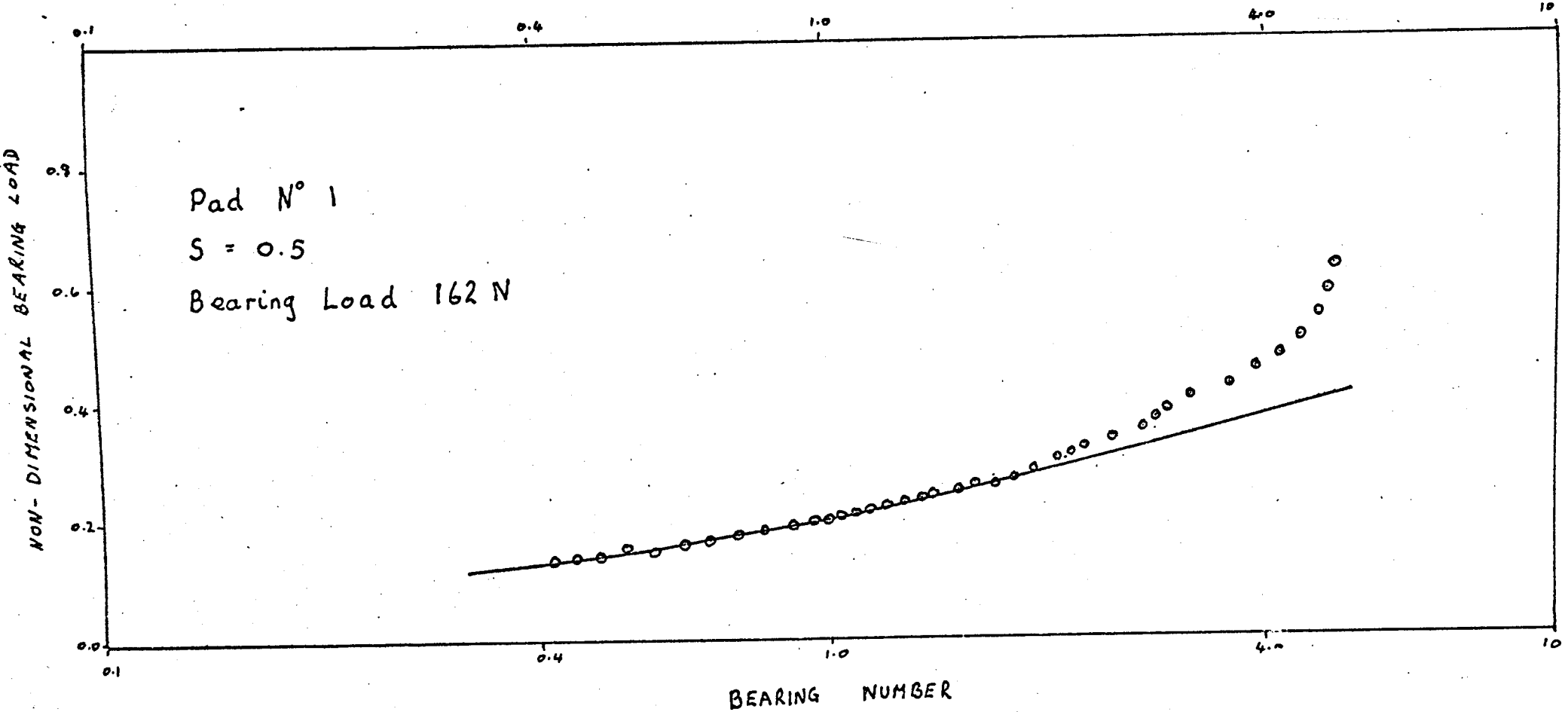

Figure 58 Comparison of the Experimentally determined and Theoretically predicted variation of Non-Dimensional Bearing Load with Bearing Number

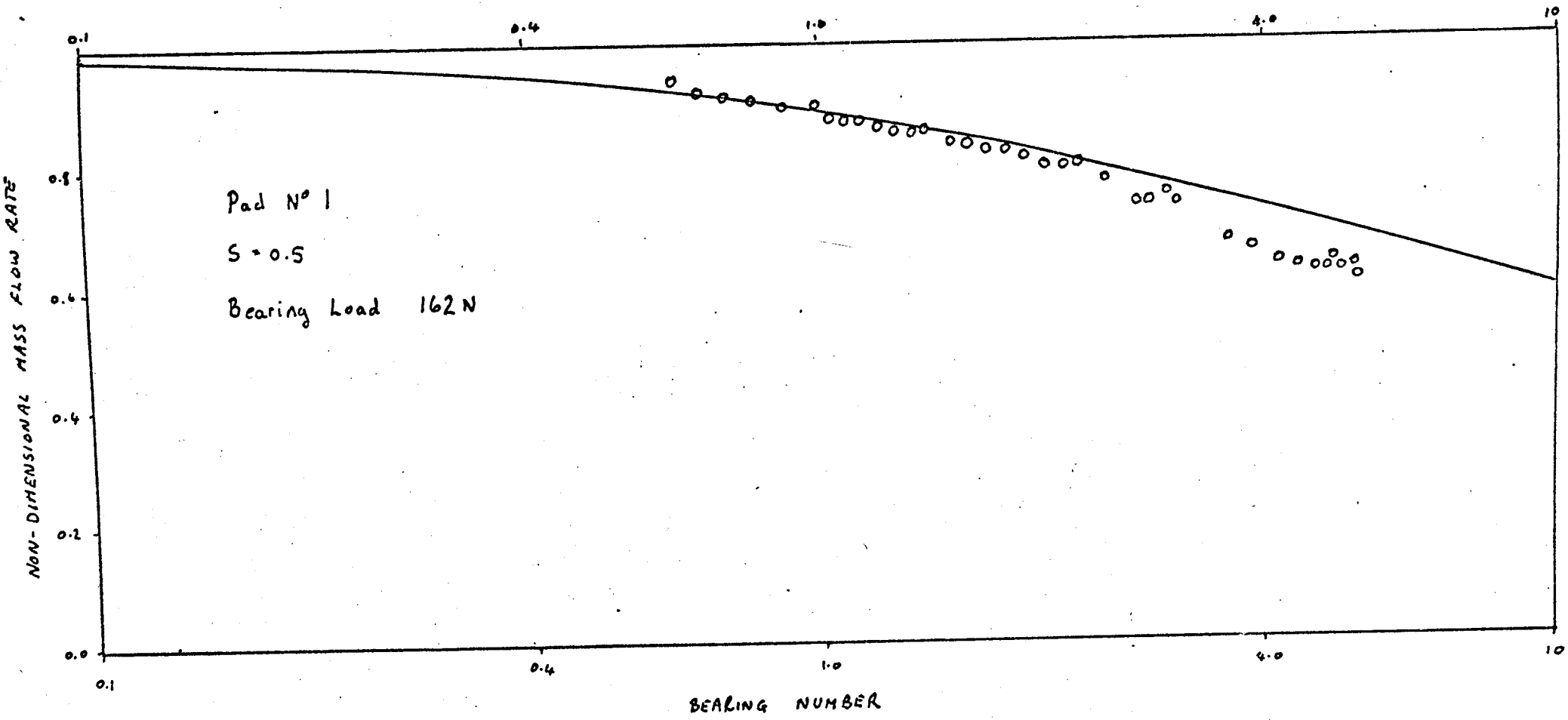

Figure 59 Comparison of the Experimentally determined and Theoretically predicted variation of Non-Dimensional Mass Flow Rate with Bearing Number

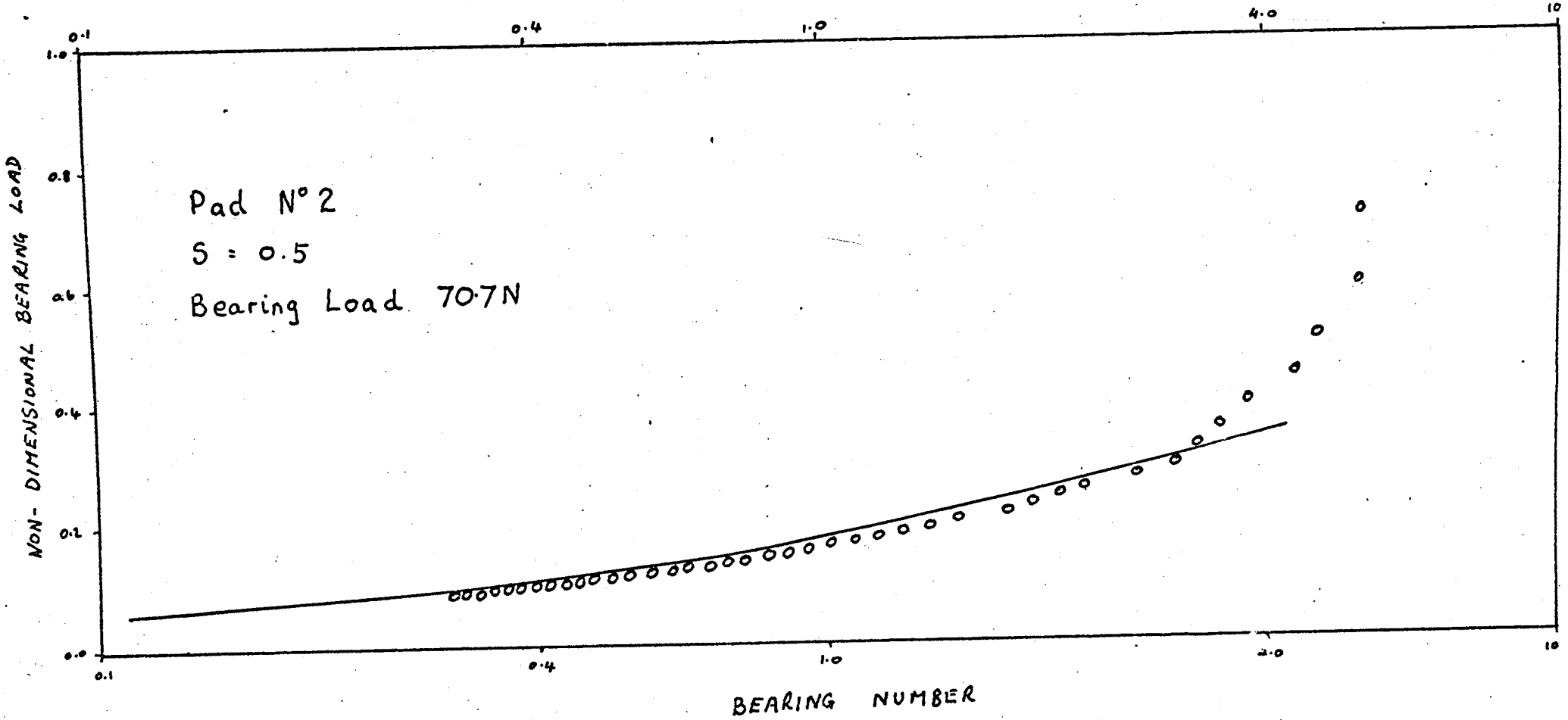

Figure 60 Comparison of the Experimentally determined and Theoretically predicted variation of Non-Dimensional Bearing Load with Bearing Number

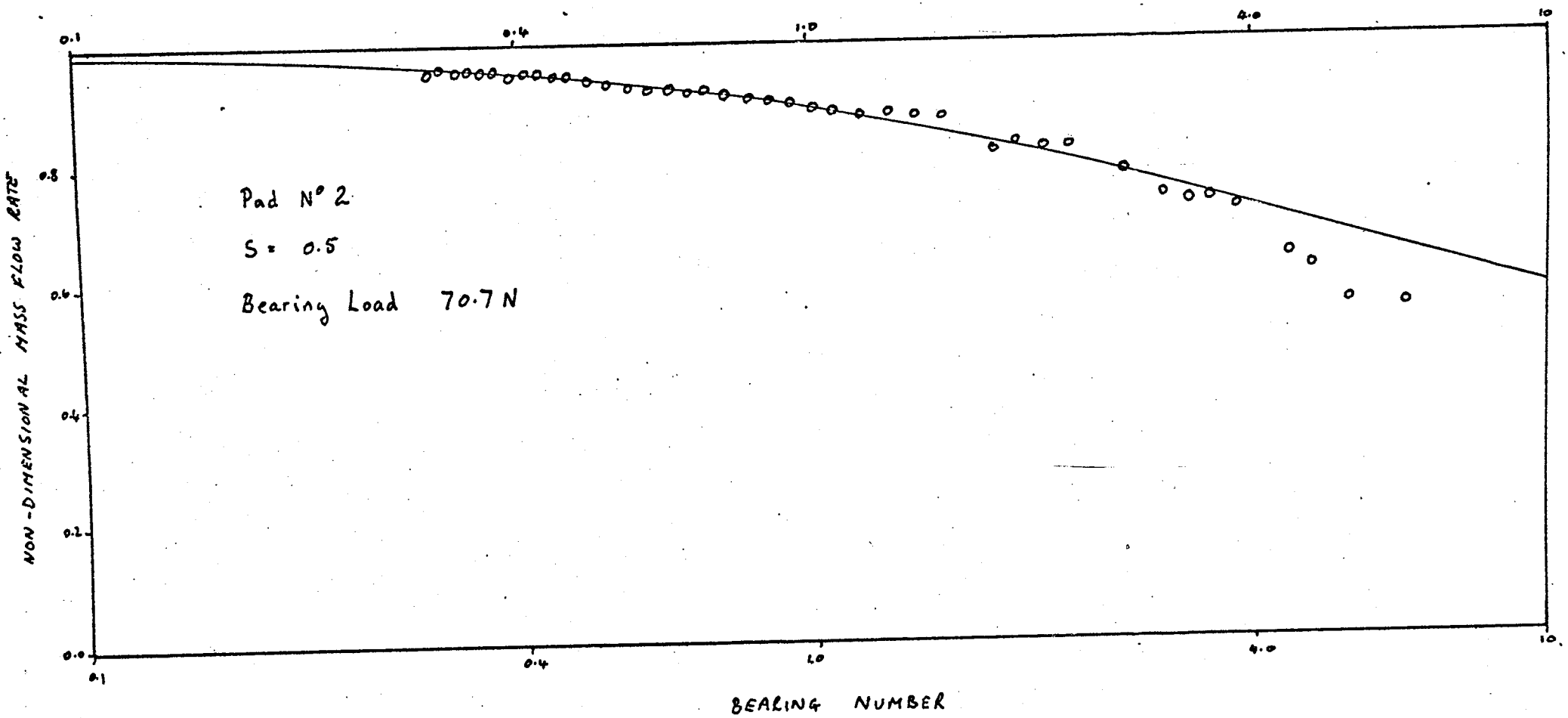

Figure 61 Comparison of the Experimentally determined and Theoretically predicted variation of Non-Dimensional Mass Flow Rate with Bearing Number

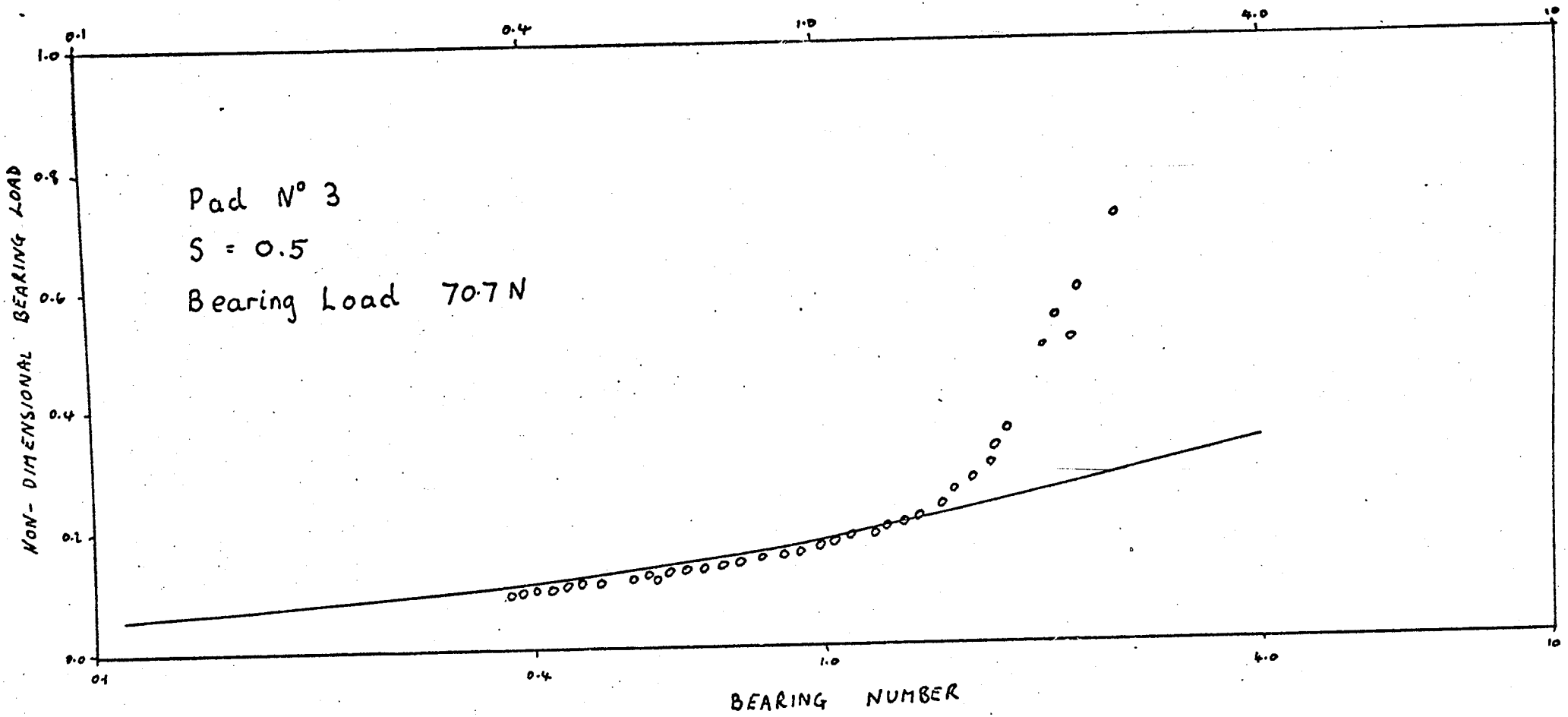

Figure 62 Comparison of the Experimentally determined and Theoretically predicted variation of Non-Dimensional Bearing Load with Bearing Number

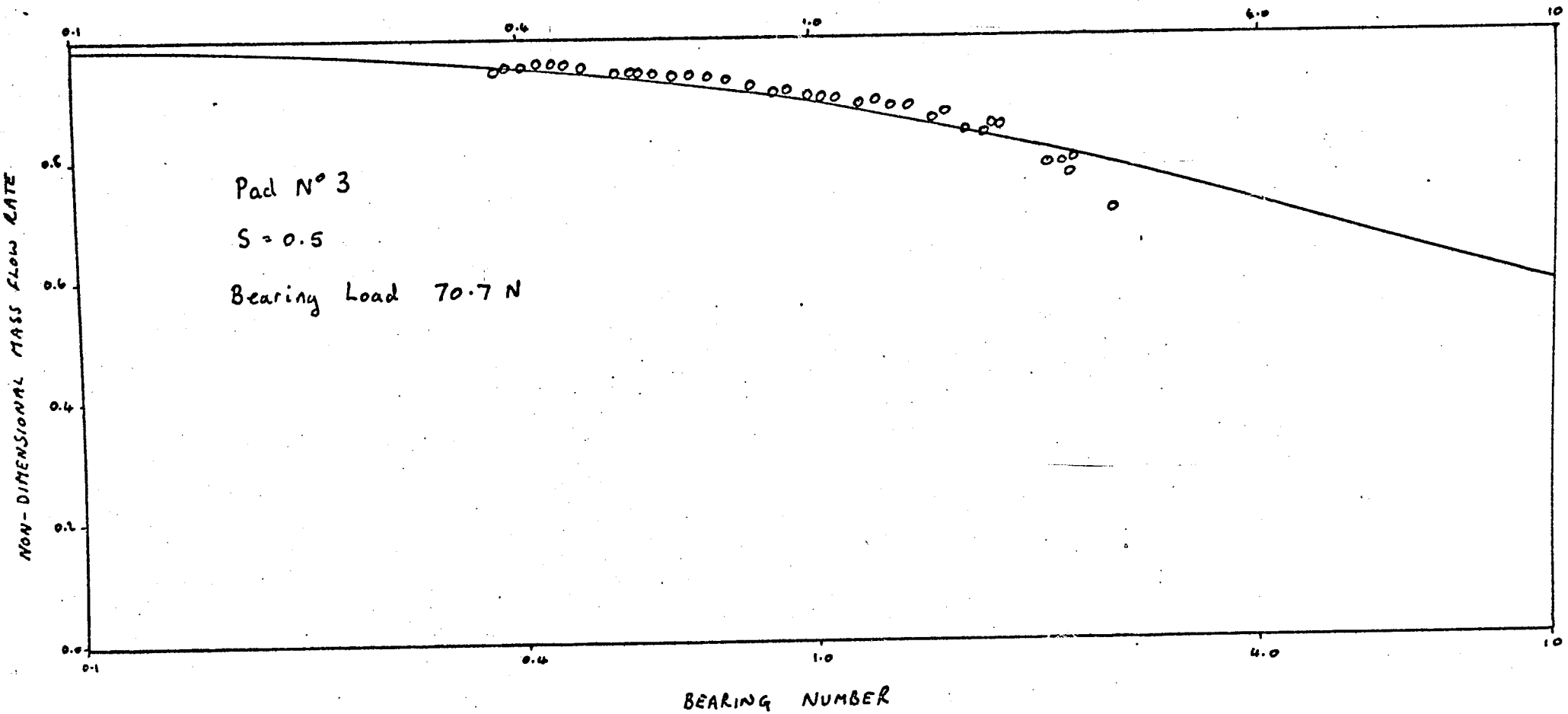

Figure 63 Comarison of the Experimentally determined and Theoretically predicted variation of Non-Dimensional Mass Flow Rate with Bearing Number

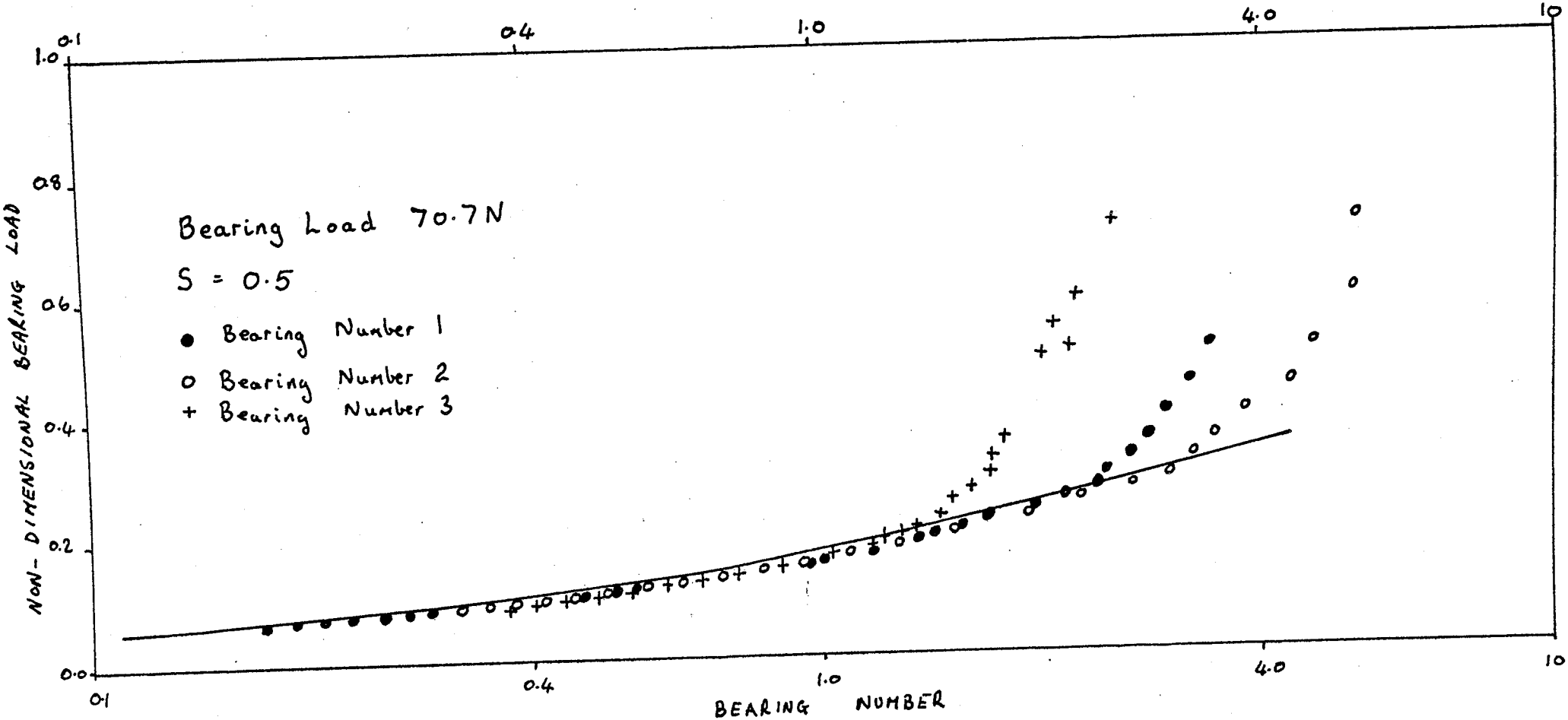

Comparison of the Experimentally determined and Theoretically predicted variation of Non-Dimensional Bearing Load with Bearing Number for Pad Numbers 1,2 & 3

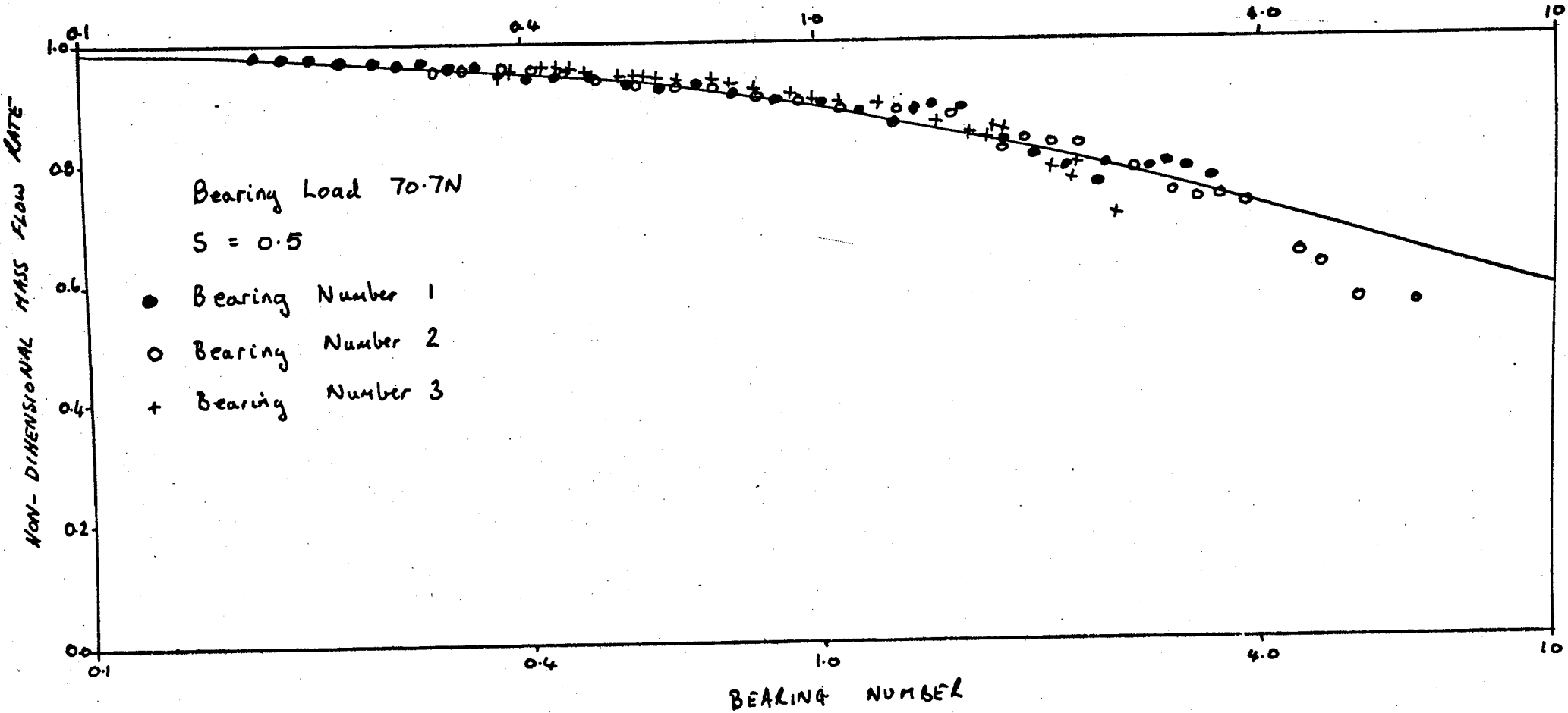

Comparison of the Experimentally determined and Theoretically predicted variation of Non-Dimension Mass Flow Rate with Bearing Number for Pad Numbers 1,2 & 3

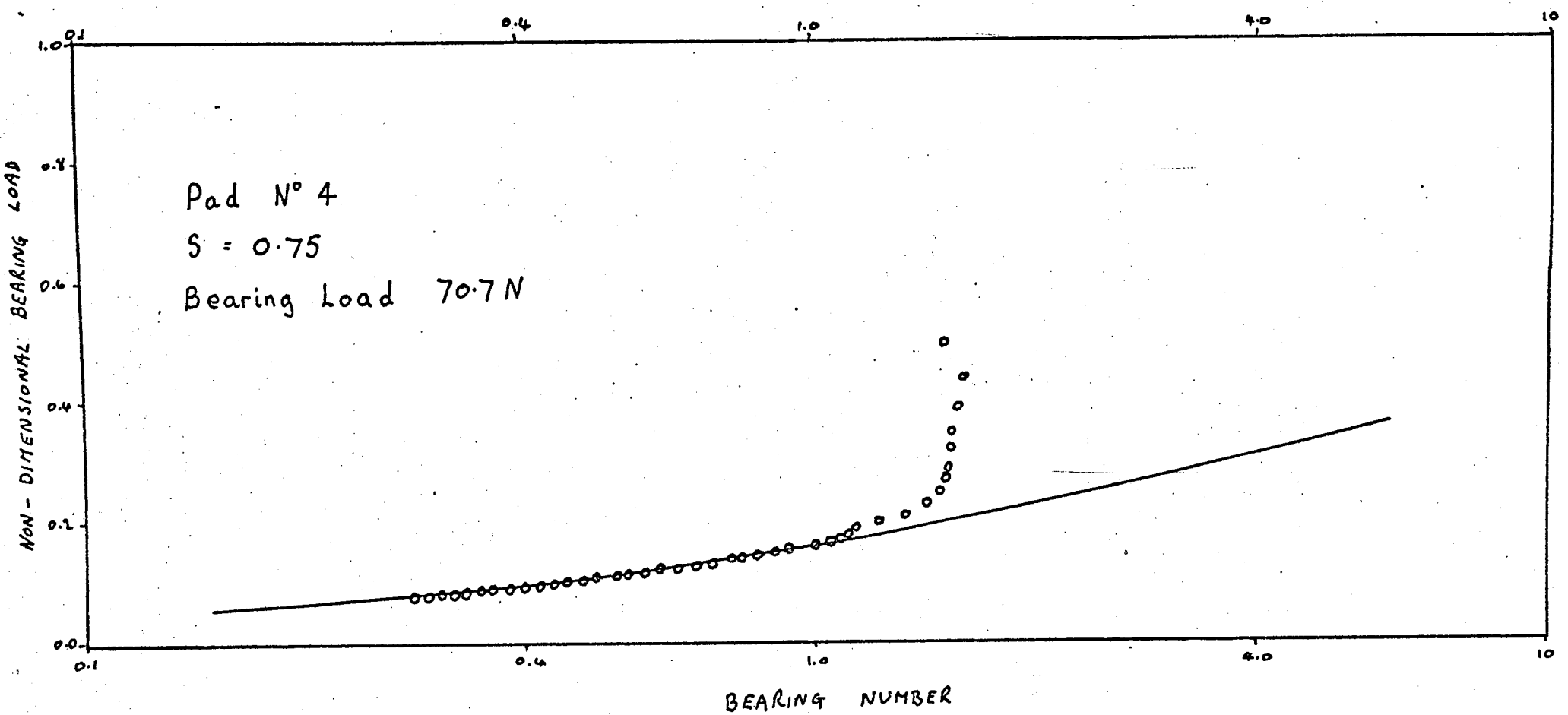

Figure 64 Comparison of the Experimentally determined and Theoretically predicted variation of Non-Dimensional Bearing Load with Bearing Number

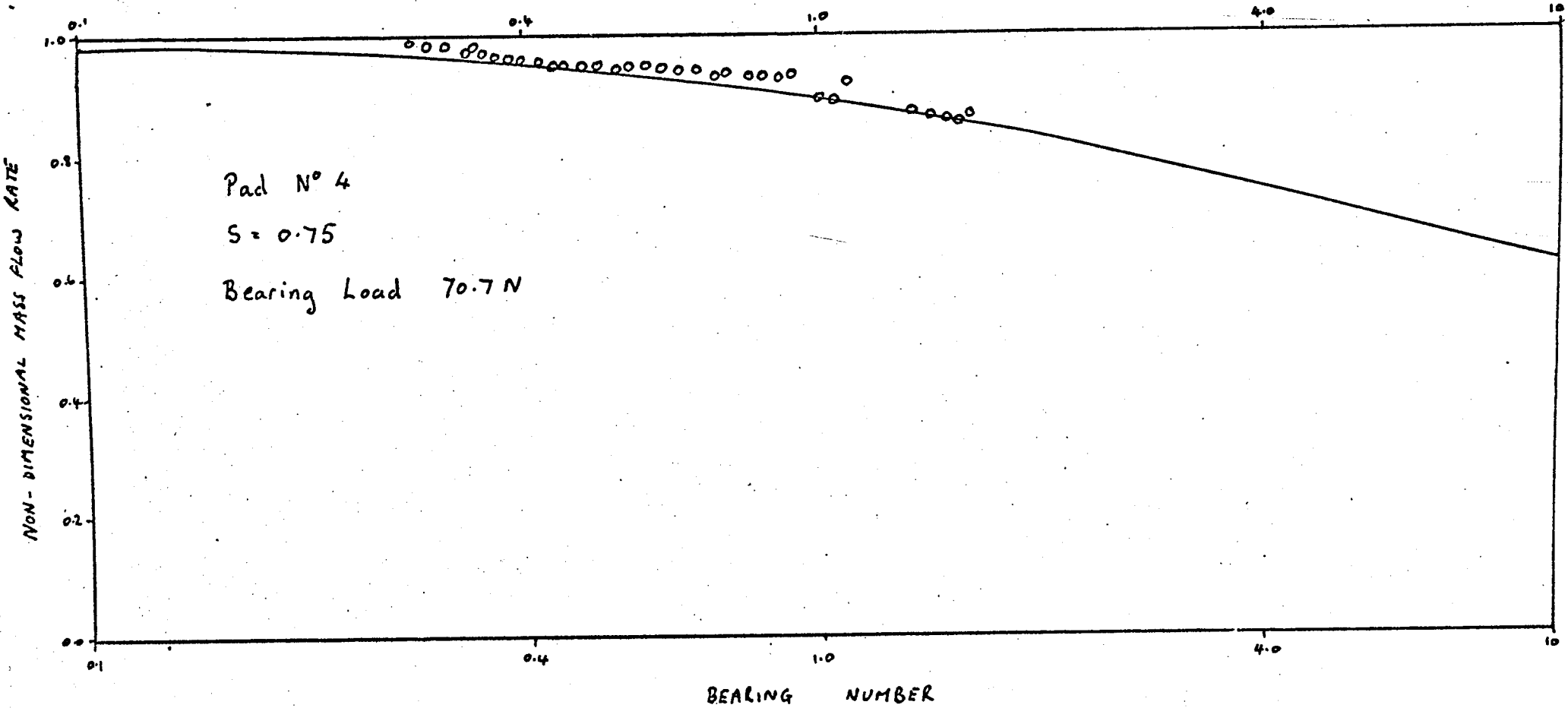

Figure 65 Comparison of the Experimentally determined and Theoretically predicted variation of Non-Dimensional Mass Flow Rate with Bearing Number

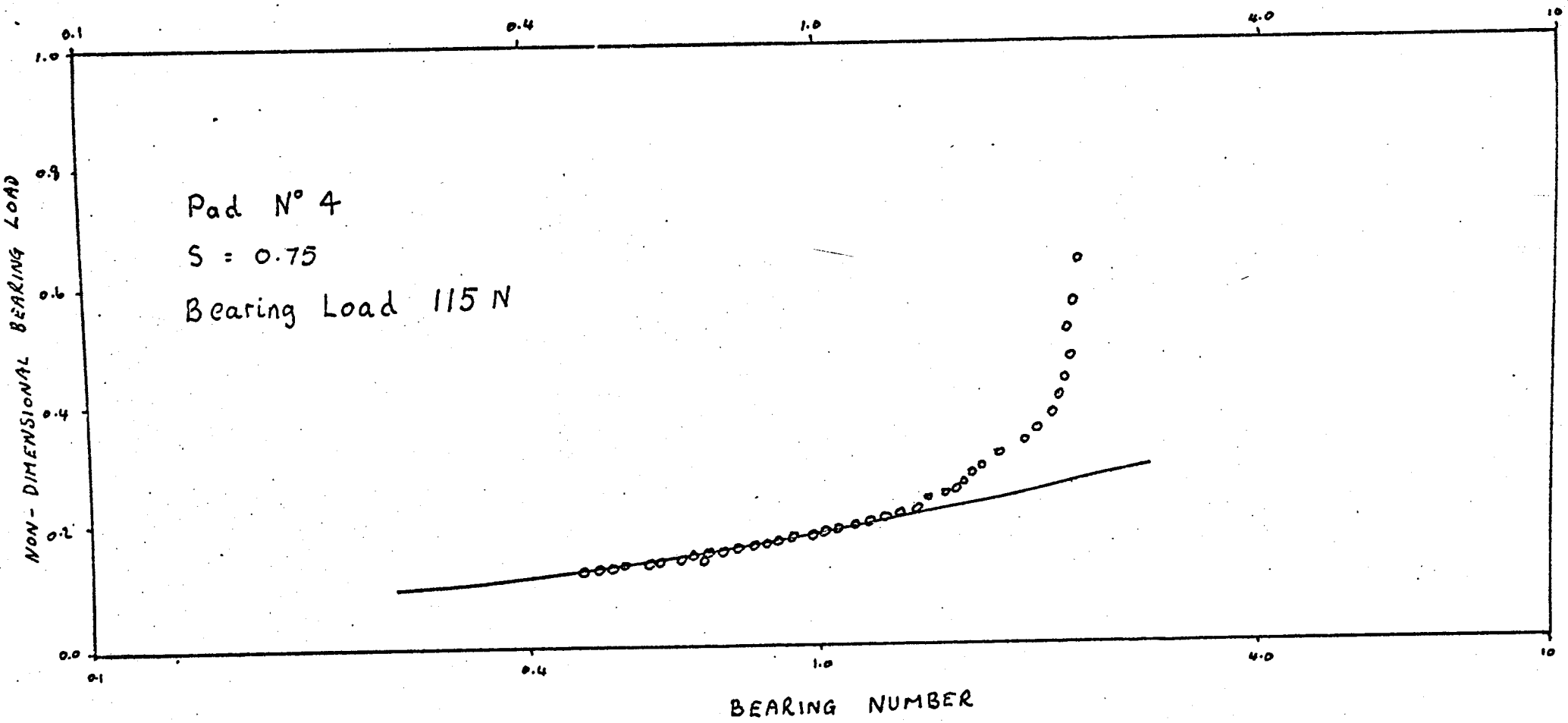

Figure 66 Comparison of the Experimentally determined and Theoretically predicted variation of Non-Dimensional Bearing Load with Bearing Number

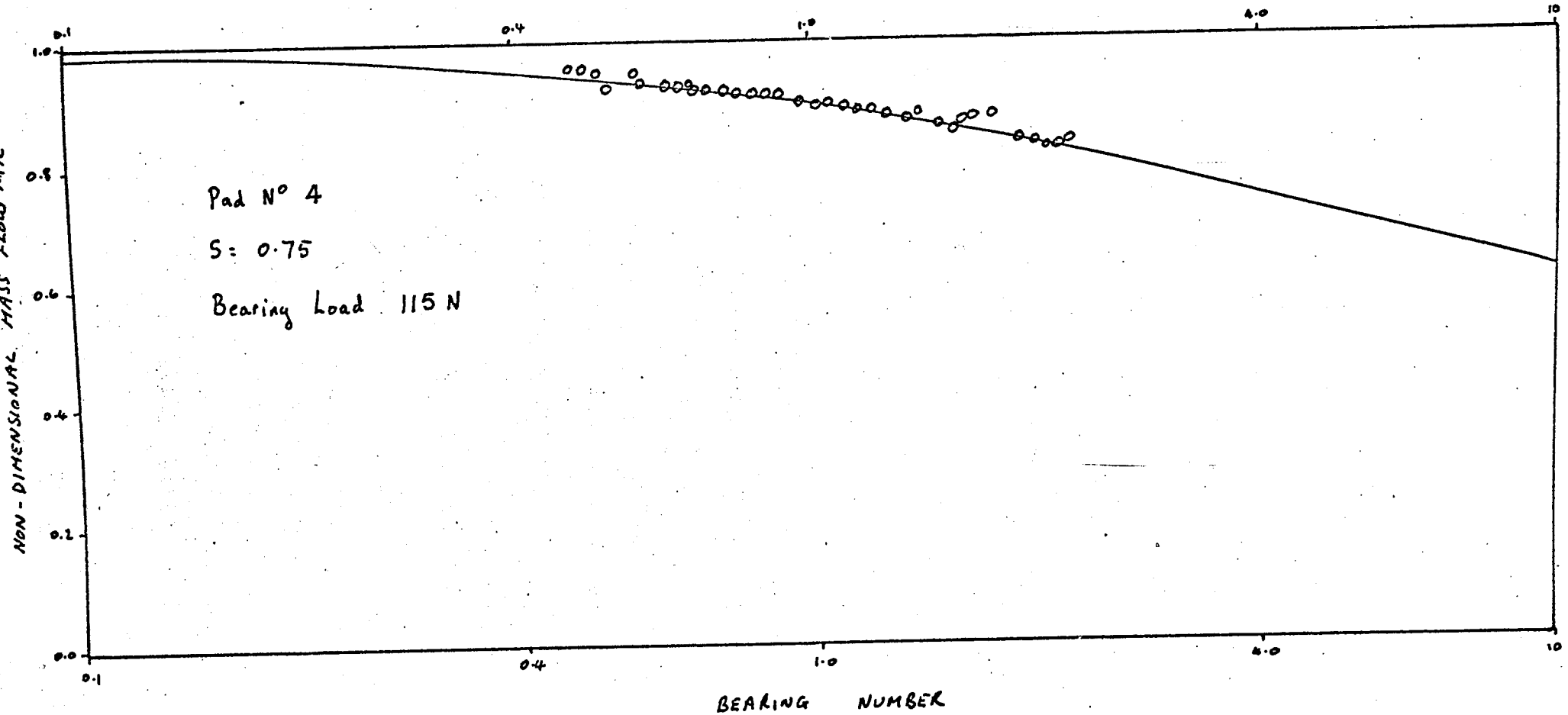

Figure 67 Comparison of the Experimentally determined and Theoretically predicted variation of Non-Dimensional Mass Flow Rate with Bearing Number

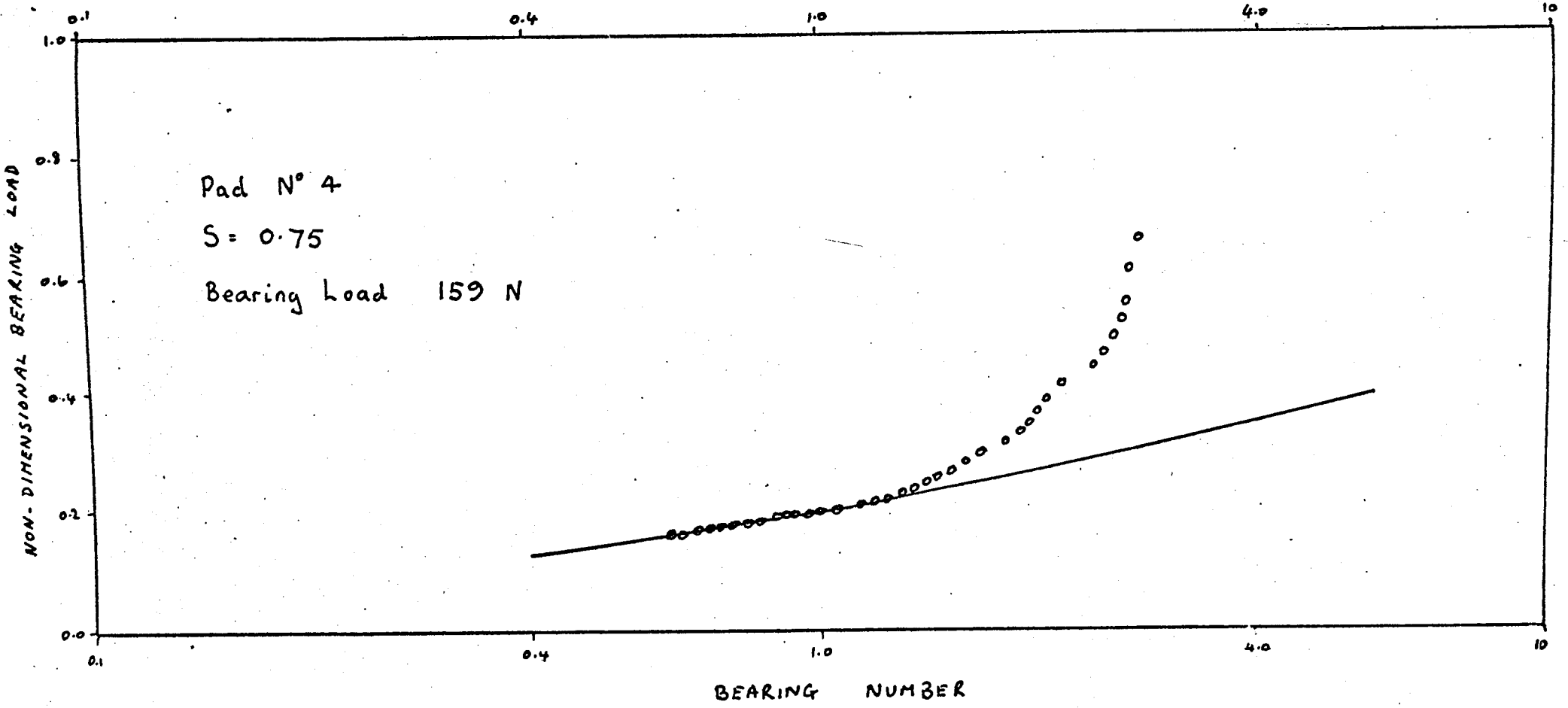

Figure 68 Comparison of the Experimentally determined and Theoretically predicted variation of Non-Dimensional Bearing Load with Bearing Number

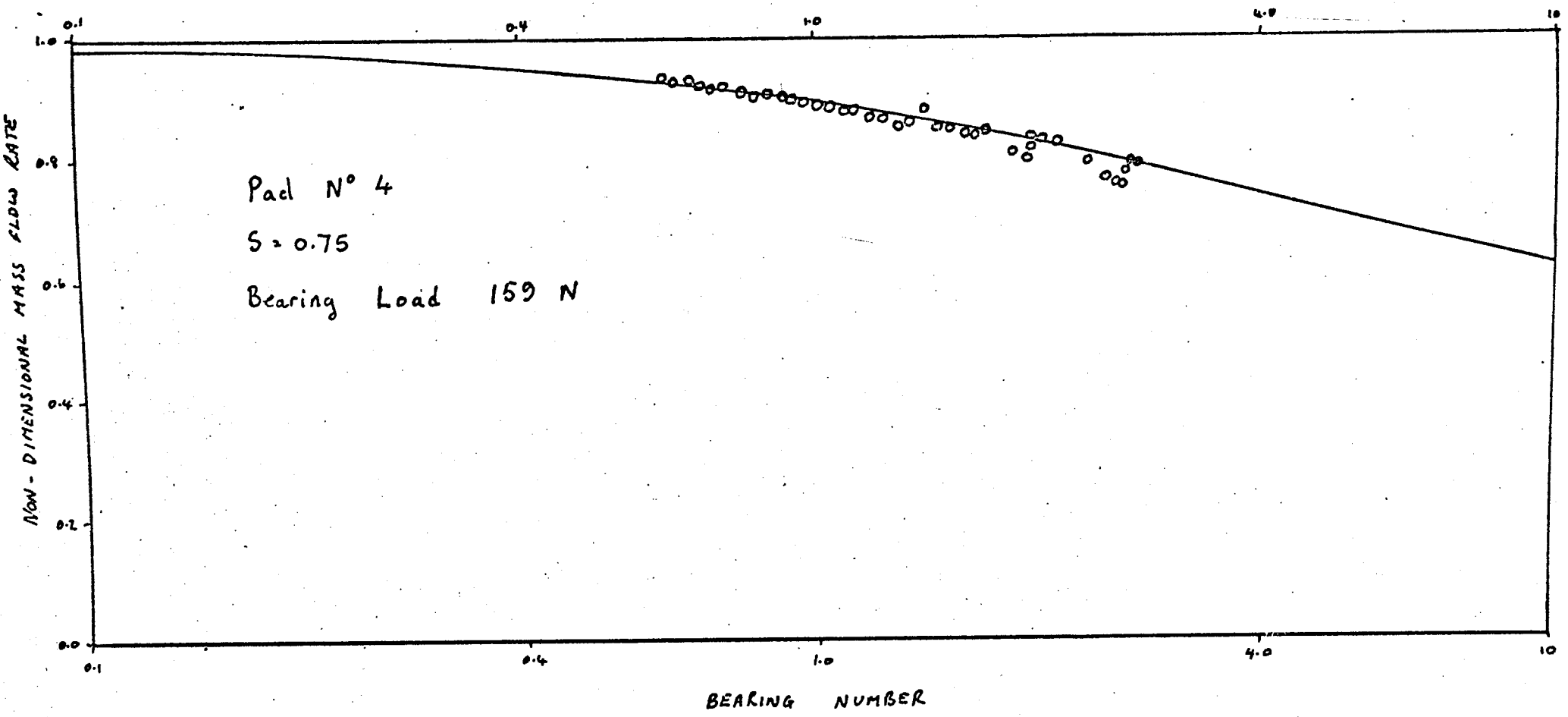

Figure 69 Comparison of the Experimentally determined and Theoretically predicted variation of Non-Dimensional Mass Flow Rate with Bearing Number

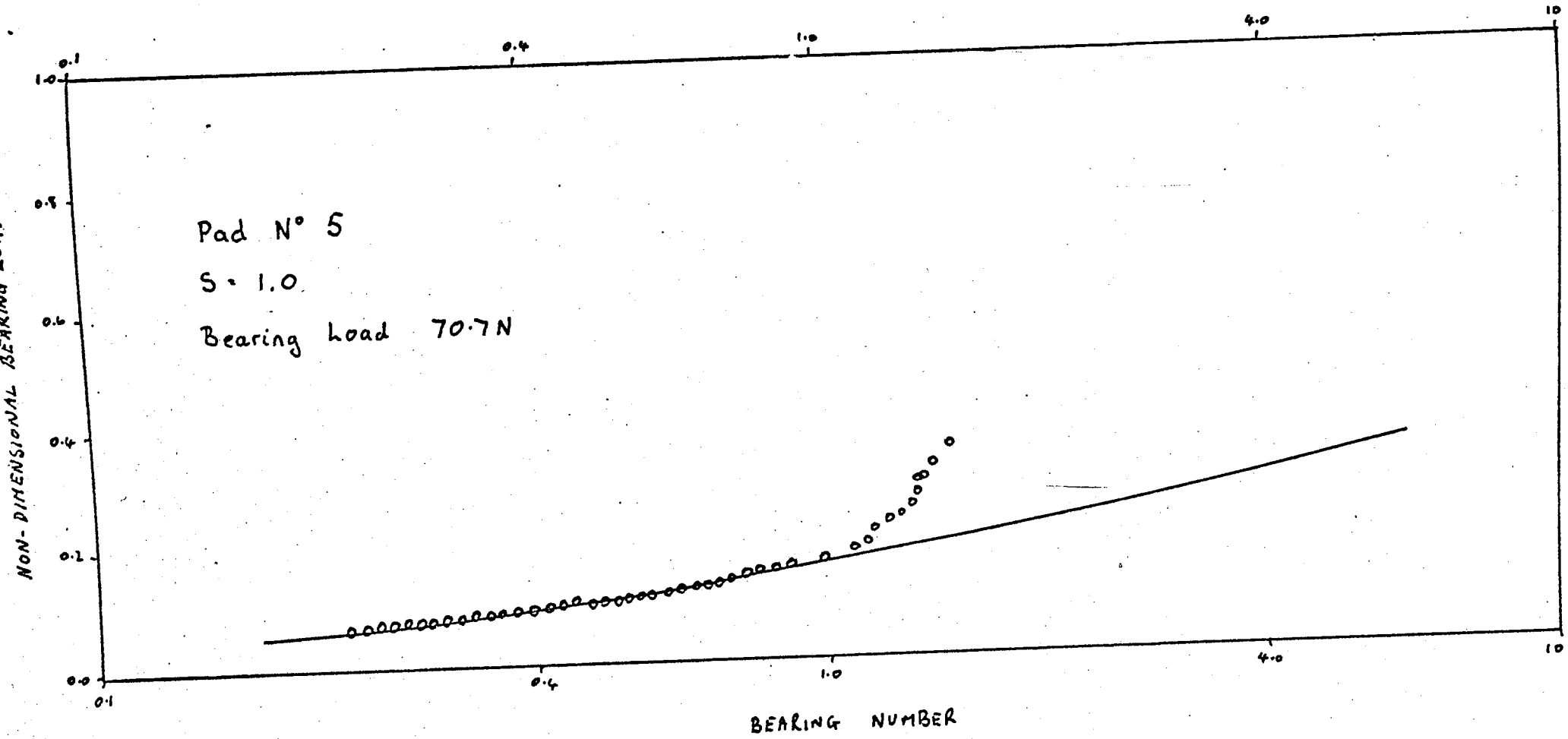

Figure 70 Comparison of the Experimentally determined and Theoretically predicted variation of the Non-Dimensional Bearing Load with Bearing Number

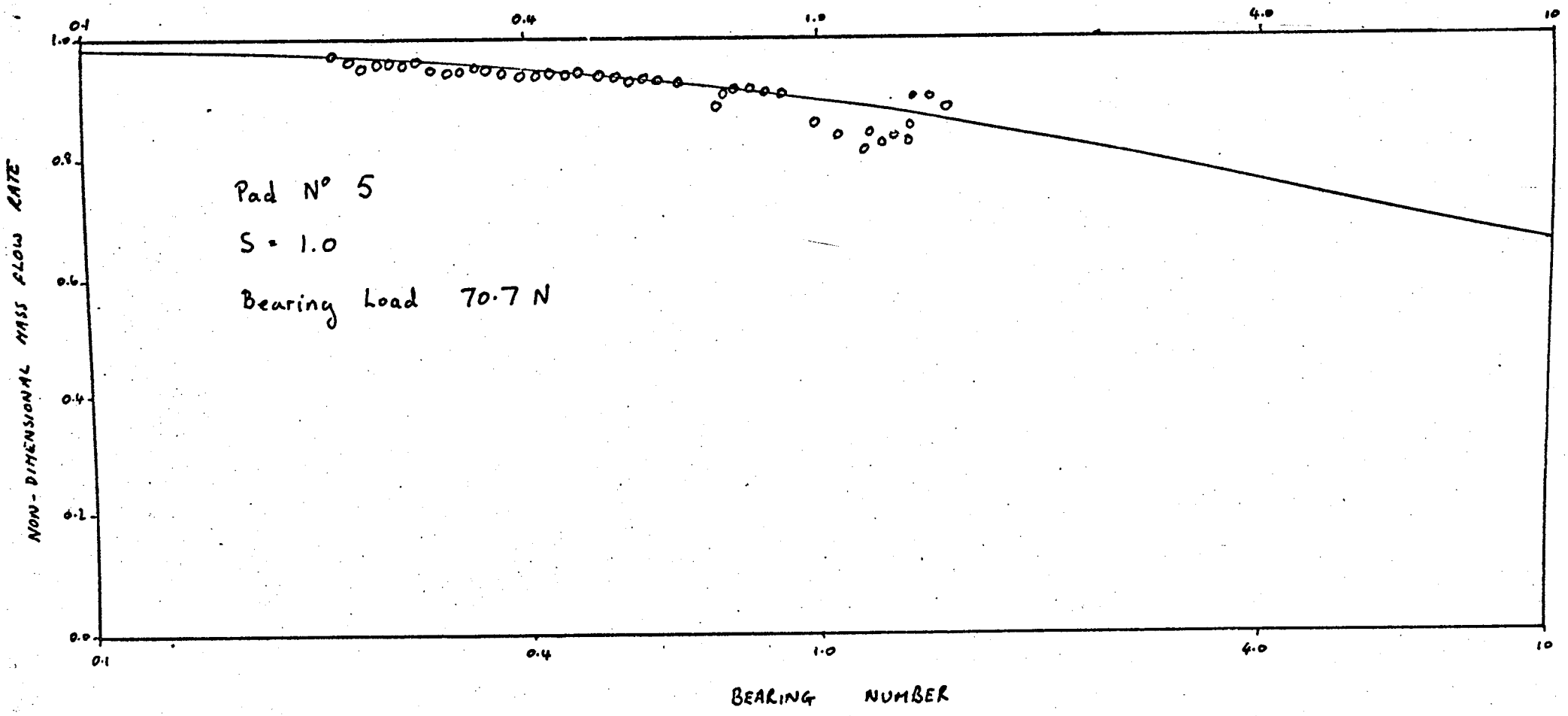

Figure 71 Comparison of the Experimentally determined and Theoretically predicted variation of Non-Dimensional Mass Flow Rate with Bearing Number

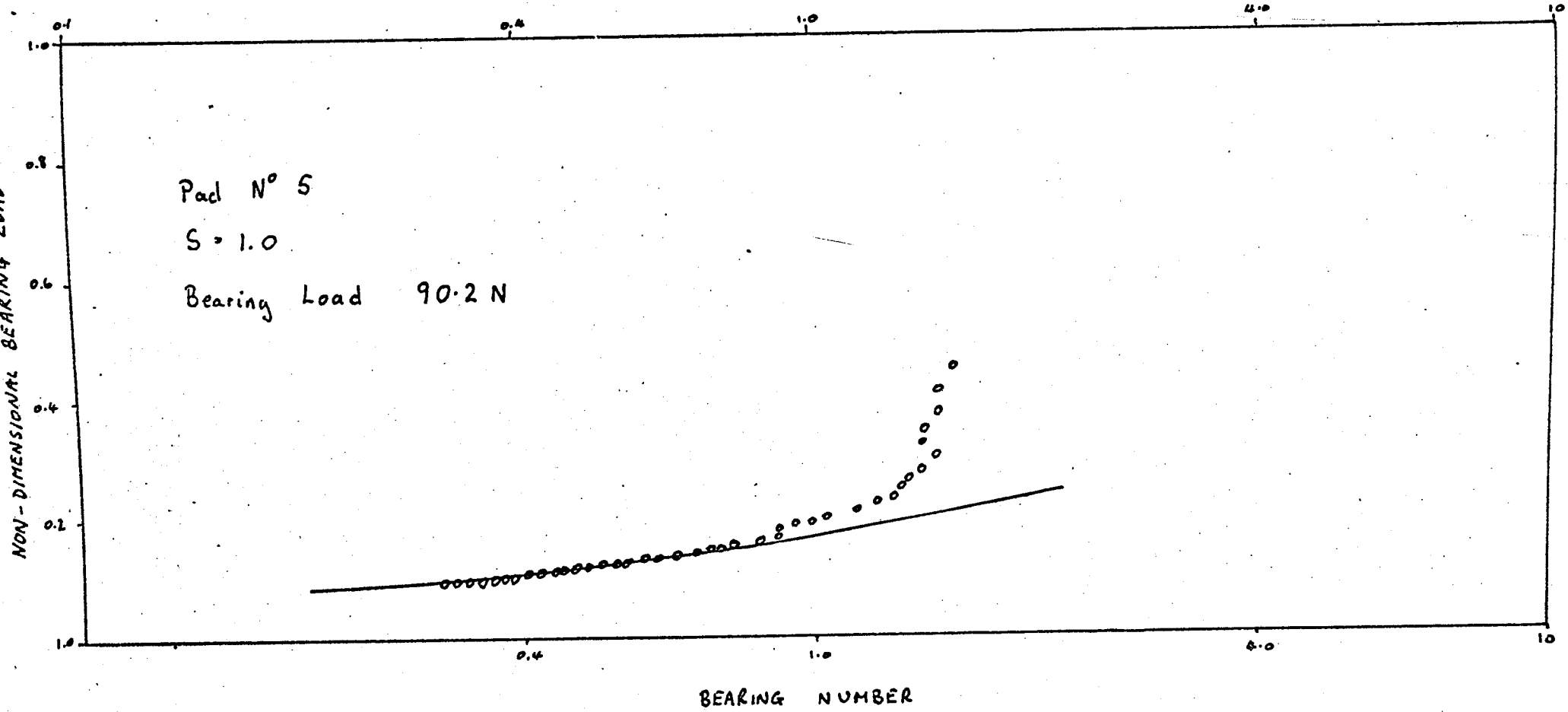

Figure 72 Comparison of the Experimentally determined and Theoretically predicted variation of the Non-Dimensional Bearing Load with Bearing Number

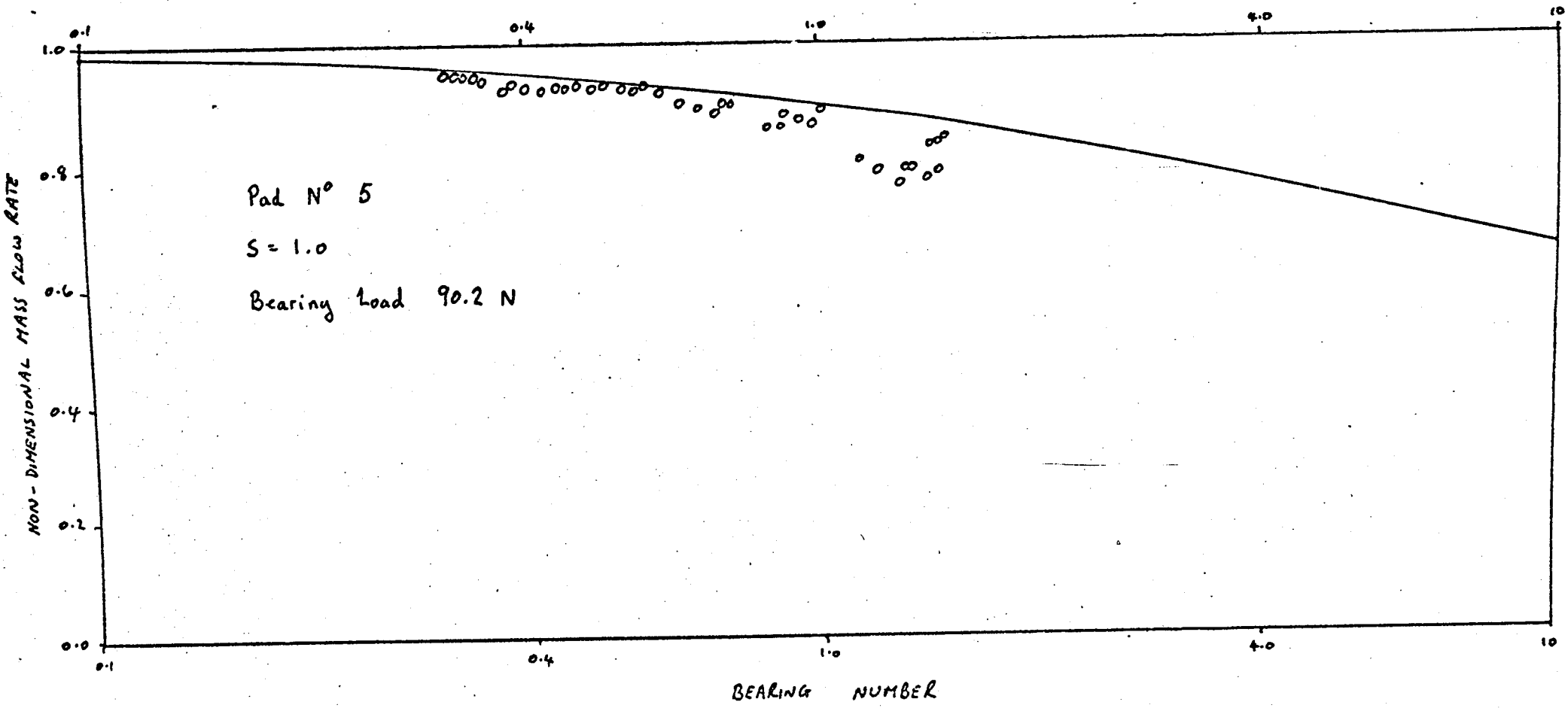

Figure 73 Comparison of the Experimentally determined and Theoretically predicted variation of Non-Dimensional Mass Flow Rate with Bearing Number

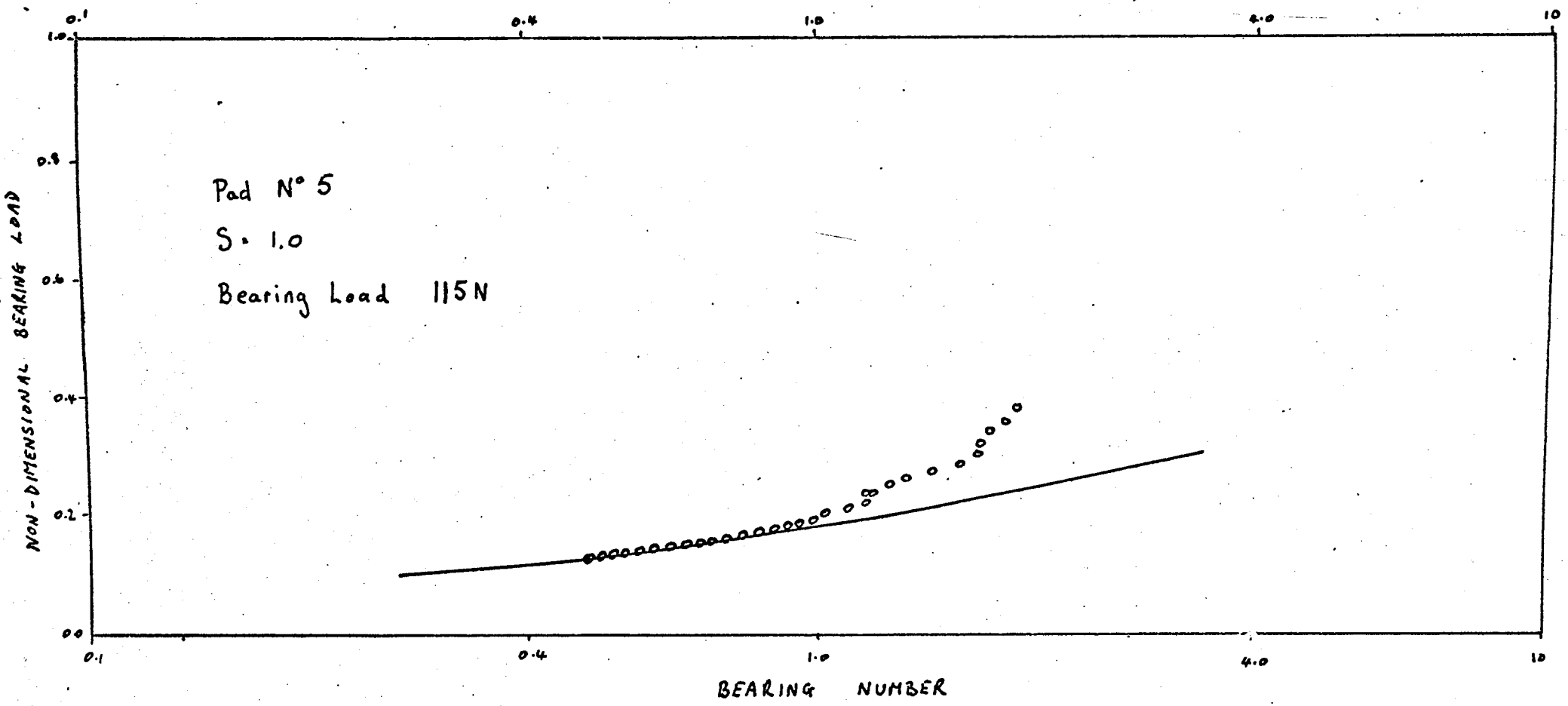

Figure 74 Comparison of the Experimentally determined and Theoretically predicted variation of the Non-Dimensional Bearing Load with Bearing Number

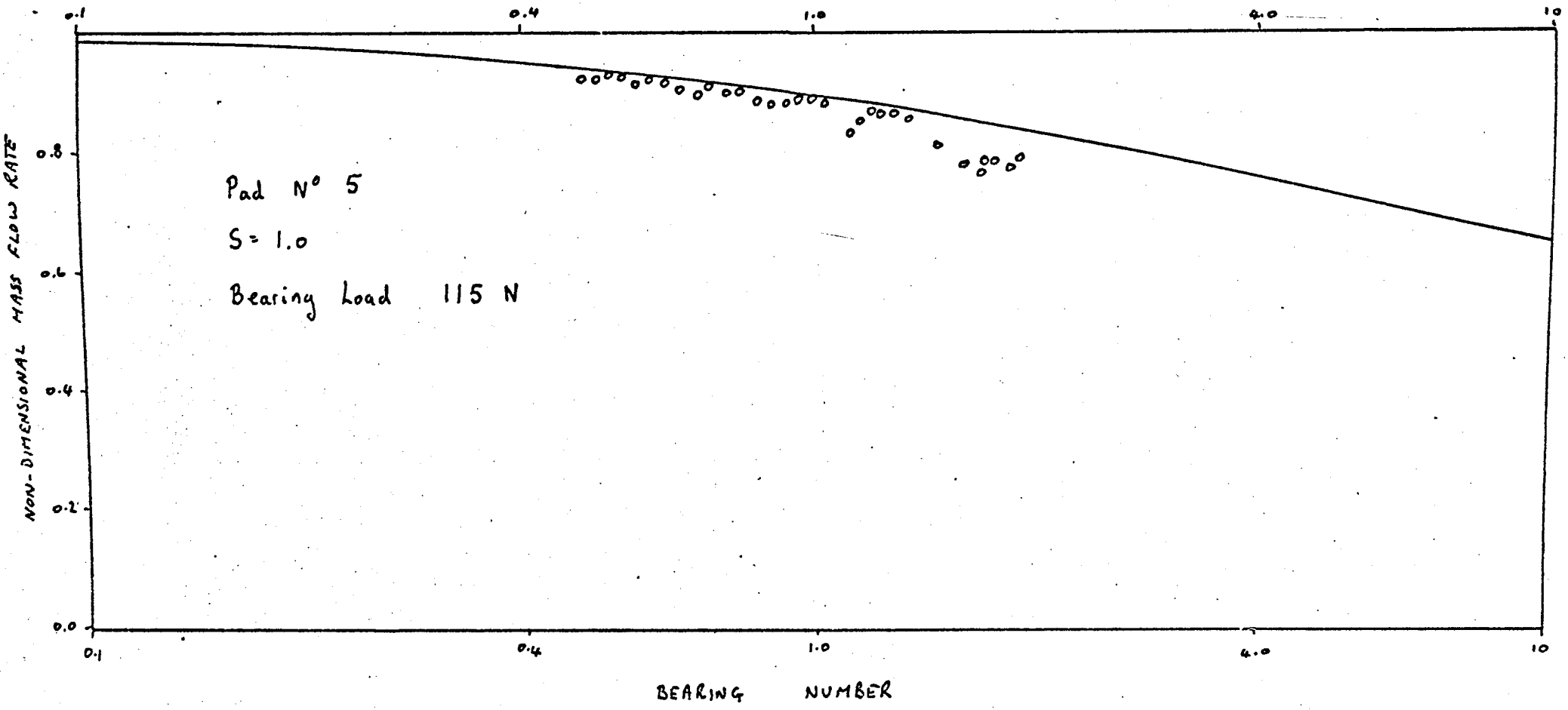

Figure 75 Comparison of the Experimentally determined and Theoretically predicted variation of Non-Dimensional Mass Flow Rate with Bearing Number

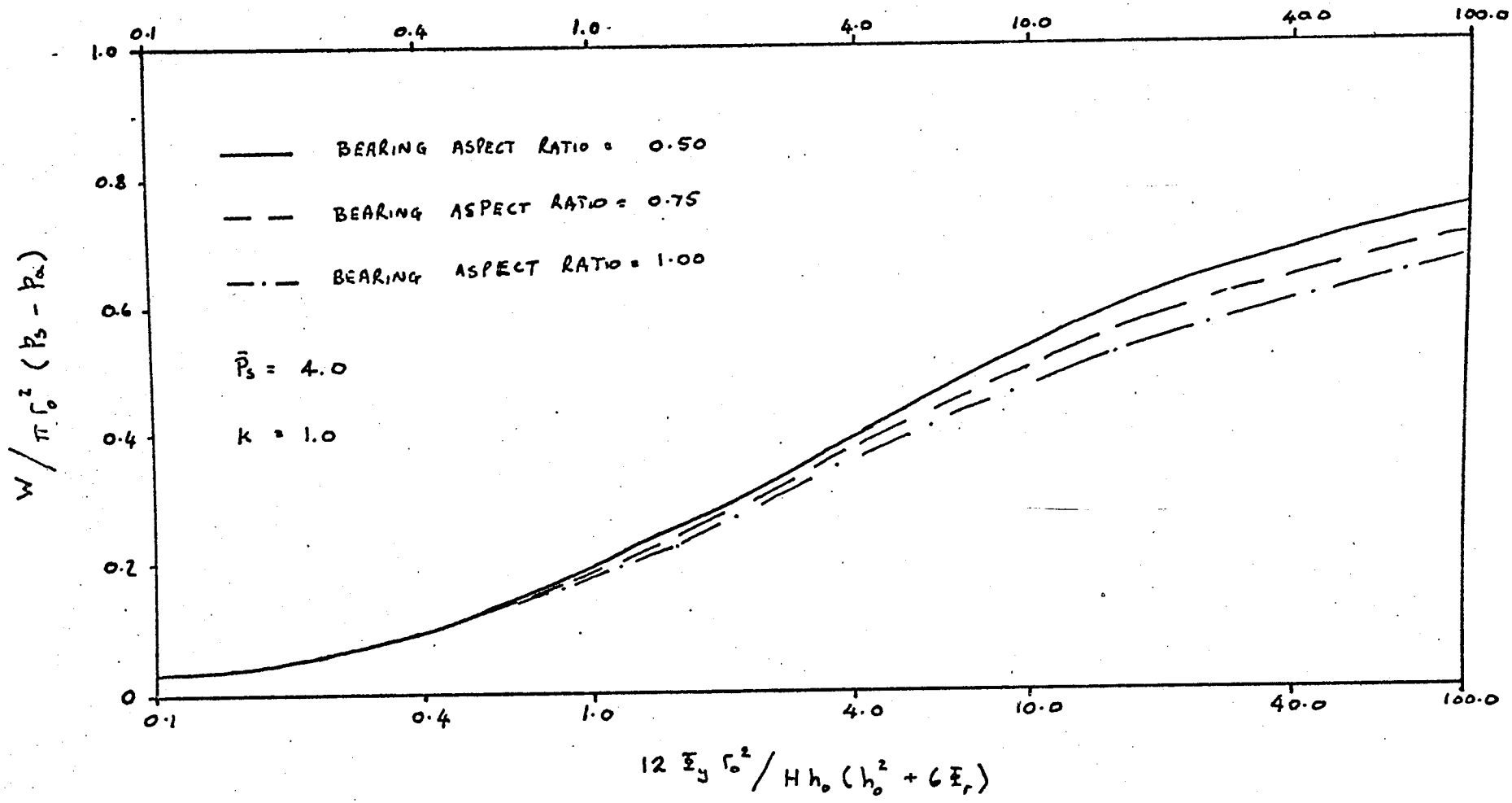

Figure 76 Variation of the Non-Dimensional Bearing Load with Bearing Number, showing the effect of the Bearing Aspect Ratio

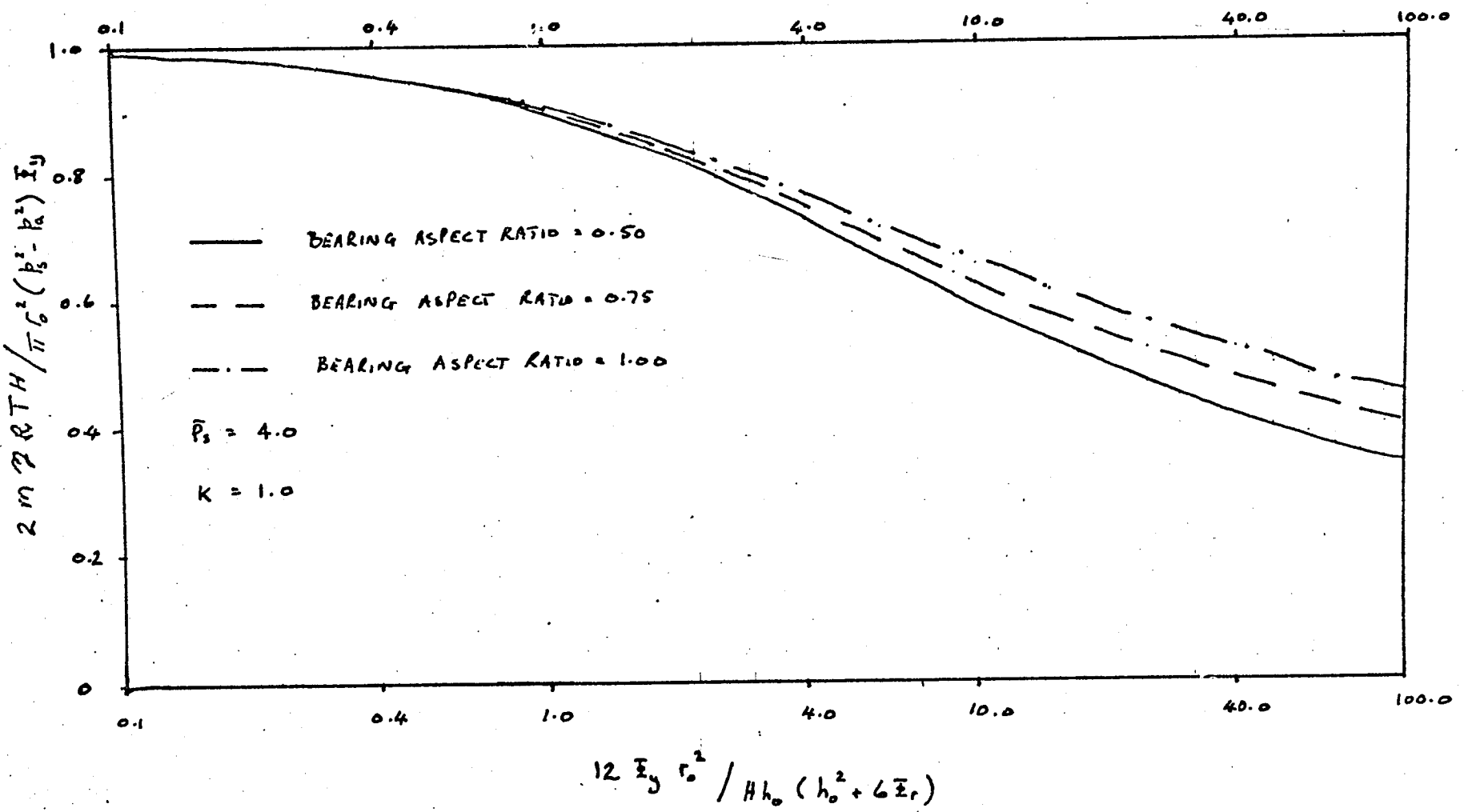

Figure 77 Variation of Non-Dimensional Mass Flow Rate with Bearing Number, showing the effect of the Bearing Aspect Ratio

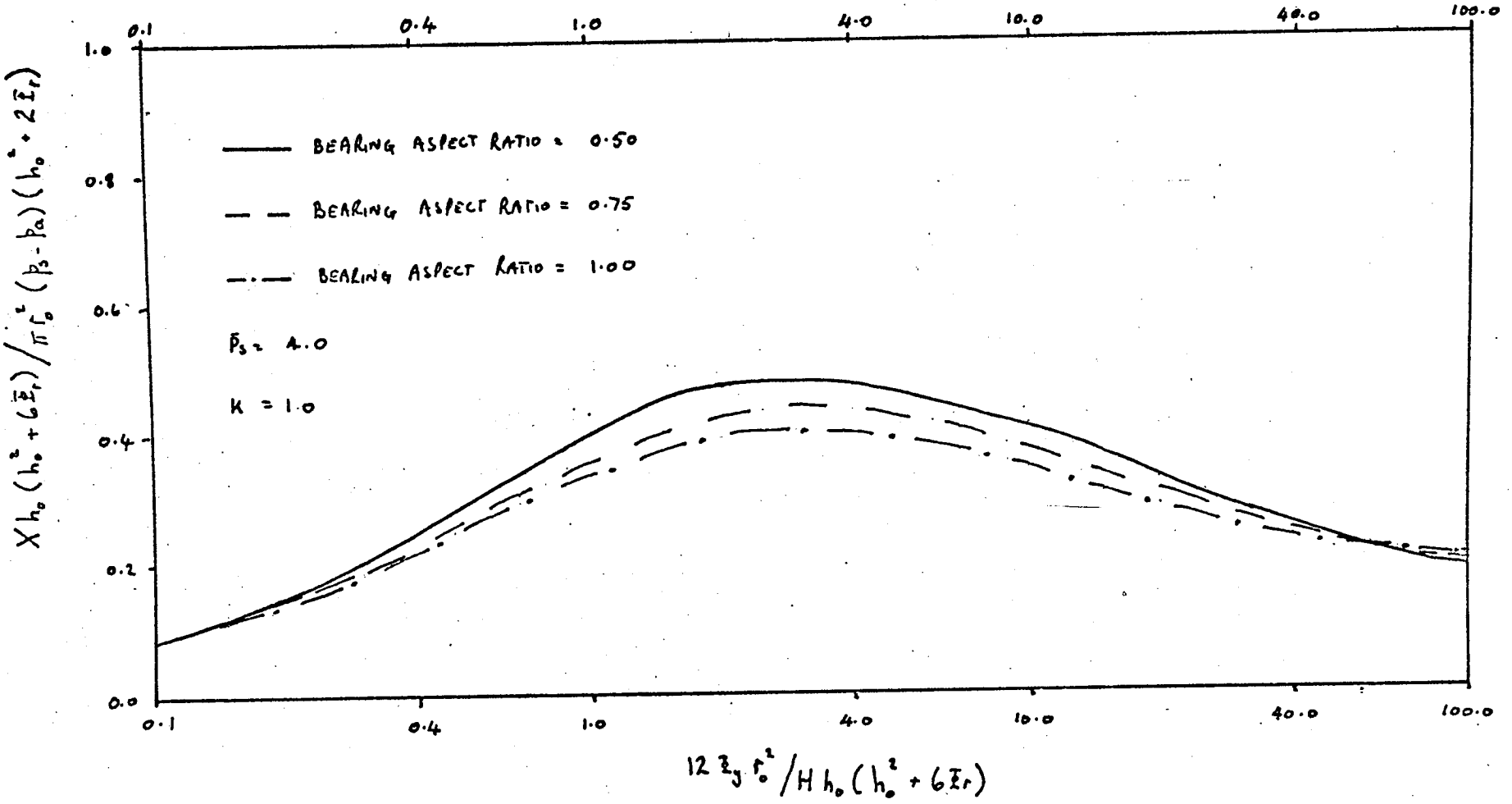

Figure 78 Variation of Non-Dimensional Bearing Static Stiffness with Bearing Number, showing the effect of the Bearing Aspect Ratio

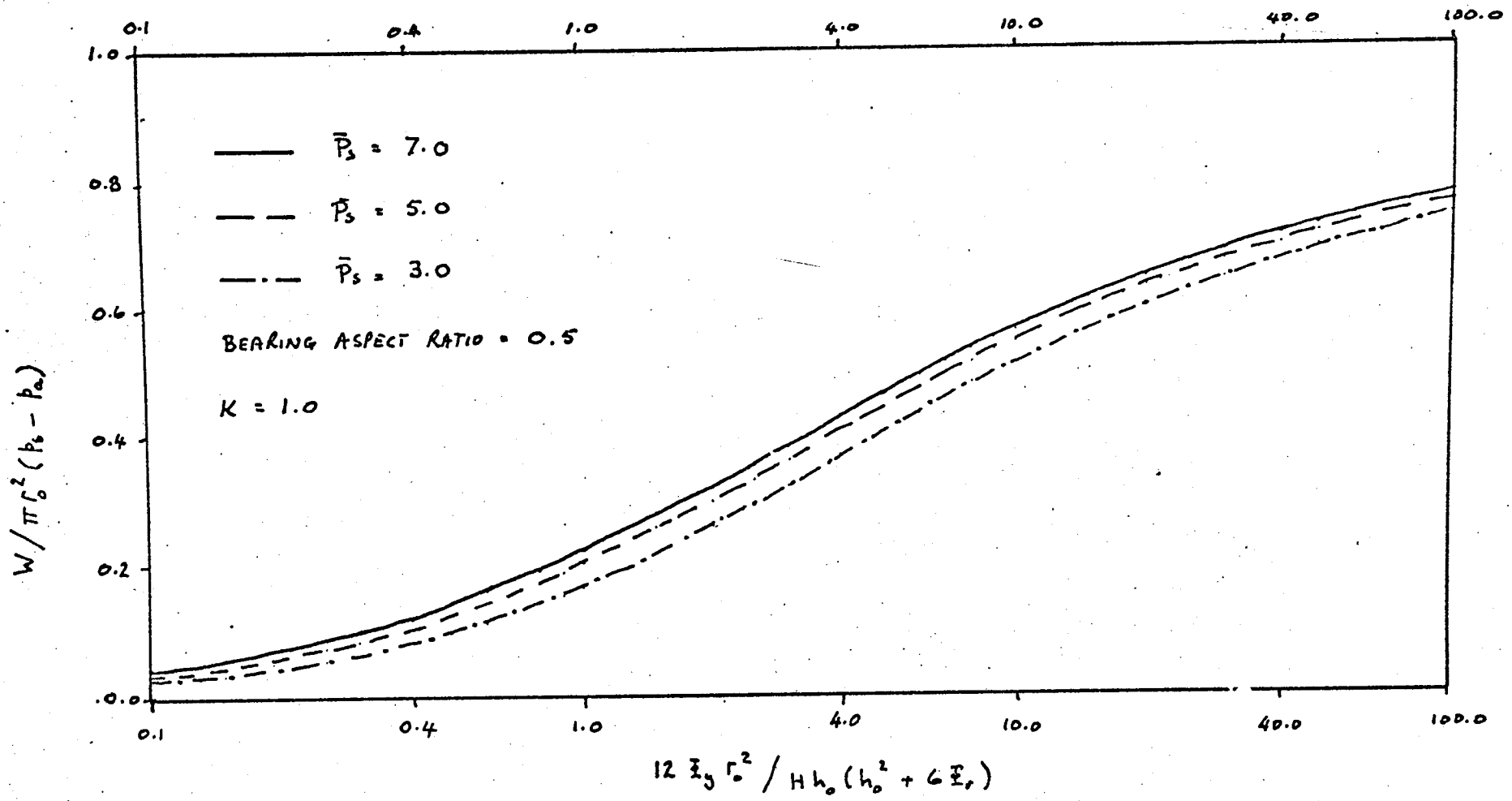

Figure 79 Variation of the Non-Dimensional Bearing Load with Bearing Number, showing the effect of Non-Dimensional Supply Pressure

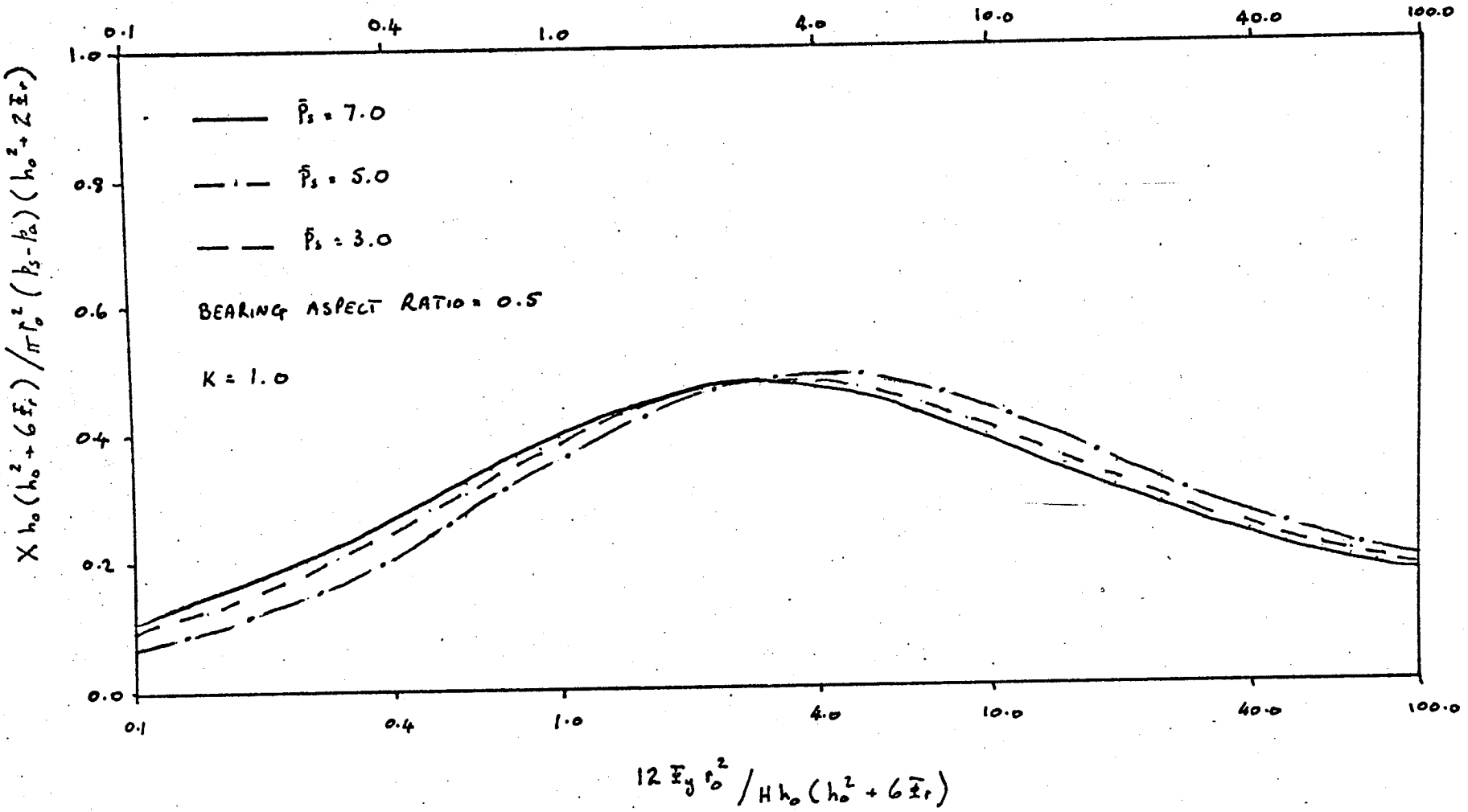

Figure 80 Variation of Non-Dimensional Bearing Static Stiffness with Bearing Number, showing the effect of Non-Dimensional Supply Pressure

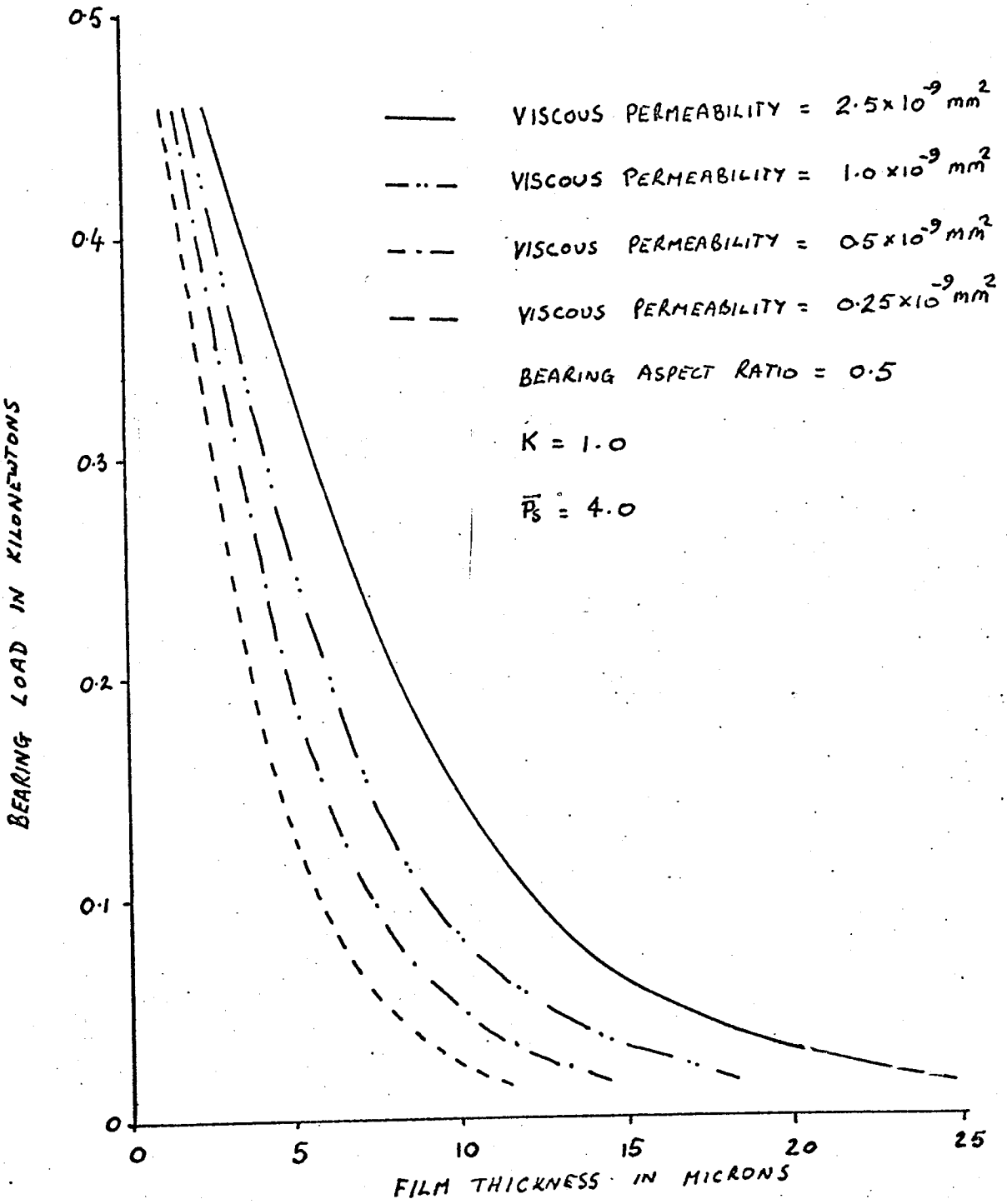

Figure 81 Variation of Bearing Load with Film Thickness for a Full Faced Porous Bearing, showing the effect of the Porous Material Viscous Permeability

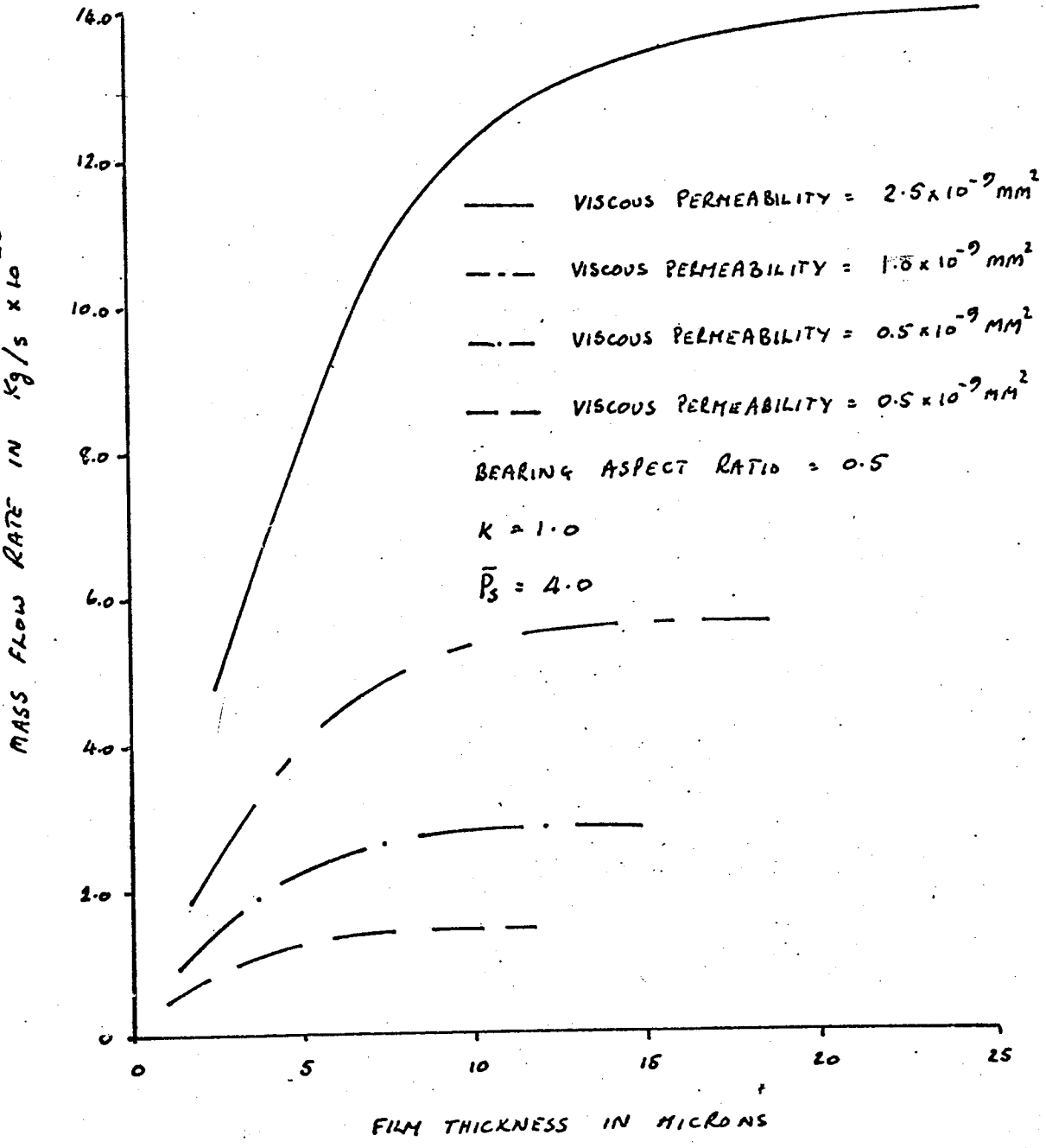

Figure 82 Variation of Mass Flow Rate with Film Thickness for a Full Faced Porous Bearing, showing the effect of the Porous Material Viscous Permeability

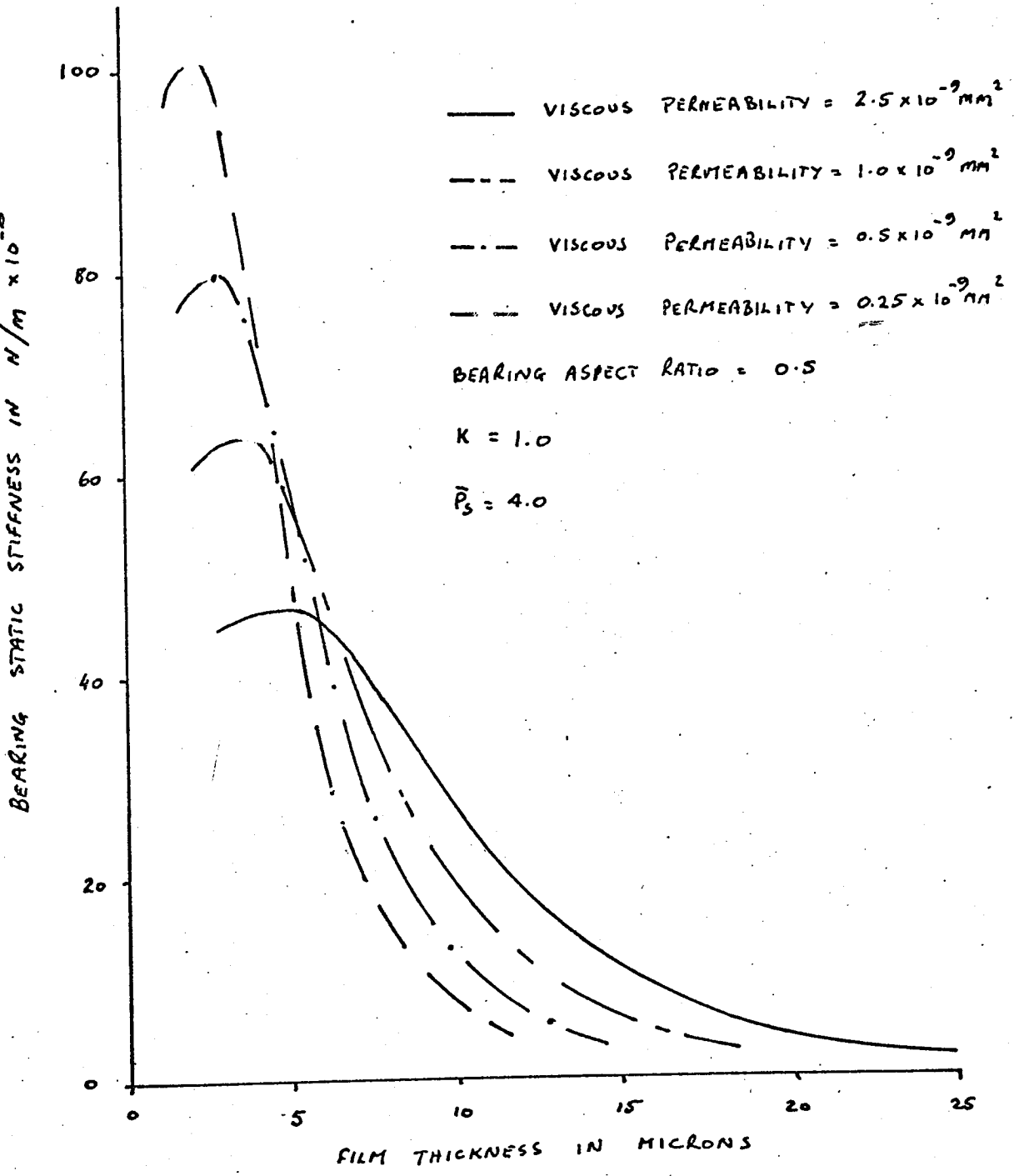

Figure 83 Variation of Bearing Static Stiffness with Film Thickness for a Full Faced Porous Bearing, showing the effect of the Porous Material Viscous Permeability

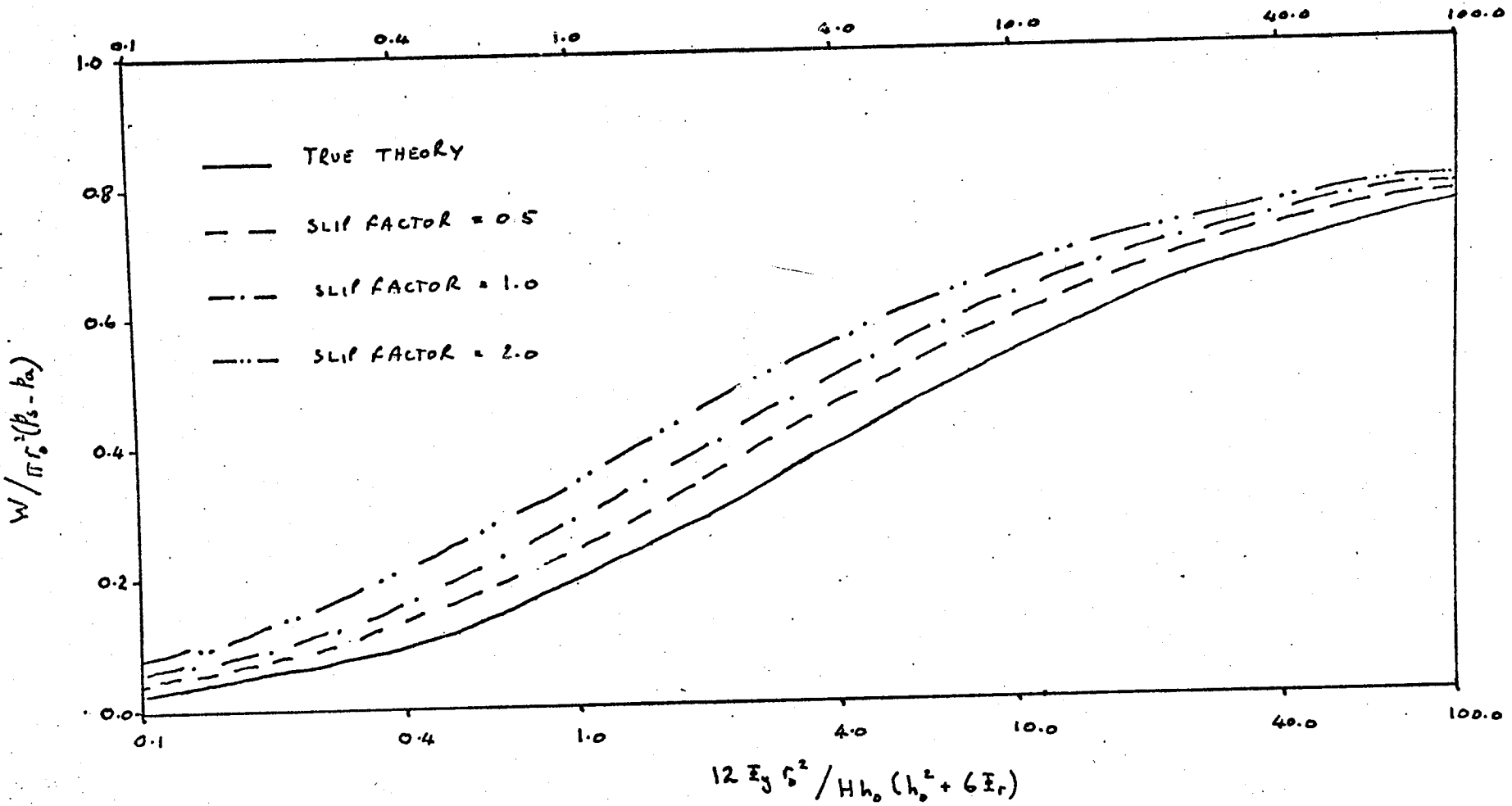

Figure 84 Variation of the Non-Dimensional Bearing Load with Bearing Number, showing the effect of Slip Factor neglection

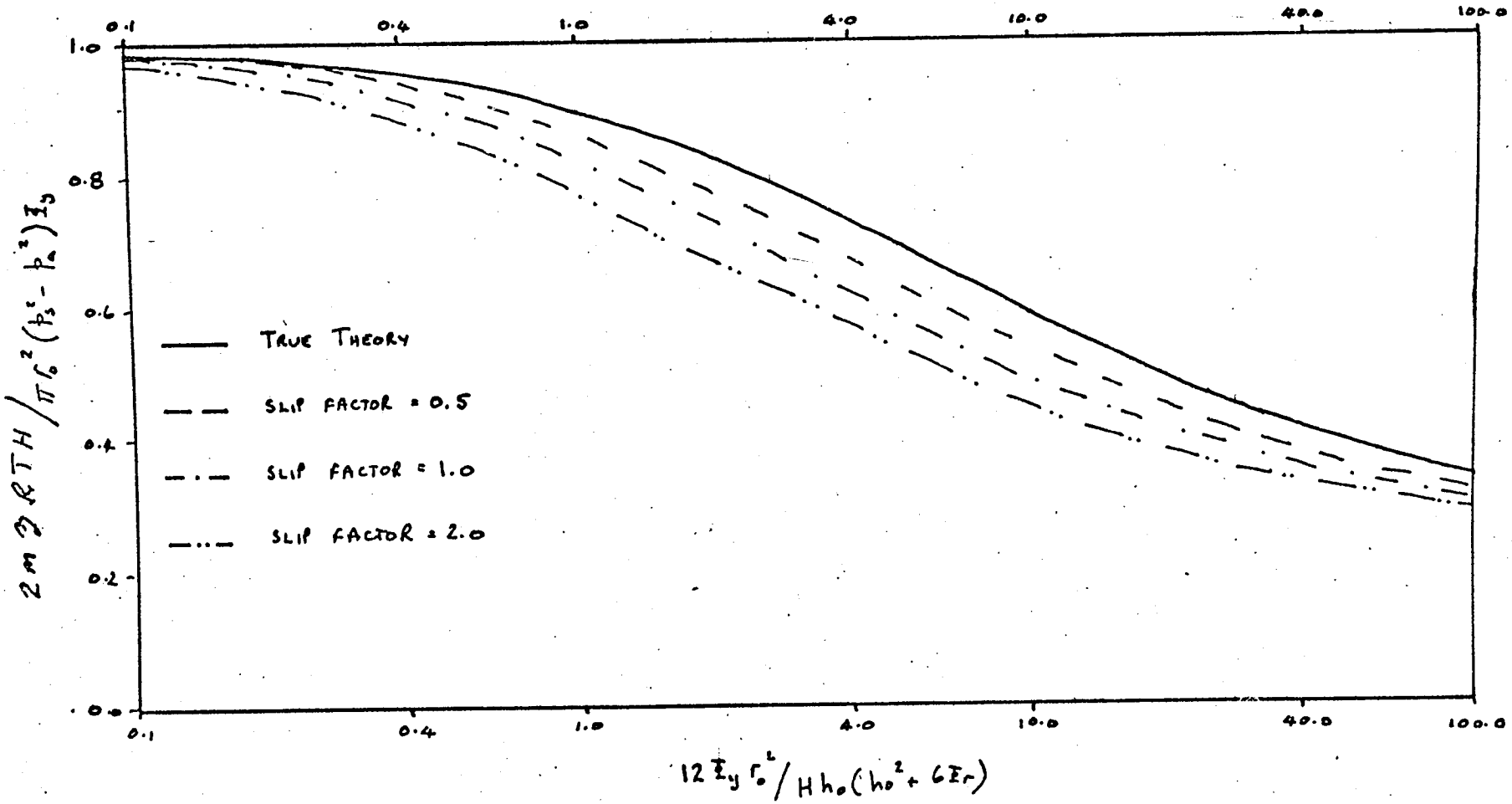

Figure 85 Variation of Non-Dimensional Mass Flow Rate with Bearing Number, showing the effect of Slip Factor Neglection

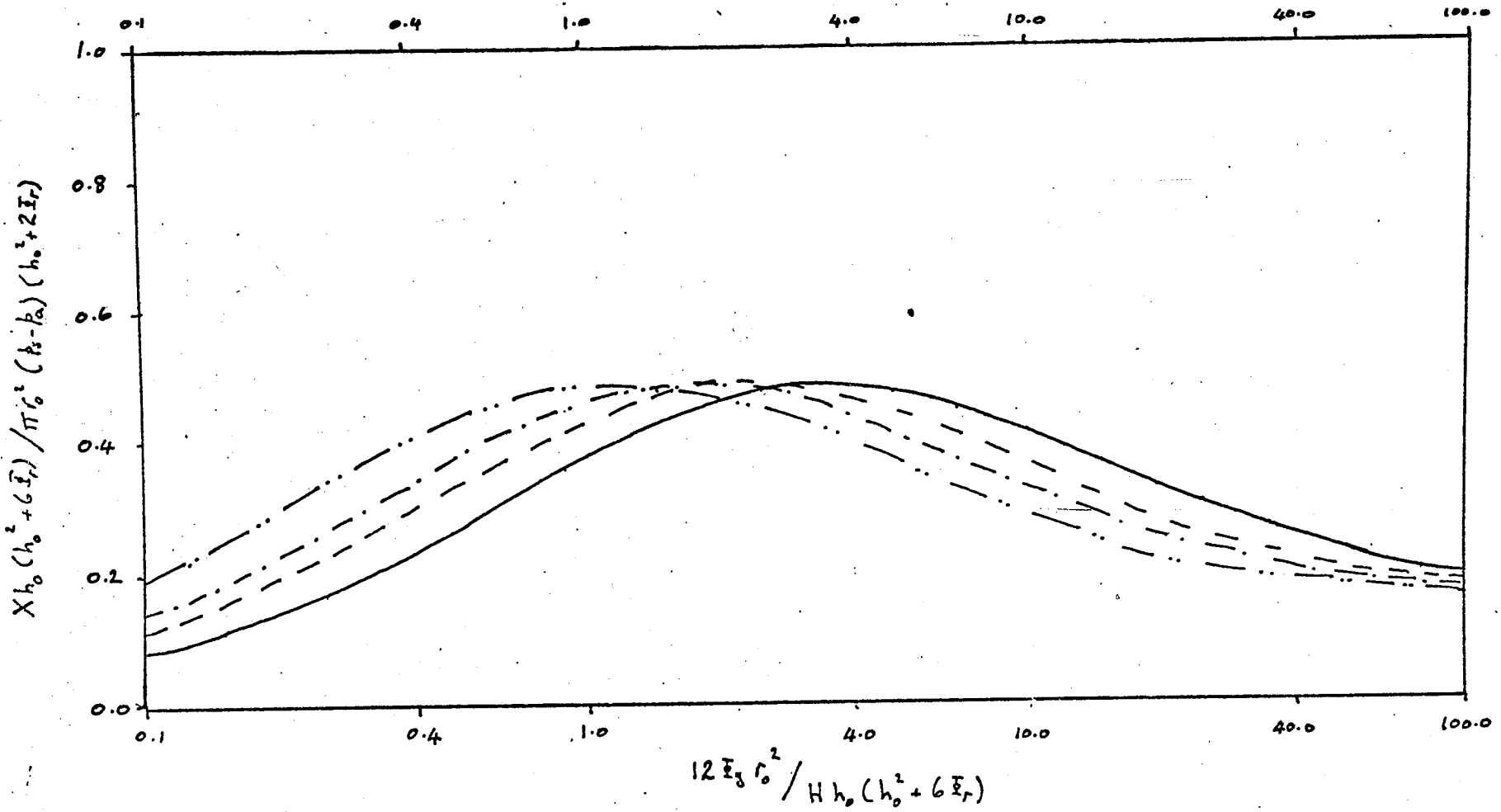

Figure 86 Variation of Non-Dimensional Bearing Static Stiffness with Bearing Number, showing the effect of Slip Factor Neglection

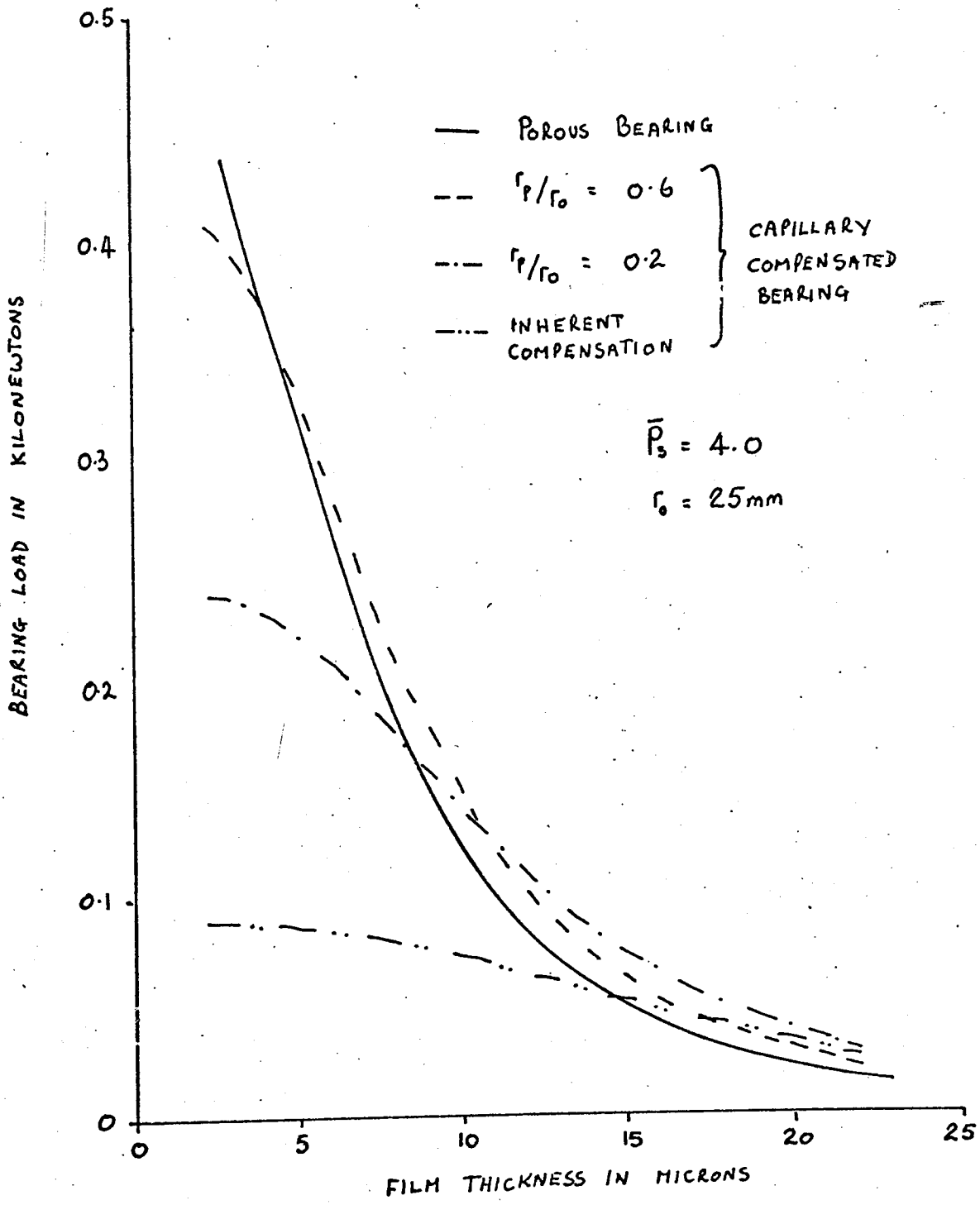

Figure 87 Comparison of the Variation of Bearing Load Capacity with Film Thickness of Capillary Compensated and Porous Thrust Bearings of equal input resistance to flow

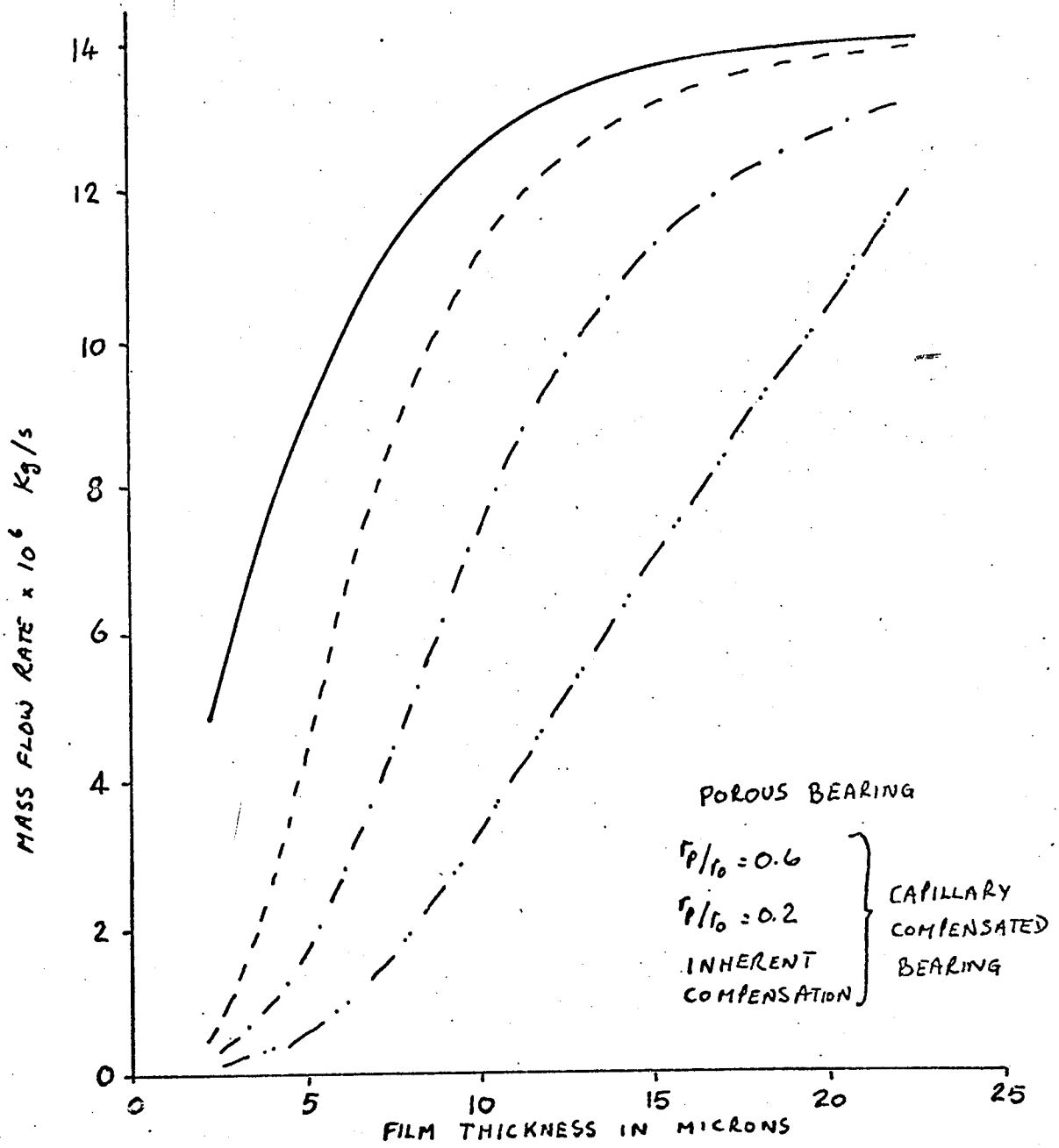

Figure 88 Comparison of the Variation of Mass Flow Rate with Film Thickness of Capillary Compensated and Porous Thrust Bearings of equal input resistance to flow

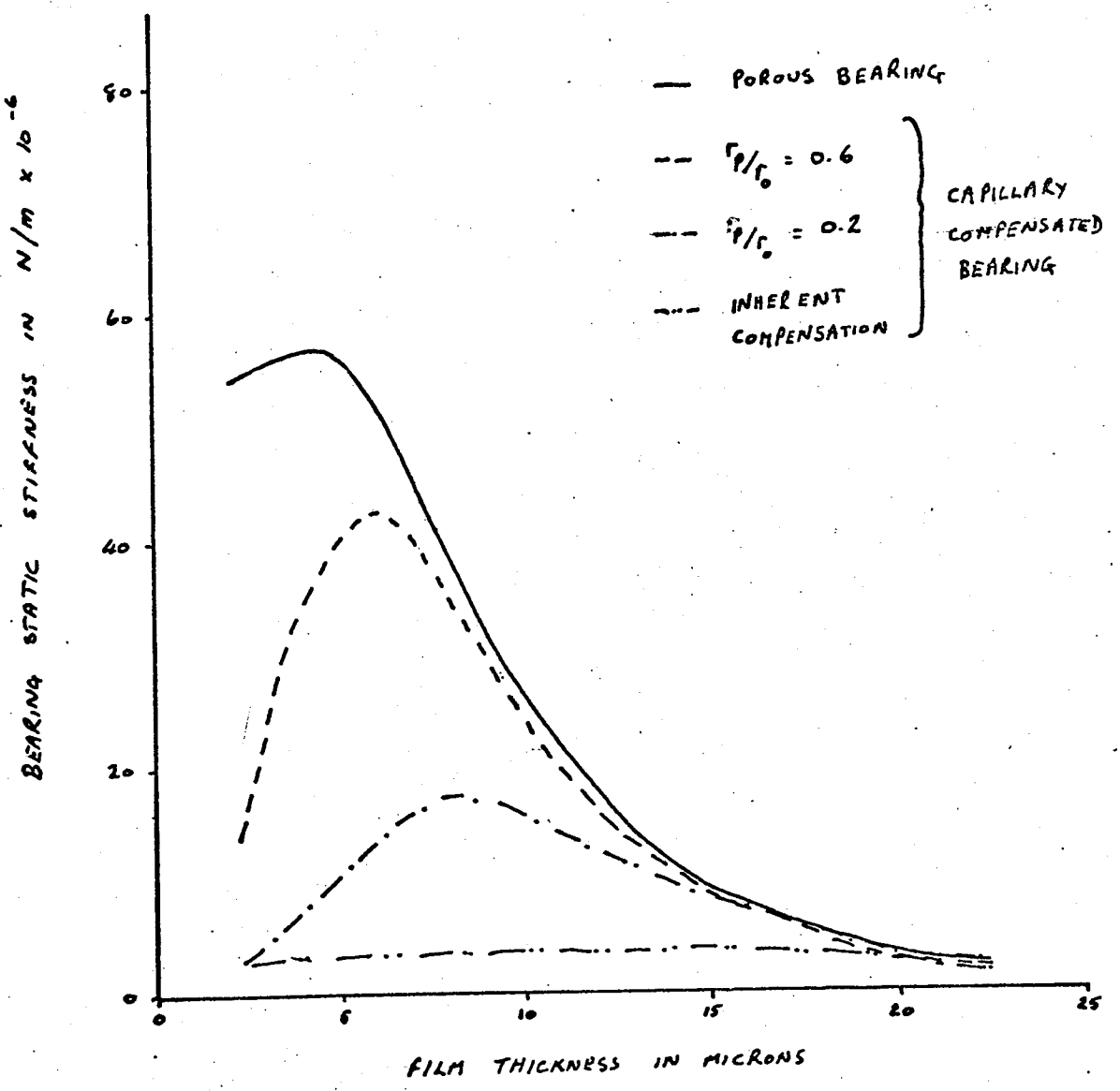

Figure 89 Comparison of the Variation of Bearing Static Stiffness with Film Thickness of Capillary Compensated and Porous Thrust Bearings of equal input resistance to flow

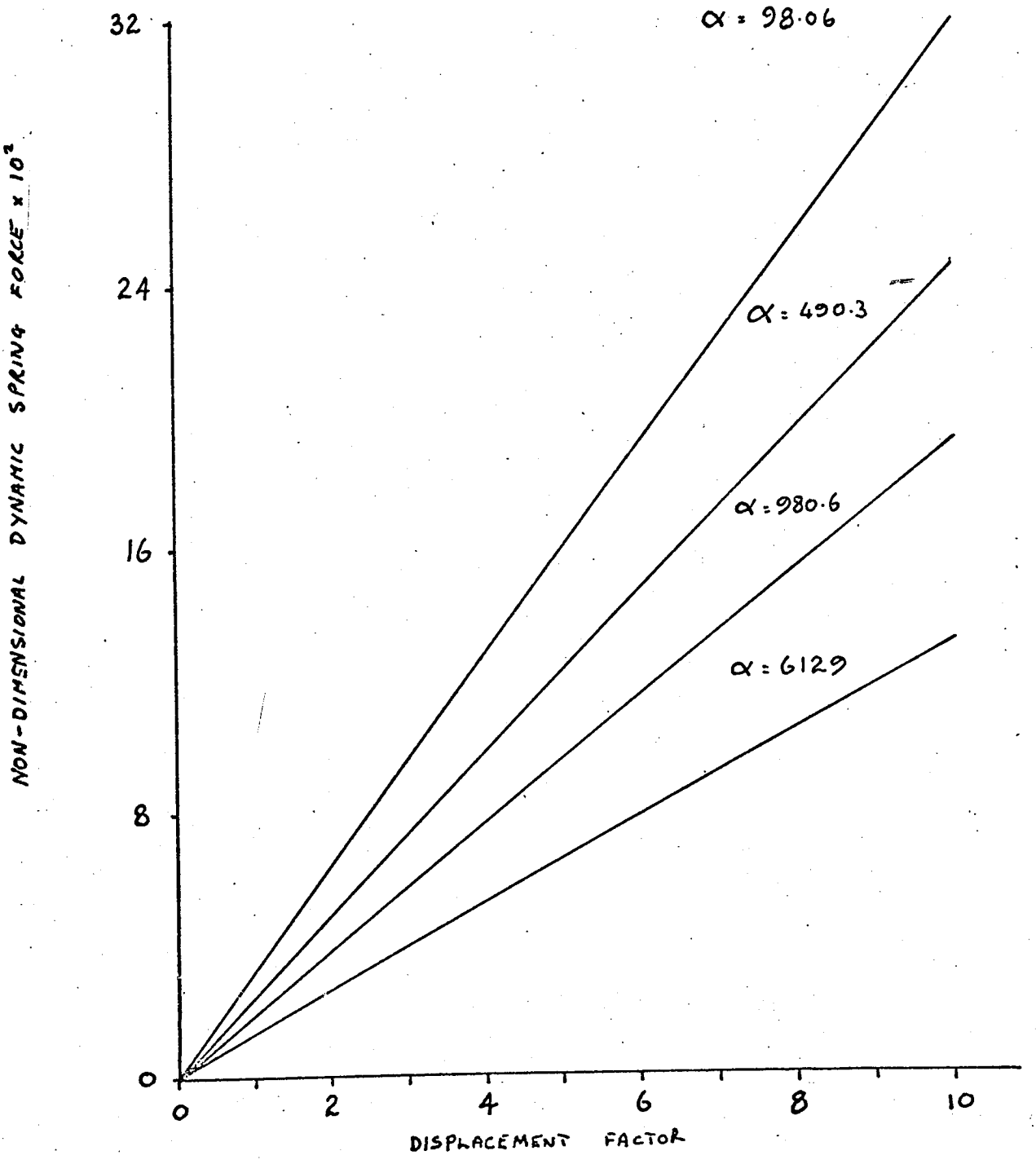

Figure 90 Variation of the Non-Dimensional Dynamic Spring Force with the Displacement Factor showing the effect of the Frequency Factor

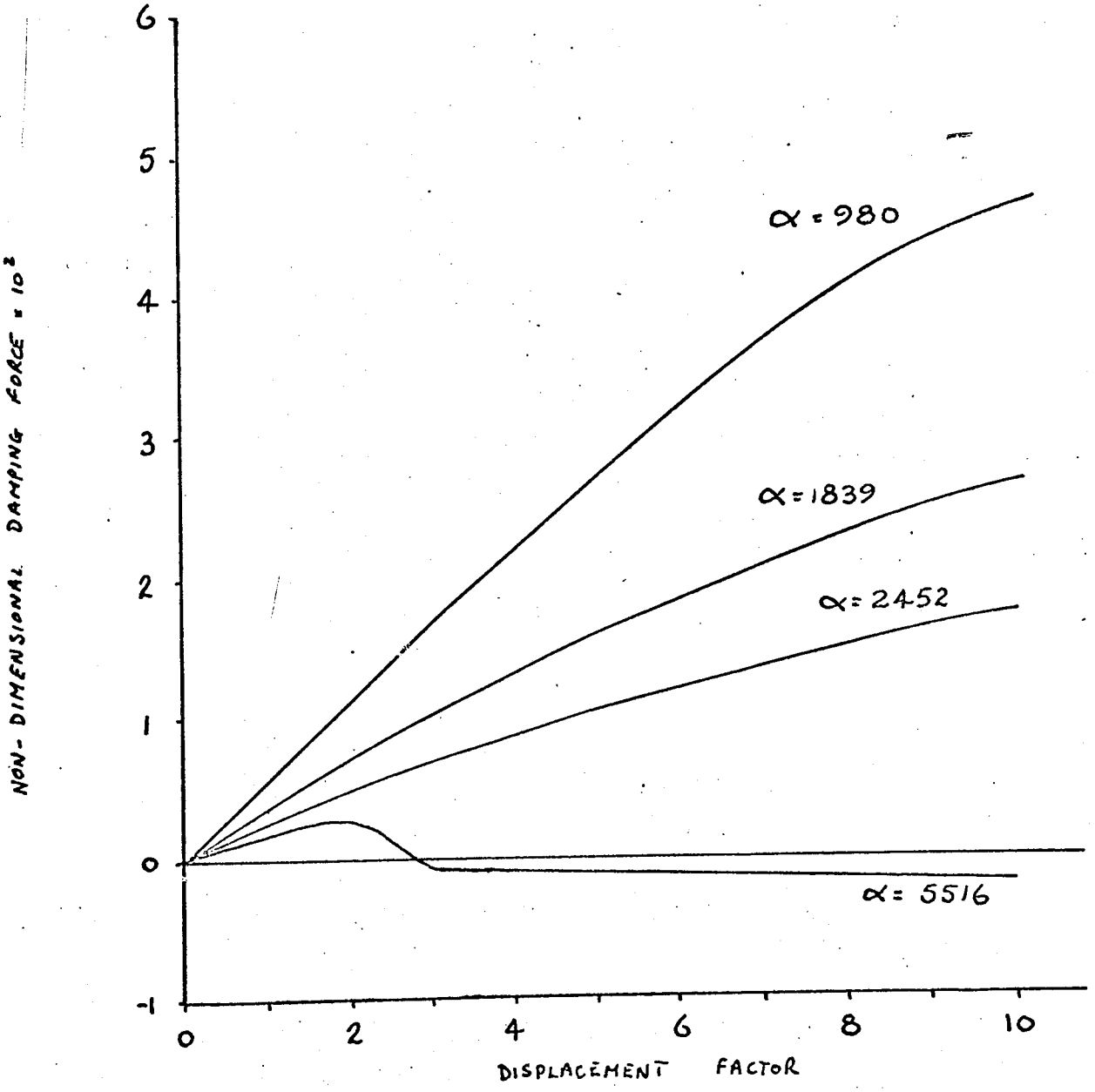

Figure 91 Variation of the Non-Dimensional Dynamic Damping Force with the Displacement Factor showing the effect of the Frequency Factor

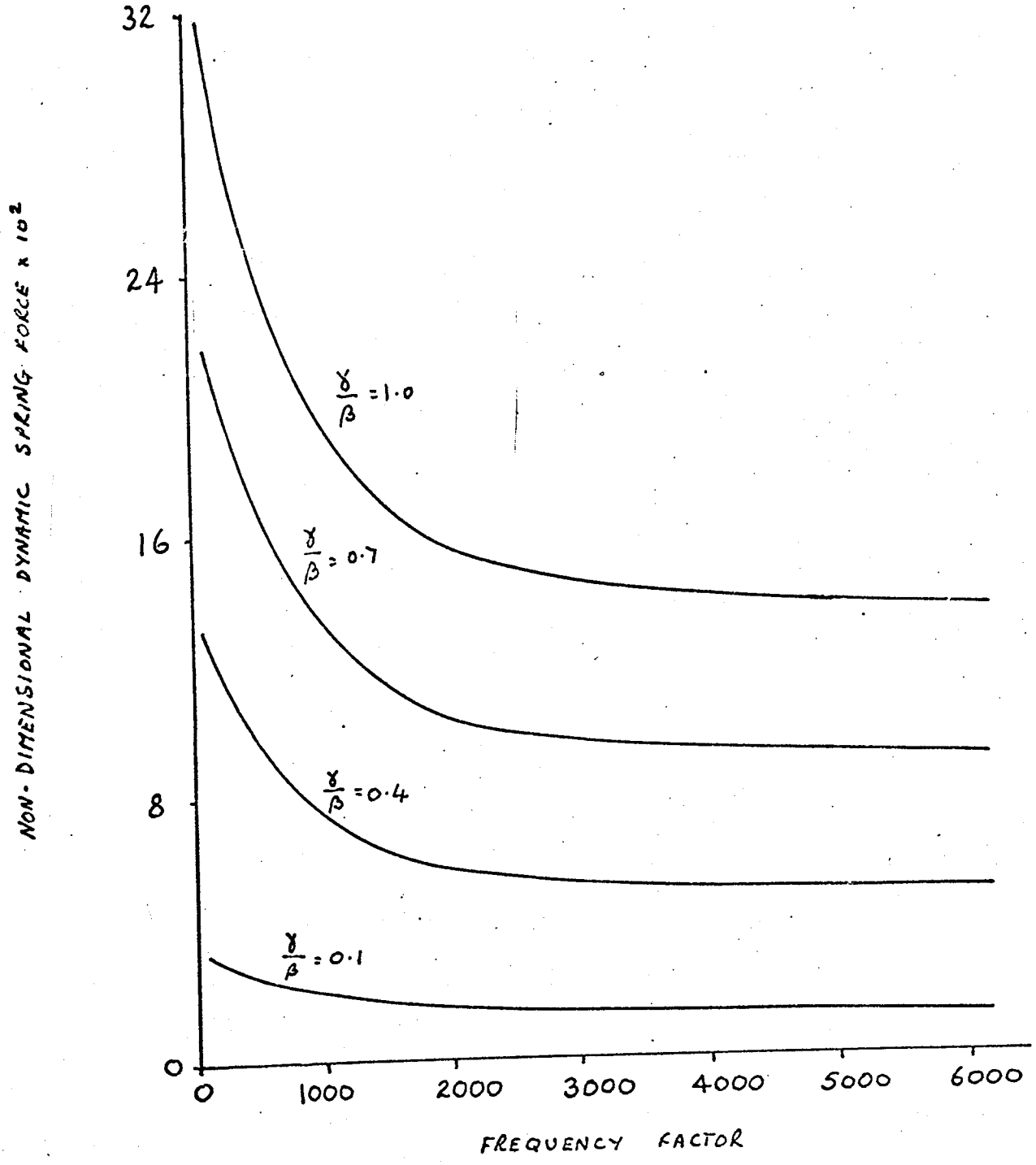

Figure 92 Variation of the Non-Dimensional Dynamic Spring Force with the Frequency Factor showing the effect of the Displacement Factor

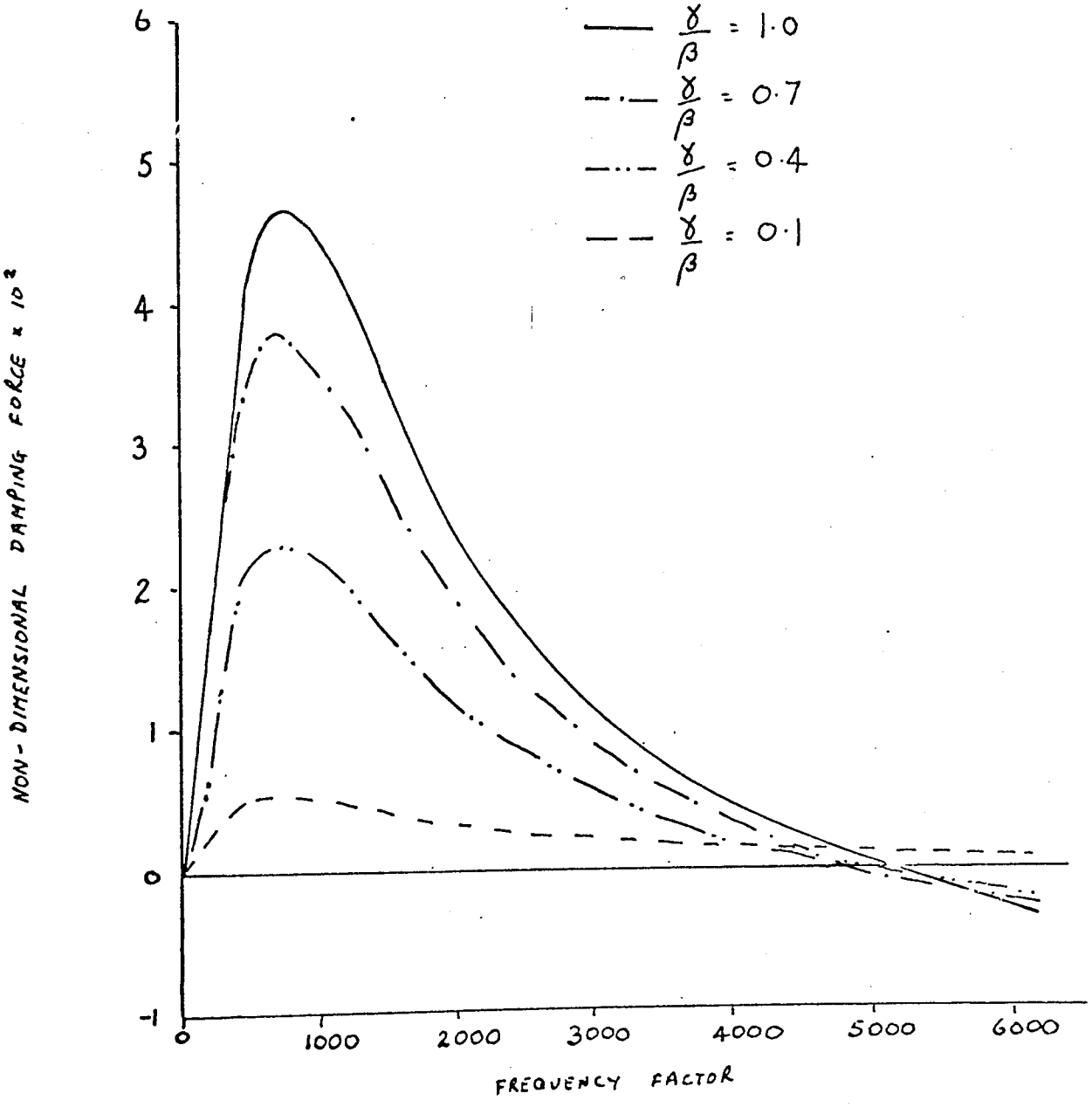

Figure 93 Variation of the Non-Dimensional Damping Force with the Frequency Factor showing the effect of the Displacement Factor

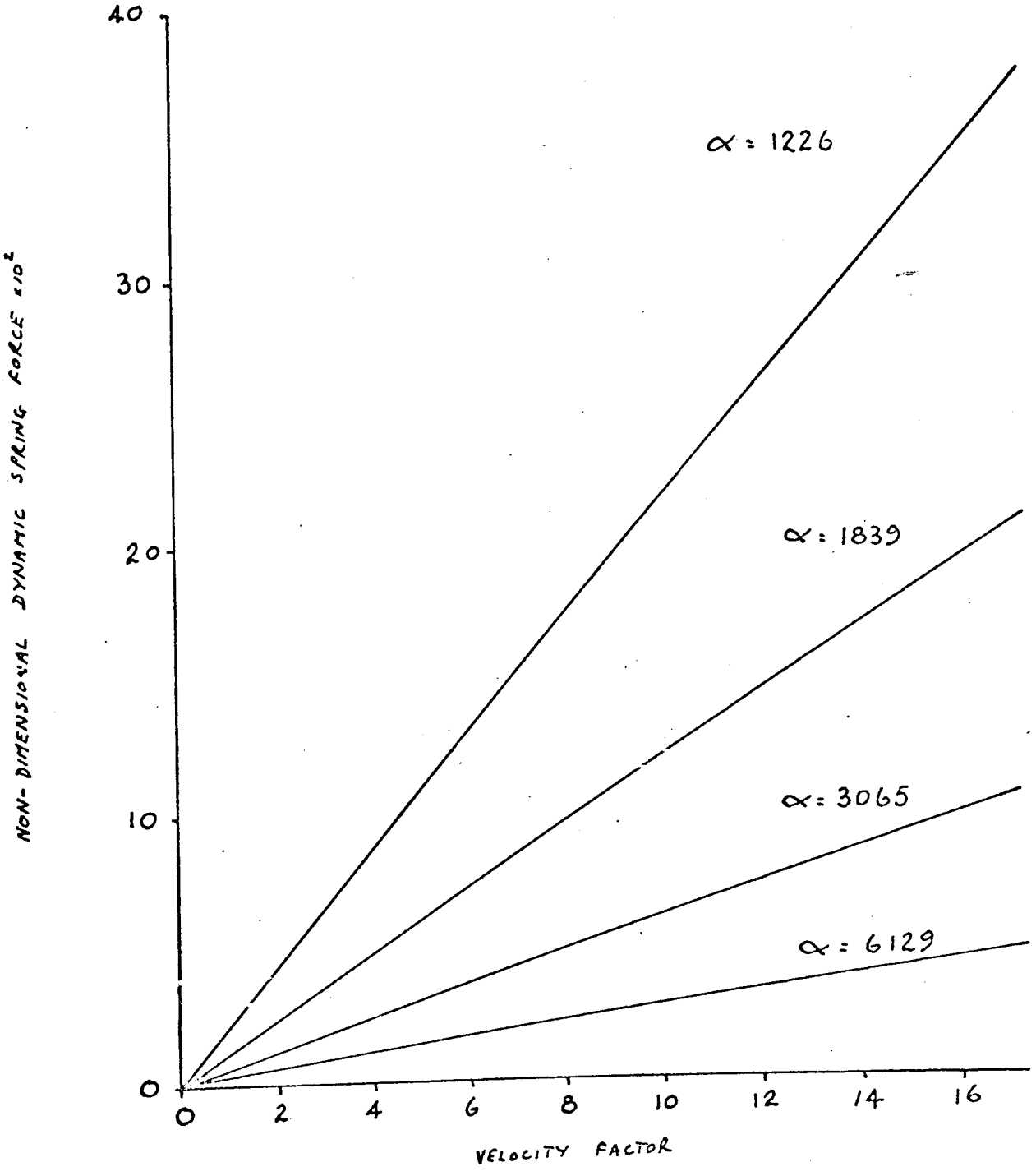

Figure 94 Variation of the Non-Dimensional Dynamic Spring Force with the Velocity Factor showing the effect of the Frequency Factor

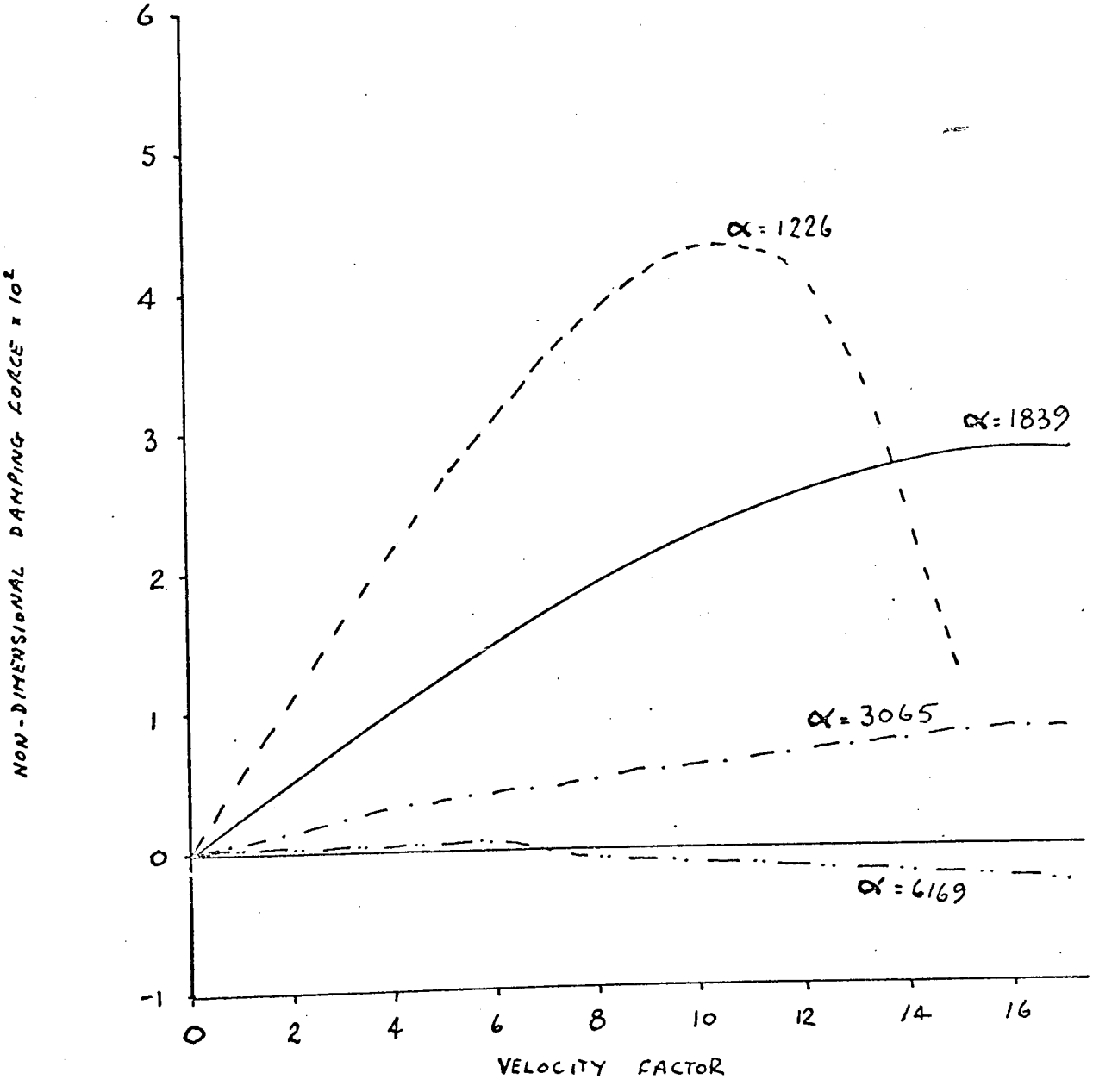

Figure 95 Variation of the Non-Dimensional Damping Force with the Velocity Factor showing the effect of the Frequency Factor

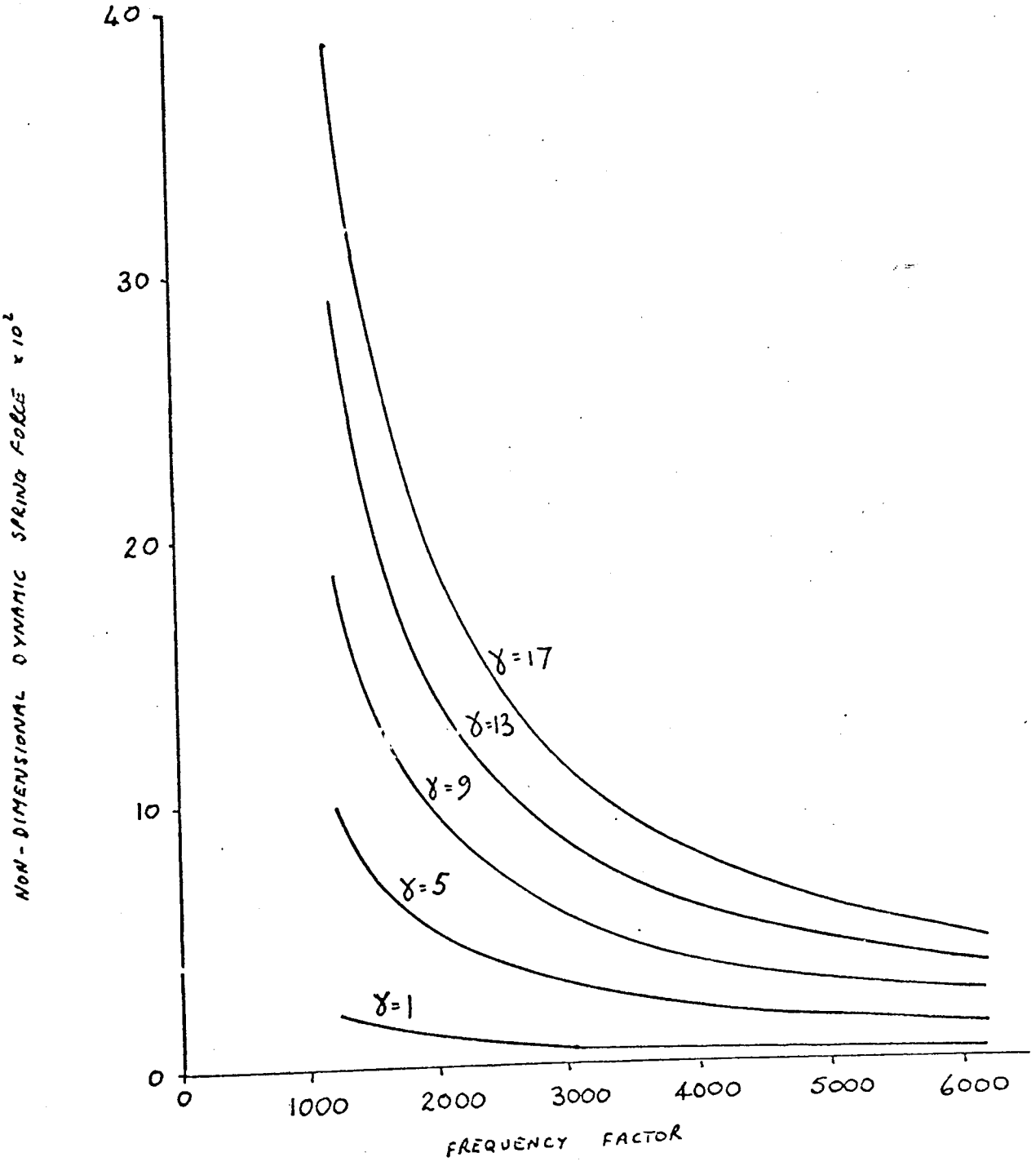

Figure 96 Variation of the Non-Dimensional Dynamic Spring Force with the Frequency Factor showing the effect of the Velocity Factor

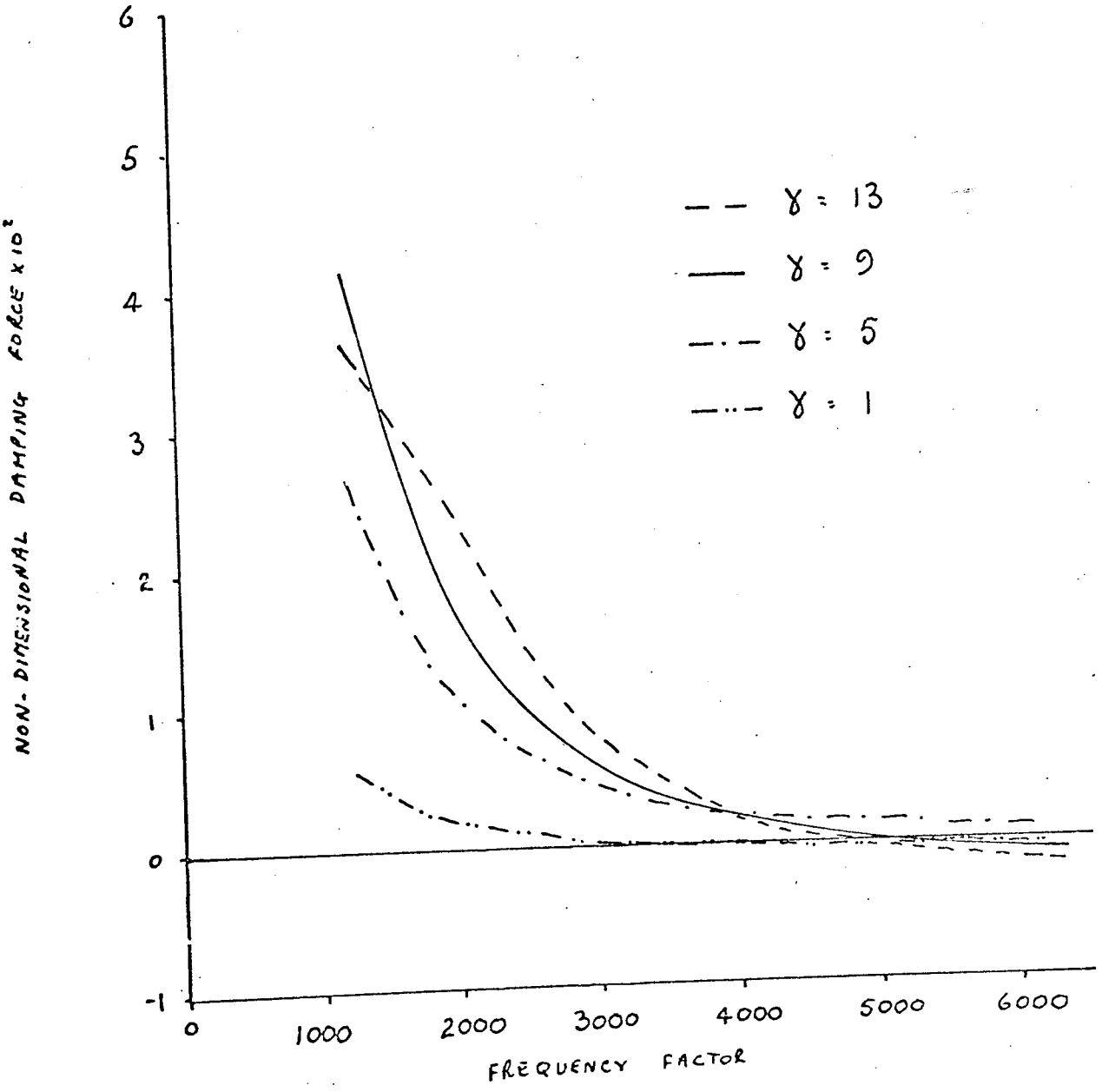

Figure 97 Variation of the Non-Dimensional Damping Force with the Frequency Factor showing the effect of the Velocity Factor

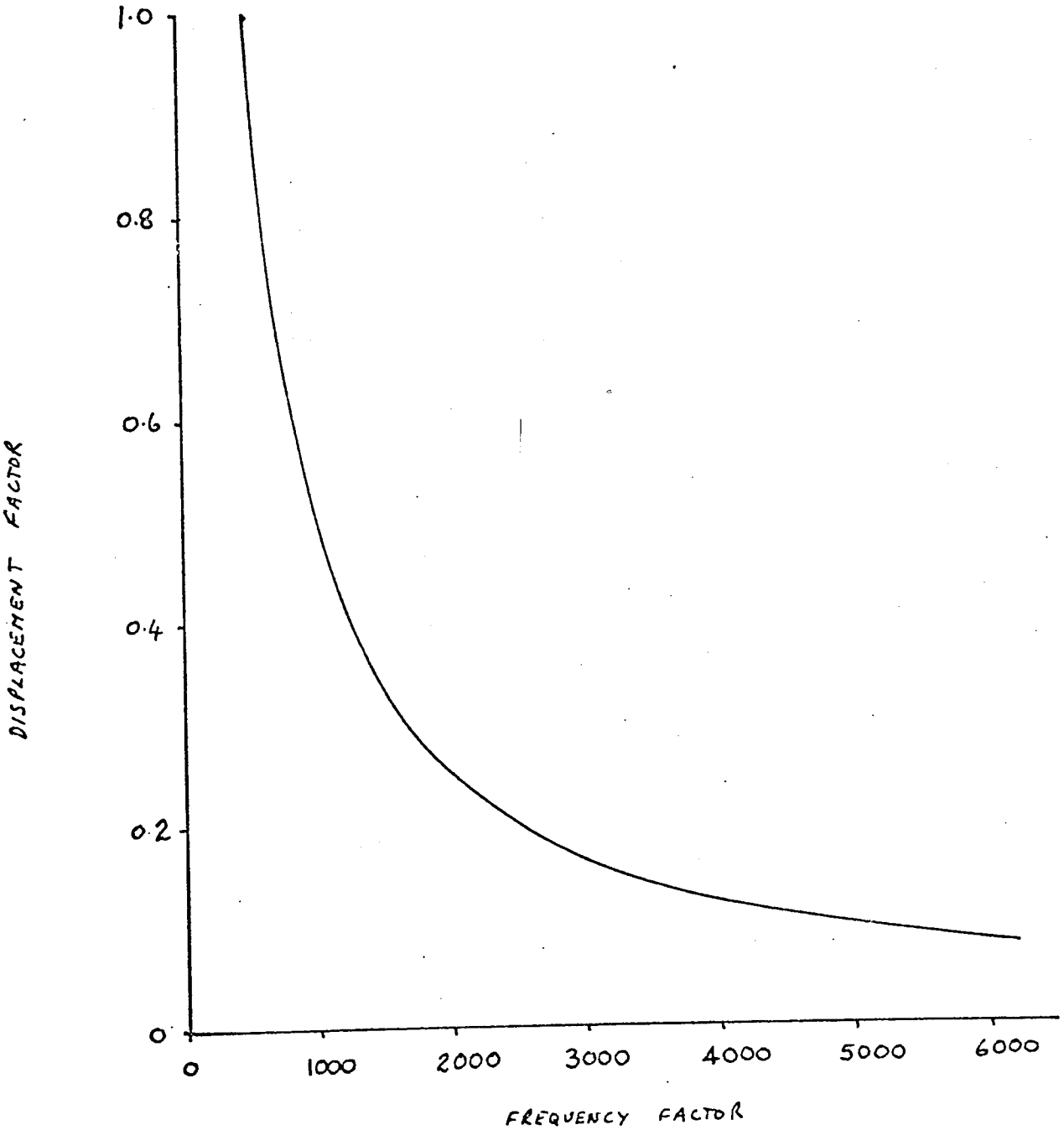

Figure 98 Variation of the Displacement Factor with the Frequency Factor for a given Velocity Factor

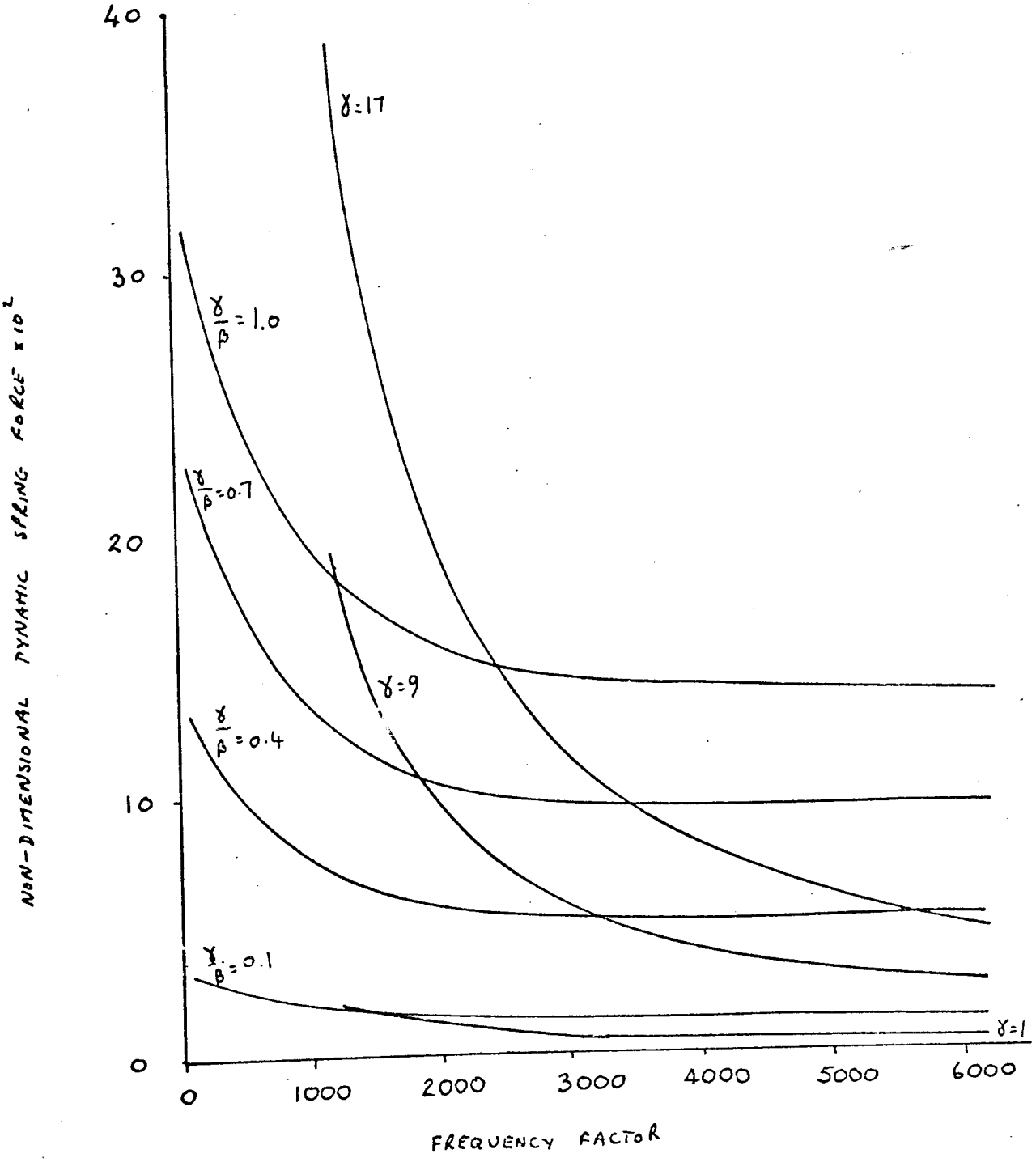

Figure 99 Variation of the Non-Dimensional Dynamic Spring Force with the Frequency Factor showing the effect of both the Displacement and the Velocity Factors

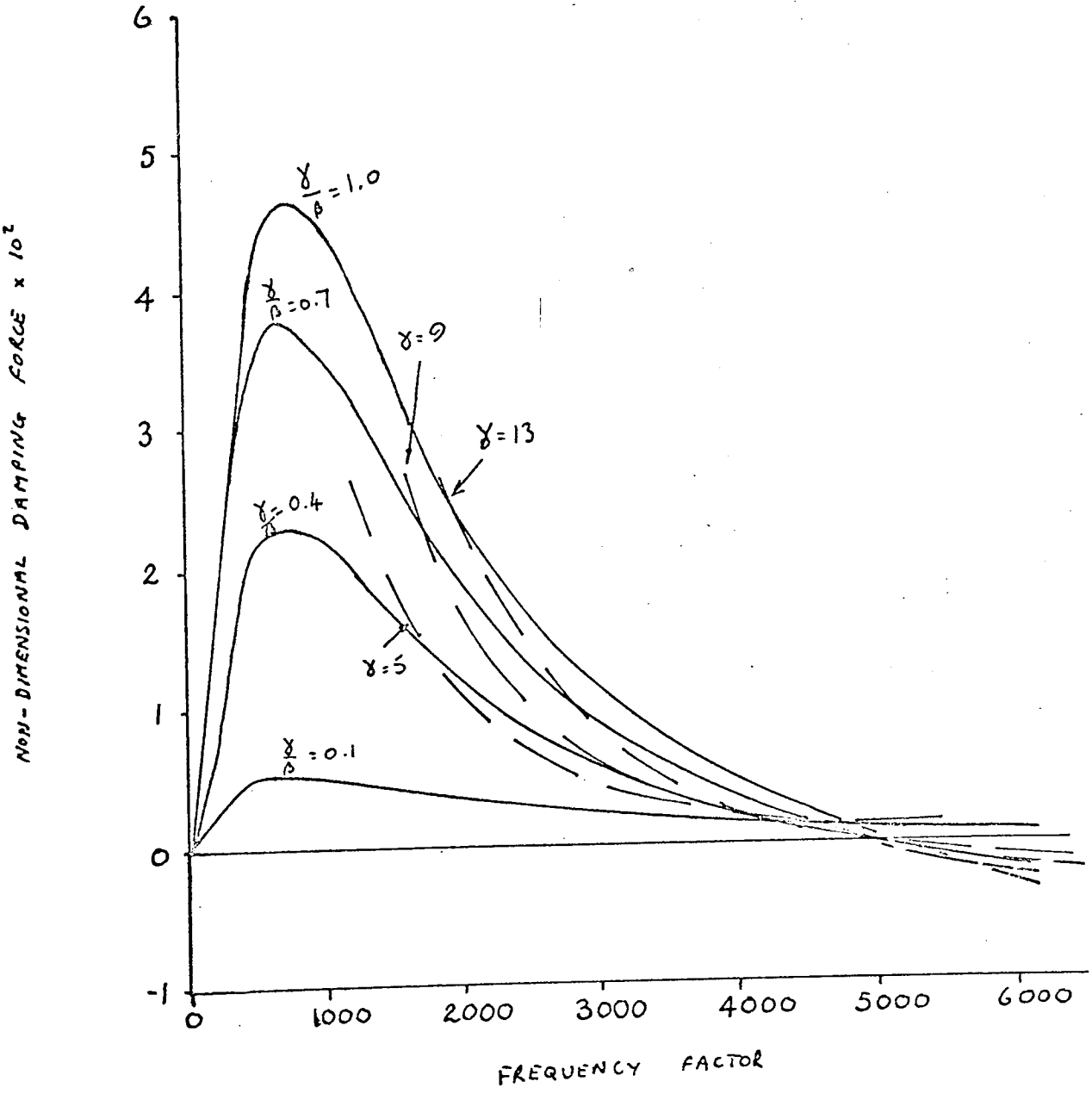

Figure 100 Variation of the Non-Dimensional Damping Force with Frequency Factor showing the effect of both the Displacement and Velocity Factors

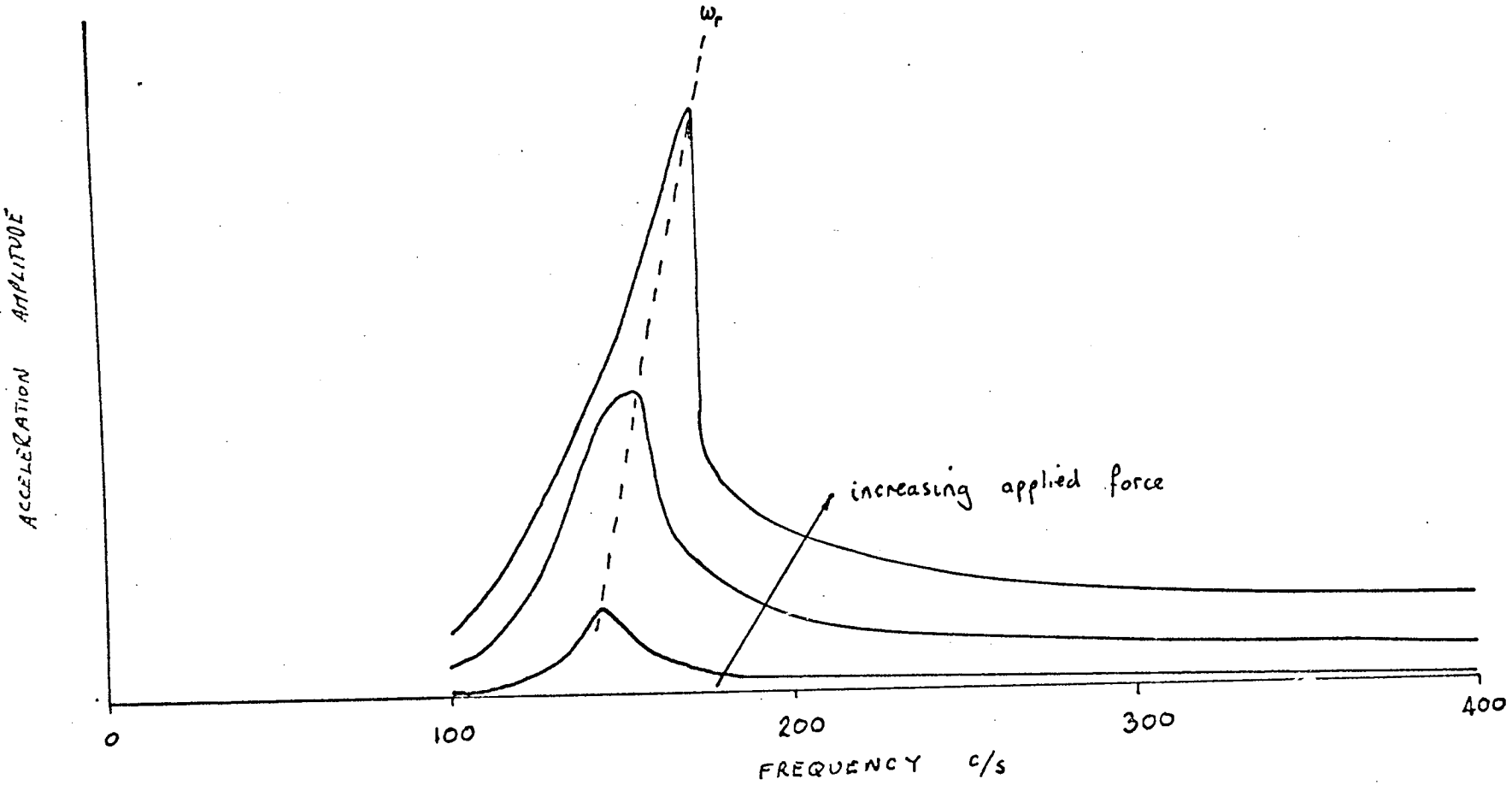

Figure 101 Resonance Curves for a Porous Thrust Bearing showing the effect of the Applied Force

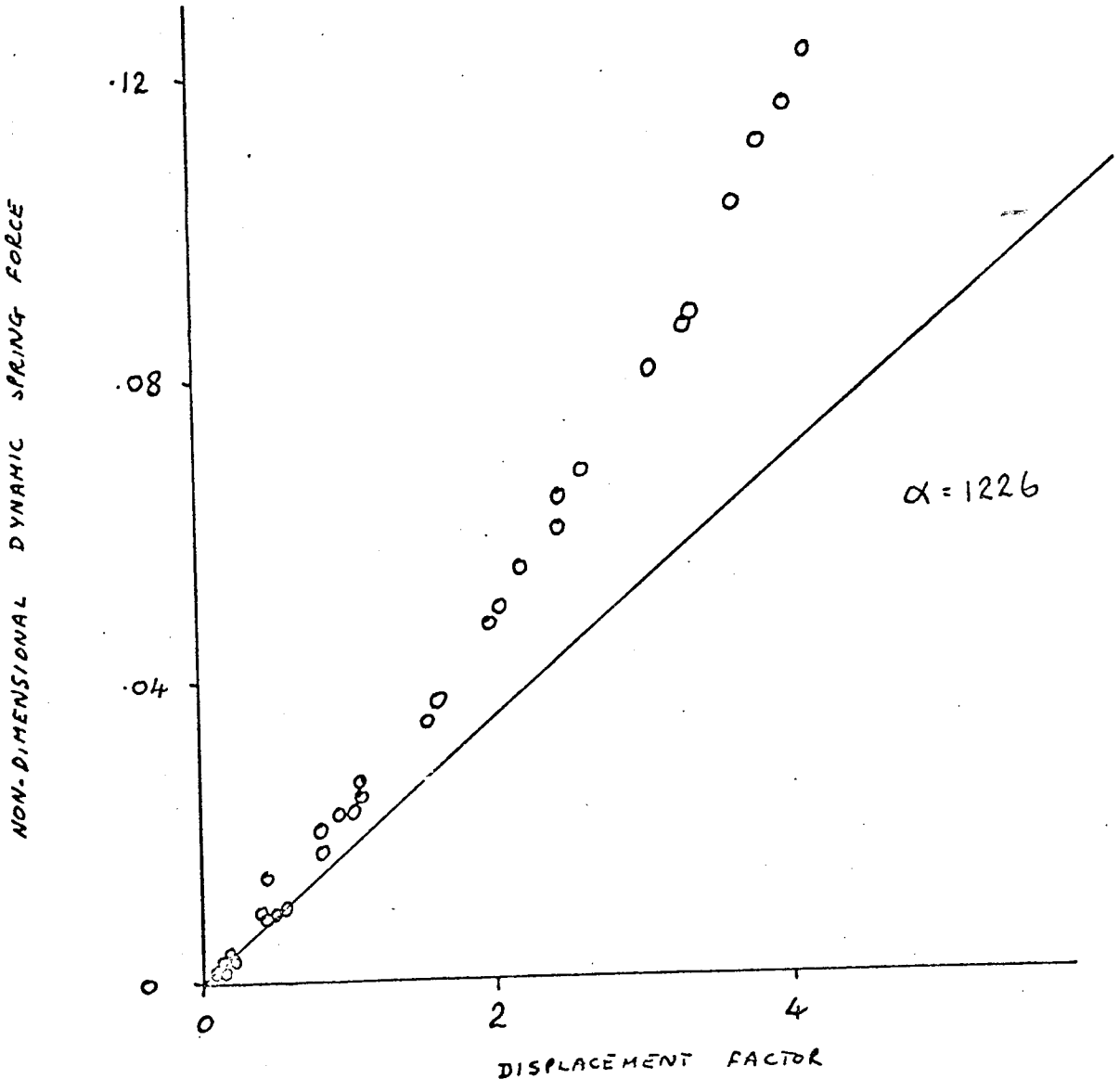

Figure 102 Comparison of the Experimentally determined and Theoretically predicted variation of the Non-Dimensional Dynamic Stiffness Force with the Displacement Factor

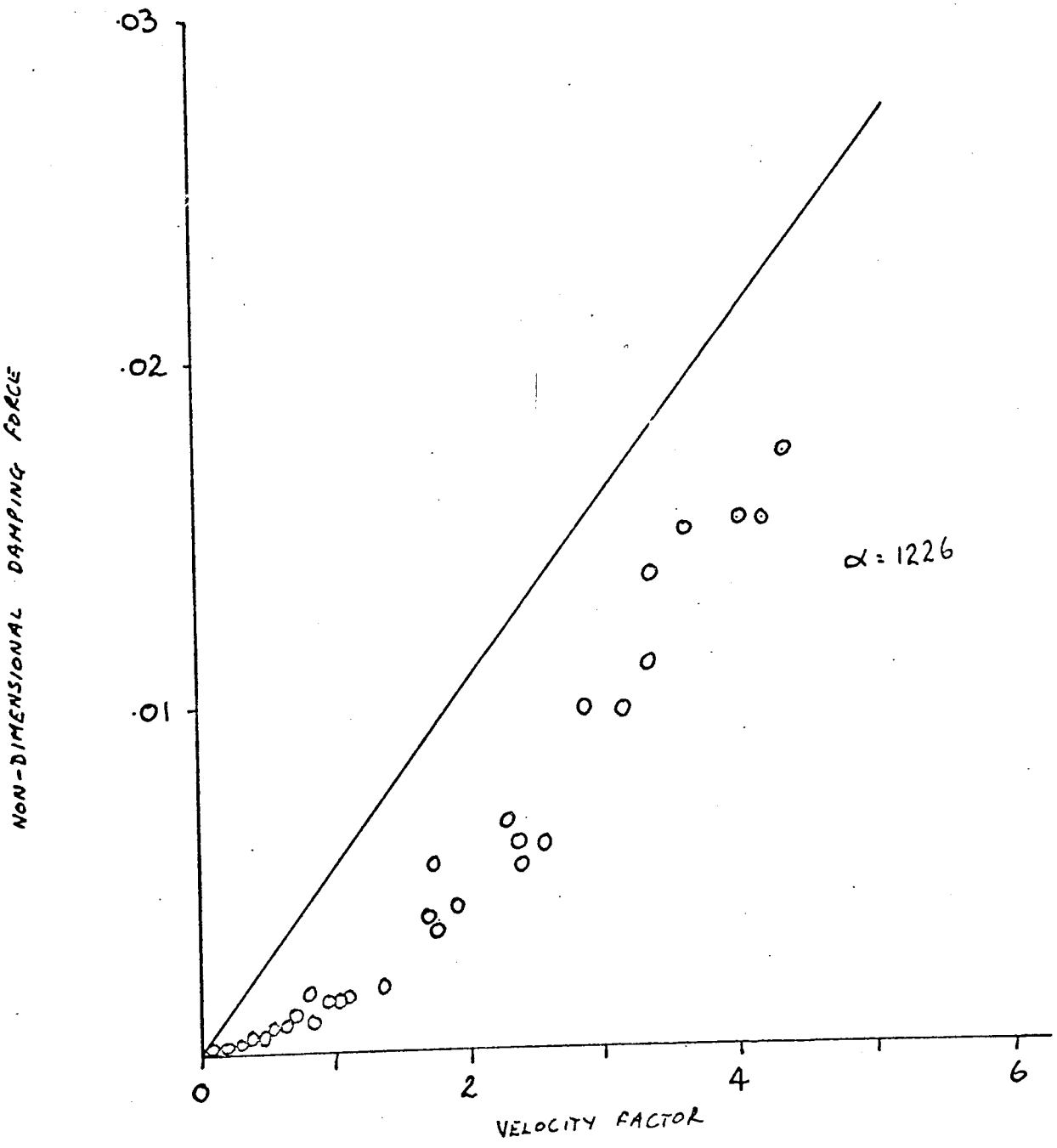

Figure 103 Comparison of the Experimentally determined and Theoretically predicted variation of the Non-Dimensional Damping Force with the Velocity Factor

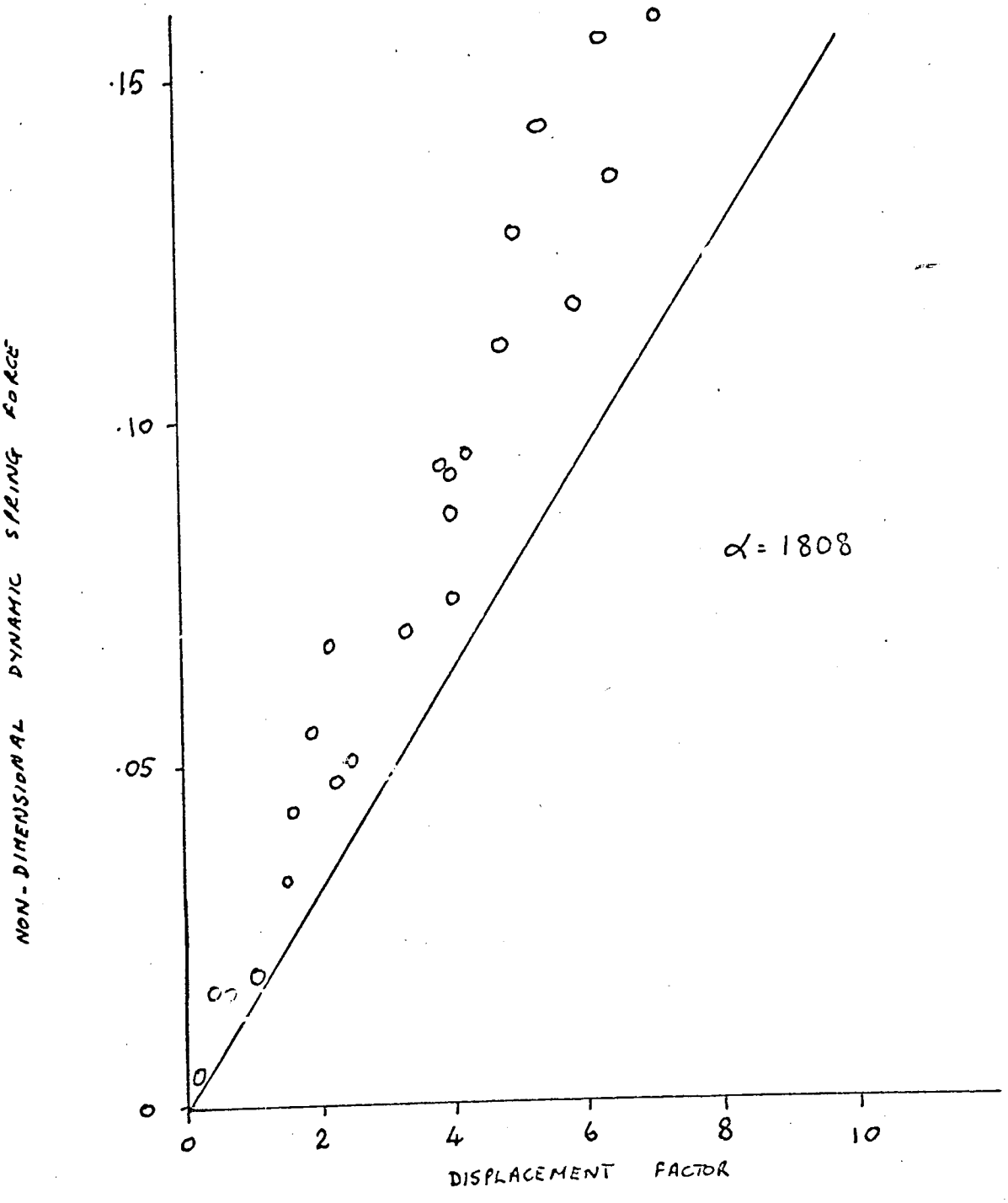

Figure 104 Comparison of the Experimentally determined and Theoretically predicted variation of the Non-Dimensional Stiffness Force with the Displacement Factor

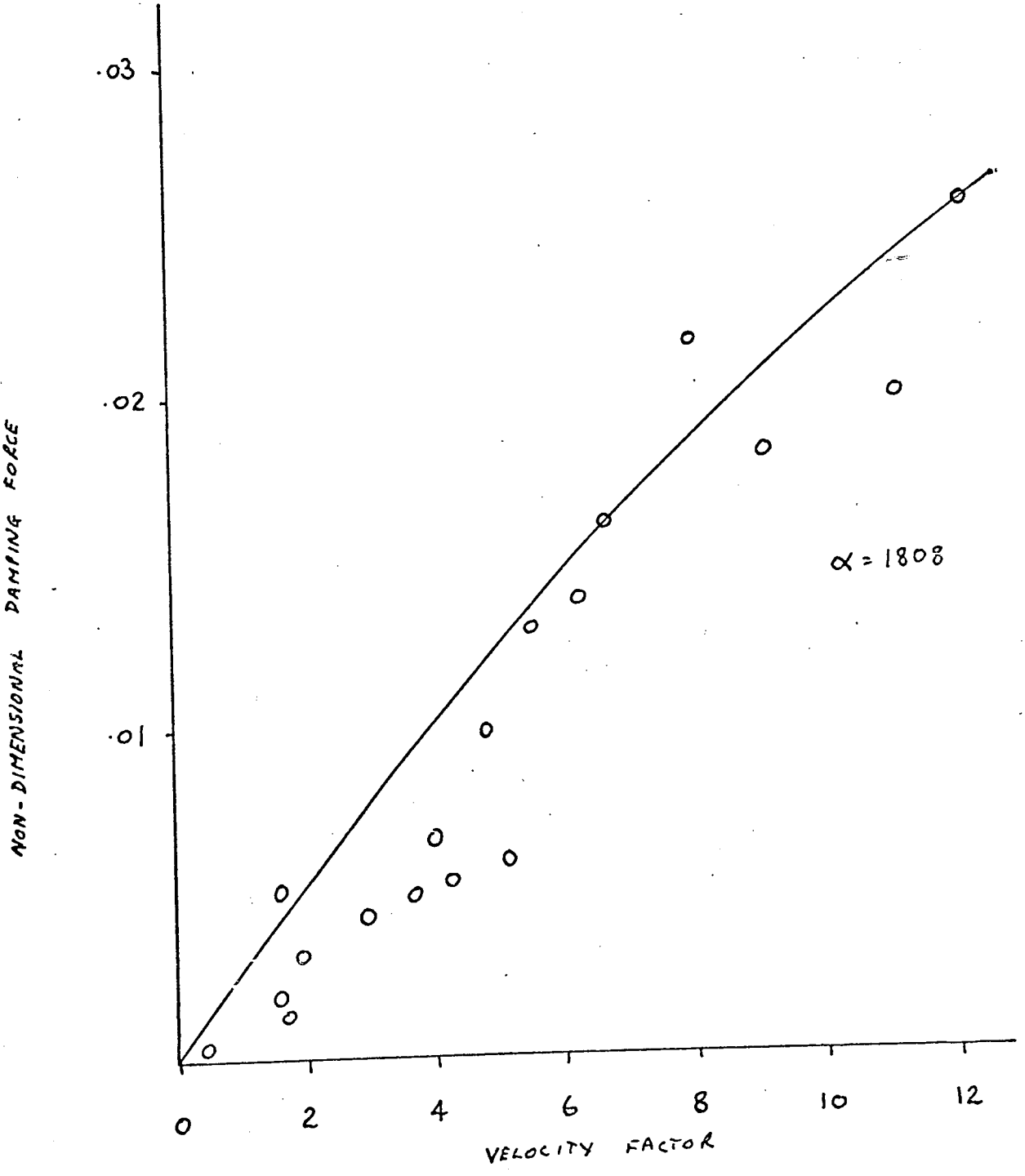

Figure 105 Comparison of the Experimentally determined and Theoretically predicted variation of the Non-Dimensional Damping Force with the Velocity Factor

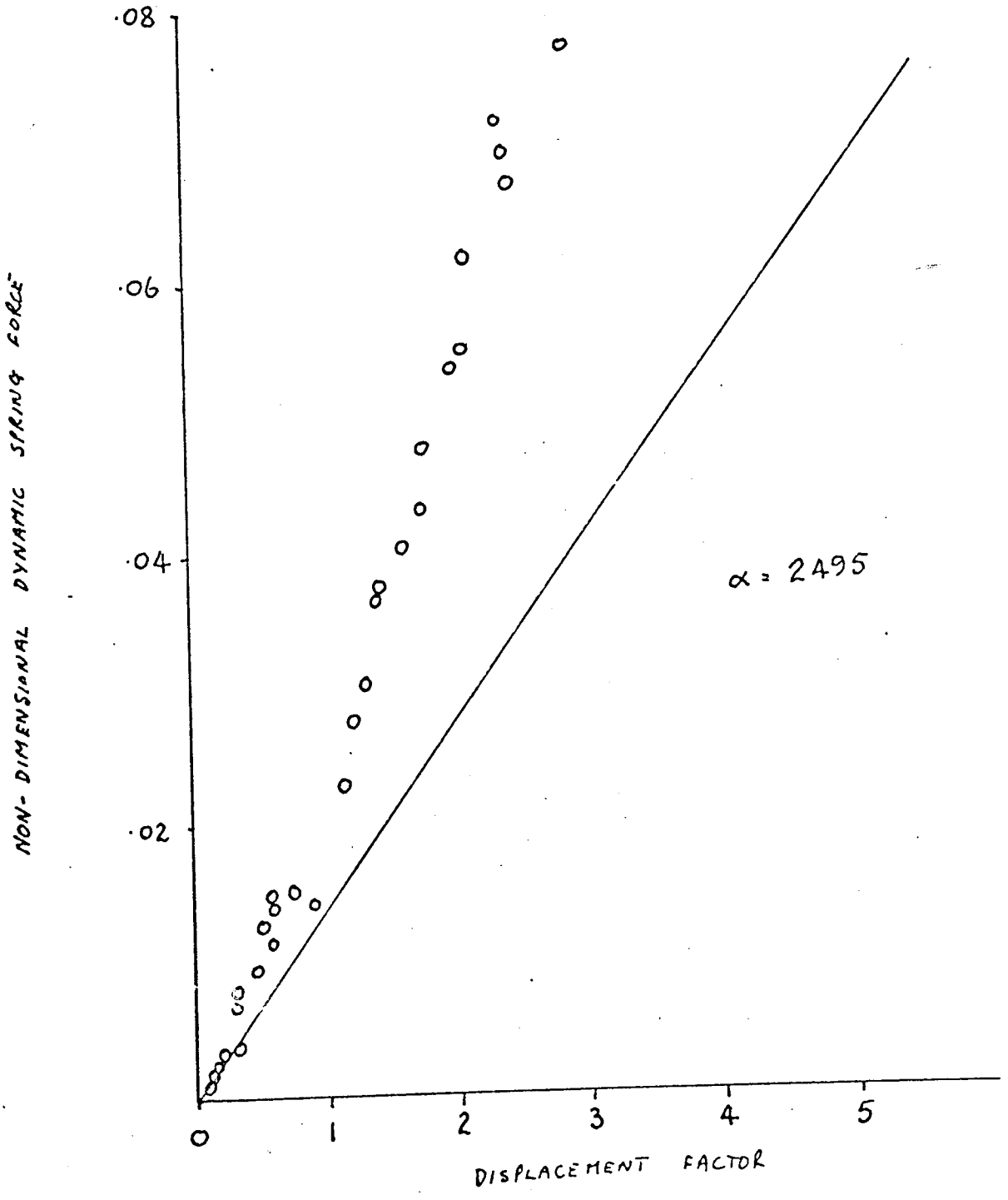

Figure 106 Comparison of the Experimentally determined and Theoretically predicted variation of the Non-Dimensional Dynamic Stiffness Force with the Displacement Factor

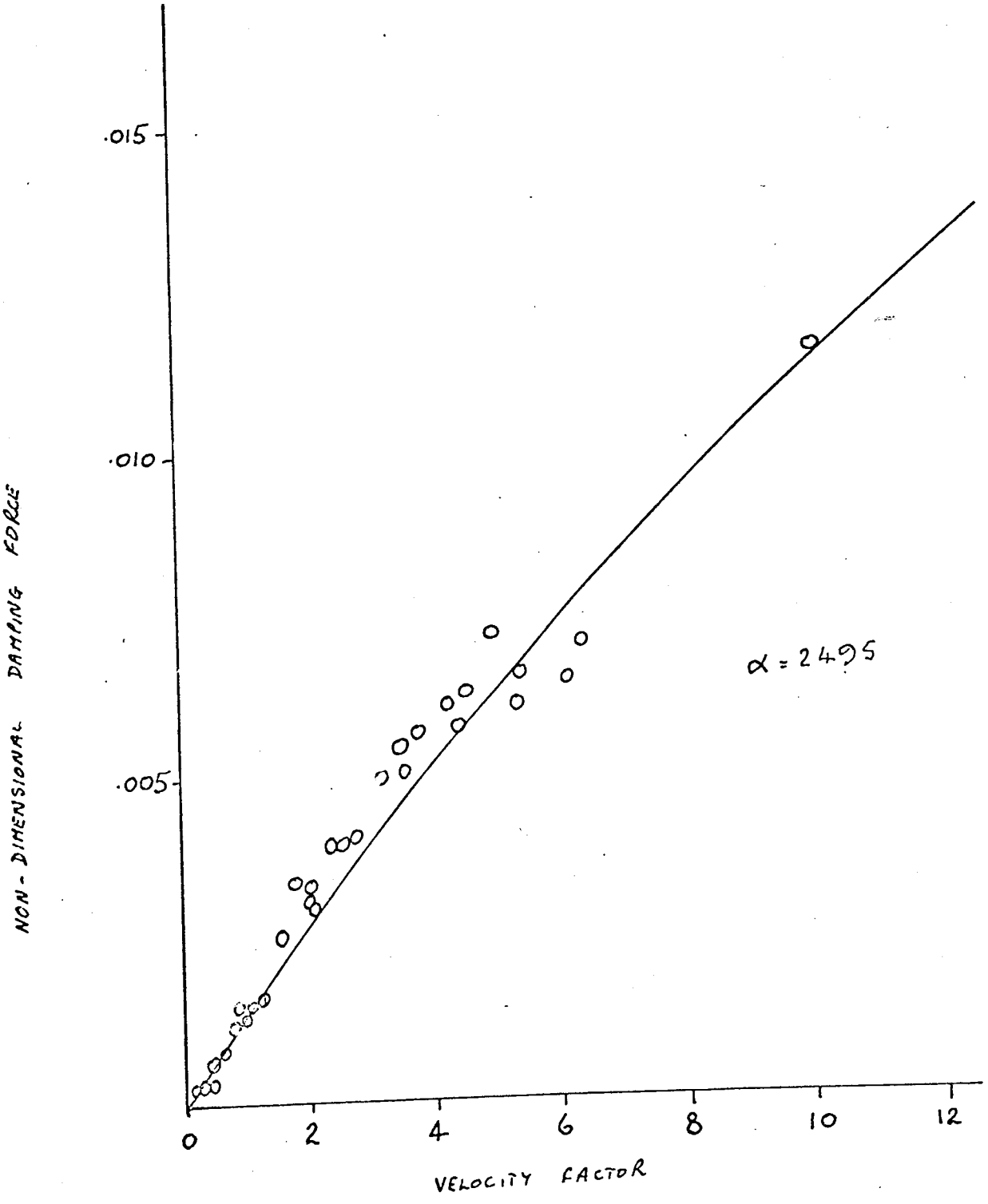

Figure 107 Comparison of the Experimentally determined and Theoretically predicted variation of the Non-Dimensional Damping Force with the Velocity Factor

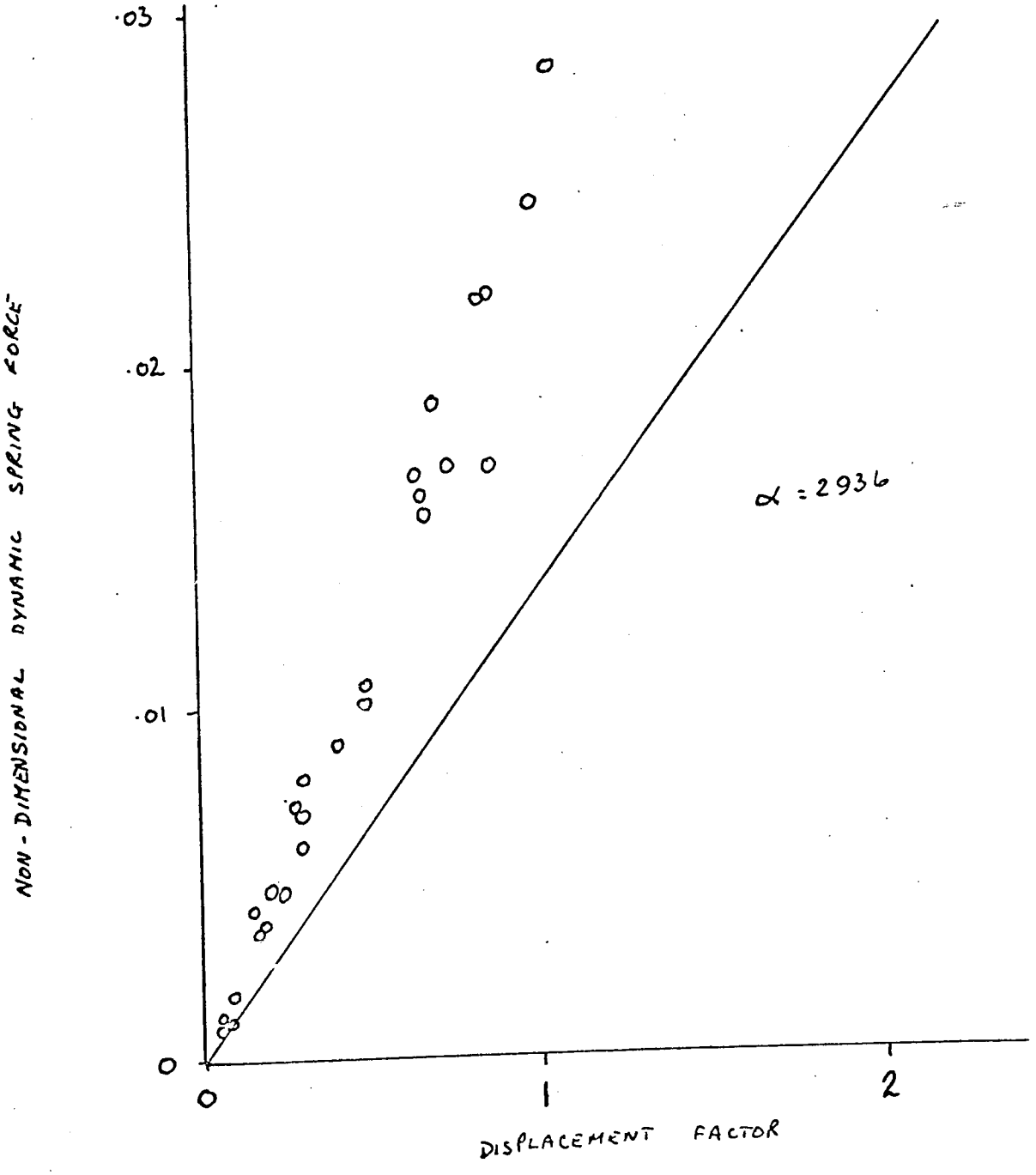

Figure 108 Comparison of the Experimentally determined and Theoretically predicted variation of the Non-Dimensional Dynamic Stiffness Force with the Displacement Factor

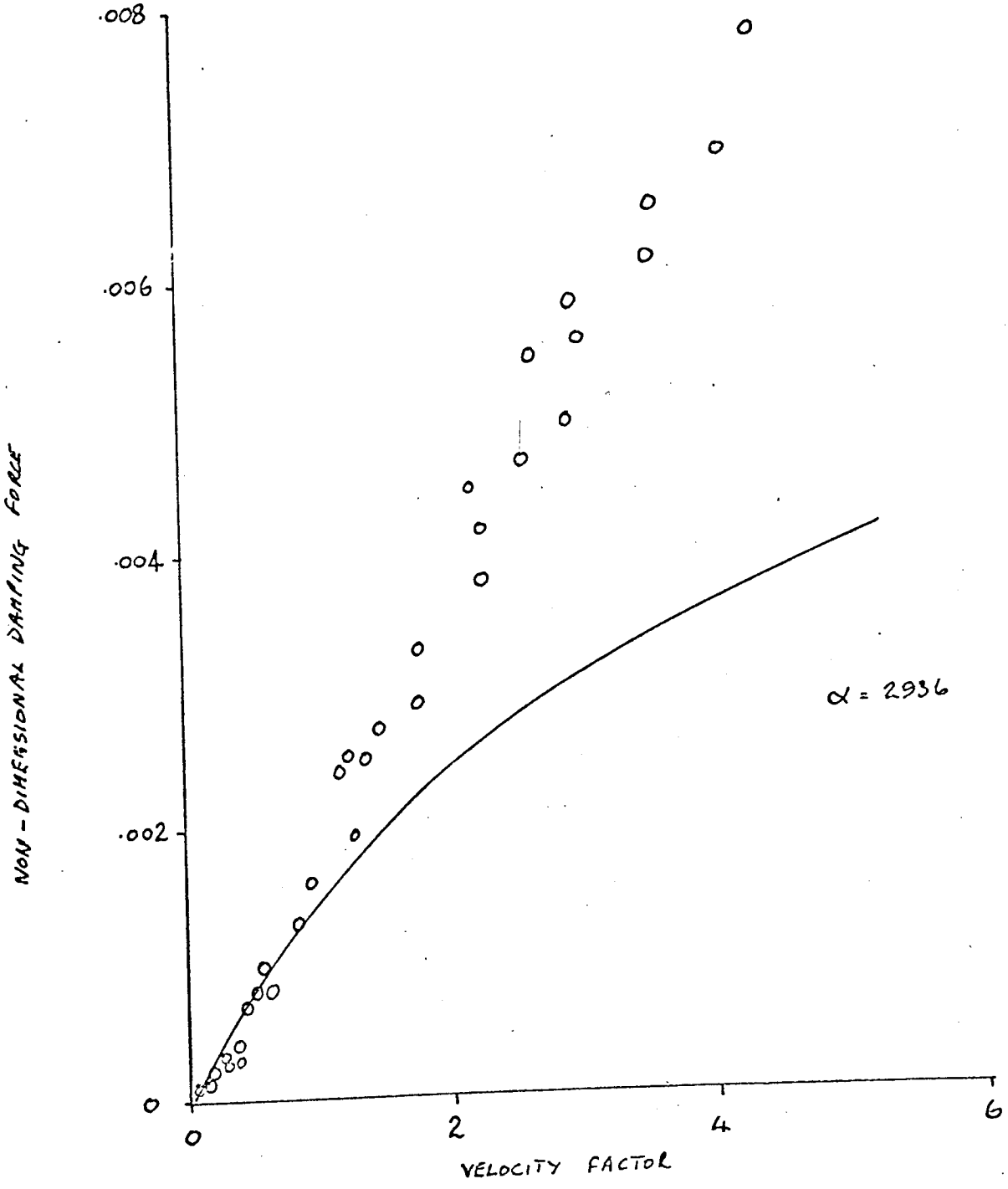

Figure 109 Comparison of the Experimentally determined and Theoretically predicted variation of the Non-Dimensional Damping Force with the Velocity Factor

APPENDIX ONE

THE CAPILLARY COMPENSATED GAS LUBRICATED CIRCULAR STEP BEARING

APPENDIX ONE

THE CAPILLARY COMPENSATED GAS LUBRICATED CIRCULAR STEP BEARING

The theory of this bearing is well known and it can be shown that under certain conditions, cf Powel (1), the modified Reynolds equation for this bearing can be expressed as:

$$\frac{d}{dr}\left(r \rho \frac{dp}{dr}\right) = 0 \qquad \text{A.1.1}$$

The bearing being considered isshown in figure 1 page 3.

If the lubricant is air then using the perfect gas law, i.e. $p = \rho RT$ the density term in equation A.1.1 may be replaced by p/RT and remembering that $2pdp = d(p^2)$ equation A.1.1 can be integrated twice to give:

$$p^2 = z_1 l_n r + z_2 \qquad \text{A.1.2}$$

Now the following boundary values apply

$$p = p_p \quad \text{at } r = r_p$$

$$p = p_a \quad \text{at } r = r_o$$

Use of these boundary values enables the constants of integration to be evaluated such that it may be

written

$$p^2 = \frac{(p_p^2 - p_a^2)}{l_n(r/rp)} \cdot (l_n\, r/r_o) + p_a^2 \qquad \text{A.1.3}$$

Now let

$$\frac{p}{p_a} = \overline{P}\ , \quad \frac{p_s}{p_a} = \overline{P}_s, \quad \frac{p_p}{p_a} = \overline{P}_p, \quad r/r_p = R_p, \quad r/r_o = R$$

substitution into equation A.1.3 gives

$$\overline{P}^2 = \frac{(\overline{P}_p^2 - 1) \cdot l_n R}{l_n R_p} + 1 \qquad \text{A.1.4}$$

Now the load capacity of the bearing is the summation of the forces acting normal to the bearing top plate thus:

$$W_c = 2\pi \int_{r_p}^{r_o} p.r.dr + \pi r_p^2 p_p - \pi r_o^2 p_a \qquad \text{A.1.5}$$

non-dimensionalising gives

$$\overline{W}_c = \frac{W_c}{\pi r_o^2 (p_s - p_a)} = \frac{2}{(\overline{P}_s - 1)} \left\{ \int_{R_p}^{1} \overline{P}.R.dR + \frac{\overline{P}_p . R_p^2}{2} - \tfrac{1}{2} \right\}$$

A.1.6

The mass flow through the bearing film is given by the integral

$$m_c = 2\pi r \int_o^h \rho . U_c . dy \qquad \text{A.1.7}$$

Remembering that $U_c = \frac{1}{\eta}\frac{dp}{dr}(y^2 - h_y)$ for this form of bearing gives

$$m_c = \frac{\pi r}{2\eta \mathcal{R}T} \cdot \frac{d(p^2)}{dr} \cdot \int_o^h (y^2 - h_y)\, d_y \qquad \text{A.1.8}$$

which upon integration and substitution of $\frac{d(p^2)}{dr}$ from differentiating equation A.1.3 gives

$$m_c = \frac{-\pi h^3 (p_p^2 - p_a^2)}{12\eta \mathcal{R}T \ln(r_p/r_o)} \qquad \text{A.1.9}$$

Non-dimensionalising gives

$$\bar{M}_c = \frac{2 m_c \eta \mathcal{R}T}{(p_s^2 - p_a^2) k_c} = \frac{-2\pi h^3}{12 \ln(R_p) k_c} \frac{(\bar{P}p - 1)}{(\bar{P}_s - 1)} \qquad \text{A.1.10}$$

where k_c is the capillary coefficients.

The mass flow through a capillary is given by the Hagen-Poiseuille law which states

$$m_c = \frac{k_c}{2\eta RT} \left(p_s^2 - p_p^2\right) \qquad \text{A.1.11}$$

Combining equations A.1.9 and A.1.11 leads to

$$p_p^2 = \left[p_s^2 - \frac{2p_a h^3 \pi}{12 l_n(R_p) . k_c}\right] \Big/ \left[1 - \frac{2h^3\pi}{l_n(R_p) . k_c}\right] \qquad \text{A.1.12}$$

in non-dimensional form

$$\bar{P}_p^2 = \left(\bar{P}_s^2 - \frac{2}{\Lambda_c l_n(R_p)}\right) \Big/ \left(1 - \frac{2}{\Lambda_c l_n(R_p)}\right) \qquad \text{A.1.13}$$

where $\Lambda_c = 12k_c/\pi h^3$

The Bearing Static Stiffness, X_c, is defined as:

$$X_c = - \frac{dW_c}{dh} \qquad \text{A.1.14}$$

which may be written as:

$$X_c = - \frac{dW_c}{dh} = - \frac{dW_c}{d\bar{W}_c} \cdot \frac{d\bar{W}_c}{d\bar{P}_p} \cdot \frac{d\bar{P}_p}{d\Lambda_c} \cdot \frac{d\Lambda_c}{dh} \qquad \text{A.1.15}$$

now from equation A.1.6

$$\frac{dW_c}{d\bar{W}_c} = \pi r_o^2 (p_s - p_a) \qquad \text{A.1.16}$$

from equations A.1.4 and A.1.6

$$\frac{d\bar{W}_c}{d\bar{P}_p} = \frac{1}{(\bar{P}_s - 1)} \left\{ \int_{R_p}^{1} \frac{2\bar{P}_p \ln(R) R.dR}{\bar{P} \ln(R_p)} + R_p^2 \right\} \qquad \text{A.1.17}$$

from equation A.1.13

$$\frac{d\bar{P}_p}{d\Lambda_c} = \frac{(1 - \bar{P}_s^2)}{\Lambda_c^2 \bar{P}_p \left(1 - \frac{2}{\Lambda_c \ln(R_p)}\right)^2 \ln R_p} \qquad \text{A.1.18}$$

from equation A.1.14

$$\frac{d\Lambda_c}{dh} = -\frac{3}{h} \Lambda_c \qquad \text{A.1.19}$$

substituting equations A.1.16 to A.1.19 into equation A.1.15 leads to

$$X_c = -\frac{3\pi r_o^2 (p_s - p_a)(\bar{P}_s + 1)}{h\Lambda_c \left(1 - \frac{2}{\Lambda_c \ln R_p}\right)^2 \ln R_p} \left\{ \int_{R_p}^{1} \frac{2 \ln(R) R.dR}{\bar{P} \ln R_p} + R_p^2 \right\}$$

A.1.20

in non-dimensional form

$$\bar{X}_c = \frac{X_c h}{\pi r_o^2 (p_s - p_a)} = -\frac{3(\bar{P}_s + 1)}{\Lambda_c \left(1 - \frac{2}{\Lambda_c \ln R_p}\right)^2 \ln R_p} \quad \ldots$$

$$\ldots \left\{ \int_{R_p}^{1} \frac{2 \ln R.R.dR}{\bar{P} \ln R_p} + R_p^2 \right\} \qquad \text{A.1.21}$$

Thus the following equations give the following non-dimensional parameters.

Equation Number	Non-dimensional Parameter
A.1.8	$\overline{W}_c$
A.1.13	$\overline{M}_c$
A.1.14	$\overline{P}_p$
A.1.21	$\overline{X}_c$

APPENDIX TWO

THE ROSCOE TECHNIQUE

APPENDIX TWO

THE ROSCOE TECHNIQUE

Before describing the Roscoe technique of discretising differential equations it is first necessary to explain why a standard technique of discretising was not used.

The use of finite difference equations to express differential equations may or may not, due to certain factors give a valid solution. An example leading to a valid solution is

$$\frac{d^2 Z}{dx^2} = 0 \qquad \text{A.2.1}$$

written in finite central difference form equation A.2.1 is expressed

$$Z_{i+1} - 2Z_i + Z_{i-1} = 0 \qquad \text{A.2.2}$$

The analytic solution of equation A.2.1 is known to be

$$Z = D_1 + D_2 x \qquad \text{A.2.3}$$

If the difference equation, equation A.2.2, is to give a valid solution then the solution of equation A.2.2

should be of a like format as equation A.2.3. That is

$$Z_i = f_1 + f_{2i} \qquad \text{A.2.4}$$

Substituting equation A.2.4 into equation A.2.2. gives

$$f_1+f_2(i+1) - 2(f_1+f_{2i}) + f_1+f_2(i-1) = 0$$

which is true. Hence equation A.2.4 is the solution of equation A.2.2.

Consider now an equation of the form

$$\frac{dZ}{dx} + \nu Z = 0 \qquad \text{A.2.5}$$

Expressing the differential term in first backward difference form we get

$$\frac{Z_i - Z_{i-1}}{\Delta_x} + \nu Z_i = 0 \qquad \text{A.2.6}$$

The analytic solution of equation A.2.5 is known to be

$$Z = f_3 e^{-\nu x} \qquad \text{A.2.7}$$

Equation A.2.6 gives

$$Z_i = Z_{i-1}\left[\frac{1}{1+\nu\Delta_x}\right] = f_4 \left(\frac{1}{1+\nu\Delta_x}\right)^i \qquad \text{A.2.8}$$

Consider (a) $\nu > 0$

As i increases Z_i tends to zero. This is in agreement with the analytic solution and the desired behaviour may result

(b) $\nu < 0$

(i) if $|\nu\Delta_x| < 1$

the desired behaviour may result.

(ii) If $|\nu\Delta_x| > 1$

for i being odd Z_i is negative

for i being even Z_i is positive

i.e. the process is unstable and the desired behaviour will not result. From this it is clear that for a set grid size the value of ν governs the validity of the finite difference technique.

The question now arises what technique should be used to express equation A.2.5 in difference form such that a valid solution is obtained for all values of ν. If we inspect the analytic solution of equation A.2.5, i.e. equation A.2.7., we see that by expressing the space variable x in finite form, $x = (i-1)\Delta$, the resulting equation is

$$Z_i = F_5(e^{-\nu\Delta})^{i-1} = F_6(e^{-\nu\Delta})^{i} \qquad \text{A.2.9.}$$

If a numerical equation could be formed such that equation A.2.9 was the solution, then the numerical equation would

give a valid solution for all values of ν. This then is the basis of the Roscoe Technique.

The Roscoe Technique

Consider a differential equation of the form

$$F_7 \frac{d^2 Z}{dx^2} + F_8 \frac{d Z}{dx} = 0 \qquad \text{A.2.10}$$

The analytic solution of this equation is known to be

$$Z = G_1 + G_2 . e^{-\frac{F_8 x}{F_7}} \qquad \text{A.2.11}$$

Replacing x by $\Delta_x(i-1)$ in equation A.2.11 gives

$$Z_i = G_1 + G_2 \left(e^{-\frac{F_8 \Delta_x}{F_7}} \right)^{i-1} \qquad \text{A.2.12}$$

Forming a secondary numerical equation from equation A.2.12 by subtracting the terms raised to the power (i-1) from a numerical operator '$\underline{m}$' gives

$$(\underline{m}-1) \left(\underline{m} - e^{-\frac{F_8 \Delta_x}{F_7}} \right) = 0 \qquad \text{A.2.13}$$

The numerical operator '$\underline{m}$' is treated in the same sense as the differential operator 'D'. Hence the numerical equation for which equation A.2.12 is the solution may be written

using equation A.2.13 as

$$Z_{i+1} - Z_i\left(1 + e^{-\frac{F_8\Delta_x}{F_7}}\right) + e^{-\frac{F_8\Delta_x}{F_y}} . Z_{i-1} = 0$$

A.2.14

The Roscoe Technique then works backwards from the analytic solution to form a numerical equation which can be used to give a valid solution of the original differential equation. This in itself may at first appear to be of no use, for if an analytic solution is known why use a numerical approximation? In the case where an analytic solution contains infinite series whose convergence rate may be slow this process is of great assistance for the numerical solution may be more rapid inconvergence.

Consider now an equation of the form

$$A_3 . \frac{\partial^2\phi}{\partial R^2} + A_4 \frac{\partial\phi}{\partial R} + A_5 \frac{\partial^2\phi}{\partial Y^2} = 0 \qquad \text{A.2.15}$$

The Roscoe approach is to split this equation into two sub-sections such that

(1) $$A_3 \frac{d^2\phi}{dR^2} + A_4 \frac{d\phi}{dR} = 0 \qquad \text{A.2.16}$$

(2) $$A_5 \frac{d^2\phi}{dY^2} = 0 \qquad \text{A.2.17}$$

and

$$(3)\qquad \mu\left(A_3 \frac{d^2\phi}{dR^2} + A_4 \frac{d\phi}{dR}\right) + A_5 \frac{d^2\phi}{dY^2}$$

$$= A_3 \frac{\partial^2\phi}{\partial R^2} + A_4 \frac{\partial\phi}{\partial R} + A_5 \frac{\partial^2\phi}{\partial Y^2} = 0 \qquad \text{A.2.18}$$

The numerical equations are formed from the solutions of the ordinary differential equations given as equations A.2.16 and A.2.17 and the multiplier μ is then found such that equation A.2.18 holds.

Equations A.2.16 and A.2.17 are similar to equations A.2.10 and A.2.1 respectively. Thus the valid numerical solutions may be written as

$$\phi_{i+1} - \phi_i\left(1 + e^{-\frac{A_4\Delta_r}{A_3}}\right) + \phi_{i-1}e^{-\frac{A_4\Delta_r}{A_3}}\Big) = 0 \qquad \text{A.2.19}$$

and

$$\frac{A_5(\phi_{j+1} - 2\phi_j + \phi_{j-1})}{(\Delta_y)^2} = 0 \qquad \text{A.2.20}$$

respectively. Here i signifies the nodal position in the R-direction and j the nodal position in the Y-direction on a two dimensional space grid.

Now the multiplier μ must be found such that

$$\mu\left(\phi_{i+ij} - \phi_{ij}\left(1 + e^{-\frac{A_4\Delta_r}{A_3}}\right) + \phi_{i-1j}.\ e^{-\frac{A_4\Delta_r}{A_3}}\right)$$

$$+ \frac{A_5(\phi_{ij+1} - 2\phi_{ij} + \phi_{ij-1})}{(\Delta_y)^2} = 0$$

A.2.21

or

$$\mu\left(\phi_{i+1j} - \phi_{ij}\left(1 + e^{-\frac{A_4\Delta_r}{A_3}}\right) + \phi_{i-1j}\ e^{-\frac{A_4\Delta_r}{A_3}}\right)$$

$$+ \frac{A_5(\phi_{ij+1} - 2\phi_{ij} + \phi_{ij-1})}{(\Delta_y)^2} = A_3\frac{\partial^2\phi}{\partial R^2} + A_4\frac{\partial\phi}{\partial R}$$

$$+ A_5\frac{\partial^2\phi}{\partial Y^2} = 0$$

A.2.22

replacing the ϕ_{ij} terms in equation A.2.22 by a difference operator '$\underline{m}$' such that

$$\underline{m}\phi_i = \phi_{i+1}$$

equation A.2.22 transposes to

$$\mu\left(m - \left(1 + e^{-\frac{A_4\Delta_r}{A_3}}\right) + m^{-1}e^{-\frac{A_4\Delta_r}{A_3}}\right)\phi_{ij}$$

$$+ \frac{A_5(\phi_{ij+1} - 2\phi_{ij} + \phi_{ij-1})}{(\Delta_y)^2}$$

$$= A_3\frac{\partial^2\phi}{\partial R^2} + A_4\frac{\partial\phi}{\partial R} + A_5\frac{\partial^2\phi}{\partial Y^2}$$

A.2.23

Now let $\phi = R^n = [\Delta_r(i-1)]^n$ equation A.2.23 may be written

$$\mu\Delta_r{}^n\left(i^n - (i-1)^n\left(1 + e^{-\frac{A_4\Delta_r}{A_3}}\right) + (i-2)^n\, e^{-\frac{A_4\Delta_r}{A_3}}\right)$$

$$+ \frac{(\phi_{ij+1} - 2\phi_{ij} + \phi_{ij-1})A_5}{(\Delta_y)^2} = A_3\, n(n-1)\Delta_r{}^{n-2}(i-1)^{n-2}$$

$$+ A_4\, n\, \Delta_r{}^{n-1}(i-1)^{n-1} + \frac{\partial^2\phi}{\partial Y^2} A_5 \qquad \text{A.2.24}$$

Now a value of μ should be found such that equation A.2.24 holds. This, however, is not possible and in order to obtain an approximate value of μ the highest powers of i are equated. After expanding the bracketed terms binomially it can be seen that the highest power of i is i^{n-1}. Equating coefficients give

$$\mu\Delta_r{}^n\left(ni^{n-1}\left(1 + e^{-\frac{A_4\Delta_r}{A_3}}\right) - 2ni^{n-1}\, e^{-\frac{A_4\Delta_r}{A_3}}\right)$$

$$= A_4\, n\, \Delta_r{}^{n-1} i^{n-1} \qquad \text{A.2.25}$$

which gives

$$\mu = \frac{A_4}{\Delta_r\left(1 - e^{-\frac{A_4\Delta_r}{A_3}}\right)} \qquad \text{A.2.26}$$

The combination of equation A.2.21 and equation A.2.26 gives the numerical equation for the differential equation, equation A.2.15, that is

$$A_3 \frac{\partial^2 \phi}{\partial R^2} + A_4 \frac{\partial \phi}{\partial R} + A_5 \frac{\partial^2 \phi}{\partial Y^2} = 0$$

is discretised such that

$$\frac{A_4}{\Delta_r\left(1 - e^{-\frac{A_4 \Delta_r}{A_3}}\right)}\left[\phi_{i+1j} - \phi_{ij}\left(1 + e^{-\frac{A_4 \Delta_r}{A_3}}\right) + \phi_{i-1j}\, e^{-\frac{A_4 \Delta_r}{A_3}}\right]$$

$$+ \frac{A_5(\phi_{ij+1} - 2\phi_{ij} + \phi_{ij-1})}{(\Delta_y)^2}$$

This then is the Roscoe Technique. It should be noted that this technique is based on the work of D. Roscoe (71). A full explanation of the mathematics involved can be found in this reference.

APPENDIX THREE

VERIFICATION OF THE ROSCOE TECHNIQUE

APPENDIX THREE

VERIFICATION OF THE ROSCOE TECHNIQUE

From Section 3.3 the governing differential equation for the steady-state pressure distribution in the porous media together with the relevant boundary conditions may be written in dimensionless form, equations A.3.1 to A.3.5, as

$$\frac{S^2 K}{R}\frac{\partial}{\partial R}\left[R\frac{\partial}{\partial R}(\bar{P}^2)\right] + \frac{\partial^2}{\partial Y^2}(\bar{P}^2) = 0$$

$$0 \leqslant R \leqslant 1, \quad 0 \leqslant Y \leqslant 1 \qquad \text{A.3.1}$$

$$\bar{P}^2 = \bar{P}_s^{\,2} \qquad 0 \leqslant R \leqslant 1, \quad Y = 0 \qquad \text{A.3.2}$$

$$\frac{\partial}{\partial R}(\bar{P}^2) = 0 \qquad 0 \leqslant Y \leqslant 1, \quad R = 0 \qquad \text{A.3.3}$$

$$\frac{\partial}{\partial R}(\bar{P}^2) = 0 \qquad 0 \leqslant Y \leqslant 1, \quad R = 1 \qquad \text{A.3.4}$$

$$\frac{1}{R}\frac{\partial}{\partial R}\left[R\frac{\partial}{\partial R}(\bar{P}^2)\right] = A\left[\frac{\partial}{\partial Y}(\bar{P}^2)\right]_{Y=1}$$

$$0 \leqslant R \leqslant 1, \quad Y = 1 \qquad \text{A.3.5}$$

Using the Roscoe technique to discretise A.3.1, see appendix 2, we obtain replacing $\bar{P}^2$ by ϕ

$$\frac{S^2K}{(\Delta_r)^2(i-1)\left(1-e^{-\frac{1}{i-1}}\right)}\left[\phi_{i+1j}-\phi_{ij}\left(1+e^{-\frac{1}{i-1}}\right)+\phi_{i-1j}e^{-\frac{1}{i-1}}\right]$$

$$+\frac{\phi_{ij+1}-2\phi_{ij}+\phi_{ij-1}}{(\Delta_y)^2} \qquad 1 \leqslant i \leqslant I, \quad 1 \leqslant j \leqslant J \qquad \text{A.3.6}$$

The boundary conditions, equations A.3.2. to A.3.5. may be written as respectively

$$\phi_{ij}=\bar{P}_s^2 \qquad 1 \leqslant i \leqslant I, \quad j = 1 \qquad \text{A.3.7}$$

$$\phi_{i+1} = \phi_{i-1} \qquad 1 \leqslant j \leqslant J, \quad i = 1 \qquad \text{A.3.8}$$

$$\phi_{i+1} = \phi_{i-1} \qquad 1 \leqslant j \leqslant J, \quad i = I \qquad \text{A.3.9}$$

$$\frac{1}{(\Delta_r)^2(i-1)\left(1-e^{-\frac{1}{i-1}}\right)}\left[\phi_{i+1j}-\phi_{ij}\left(1+e^{-\frac{1}{i-1}}\right)+\phi_{i-1j}e^{-\frac{1}{i-1}}\right]$$

$$=\frac{\Lambda(\phi_{ij}-\phi_{ij-1})}{\Delta_y} \qquad 1 \leqslant i \leqslant I, \quad j = J \qquad \text{A.3.10}$$

Equations A.3.6 to A.3.10 then are the set of difference equations which replace the set of differential equations. However, they are not in a form acceptable for a computer solution, i.e. explicit in ϕ_{ij}. Hence re-orientating equation A.3.6 to a form that is acceptable gives

$$\phi_{ij} = \frac{B_4[\phi_{i+1j} + \phi_{i-1j}\ B_3] + B_5[\phi_{ij+1} + \phi_{ij-1}]}{B_4(1 + B_3) + 2B_5}$$

A.3.11

where

$$\left.\begin{aligned} B_3 &= e^{-\frac{1}{i-1}} \\ B_4 &= \frac{1}{(\Delta_r)^2}\frac{S^2K}{(i-1)(1-B_3)} \\ B_5 &= \frac{1}{(\Delta_y)^2} \end{aligned}\right\} \quad \text{A.3.12}$$

Equation A.3.11 along with equation A.3.12 is used to solve the pressure at each internal grid point, i.e. $1 < i < I$ and $1 < j < J$, see figure 11 page 65 for nomenclature.

Now at $j = 1$, $1 < i < I$ both equations A.3.6 and A.3.7 apply and therefore both must be satisfied. However, equation A.3.7 shows that $\phi_{i1} = \overline{P}_s^{\,2}$ hence as the value is known at this point equation A.3.6 need not be applied. Similarly this applies to points $j = 1$, $i = 1$ and $j = 1$, $i = I$ where equations A.3.6, A.3.7, A.3.8. and equations A.3.6, A.3.7, A.3.9, apply respectively. Hence

$$\phi_{ij} = \overline{P}_s^{\,2} \qquad 1 \leq i \leq I, \quad j = 1 \qquad \text{A.3.13}$$

At points i = 1, $1 < j < J$ both equations A.3.6 and A.3.8 apply and therefore both must be satisfied. It should be noted that both equations hold a point outside the bounds of the grid. By combining both equation A.3.6 and A.3.8 this point may be eliminated and at the same time both equations will be satisfied. Thus

$$\phi_{ij} = \frac{(1+B_3) \cdot B_4 \cdot \phi_{i+1j} + (\phi_{ij+1} + \phi_{ij-1}) B_5}{(1+B_3) B_4 + 2B_5} \qquad \text{A.3.14}$$

It should be noted that for R = 0, i.e. i = 1, the constants B_3 and B_4 produce singularities. This is overcome by replacing (i-1) by i, i.e. $R = \Delta_r i$ not $\Delta_r(i-1)$. It can be seen that in the limit as $i \to \infty$ and hence Δ_r becomes small that $\Delta_r(i-1) \to \Delta_{ri}$.

This then leaves the grid point i = 1, j = J undefined. This point will be defined later.

At points i = I, $1 < j < J$ both equations A.3.5 and A.3.9 apply and therefore both must be satisfied. The same approach is used as was used for points i = 1, giving

$$\phi_{ij} = \frac{(1+B_3) B_4 \phi_{i-1j} + (\phi_{ij+1} + \phi_{ij-1}) B_5}{(1+B_3) B_4 + 2B_5}$$

$$i = I, \quad 1 < j < J$$

A.3.15

This leaves the grid point i = I, j = J undefined. At this point atmospheric conditions prevail and therefore it may be written

$$\phi_{ij} = 1.0 \qquad i = I, \quad j = J \qquad \text{A.3.16}$$

At the grid points j = J, 1 < i < I both equations A.3.6 and A.3.10 apply so both must be satisfied. Equation A.3.6 holds a point outside the bounds of the grid. A similar technique as that used at the boundaries R = 0 and R = 1 may be considered. However, this technique cannot be used at this boundary for it assumes that the pressure gradient is continuous. This is not the case. The pressure across the film is assumed constant and by virtue of this a discontinuity in the pressure gradient must occur at this boundary. At this boundary only Reynolds equation is used. Upon examination of the Reynolds equation it can be seen that it contains a term which includes the axial pressure gradient. As the main equation has been used to determine the ϕ values at the nodal points used to express this gradient then the main equation is inherently used. Thus it may be written for j = J, 1 < i < I

$$\phi_{ij} = \frac{\frac{B_4}{SK}(\phi_{i+1j}+B_3\phi_{i-1,j}) + B_6\phi_{ij-1}}{\frac{B_4}{SK}(1+B_3) + B_6} \qquad \text{A.3.17}$$

where

$$B_6 = \Lambda / \Delta_y$$

This then leaves the nodal point i = 1, j = J undefined. At this point the two boundary conditions, equation A.3.8 and A.3.10 are combined to eliminate the term, held in both equations, outside the bounds of the grid, i.e. ϕ_{i-1j} giving

$$\phi_{ij} = \frac{\frac{B_4(1+B_3)}{SK}\phi_{i+1j} + B_6\phi_{ij-1}}{\frac{B_4(1+B_3)}{SK} + B_4} \qquad \text{A.3.18}$$

Equations A.3.11 to A.3.18 are in a form acceptable to the computer. A relaxation process is used in the program to assist convergence, convergence being achieved when each new calculated value of ϕ is within an acceptable percentage, in this case 0.1%, of the previous calculated value of ϕ for each nodal point.

A typical comparison of the gas film pressures obtained from the above numerical procedure and the analytic solution of Jones et al is shown below in tabulated form. Figure 110, page 324 shows this comparison graphically. The maximum error involved in this case occurred at R = 0.9 and the magnitude of the error is 1.54%.

From this it can be seen that at the boundary R = 0 the assumption that

$$\Delta_r i = R \qquad \text{not} \qquad \Delta_r(i-1) = R$$

does not incur large errors. Therefore for all cases at this boundary when singularities arise this assumption can be made without incurring large errors.

A sample computer program is given in appendix 7.

COMPARISON OF ANALYTIC AND NUMERIC SOLUTIONS OF FILM PRESSURE

Bearing Data

Pad outer radius	38.1 mm
Pad thickness	10.0 mm
Pad Permeability (viscous)	$1.423 \times 10^{-12} cm^2$
Ratio of viscous permeabilities	1.0
Supply pressure (gauge)	1.0 Bar
Atmospheric pressure	1.013 Bar
Gas film thickness	12.7 microns
Numeric grid size	0.1

Dimensionless Radial Position	Dimensionless Pressure		% Error Assuming Analytic solution correct
	Analytic Solution	Numeric Solution	
0	1.84329	1.85186	0.465
0.1	1.83972	1.84589	0.335
0.2	1.82866	1.83505	0.338
0.3	1.80971	1.81671	0.387
0.4	1.78064	1.78902	0.471
0.5	1.73896	1.74927	0.593
0.6	1.68052	1.69333	0.762
0.7	1.59865	1.61456	0.995
0.8	1.48189	1.50107	1.294
0.9	1.30674	1.32692	1.544
1.0	1.00000	1.00000	0

% error in load capacity incurred via numerical technique = 2.515%

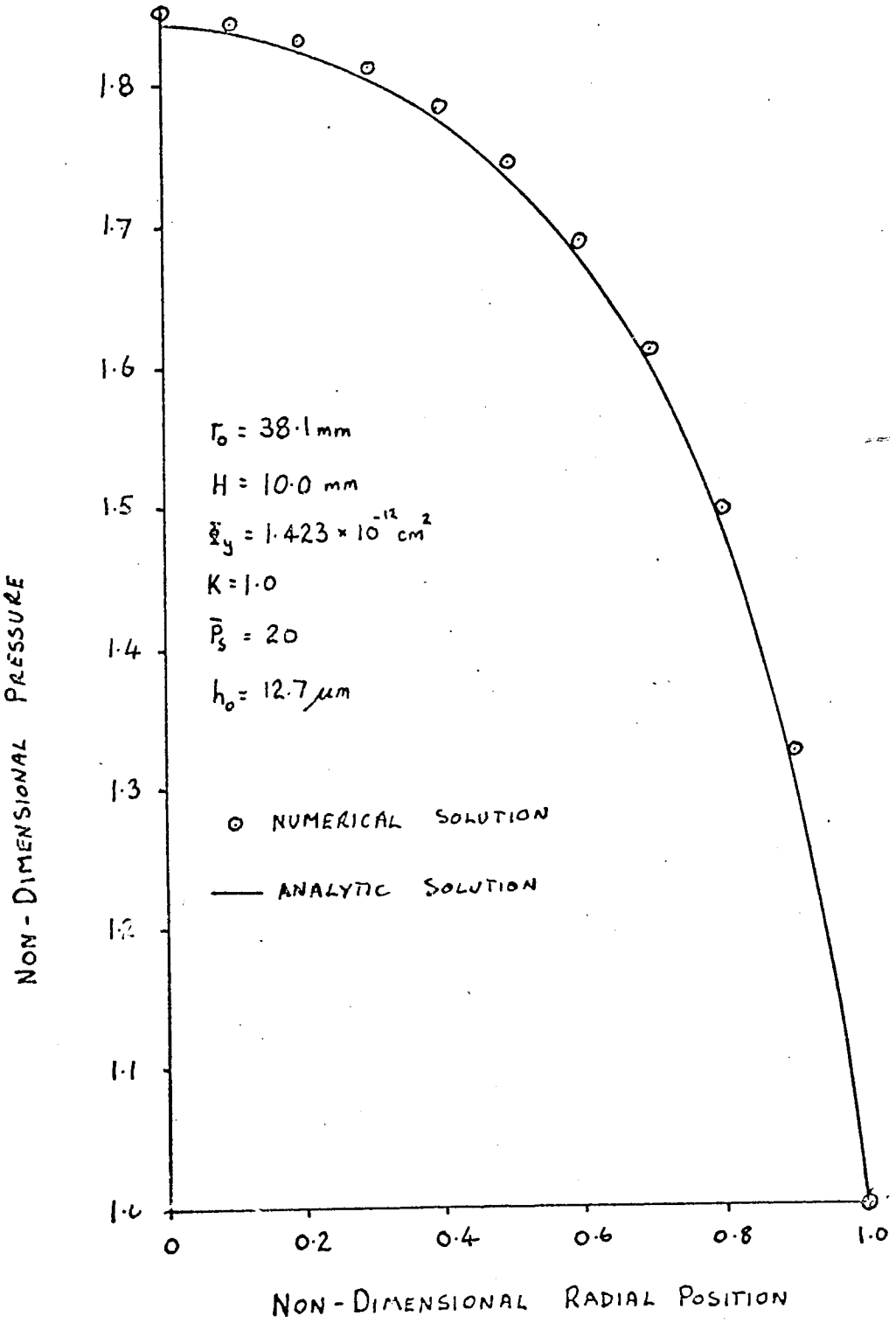

Figure 110 Comparison of the Gas Film Pressures obtained using the Numerical method of Roscoe and the Analytic solution of Jones

APPENDIX FOUR

THE FORMULATION AND SOLUTION OF THE DIFFERENCE EQUATIONS FOR THE TIME DEPENDENCE CASE

APPENDIX FOUR

THE FORMULATION AND SOLUTION OF THE DIFFERENCE EQUATIONS FOR THE TIME DEPENDENCE CASE

The governing differential equation along with its boundary conditions for the time dependence case may be written in dimensionless form as, Section 3.2.

$$\frac{S^2K}{R}\frac{\partial}{\partial R}\left[R\frac{\partial}{\partial R}(\bar{P}^2)\right]+\frac{\partial^2}{\partial Y^2}(\bar{P}^2)=\frac{\alpha}{\bar{P}}\frac{\partial}{\partial \bar{T}}(\bar{P}^2)$$

$$0 \leqslant R \leqslant 1,\ 0 \leqslant Y \leqslant 1,\ 0 \leqslant \bar{T} \leqslant 1 \qquad \text{A.4.1.}$$

$$\bar{P}=\bar{P}_s \qquad Y=0,\quad 0 \leqslant R \leqslant 1,\ 0 \leqslant \bar{T} \leqslant 1 \qquad \text{A.4.2.}$$

$$\frac{\partial}{\partial R}(\bar{P}^2)=0 \qquad R=0,\quad 0 \leqslant Y \leqslant 1,\ 0 \leqslant \bar{T} \leqslant 1 \qquad \text{A.4.3.}$$

$$\frac{\partial}{\partial R}(\bar{P}^2)=0 \qquad R=1,\quad 0 \leqslant Y \leqslant 1,\ 0 \leqslant \bar{T} \leqslant 1 \qquad \text{A.4.4.}$$

$$\frac{1}{\bar{P}}\frac{\partial}{\partial R}\left[R\frac{\partial}{\partial R}(\bar{P}^2)\right]=\Lambda\left[\frac{\partial}{\partial Y}(\bar{P}^2)\right]_{Y=1}+\frac{\beta}{\bar{P}}\frac{\partial}{\partial \bar{T}}(\bar{P}^2)+\gamma\bar{P}$$

$$Y=1,\quad 0 \leqslant R \leqslant 1,\ 0 \leqslant \bar{T} \leqslant 1 \qquad \text{A.4.5.}$$

$$\bar{P}(\bar{T})=\bar{P}(\bar{T}+1) \qquad 0 \leqslant Y \leqslant 1,\ 0 \leqslant R \leqslant 1 \qquad \text{A.4.6.}$$

It is well known that the use of explicit differencing techniques for the solution of time dependence equations require, due to an instability problem, an uneconomically large number of time steps of limited size. The use of a

full implicit procedure in which both space second derivatives are replaced by second differences evaluated in terms of forward time leads to a large set of simultaneous equations which can only be solved, practically by iteration.

Peaceman and Rachford (58) suggested that only one of the space second derivatives should be replaced by a second difference evaluated in forward time while the other derivative is replaced by a second difference in terms of known values. At the next time step the procedure is repeated but implicit in the second space variable in this case. This they termed an 'Alternating-direction implicit method', (A.D.I.).

This procedure has been adopted for the solution of the time dependence governing differential equation. Thus writing equation A.4.1. in a difference form obtained by applying the Roscoe technique and remembering for the A.D.I. procedure two forms of this equation are required, firstly implicit in the R-direction only

$$\left[\frac{\phi_{ij}^{2m+1} - \phi_{ij}^{2m}}{\Delta_t}\right] \frac{\alpha}{(\phi_{ij}^{2m+1})^{\frac{1}{2}}} = \frac{S^2 K}{(i-1)\left(1-e^{-\frac{1}{i-1}}\right)} \quad \ldots.$$

$$\ldots\left[\frac{\phi_{i+1j}^{2m+1} - \phi_{ij}^{2m+1}\left(1+e^{-\frac{1}{i-1}}\right) + e^{-\frac{1}{i-1}}\,\phi_{i-1j}^{2m+1}}{(\Delta_r)^2}\right]$$

$$+ \frac{\phi_{ij+1}^{2m} - 2\phi_{ij}^{2m} + \phi_{ij-1}^{2m}}{(\Delta_y)^2} \qquad \text{A.4.7.}$$

and secondly implicit in the Y-direction only

$$\left[\frac{\phi_{ij}^{2m+2} - \phi_{ij}^{2m+1}}{\Delta_t}\right] \frac{\alpha}{(\phi_{ij}^{2m+2})^{\frac{1}{2}}} = \frac{S^2K}{(i-1)\left(1-e^{-\frac{1}{i-1}}\right)} \quad \ldots\ldots$$

$$\ldots \left[\frac{\phi_{i+1j}^{2m+1} - \phi_{ij}^{2m+1}\left(1+e^{-\frac{1}{i-1}}\right) + e^{-\frac{1}{i-1}}\,\phi_{i-1j}^{2m+1}}{(\Delta_r)^2}\right]$$

$$+ \frac{\phi_{ij+1}^{2m+2} - 2\phi_{ij}^{2m+2} + \phi_{ij-1}^{2m+2}}{(\Delta_y)^2} \qquad \text{A.4.8.}$$

where

$$\phi = \overline{P}^2$$

Now for a square space grid

$$\Delta_r = \Delta_y = \Delta$$

Let

$$\frac{\Delta^2}{\Delta_t} = \delta$$

By re-arranging equations A.4.7 and A.4.8 such that only implicit terms appear on the left hand sides of the equations we get

$$\frac{S^2K}{(i-1)\left(1-e^{-\frac{1}{i-1}}\right)}\left[\phi_{i+1j}^{2m+1}+e^{-\frac{1}{i-1}}\cdot\phi_{i-1j}^{2m+1}\right]\quad\cdots$$

$$\cdots-\left[\frac{S^2K\left(1+e^{-\frac{1}{i-1}}\right)}{(i-1)\left(1-e^{-\frac{1}{i-1}}\right)}+\frac{\delta\alpha}{(\phi_{ij}^{2m+1})^{\frac{1}{2}}}\right]\phi_{ij}^{2m+1}$$

$$=-\phi_{ij+1}^{2m}+\left(2-\frac{\delta\alpha}{(\phi_{ij}^{2m+1})^{\frac{1}{2}}}\right)\phi_{ij}^{2m}-\phi_{ij-1}^{2m}$$

A.4.9.

and

$$\phi_{ij+1}^{2m+2}-\left[2+\frac{\delta\alpha}{(\phi_{ij}^{2m+2})^{\frac{1}{2}}}\right]\phi_{ij}^{2m+2}+\phi_{ij-1}^{2m+2}$$

$$=-\frac{S^2K}{(i-1)\left(1-e^{-\frac{1}{i-1}}\right)}\left[\phi_{i+1j}^{2m+1}+\phi_{i-1j}^{2m+1}\cdot e^{-\frac{1}{i-1}}\right]$$

$$+\left[\frac{S^2K\left(1+e^{-\frac{1}{i-1}}\right)}{(i-1)\left(1-e^{-\frac{1}{i-1}}\right)}-\frac{\delta\alpha}{(\phi_{ij}^{2m+2})^{\frac{1}{2}}}\right]\phi_{ij}^{2m+1}$$

A.4.10.

Use of equations A.4.9. and A.4.10. at each time step leads to N sets of N simultaneous equations, where N is the number of nodal points on the space grid. The solution

of these equations is obtained by following the procedure of Peaceman and Rachford.

Consider first the use of equation A.4.9. within the region $0 \leqslant R \leqslant 1$, $0 \leqslant Y \leqslant 1$ for a given time step and axial position, i.e. constant m and j values. Let

$$\left.\begin{aligned}
[G_i]_j &= -\phi^{2m}_{ij+1} + \left(2 - \frac{\delta\alpha}{(\phi^{2m+1}_{ij})^{\frac{1}{2}}}\right)\phi^{2m}_{ij} - \phi^{2m}_{ij-1} \\
[F_i]_j &= \frac{S^2K}{(i-1)\left(1-e^{-\frac{1}{i-1}}\right)} \\
[E_i]_j &= -\left[\frac{S^2K\left(1+e^{-\frac{1}{i-1}}\right)}{(i-1)\left(1-e^{-\frac{1}{i-1}}\right)} + \frac{\delta\alpha}{(\phi^{2m+1}_{ij})^{\frac{1}{2}}}\right] \\
[D_i]_j &= \left([F_i]_j . e^{-\frac{1}{i-1}}\right)
\end{aligned}\right\} \quad \text{A.4.11.}$$

Now at $R = 0$, i.e. $i = 1$, $\frac{\partial}{\partial R}(\bar{P}^2) = 0$, boundary condition expressed in equation A.4.3. Therefore $\phi_{i+1} = \phi_{i-1}$. Equation A.4.9. may be written, using the definition given in equation A.4.10 as

$$[E_1]_j \phi_1 + ([D_1]_j + [F_1]_j)\phi_2 = [G_1]_j \qquad \text{A.4.12.}$$

For $0 < R < 1$, i.e. $1 < i < I$ equation A.4.9. may be

written

$$[D_i]_j \phi_{i-1} + [E_i]_j \phi_i + [F_i]_j \phi_{i+1} = [G_i]_j$$

A.4.13.

Now at R = 1, i.e. i = I, $\frac{\partial}{\partial R}(\overline{P^2}) = 0$, boundary condition expressed in equation A.4.4. Therefore $\phi_{i+1} = \phi_{i-1}$.

Equation A.4.9. may thus be written

$$([D_I]_j + [F_I]_j)\phi_{I-1} + [E_I]_j \phi_I = [G_I]_j$$

A.4.14.

The N simultaneous equations given by equation A.4.12 to A.4.14 may be solved directly by writing

$$\left.\begin{aligned}
a_{1j} &= [E_1]_j \\
a_{ij} &= [E_i]_j - [D_i]_j . b_{i-1j} && 1 < i \leqslant I \\
b_{1j} &= ([D_1]_j + [F_1]_j)/a_{1j} \\
b_{ij} &= [F_i]_j / a_{ij} && 1 < i \leqslant I \\
g_{1j} &= [G_1]_j / a_{1j} \\
g_{ij} &= ([G_i]_j - [D_i]_j . g_{i-1j})/a_{ij} && 1 < i \leqslant I
\end{aligned}\right\} \text{A.4.15}$$

From equation A.4.12 by using the definitions given in equation A.4.15 it can be seen that

$$\phi_1 = g_{1j} - b_{1j}\phi_2 \qquad \text{A.4.16}$$

From equation A.4.13 for i = 2

$$[D_2]_j \phi_1 + [E_2]_j \phi_2 + [F_2]_j \phi_3 = [G_2]_j$$

substituting from equation A.4.16

$$[D_2]_j g_{1j} - [D_2]_j . b_{ij} . \phi_2 + [E_2]_j \phi_2 + [F_2]_j \phi_3 = [G_2]_j$$

hence

$$\phi_2 = g_{2j} - b_{2j} \phi_3$$

This can be shown to hold for all values of i up to i = I-1, simply by repeating the above process for i = 3,4,....I-1. Hence the general equation can be formed

$$\phi_i = g_{ij} - b_{ij} . \phi_{i+1} \quad 1 < i < I$$

A.4.17.

From equation A.4.14 it can be shown that

$$\phi_I = g_{Ij}$$

A.4.18.

Hence the solution of the N simultaneous equations for a given time and axial position is given by: -

$$\left.\begin{aligned} \phi_I &= g_{Ij} \\ \phi_i &= g_{ij} - b_{ij}\phi_{i+1} \qquad 1 \leqslant i < I \end{aligned}\right\} \qquad \text{A.4.19.}$$

Thus a_{ij}, b_{ij} and g_{ij} are computed in order of increasing i and ϕ_i is computed in decreasing order of i. The axial boundaries of the grid must now be considered.

Y = 0, j = 1, $\overline{P}^2 = \overline{P}_s^2$, boundary condition expressed by equation A.4.2. This is so for all time steps and radial position. Hence having once set these values no numerical calculation at this boundary is required.

Y = 1, j = J. At this boundary Reynolds equation for the porous bearing is used to solve the pressure squared values, see Appendix A.3. Remembering that at this time step the equations are written implicit in the R-direction only, this boundary condition may be written as, again using the Roscoe technique : -

$$\frac{1}{(i-1)\left(1-e^{-\frac{1}{i-1}}\right)}\left[\phi_{i+1j}^{2m+1} - \phi_{ij}^{2m+1}\left(1+e^{-\frac{1}{i-1}}\right) + e^{-\frac{1}{i-1}}.\phi_{i-1j}^{2m+1}\right]$$

$$= \frac{\Delta\Delta}{2}\left[\phi_{ij}^{2m} - \phi_{ij-1}^{2m}\right] + \frac{\beta\delta}{(\phi_{ij}^{2m+1})^{\frac{1}{2}}}\left[\phi_{ij}^{2m+1} - \phi_{ij}^{2m}\right]$$

$$+ \frac{\Delta^2\gamma\phi_{ij}^{2m}}{(\phi_{ij}^{2m})^{\frac{1}{2}}} \qquad \text{A.4.20.}$$

Re-arranging equation A.4.20 such that only implicit terms appear on the left hand side of the equation gives

$$\frac{1}{(i-1)\left(1-e^{-\frac{1}{i-1}}\right)}\ \phi_{i+1j}^{2m+1} + e^{-\frac{1}{i-1}}\ \phi_{i-1j}^{2m+1}$$

$$-\frac{\left(1+e^{-\frac{1}{i-1}}\right)}{(i-1)\left(1-e^{-\frac{1}{i-1}}\right)} + \frac{\beta\delta}{(\phi_{ij}^{2m+1})^{\frac{1}{2}}}\ \phi_{ij}^{2m+1}$$

$$= \frac{\Lambda\Delta}{2}\left[\phi_{ij}^{2m} - \phi_{ij-1}^{2m}\right] - \frac{\beta\delta}{(\phi_{ij}^{2m+1})^{\frac{1}{2}}}\cdot\phi_{ij}^{2m} + \frac{\Delta^2\gamma\phi_{ij}^{2m}}{(\phi_{ij}^{2m})^{\frac{1}{2}}}$$

A.4.21

Let

$$\left.\begin{aligned}
[G_i]_J &= \left[\frac{\Lambda\Delta}{2} - \frac{\beta\delta}{(\phi_{ij}^{2m+1})^{\frac{1}{2}}} + \frac{\Delta^2\gamma}{(\phi_{ij}^{2m})^{\frac{1}{2}}}\right]\phi_{ij}^{2m} - \frac{\Lambda\Delta}{2}\phi_{ij-1}^{2m} \\
[F_i]_J &= \frac{1}{(i-1)\left(1-e^{-\frac{1}{i-1}}\right)} \\
[E_i]_J &= -\left[\frac{\left(1+e^{-\frac{1}{i-1}}\right)}{(i-1)\left(1-e^{-\frac{1}{i-1}}\right)} + \frac{\beta\delta}{(\phi_{ij}^{2m+1})^{\frac{1}{2}}}\right] \\
[D_i]_J &= \left([F_i]_J \cdot e^{-\frac{1}{i-1}}\right)
\end{aligned}\right\}\ \text{A.4.22}$$

Now at R = 0, i.e. i = 1, $\frac{\partial}{\partial R}(\overline{P}^2) = 0$, boundary condition expressed in equation A.4.3. Therefore $\phi_{i+1} = \phi_{i-1}$. Equation A.4.21 may be written, using the definitions given in equation A.4.22, as

$$[E_i]_J \phi_1 + ([D_1]_J + [F_1]_J)\phi_2 = [G_1]_J \qquad \text{A.4.23}$$

For 0 < R < 1, i.e. 1 < i < I equation A.4.21 may be written

$$[D_i]_J \phi_{i-1} + [E_i]_J \phi_i + [F_i]_J \phi_{i+1} = [G_i]_J \qquad \text{A.4.24}$$

Now at R = 1, i.e. i = I atmospheric conditions prevail i.e.

$$\overline{P}^2 = 1.0 = \phi_I \qquad \text{A.4.25}$$

The N simultaneous equations formed by equations A.4.23 to A.4.25 may be solved by the technique used previously.

Define

$$\left.\begin{aligned} a_{1J} &= [E_1]_J \\ a_{iJ} &= [E_i]_J - [D_i]_J . b_{i-1J} && 1 < i \leqslant I \\ b_{1J} &= ([D_1]_J + [F_1]_J) / a_{1J} \\ b_{iJ} &= [F_i]_J / a_{iJ} && 1 < i \leqslant I \end{aligned}\right\} \qquad \text{A.4.26}$$

$$g_{iJ} = [G_i]_J \;/\; a_{iJ}$$

$$g_{iJ} = ([G_i]_J - [D_i]_J \cdot g_{i-1J}) \;/\; a_{iJ} \qquad 1 < i \leqslant I$$

} A.4.26

Hence it can be shown the solution is -

$$\phi_I = 1.0$$

$$\phi_i = g_{iJ} - b_{iJ} \cdot \phi_{i+1} \qquad 1 \leqslant i < I$$

} A.4.27

Again a_{iJ}, b_{iJ} and g_{iJ} are computed in order of increasing i and ϕ_i is computed in decreasing order of i. Consider now the next time step for which equation A.4.10. is used. For the region $0 \leqslant Y \leqslant 1$, $0 \leqslant R \leqslant 1$ for a given time value and radial position, let,

$$[G_j]_i = -\frac{S^2K}{(i-1)\left(1-e^{-\frac{1}{i-1}}\right)}\left[\phi_{i+1j}^{2m+1} + \phi_{i-1j}^{2m+1} \cdot e^{-\frac{1}{i-1}}\right]$$

$$+\left[\frac{S^2K\left(1+e^{-\frac{1}{i-1}}\right)}{(i-1)\left(1-e^{-\frac{1}{i-1}}\right)} - \frac{\delta\alpha}{(\phi_{ij}^{2m+2})^{\frac{1}{2}}}\right]\phi_{ij}^{2m+1}$$

$$[F_j]_i = 1.0$$

$$[E_j]_i = -\left(2 + \frac{\delta\alpha}{(\phi_{ij}^{2m+2})^{\frac{1}{2}}}\right)$$

$$[D_j]_i = 1.0$$

} A.4.28

Equation A.4.10 may be written

$$[D_j]_i \phi_{j-1} + [E_j]_i \phi_j + [F_j]_i \phi_{j+1} = [G_j]_i \qquad \text{A.4.29}$$

at Y = 0, i.e. j = 1 $\overline{P}^2 = \overline{P}_s^2$ hence no computation required. At Y = 1, i.e. j = J the Reynolds equation holds. The Reynolds equation written in this case implicit in the Y-direction and re-orientated such that implicit terms only appear on the left hand side of the equation is:

$$\left[\frac{\Lambda\Delta}{2} + \frac{\beta\delta}{(\phi_{ij}^{2m+2})^{\frac{1}{2}}} \right] \phi_{ij}^{2m+2} - \frac{\Lambda\Delta}{2} \cdot \phi_{ij-1}^{2m+2} = \frac{\Delta^2\gamma}{(\phi_{ij}^{2m+1})^{\frac{1}{2}}} \cdot \phi_{ij}^{2m+1}$$

$$+ \frac{1}{(i-1)\left(1-e^{-\frac{1}{i-1}}\right)} \left[\phi_{i+1j}^{2m+1} + e^{-\frac{1}{i-1}} \cdot \phi_{i-1j}^{2m+1} \right]$$

$$- \left[\frac{\left(1 + e^{-\frac{1}{i-1}}\right)}{(i-1)\left(1-e^{-\frac{1}{i-1}}\right)} - \frac{\beta\delta}{(\phi_{ij}^{2m+2})^{\frac{1}{2}}} \right] \phi_{ij}^{2m+1} \qquad \text{A.4.30}$$

Let

$$[G_J]_i = \frac{\Delta^2\gamma}{(\phi_{ij}^{2m+1})^{\frac{1}{2}}} \cdot \phi_{ij}^{2m+1} + \frac{1}{(i-1)\left(1-e^{-\frac{1}{i-1}}\right)} \cdot$$

$$\left[\phi_{i+1j}^{2m+1} + e^{-\frac{1}{i-1}} \cdot \phi_{i-1j}^{2m+1} \right] - \left[\frac{\left(1 + e^{-\frac{1}{i-1}}\right)}{(i-1)\left(1-e^{-\frac{1}{i-1}}\right)} \right.$$

$$\left. - \frac{\beta\delta}{(\phi_{ij}^{2m+2})^{\frac{1}{2}}} \right] \phi_{ij}^{2m+1}$$

A.4.31

$$\left.\begin{aligned} [E_J]_i &= \left[\frac{\Delta\Delta}{2} + \frac{\beta\delta}{(\phi_{ij}^{2m+2})^{\frac{1}{2}}} \right] \\ [D_J]_i &= \frac{\Delta\Delta}{2} \end{aligned}\right\} \quad \text{A.4.31 cont.}$$

Thus

$$[D_J]_i \cdot \phi_{J-1} + [E_J]_i \phi_J = [G_J]_i \qquad \text{A.4.32}$$

Now let

$$\left.\begin{aligned} a_{2i} &= [E_2]_i \\ a_{ji} &= [E_j]_i - [D_j]_i \cdot b_{j-1i} \qquad 2 < j \leqslant J \\ g_{2i} &= ([G_2]_i - [D_2]_i \cdot \bar{P}_s^2) / a_{2i} \\ g_{ji} &= [G_j]_i - [D_j]_i \cdot g_{j-1i} / a_{ji} \qquad 2 < j \leqslant J \\ b_{ji} &= f_{ji} / a_{ji} \end{aligned}\right\} \quad \text{A.4.33}$$

The solution of the set of simultaneous equation expressed by equation A.4.29 and A.4.32 is given by

$$\left.\begin{aligned} \phi_{Ji} &= g_{Ji} \\ \phi_{ji} &= g_{ji} - b_{ji} \cdot \phi_{j+1} \qquad 1 < j < J \end{aligned}\right\} \quad \text{A.4.34}$$

also

$$\phi_{1i} = \overline{P}_s^2 \qquad \text{A.4.35}$$

Again a_{ji}, b_{ji} and g_{ji} are computed in increasing order of j and ϕ_j computed in order of decreasing j. The radial boundary conditions must now be considered R = 0, i.e. i = 1.

$$Y = 0 \text{ i.e. } j = 1 \quad \phi_1 = \overline{P}_s^2$$

$$0 < Y < 1 \quad \text{i.e. } 1 < j < J$$

only the definition of $[G_j]_i$ need be modified as the other term definitions are identical to the previous section

$$[G_j]_{i=1} = -\left[\frac{S^2K\left(1 + e^{-\frac{1}{i-1}}\right)}{(i-1)\left(1-e^{-\frac{1}{i-1}}\right)}\right]\phi_{i+1j}^{2m+1}$$

$$+\left[\frac{S^2K\left(1 + e^{-\frac{1}{i-1}}\right)}{(i-1)\left(1-e^{-\frac{1}{i-1}}\right)} - \frac{\delta\alpha}{(\phi_{ij}^{2m+2})^{\frac{1}{2}}}\right]\phi_{ij}^{2m+1}$$

A.4.36

Use has been made of the boundary conditions expressed in equation A.4.3.

$$Y = 1, \quad j = J$$

Again only the definition of $[G_J]_i$ need be modified.

$$[G_J]_{i=1} = \frac{\Delta^2\gamma}{(\phi_{ij}^{2m+1})^{\frac{1}{2}}}\phi_{ij}^{2m+1} + \frac{\left(1+e^{-\frac{1}{i-1}}\right)}{(i-1)\left(1-e^{-\frac{1}{i-1}}\right)}\phi_{i+1j}$$

$$-\left[\frac{\left(1+e^{-\frac{1}{i-1}}\right)}{(i-1)\left(1-e^{-\frac{1}{i-1}}\right)} - \frac{\beta\delta}{(\phi_{ij}^{2m+2})^{\frac{1}{2}}}\right]\phi_{ij}^{2m+1}$$

A.4.37

The solution of this set of simultaneous equations is then identical to the previous set.

$R = 1, \quad i = I$

$Y = 0$, i.e. $j = 1 \quad \phi_1 = \overline{P}_s^2$

$0 < Y < 1$, i.e. $1 < j < J$

$$[G_j]_{i=I} = -\frac{S^2K\left(1+e^{-\frac{1}{i-1}}\right)}{(i-1)\left(1-e^{-\frac{1}{i-1}}\right)}\phi_{i-1}$$

$$+\left[\frac{S^2K\left(1+e^{-\frac{1}{i-1}}\right)}{(i-1)\left(1-e^{-\frac{1}{i-1}}\right)} - \frac{\delta\alpha}{(\phi_{ij}^{2m+2})^{\frac{1}{2}}}\right]\phi_{ij}^{2m+1}$$

A.4.38

Use has been made of the boundary condition expressed in equation A.4.4.

$$Y = 1, \qquad j = J$$

$$\phi_I = 1.0$$

Hence the simultaneous equations to be solved are

$$\left.\begin{aligned} \phi_1 &= \overline{P}_s^2 \\ [D_j]_i \phi_j + [E_j]_i \phi_j + [F_j]_i \phi_{j+1} &= [G_j]_i \quad 1 < j < J \\ \phi_I &= 1.0 \end{aligned}\right\} \text{A.4.39}$$

Using the nomenclature of the previous solution this solution is given by

$$\left.\begin{aligned} \phi_J &= 1.0 \\ \phi_j &= g_{ji} - b_{ji}\phi_{j-1} \quad 1 < j < J \\ \phi_1 &= \overline{P}_s^2 \end{aligned}\right\} \text{A.4.40}$$

Once again a_{ij}, b_{ij}, and g_{ij} are solved for increasing order of j and ϕj for decreasing order of j.

Hence the N sets of N simultaneous equations can be solved. However, iteration is required as some of the terms expressed in the functions nominated as

$$[G_i]_j, [G_j]_i, [G_i]_J, [G_j]_I, [E_i]_j, [E_i]_J,$$

$$[E_j]_I, [E_j]_i.$$

have forward time positions.

The technique of solution by computer then is -

(a) Initialise values of ϕ_{ij}^m for $1 \leqslant i \leqslant I$, $1 \leqslant j \leqslant J$ and $1 \leqslant m \leqslant \underline{M}$.

(b) Solve using A.D.I. for ϕ_{ij}^m for $1 \leqslant i \leqslant I$, $1 \leqslant j \leqslant J$ and $1 \leqslant m \leqslant \underline{M}$.

(c) Test for convergence i.e. compare $\phi_{ij\ old}^m$ against $\phi_{ij\ new}^m$ for $1 \leqslant i \leqslant I$, $1 \leqslant j \leqslant J$, $1 \leqslant m \leqslant \underline{M}$.

(d) Use values of $\phi_{ij}^{\underline{M}}$ previously calculated in (b) to initiate ϕ_{ij}^1.

(e) Repeat (b), (c) and (d) until convergence.

APPENDIX FIVE

ERROR ANALYSIS OF A.D.I. SCHEME

APPENDIX FIVE

ERROR ANALYSIS OF A.D.I. SCHEME

In the A.D.I. procedure two different equations are used. These are dealt with separately.

In this error analysis it is assumed that the errors involved are small.

The first step in the A.D.I. scheme uses equation A.4.9, Appendix 4.

$$\frac{S^2K}{(i-1)\left(1-e^{-\frac{1}{i-1}}\right)}\left[\phi_{i+1j}^{2m+1}+\phi_{i-1j}^{2m+1}\right]-\left[\frac{S^2K\left(1+e^{-\frac{1}{i-1}}\right)}{(i-1)\left(1-e^{-\frac{1}{i-1}}\right)}\cdots\right.$$

$$\left..+\frac{\delta\alpha}{(\phi_{ij}^{2m+1})^{\frac{1}{2}}}\right]\phi_{ij}^{2m+1}=-\phi_{ij}^{2m}+\left[2-\frac{\delta\alpha}{(\phi_{ij}^{2m+1})^{\frac{1}{2}}}\right]\phi_{ij}^{2m}-\phi_{ij-1}^{2m} \qquad \text{A.5.1}$$

Assume that the initial error in initiated values of ϕ_{ij}^{2m} are such that we may write

$$[\phi_{ij}^{2m}]=[\phi_{ij}^{2m}]_T+\Sigma_{ij}^{2m} \qquad \text{A.5.2}$$

where $[\phi_{ij}^{2m}]$ is the initiated value

$[\phi_{ij}^{2m}]_T$ is the true value

Σ_{ij}^{2m} is the error.

Substitution of equation A.5.2 into equation A.5.1 yields

$$\frac{S^2K}{(i-1)\left(1-e^{-\frac{1}{i-1}}\right)}\left[\left[\phi_{ij}^{2m+1}\right]+e^{-\frac{1}{i-1}}\left(\left[\phi_{i-1j}^{2m+1}\right]\right)\right]-\ \ldots\ldots$$

$$\ldots\left[\frac{S^2K\left(1+e^{-\frac{1}{i-1}}\right)}{(i-1)\left(1-e^{-\frac{1}{i-1}}\right)}+\frac{\delta\alpha}{\left(\left[\phi_{ij}^{2m+1}\right]\right)^{\frac{1}{2}}}\right]\phi_{ij}^{2m+1}\ =-\ \phi_{ij}^{2m}$$

$$+\left[2-\frac{\delta\alpha}{\left(\left[\phi_{ij}^{2m+1}\right]\right)^{\frac{1}{2}}}\right]\left[\phi_{ij}^{2m}\right]-\left[\phi_{ij-1}^{2m}\right] \qquad \text{A.5.3.}$$

Now the true values of ϕ must satisfy equation A.5.1. By subtracting equation A.5.1. from equation A.5.3. an equation regarding the error in the initiated values will be formed. However, upon inspection of the second term on the left hand side and the second term of the right hand side of these equations it can be seen that the denominator of the terms containing $\delta\alpha$ changes and hence straight forward subtraction will not yield the desired result. This is because the equations are not linear. However, as it has been assumed that the error involved is small the square rooting of these terms halves the error involved. Hence assume that

$$\frac{1}{([\phi_{ij}^{2m}])^{\frac{1}{2}}} = \frac{1}{([\phi_{ij}^{2m}]_T)^{\frac{1}{2}}} = \frac{1}{(\phi_{ij}^{2m})^{\frac{1}{2}}}$$

Hence the analysis can continue. Upon subtraction we get -

$$\frac{S^2K}{(i-1)\left(1-e^{-\frac{1}{i-1}}\right)}\left[\Sigma_{i+1j}^{2m+1} + e^{-\frac{1}{i-1}} \cdot \Sigma_{i-1j}^{2m+1}\right]$$

$$-\left[\frac{S^2K\left(1+e^{-\frac{1}{i-1}}\right)}{(i-1)\left(1-e^{-\frac{1}{i-1}}\right)} + \frac{\delta\alpha}{(\phi_{ij}^{2m})^{\frac{1}{2}}}\right] \Sigma_{ij}^{2m+1}$$

$$= -\Sigma_{ij+1}^{2m} + \left(2 - \frac{\delta\alpha}{(\phi_{ij}^{2m+1})^{\frac{1}{2}}}\right) \Sigma_{ij}^{2m} - \Sigma_{ij-1}^{2m} \qquad \text{A.5.4.}$$

Now expressing the error as a finite double series of orthogonal functions that satisfies the boundary conditions

$$\Sigma_{ij}^{2m} = \sum_{i=1}^{I} \sum_{j=1}^{J} A_{ij}^{2m} \cos(\psi_i R) \cos(\psi_j (1-Y)) \qquad \text{A.5.5.}$$

where

$$\psi_i = 2\pi_i, \quad \psi_j = (2_{j+1})\pi/2$$

Substituting equation A.5.5. into equation A.5.4. gives,

examining each term in the series separately.

$$A_{ij}^{2m+1}\left[\frac{S^2K}{(i-1)\left(1-e^{-\frac{1}{i-1}}\right)}\left[\cos(\psi_i(R+\Delta))\cos(\psi_j(1-Y))\right.\right.$$

$$\left.+\ e^{-\frac{1}{i-1}}\cdot\left[\cos(\psi_i(R-\Delta))\cos(\psi_j(1-Y))\right]\right]-\left[\frac{S^2K\left(1+e^{-\frac{1}{i-1}}\right)}{(i-1)\left(1-e^{-\frac{1}{i-1}}\right)}\right.$$

$$\left.+\ \frac{\delta\alpha}{(\phi_{ij}^{2m+1})^{\frac{1}{2}}}\right]\cos(\psi_iR)\cos(\psi_j(1-Y))\Big] = A_{ij}^{2m}\Big[-\cos(\psi_iR)\cos\ \ldots$$

$$\ldots\ (\psi_j((1-Y)+\Delta))\ +\left(2-\frac{\delta\alpha}{(\phi_{ij}^{2m+1})^{\frac{1}{2}}}\right)\cos(\psi_iR)\cos(\psi_j(1-Y))\ \ldots$$

$$\ldots-\cos(\psi_iR)\cos(\psi_j((1-Y)-\Delta))\Big] \qquad \text{A.5.6.}$$

Dividing equation A.5.6. by $A_{ij}^{2m}\cos(\psi_iR)\cos(\psi_j(1-Y))$ gives

$$\frac{A_{ij}^{2m+1}}{A_{ij}^{2m}}\left[\frac{S^2K}{(i-1)\left(1-e^{-\frac{1}{i-1}}\right)}\left[\frac{\cos(\psi_i(R+\Delta))}{\cos(\psi_iR)}+e^{-\frac{1}{i-1}}\left[\frac{\cos(\psi_i(R-\Delta))}{\cos(\psi_iR)}\right]\right]\right.$$

$$\left.-\left[\frac{S^2K\left(1+e^{-\frac{1}{i-1}}\right)}{(i-1)\left(1-e^{-\frac{1}{i-1}}\right)}+\frac{\delta\alpha}{(\phi_{ij}^{2m+1})^{\frac{1}{2}}}\right]\right] =$$

$$-\frac{\cos(\psi_j((1-Y)+\Delta)}{\cos(\psi_i(1-Y))}+\left(2-\frac{\delta\alpha}{(\phi_{ij}^{2m+1})^{\frac{1}{2}}}\right)-\frac{\cos(\psi_j((1-Y)-\Delta)}{\cos(\psi_j(1-Y))}$$

A.5.7.

Now

$$2\cos(\psi_j\Delta) = \frac{\cos(\psi_j((1-Y)+\Delta) + \cos(\psi_j((1-Y)-\Delta)}{\cos(\psi_j(1-Y))} \qquad \text{A.5.8.}$$

Also the left hand side of the equations can be reduced to

$$\frac{A_{ij}^{2m+1}}{A_{ij}^{2m}}\left[\frac{S^2K\left(1+e^{-\frac{1}{i-1}}\right)}{(i-1)\left(1-e^{-\frac{1}{i-1}}\right)}\left[\cos(\psi_i\Delta)-1\right] - \frac{S^2K}{(i-1)}\cdots\right.$$

$$\left.\cdots\ \tan(\psi_i R)\sin(\psi_i\Delta) - \frac{\delta\alpha}{(\phi_{ij}^{2m+1})^{\frac{1}{2}}}\right] \qquad \text{A.5.9.}$$

Equation A.5.7. after re-arrangement may be written: -

$$\frac{A_{ij}^{2m+1}}{A_{ij}^{2m}} = \left[\frac{2 - \frac{\delta\alpha}{(\phi_{ij}^{2m+1})^{\frac{1}{2}}} - 2\cos(\psi_i\Delta)}{\frac{S^2K}{(i-1)\left(1-e^{-\frac{1}{i-1}}\right)}\left[\cos(\psi_i\Delta)-1\right] - \frac{S^2K}{(i-1)}\cdot\tan(\psi_i R)\sin(\psi_i\Delta) - \frac{\delta\alpha}{(\phi_{ij}^{2m+1})^{\frac{1}{2}}}}\right]$$

A.5.10

The ratio of $A_{ij}^{2m+1}/A_{ij}^{2m}$ is the amplification factor for the numerical procedure, using only equation A.5.1. The second part of the numerical procedure uses equation A.4.10 Appendix 4.

$$\phi_{ij+1}^{2m+2} - \left[2 - \frac{\delta\alpha}{(\phi_{ij}^{2m+2})^{\frac{1}{2}}} \right] + \phi_{ij-1}^{2m+2}$$

$$= - \frac{S^2K(\phi_{i+1j}^{2m+1} + e^{-\frac{1}{i-1}} \cdot \phi_{i-1j}^{2m+1})}{(i-1)\left(1 - e^{-\frac{1}{i-1}}\right)} + \left[\frac{S^2K\left(1+e^{-\frac{1}{i-1}}\right)}{(i-1)\left(1-e^{-\frac{1}{i-1}}\right)} \right.$$

$$\left. - \frac{\delta\alpha}{(\phi_{ij}^{2m+2})^{\frac{1}{2}}} \right] \phi_{ij}^{2m+1} \qquad \text{A.5.11.}$$

Using a procedure identical to the one previously used to obtain an equation regarding the error gives

$$\Sigma_{ij+1}^{2m+2} - \left(2 + \frac{\delta\alpha}{(\phi_{ij}^{2m+2})^{\frac{1}{2}}} \right) \Sigma_{ij}^{2m+2} + \Sigma_{ij-1}^{2m+2}$$

$$= - \frac{S^2K\left(\Sigma_{i+1j}^{2m+1} + e^{-\frac{1}{i-1}} \Sigma_{i-1j}^{2m+1}\right)}{(i-1)\left(1 - e^{-\frac{1}{i-1}}\right)} + \left[\frac{S^2K\left(1+e^{-\frac{1}{i-1}}\right)}{(i-1)\left(1-e^{-\frac{1}{i-1}}\right)} \right.$$

$$\left. - \frac{\delta\alpha}{(\phi_{ij}^{2m+2})^{\frac{1}{2}}} \right] \Sigma_{ij}^{2m+1} \qquad \text{A.5.12}$$

Substituting from equation A.5.5. into equation A.5.12 and examining each term separately leads to -

$$\frac{A_{ij}^{2m+2}}{A_{ij}^{2m+1}} = \left[\frac{\frac{S^2K\left(1+e^{-\frac{1}{i-1}}\right)}{(i-1)\left(1-e^{-\frac{1}{i-1}}\right)}\left(\cos(\psi_i\Delta) - 1\right) - \frac{S^2K}{(i-1)}\left[\tan(\psi_i R)\sin(\psi_i\Delta)\right] + \frac{\delta\alpha}{(\phi_{ij}^{2m+2})^{\frac{1}{2}}}}{\left[2 + \frac{\delta\alpha}{(\phi_{ij}^{2m+2})^{\frac{1}{2}}} - 2\cos(\psi_j\Delta)\right]} \right]$$

A.5.13.

The ratio of A_{ij}^{2m+2} / A_{ij}^{2m+1} is the amplification factor for the numerical procedure using only equation A.511. Multiplying equations A.5.10 and A.5.13 gives the amplification factor for the use of two time step equations. Remembering that

$$\cos 2A = 1 - 2\sin^2 A$$

the multiplication of the two equations A.5.10 and A.5.13. gives

$$\frac{A_{ij}^{2m+2}}{A_{ij}^{2m}} = \frac{\left[E_1 - \frac{\delta\alpha}{(\phi_{ij}^{2m+1})^{\frac{1}{2}}}\right]\left[E_2 - E_3 + \frac{\delta\alpha}{(\phi_{ij}^{2m+2})^{\frac{1}{2}}}\right]}{\left[E_1 + \frac{\delta\alpha}{(\phi_{ij}^{2m+2})^{\frac{1}{2}}}\right]\left[E_2 - E_3 - \frac{\delta\alpha}{(\phi_{ij}^{2m+1})^{\frac{1}{2}}}\right]}$$

A.5.14.

where

$$\left.\begin{aligned} E_1 &= 4\sin^2\left(\frac{\psi_i \Delta}{2}\right) \\ E_2 &= \frac{S^2 K\left(1+e^{-\frac{1}{i-1}}\right)}{(i-1)\left(1-e^{-\frac{1}{i-1}}\right)} \cdot (\cos(\psi_i \Delta) - 1 \\ E_3 &= \left(\frac{S^2 K}{i-1}\right)(\tan(\psi_i R)\sin\psi_i \Delta) \end{aligned}\right\} \quad \text{A.5.15}$$

Evaluation of the trigonometric functions show that

$$\begin{aligned} 0 \leqslant E_1 &\leqslant 4 \\ E_2 &\leqslant 0 \\ -\infty \leqslant E_3 &\leqslant \infty \end{aligned}$$

By substituting the above values into equation A.5.15. it can be seen that the amplification factor modulas can never be greater than unity. Therefore the numerical procedure is inherently stable for all values of time step.

APPENDIX SIX

THE CONVERGENCE OF THE NUMERICAL SYSTEM

APPENDIX SIX

THE CONVERGENCE OF THE NUMERICAL SYSTEM

Although the numerical method outlined in Appendix 4 has been shown to be inherently stable the convergence rate of this numerical method may be slow, i.e. the amplification factor modulas mentioned in Appendix 5 may be close to unity, giving high computational run time and thus high computer costs. If this is so, then the rate of convergence must be increased purely for economical reasons. This increase in convergence rate can be achieved by using an 'Extrapolated Liebmann Relaxation Parameter' (76).

In order to verify the need for a relaxation parameter a computer analysis using the numerical method given in Appendix 4 was made. The convergence rate was such that the computational run time was prohibitive, approximately 5000 mill units (where 1 mill unit is approximately one second). This programme was run for only 2000 mill and the convergence rate achieved is shown in figure 111 page 354

In (76) an analytic method is outlined to obtain an optimum relaxation parameter for a system of equations. However, Frankel states that 'The usefulness of the extrapolated Liebmann method is limited by the difficulty of determining the optimum relaxation parameter value for

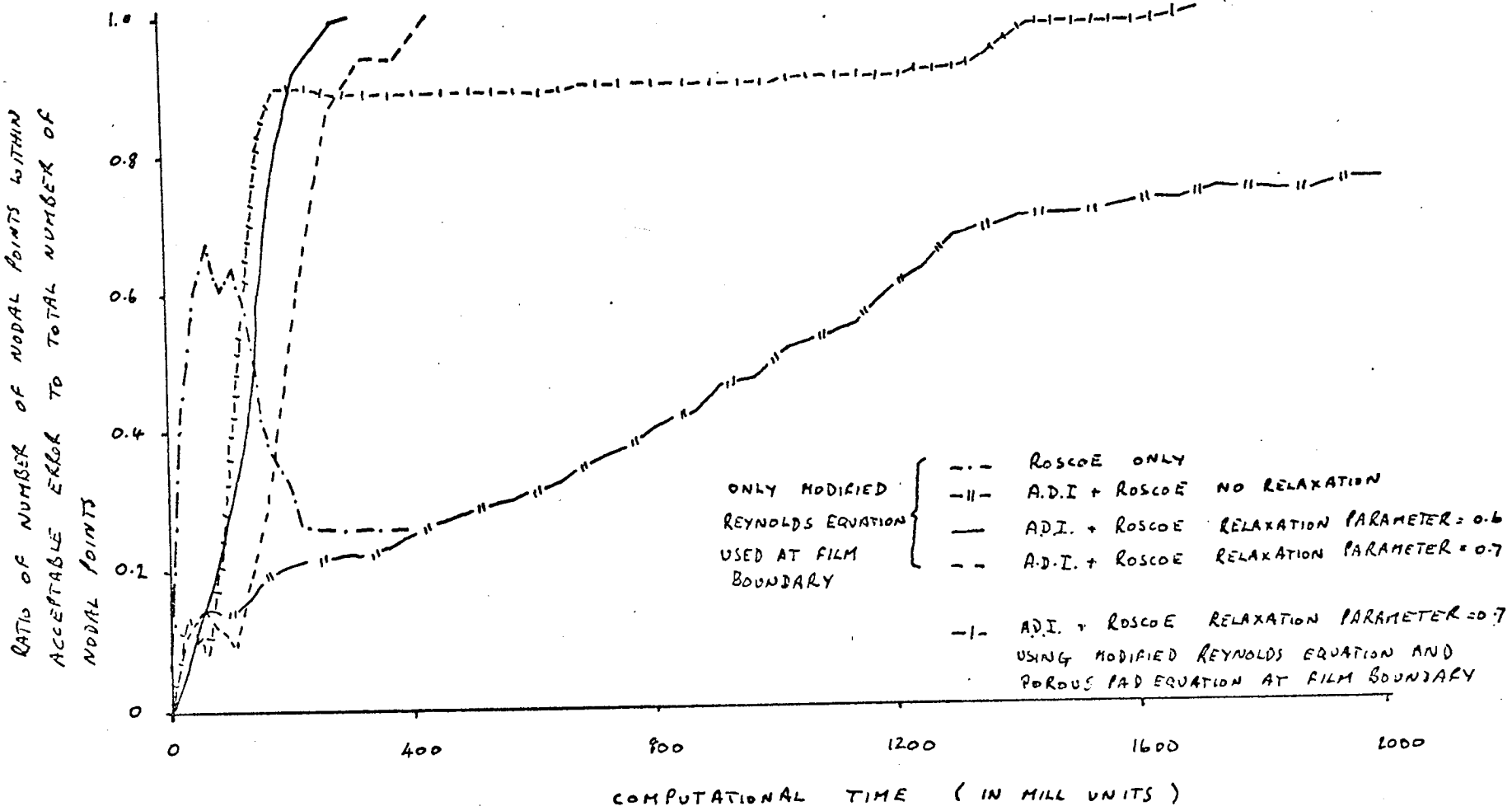

Figure 111 Variation of Convergence Rates for Various Numerical Methods

more complex problems'. Thus an empirical technique was employed to optimise the relaxation parameter value.

Using Frankel's definition of the relaxation parameter, i.e.

$$0 < Rel < 1$$

$$\phi_{new} = (1 - Rel)\ \phi_{old} + Rel \quad \text{(difference equation)}$$

the above computer program was modified such that a relaxation parameter (rel) was used for eight iterations and the resulting number of converged points outputed for each iteration. The relaxation parameter was changed and the above process was repeated from the same start point. The resulting convergence rates for various relaxation parameters are shown in figure 112, page 356 Figure 113, page 357 shows the convergence rate after eight iterations for each relaxation parameter. From figure 113, page 357 it can be seen that the optimum value of the relaxation parameter is approximately 0.6.

This relaxation parameter value was then used to obtain a full solution and the resulting convergence time is shown in figure 111, page 354 . Also shown is a computational run using a relaxation parameter value of 0.7. It can be seen that, in comparison to the non-relaxed computation run, the convergence time for a relaxation parameter of 0.7 as compared to 0.6 is not

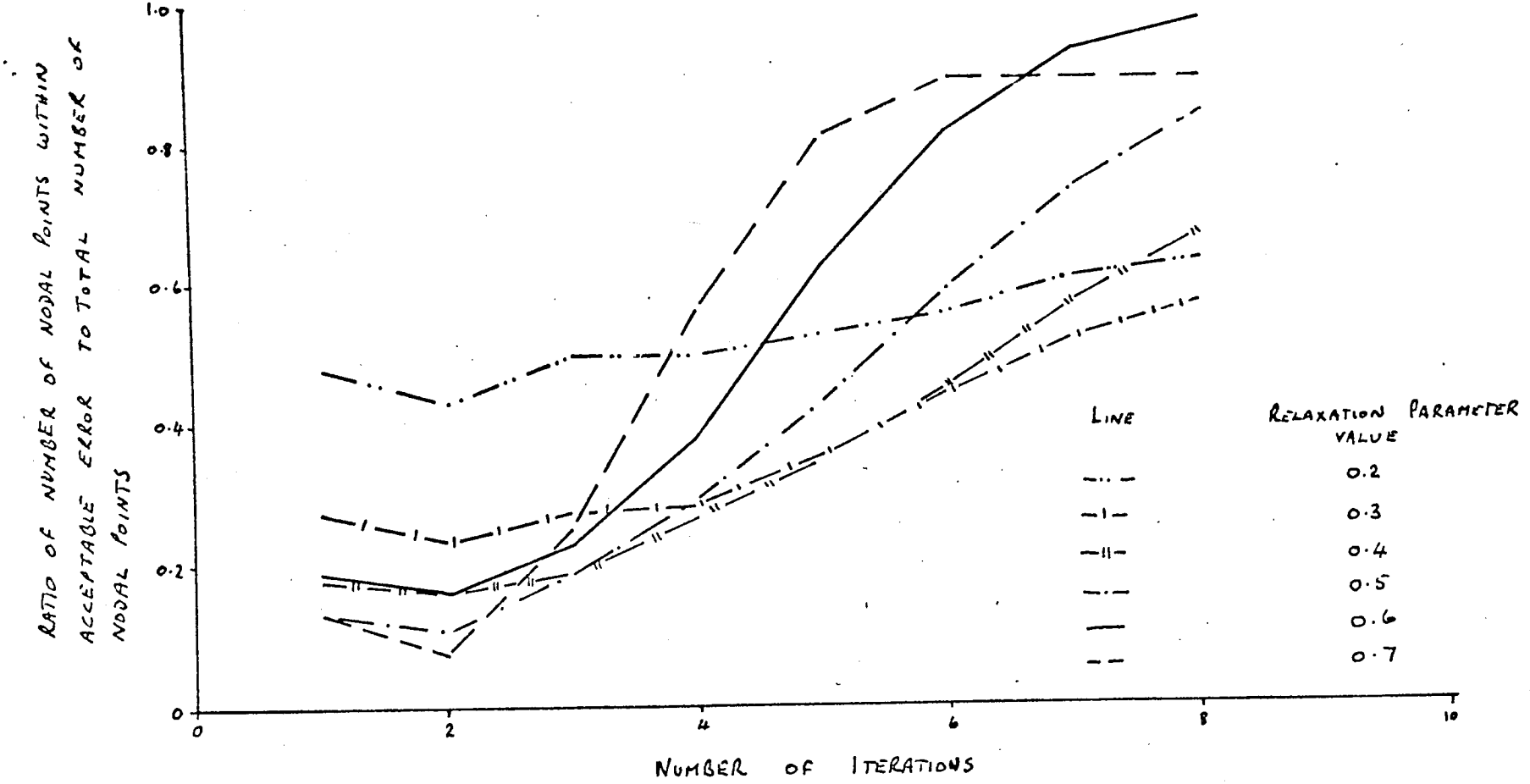

Figure 112 Variation of Convergence for Various Values of Relaxation Parameter

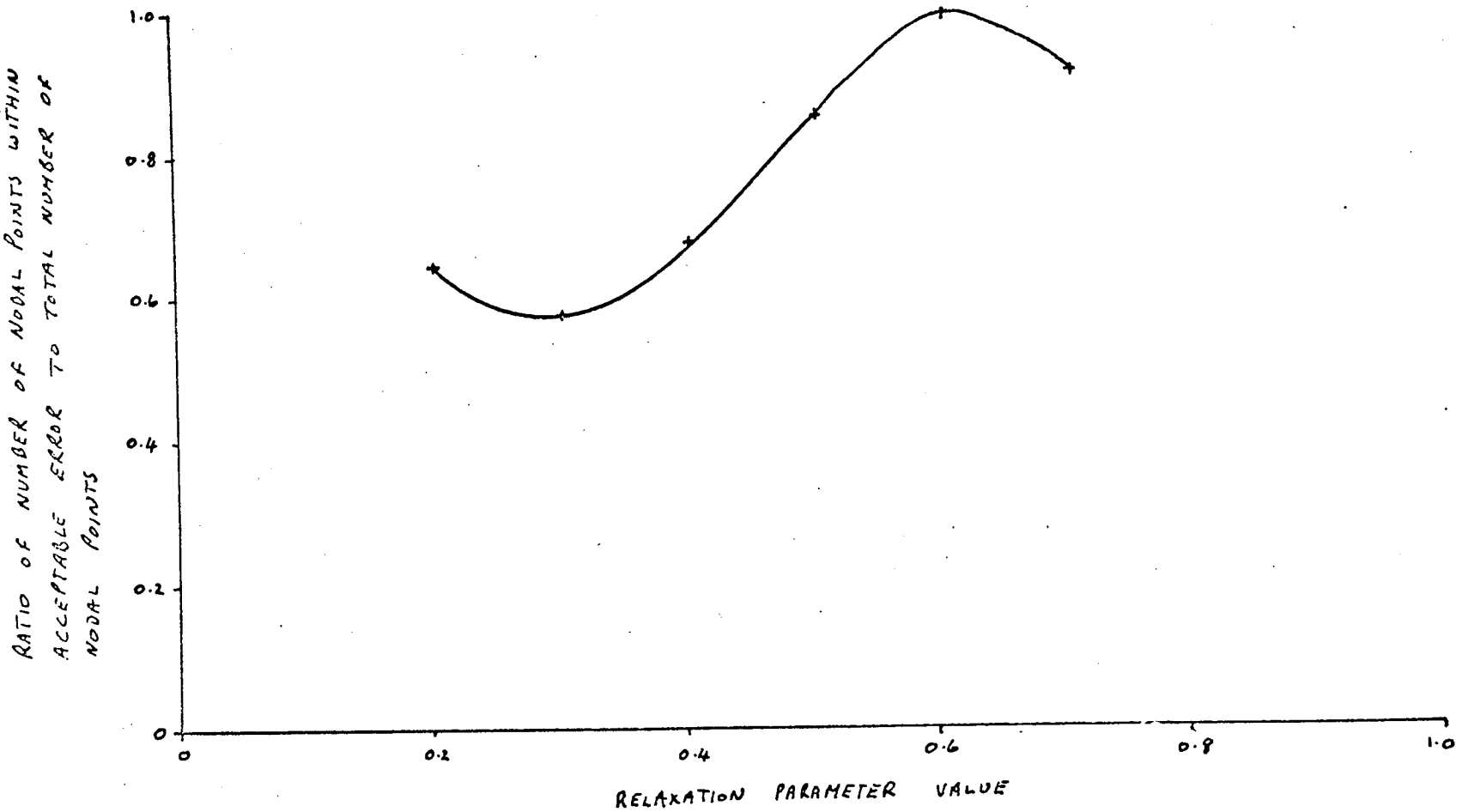

Figure 113 Variation of Convergence after Eight Iterations with Relaxation Parameter

drastically increased.

The relaxation parameter optimum may depend upon bearing parameters, however, more computational time may be spent determining optimum values of the relaxation parameter for each bearing configuration than assuming the optimum value for all bearing configurations is 0.6. Thus for all computation a relaxation parameter value of 0.6 has been used.

It may be recalled that in Appendix 3 it was stated that only Reynolds equation is used at the boundary marked by the gas film in solving pressure distributions. The combination of the Reynolds equation with the main governing differential equation mathematically assumes a continuity in the pressure gradient. It is known that there would then be a conflict in assumptions as it has previously been assumed that the pressure does not vary across the gas film. This conflict of assumptions would lead to greater computational run time. To show that this is so, a computational run was made where both the governing differential equation and the Reynolds equation were used, i.e. no discontinuity in the pressure gradient. It can be seen in figure 111, page 354 that the convergence time is greatly increased.

APPENDIX 7

COMPUTER PROGRAMMES

COMPUTER PROGRAMME FOR DETERMINING THE STEADY-STATE PERFORMANCE DATA FOR A UNIFORM FILM AIR LUBRICATED POROUS THRUST BEARING USING THE ANALYTIC SOLUTION OF JONES ET. AL.

```
      MASTER(ROY)
C    LOAD CARRYING CAPACITY AND FLOW RATES USING JONES-DARCY THEORY
C   FOR UNIFORM FILM AND 100% SUPPLY AREA UNDER STEADY STATE CONDITIONS
      DIMENSION A(50),EN(50),ALAM(50),B(50),C(50),P(101),V(50),PHI(11)
      DIMENSION CN(50),ROY(101)
C     READING IN ROOTS OF EQUATION JO(KN)=0
      DO 4 I=1,50
      READ(1,3) A(I)
    3 FORMAT(E0.0)
    4 CONTINUE
      DENSE=0.001248
      VISCE=0.01812
C UNITS OF PAD PERMEABILITY ARE CM**2
C UNITS OF PRESSURE ARE BARS
      READ(1,6)PA,PERMY
    6 FORMAT(2E0.0)
      PERMY=PERMY/100000.0
      PERMY=PERMY/100000.0
   16 READ(1,8) AK
    8 FORMAT(E0.0)
      IF(AK.EQ.0.0)GOTO31
C UNITS OF PAD THICKNESS AND RADUS ARE CM
      READ(1,5)H,OR
    5 FORMAT(2E0.0)
      S=H/OR
      PERMR=PERMY*AK
      I=0
    7 I=I+1
      ALAM(I)=S*A(I)*SQRT(AK)
      CALL F4J0 (A(I),B(I))
      IF(I.LT.50)GOTO7
 2002 READ(1,2001)PS
 2001 FORMAT(E0.0)
      IF(PS.EQ.0.0)GOTO16
      WRITE(2,1001) PS,PA,PERMY,OR,H
 1001 FORMAT(F6.3,6X,F6.3,6X,1PE20.10,6X,1PE10.3,6X,1PE10.3)
      PS=PS+PA
```

```
      PBARS=(PS/PA)**2
   11 READ(1,12)BEARNO
   12 FORMAT(E0.0)
      IF(BEARNO.EQ.0.0)GOTO2002
      SUMEN=0
      SUMEN2=0.0
      I=0
   13 I=I+1
      EN(I)=ALAM(I)/(A(I)*A(I)*(BEARNO*ALAM(I) + A(I)*A(I)*TANH(ALAM(I))
     1))
      SUMEN=SUMEN + EN(I)
      SUMEN2=SUMEN2+((EN(I)*A(I))**2)

      IF(I.LT.50)GOTO13
      CONST2=(PBARS - 1.0)/(BEARNO*BEARNO*SUMEN - BEARNO/8.0 - 1.0)
      CONST1=(-1)*BEARNO*((CONST2)**2)*(2.0*BEARNO*SUMEN-BEARNO*BEARNO*S
     9UMEN2-1.0/8.0)/(PBARS-1.0)
      I=0
   14 I=I+1
      C(I)=BEARNO*CONST2/(B(I)*(A(I)*A(I)*SINH(ALAM(I)) + BEARNO*ALAM(I)
     9*COSH(ALAM(I))))
      CN(I)=C(I)*(1.0+CONST1/CONST2-BEARNO*ALAM(I)/(A(I)*A(I)*TANH(AL
     9AM(I))+BEARNO*ALAM(I)))

      IF(I.LT.50)GOTO14
      DO 15 IR=1,101
      R=((IR*1.0) - 1.0)/100.0
      IF(IR.EQ.1)GOTO17
      IF(IR.EQ.101)GOTO18
      SUM=0

      SUM1=0.0
      N=0
   19 N=N+1
      CALL F4J0 ((R*A(N)),V(N))
      TERM=ALAM(N)*C(N)*(B(N)-V(N))*COSH(ALAM(N))/(A(N)*A(N))
      TERM1=TERM+TERM*CN(N)/C(N)
      SUM=SUM + TERM
```

```
      SUM1=SUM1+TERM1
      IF(N.LT.50)GOTO19
      PSQ=1.0 + BEARNO*CONST2*((R*R) - 1.0)/4.0 + BEARNO*SUM
      P(IR)=SQRT(PSQ)
      ROY(IR)=(((R*R)-1.0)*(CONST2+CONST1)/4.0+SUM1)/P(IR)

      GOTO15
   17 J=0
      SUM=0
      SUM1=0.0
   23 J=J+1
      TERM=ALAM(J)*C(J)*(B(J) - 1.0)*COSH(ALAM(J))/(A(J)*A(J))
      TERM1=TERM+TERM*CN(J)/C(J)
      SUM=SUM + TERM
      SUM1=SUM1+TERM1
      IF(J.LT.50)GOTO23
      PSQ=1.0-BEARNO*CONST2/4.0+BEARNO*SUM
      P(IR)=SQRT(PSQ)
      ROY(IR)=((-.25)*(CONST2+CONST1)+SUM1)/P(IR)
      GOTO15
   18 P(IR)=1.0

      ROY(IR)=0.0
   15 CONTINUE
      DO 401IR=1,101,10
      WRITE(2,400)P(IR)
  400 FORMAT(1PE15.8)
  401 CONTINUE
   81 WBAR=0.0
      DO 27 IR=1,101

      R=((IR*1.0)-1.0)/100.0
      ROY(IR)=ROY(IR)*R
   27 P(IR)=(P(IR)-1.0)*R
      ROD=0.0
      REVE=0.0
      RODD=0.0
```

```
      REVEN=0.0
      DO 25 IR=2,98,2
      ROD=ROD+ROY(IR+1)
      REVE=REVE+ROY(IR)
      RODD=RODD+P(IR+1)
   25 REVEN=REVEN+P(IR)
      REVE=REVE+ROY(100)
      REVEN=REVEN+P(100)
      WBAR=4.0*REVEN+2.0*RODD
      WBAR=WBAR/300.0
   83 WBAR=2.0*WBAR/((PS/PA)-1.0)
      W=WBAR*3.14159265*OR*OR*(PS-PA)*10.0/9.81
CUNITS OF FLOWRATE ARE CM↑3/MIN
      FRBAR=CONST2/(1.0-PBARS)
      FR=PA*FRBAR*3.14159265*OR*OR*(PS*PS-PA*PA)*PERMY
      FR=FR/(2.0*VISCE*0.2871*293.0*H*PS*DENSE)
      FR=FR*60.0*10000.0*1000.0
      WRITE(2,29)BEARNO
   29 FORMAT(1PE10.3)
      WRITE(2,1000)W,WBAR
 1000 FORMAT(8H L.C.C.=,1PE20.10,12H N.D.L.C.C.=,1PE20.10)
      WRITE(2,2000)FR,FRBAR
 2000 FORMAT(6H F.R.=,1PE20.10,12H N.D.M.F.R.=,1PE20.10)
      SPRING=(4.0*REVE+2.0*ROD)*BEARNO/(300.0*(PS/PA-1.0))
      WRITE(2,3003)SPRING
 3003 FORMAT(13H STAT.SPRING=,1PE20.10)
      GOTO11
   31 STOP
      END
      FINISH
****
```

COMPUTER PROGRAMME FOR DETERMINING THE STEADY-STATE PRESSURE SQUARED PROFILE IN THE AIR FILM OF A UNIFORM FILM AIR LUBRICATED POROUS THRUST BEARING USING THE NUMERICAL METHOD DEVISED BY D. ROSCOE

```
      MASTER(ROY)
C  PROGRAM FOR FILM PRESSURE DISTRIBUTION FOR
C  UNIFORM FILM AND 100% SUPPLY AREA
C  UNDER STEADY STATE CONDITIONS
      DIMENSION PHI(11,11)
      READ(1,96) H,OR
   96 FORMAT(2E0.0)
      READ(1,3)PS,PA,PERMY
    3 FORMAT(3E0.0)
      PERMY=PERMY/100000.0
      PERMY=PERMY/100000.0
      READ(1,4)AK,DEL,EPSI
    4 FORMAT(3E0.0)
      S=H/OR
      PBAR2=PS*PS/(PA*PA)
      PERMR=PERMY*AK
   41 READ(1,5)FT
    5 FORMAT(E0.0)
      IF(FT.EQ.0.0)GOTO40
      FT=FT/1000.0
      FT=FT*2.54
      BEARNO=12.0*PERMY*OR*OR/(FT*H*(FT*FT + 6.0*PERMR))
      J=1
      DO 6 I=1,11
    6 PHI(I,J)=PBAR2
      J=11
      DO 7 I=1,11
    7 PHI(I,J)=PBAR2 - ((PBAR2 -1.0)*(I-1)/10.0)
      DO 8 J=2,10
      DO 9 I=1,11
    9 PHI(I,J)=PHI(I,1)-((PHI(I,1)-PHI(I,11))*(J-1)/10.0)
    8 CONTINUE
  103 L=0
  100 K=0
   20 N=0
      K=K+1
      DO 10 J=1,11
```

```
      DO 11 I=1,11
      OLD=PHI(I,J)
      IF(J.EQ.1)GOTO77
      IF(I.EQ.1)GOTO12
      IF(I.EQ.11)GOTO13
      IF(J.EQ.11)GOTO14
      B1=1.0/(EXP(1.0/(I-1)))
      B2=S*S*AK/(DEL*(1.0-B1)*DEL*(I-1))
      B3=1.0+B1
      PHI(I,J)=0.1*PHI(I,J)+0.9*((B2*(PHI(I+1,J)+B1*PHI(I-1,J))+(
     1PHI(I,J+1)+PHI(I,J-1))/(DEL*DEL))/(B2*B3+2.0/(DEL*DEL)))
      GOTO16
   77 PHI(I,J)=PBAR2
      GOTO16
   13 IF(J.EQ.11)GOTO17
      PHI(I,J)=PHI(I-1,J)
      GOTO16
   17 PHI(I,J)=1.0
      GOTO16
   12 IF(J.EQ.11)GOTO15
      B1=1.0/(EXP(1.0))
      B2=S*S*AK/(DEL*(1.0-B1)*DEL)
      B3=1.0+B1
      PHI(I,J)=0.1*PHI(I,J)+0.9*((B2*B3*PHI(I+1,J))+(PHI(I,J+1)+PHI(I,J-
     21))/(DEL*DEL))/(B2*B3+2.0/(DEL*DEL))
      GOTO16
   15 A1=1.0/(EXP(1.0))
      A2=1.0/(DEL*(1.0-A1)*DEL)
      A3=1.0+A1
      PHI(I,J)=0.1*PHI(I,J)+0.9*((A2*A3*PHI(I+1,J))+PHI(I,J-1)*BEARNO/
     3DEL)/(A2*A3+BEARNO/DEL)
      GOTO16
   14 A1=1.0/(EXP(1.0/(I-1)))
      A2=1.0/(DEL*(1.0-A1)*DEL*(I-1))
      PHI(I,J)=0.1*PHI(I,J)+0.9*((A2*(PHI(I+1,J)+PHI(I-1,J)*A1)+
     4PHI(I,J-1)*BEARNO/DEL)/((1.0+A1)*A2+BEARNO/DEL))
   16 REM=ABS(OLD-PHI(I,J))
```

```
      IF(REM.EQ.0.0)GOTO19
      PER=REM/OLD
      IF(PER.GE.EPSI)GOTO11
   19 N=N+1
   11 CONTINUE
   10 CONTINUE
      IF(N.LT.121)GOTO98
      J=11
      DO 999 I=1,11
      WRITE(2,999) PHI(I,J)
  999 FORMAT(1PE20.10)
      GOTO41
   98 WRITE(2,111)PHI(6,6),PHI(6,11)
  111 FORMAT(1PE20.10,6X,1PE20.10)
      IF(K.EQ.10)GOTO97
      GOTO20
   97 L=L+1
      WRITE(2,99)N,L
   99 FORMAT(I6,6X,I6)
      IF(L.EQ.5)GOTO101
      GOTO100
  101 J=11
      DO 102 I=1,11
      WRITE(2,102) PHI(I,J)
  102 FORMAT(1PE20.10)
      GOTO103
   40 STOP
      END
      FINISH
****
```

COMPUTER PROGRAMME FOR DETERMINING THE STEADY STATE PERFORMANCE DATA FOR A NON-UNIFORM FILM AIR LUBRICATED POROUS THRUST BEARING USING THE NUMERICAL METHOD DEVISED BY D. ROSCOE

(NON-UNIFORMITY OF FILM DUE TO POROUS PAD FLEXURE CAUSED BY SUPPLY PRESSURE LOADING)

```
      MASTER(ROY)
      DIMENSION A(50),ALAM(50),B(50),CN2(50),PHI(11,11),VAL(50)
      DIMENSION R(11),SL(11),D(11),Z(10,11),X(11),PRESS(11)
C  USING JONES-DARCY THEORY FOR UNIFORM FILM TO SET INITIAL VALUES FOR
C  PRESSURE IN THE PAD AND FILM
      READ(1,3) (A(N),N=1,50)
    3 FORMAT(E0.0)
      READ(1,4) PERMY,AK,PS,PA,H,OR
    4 FORMAT(6E0.0)
      PERMY=PERMY/100000
      PERMY=PERMY/100000
      S=H/OR
      PERMR=PERMY*AK
      PSBAR=PS/PA
      PSBAR2=PSBAR**2
      DEL=0.1
      EPSI=0.0001
      DO 5 N=1,50
      ALAM(N)=S*A(N)*SQRT(AK)
    5 CALL F4J0 (A(N),B(N))
      DO 17 N=1,11
   17 R(N)=(N-1)/10.0
    6 READ(1,7) E
    7 FORMAT(E0.0)
      IF(E.EQ.0.0)GOTO 55
    8 READ(1,9) PO
    9 FORMAT(E0.0)
      IF(PO.EQ.1.0)GOTO6
      DD=E*H*H*H/(12.0*(1.0-(PO*PO)))
      WRITE(2,1002)E,PO,DD
 1002 FORMAT(1PE20.12,6X,1PE20.10,6X,1PE20.10)
   64 READ(1,10) FT
   10 FORMAT(E0.0)
      ROY=1.0
      IF(FT.EQ.0.0)GOTO 8
      FT=FT*2.54/1000.0
```

```
      BEARNO=12.0*PERMY*OR*OR/(FT*H*(FT*FT + 6.0*PERMR))
      SUMEN=0.0
      DO 11 N=1,50
      TERM=ALAM(N)/(A(N)*A(N)*(BEARNO*ALAM(N) + A(N)*A(N)*TANH(ALA
     2M(N))))
   11 SUMEN=SUMEN+TERM
      C2=(PSBAR2 - 1.0)/(BEARNO*BEARNO*SUMEN - BEARNO/8.0 - 1.0)
      DO 12 N=1,50
      CN2(N)=BEARNO*C2/(B(N)*(A(N)*A(N)*TANH(ALAM(N)) + BEARNO*ALAM(N)))
   12 CONTINUE
      J=11
      DO 13 I=1,11
      IF(I.EQ.1)GOTO14
      IF(I.EQ.11)GOTO15
      SUM=0
      DO 16 N=1,50
      CALL F4J0 ((A(N)*R(I)),VAL(N))
      TERM =ALAM(N)*CN2(N)*(B(N)-VAL(N))/(A(N)*A(N))
   16 SUM=SUM+TERM
      PHI(I,J)=1.0+BEARNO*C2*(R(I)*R(I)-1.0)/4.0+BEARNO*SUM
      GOTO13
   15 PHI(I,J)=1.0
      GOTO13
   14 SUM=0.0
      DO 1003 N=1,50
      TERM=ALAM(N)*CN2(N)*(B(N)-1.0)/(A(N)*A(N))
 1003 SUM=SUM+TERM
      PHI(I,J)=1.0-BEARNO*C2/4.0+BEARNO*SUM
   13 CONTINUE
      J=1
      DO 1004 I=1,11
 1004 PHI(I,J)=PSBAR2
      DO 1005 J=2,11
      Y=(J-1)/10.0
      DO 1006 I=1,11
 1006 PHI(I,J)=PHI(I,1)-((PHI(I,1)-PHI(I,11))*Y)
 1005 CONTINUE
      J=11
```

```
      WRITE(2,2000)
 2000 FORMAT(17H PRESSURE PROFILE)
      DO 320 I=1,11
      PRESS(I)=SQRT(PHI(I,J))
      WRITE(2,31)PRESS(I)
   31 FORMAT(1PE20.10)
  320 CONTINUE
      FRBAR=C2/(1.0-PSBAR2)
      WRITE(2,202)
  202 FORMAT(56H BEARING NUMBER   NONDIMEN.LOADCARRY   NONDIMEN.FLOWRATE
     1)
      WRITE(2,201)BEARNO,WBAR,FRBAR
  201 FORMAT(1PE15.7,6X,1PE15.7,6X,1PE15.8)
   32 M=0
      CON1=PS/(2.0*DD)
      SUM=0.0
C USING GAUSS ELIMINATION METHOD IN ORDER TO SOLVE POLYNOMIAL
      DO 300 I=1,10
      DO 301 J=1,10
  301 Z(I,J)=(R(I+1)*OR)**J
      J=11
  300 Z(I,J)=PA*(PRESS(I+1)-PRESS(1))
      I=2
  303 DO 302 M=I,10
      DO 302 N=I,11
  302 Z(M,N)=Z(M,N)-Z(I-1,N)*Z(M,I-1)/Z(I-1,I-1)
      I=I+1
      IF(I-10)303,303,304
  304 DO 305 K=1,9
      X(11-K)=Z(11-K,11)/Z(11-K,11-K)
      DO 305 J=1,10-K
  305 Z(11-K-J,11)=Z(11-K-J,11)-Z(11-K-J,11-K)*X(11-K)
      X(1)=Z(1,11)/Z(1,1)
      I=12
      DO 308 J=1,10
  308 X(I-J)=X(I-(J+1))
      X(1)=PRESS(1)*PA
```

```
      DO 97 I=1,11
      DO 96 J=1,11
      TERM = (X(J)) * (OR**(J+2))*(R(I)-(R(I)**(J+2)))/((((J+2)**2)-1.0)
     9*(J+1))
   96 SUM=SUM+TERM
   97 SL(I)=SUM*1.0/DD+CON1*(OR**3)*((R(I)**3)-R(I))/8.0
      M=0
      DO 95 I=1,10
      SUM=0.0
      OLD=D(I)
      DO 94 J=1,11
      TERM=X(J)*((J+1)-(J+3)*R(I)*R(I)+2.0*(R(I)**(J+3)))*(OR**(J+
     13))/(2.0*((J+2)*(J+2)-1.0)*(J+1)*(J+3))
   94 SUM=SUM+TERM
      D(I)=CON1*(((OR**2)*(1.0-R(I)*R(I)))**2)/32.0-SUM*1.0/DD
      IF(ROY.EQ.1.0)GOTO95
      REM=(OLD-D(I))/10.0
      IF(REM.EQ.0.0)GOTO57
      PER=REM/OLD
      IF(ABS(PER).GT.EPSI)GOTO95
   57 M=M+1
      IF(M.EQ.10)GOTO60
   95 CONTINUE
      D(11)=0.0
      ROY=2.0
C USING ROSCOE TECHNIQUE TO SOLVE NON UNIFORM FILM EQUATIONS
   37 N=0
      DO38 J=2,11
      DO39 I=1,11
      OLD=PHI(I,J)
      IF(I.EQ.1)GOTO40
      IF(I.EQ.11)GOTO41
      IF(J.EQ.11)GOTO42
      BB1=1.0/(EXP(1.0/(I-1)))
      BB2=S*S*AK/(DEL*(1.0-BB1)*DEL*(I-1))
      BB3=1.0+BB1
      PHI(I,J)=0.1*PHI(I,J)+0.9*((BB2*(PHI(I+1,J)+BB1*PHI(I-1,J))+(
```

```
     6PHI(I,J+1)+PHI(I,J-1))/(DEL*DEL))/(BB2*BB3+2.0/(DEL*DEL)))
      GOTO43
   41 IF(J.EQ.11)GOTO44
      PHI(I,J)=PHI(I-1,J)
      GOTO43
   44 PHI(I,J)=1.0
      GOTO43
   40 IF(J.EQ.11)GOTO45
      BB1=1.0/(EXP(1.0))
      BB2=S*S*AK/(DEL*(1.0-BB1)*DEL)
      PHI(I,J)=0.1*PHI(I,J)+0.9*((BB2*(1.0+BB1)*PHI(I+1,J))+(PHI(I,J+1)+
     7PHI(I,J-1))/(DEL*DEL))/(BB2*(1.0+BB1)+2.0/(DEL*DEL))
      GOTO43
   42 FF=FT+D(1)-D(I)
      AD1=H*(FF**3)/(12.0*OR*OR*PERMY)+H*PERMR*FF/(2.0*OR*OR*PERMY)
      AD2=AD1/(DEL*(I-1))+(3.0 *H*FF*FF/(12.0*OR*OR*PERMY)+H*PERMR/(2.0*
     8OR*OR*PERMY))*SL(I)*OR
      BB1=1.0/(EXP(AD2*DEL/AD1))
      BB2=AD2/(DEL*(1.0-BB1))
      BB3=1.0+BB1
      PHI(I,J)=0.1*PHI(I,J)+0.9*((BB2*(PHI(I+1,J)+BB1*PH1(I-1,J))+
     9PHI(I,J-1)/DEL)/(BB2*BB3+1.0/DEL))
      GOTO43
   45 FF=FT+D(1)-D(I)
      AD1=H*((FF)**3)/(12.0*OR*OR*PERMY)+H*PERMR*FF/(2.0*OR*
     1OR*PERMY)
      AD2=AD1/(DEL*I)+(3.0*FF*FF*H/(12.0*PERMY*OR*OR)+PERMR*H/(2.0
     9*PERMY*OR*OR))*SL(I)*OR
      BB1=1.0/(EXP(AD2*DEL/AD1))
      BB2=AD2/(DEL*(1.0-BB1))
      PHI(I,J)=0.1*PHI(I,J)+0.9*(BB2*(1.0+BB1)*PHI(I+1,J)+PHI(I,J-1)/DEL
     2)/(BB2*(1.0+BB1)+1.0/DEL)
   43 REM=ABS(OLD-PHI(I,J))
      IF(REM.EQ.0.0)GOTO46
      PER=REM/OLD
      IF(PER.GT.EPSI)GOTO39
   46 N=N+1
   39 CONTINUE
```

```
 38 CONTINUE
    IF(N.LT.110)GOTO37
    DO 61 N=1,11
    PRESS(N)=SQRT(PHI(N,11))
    WRITE(2,62) N,D(N),PRESS(N)
 62 FORMAT(I3,6X,1PE20.10,6X,1PE20.10)
 61 CONTINUE
    GOTO32
 60 WRITE(2,63)BEARNO,PERMY,AK,OR,H,PS,FT
 63 FORMAT(1PE20.10,6X,1PE20.10,6X,1PE5.2,6X,1PE5.3,6X,1PE6.3,6X,
   21PE5.3,6X,1PE6.4)
    SUM=0.0
    DO 203 I=1,11
    TERM=X(I)*(OR**(I+1))/(I+1)
203 SUM=SUM+TERM
    AWBAR=2.0*(SUM-PA*OR*OR/2.0)/(OR*OR*(PS-PA))
C CALCULATING LOAD AND FLOW USING SIMPSONS RULE
    SUM=0.0
    RODD=0.0
    REVEN=0.0
    DO 200 I=2,10,2
    REVEN=REVEN+(PRESS(I)-1.0)*R(I)
200 RODD=RODD+(PRESS(I+1)-1.0)*R(I+1)
    WBAR=2.0*(4.0*REVEN+2.0*RODD)/(30.00*((PS/PA)-1.0))
    RODD=0.0
    REVEN=0.0
    DO 205 I=2,10,2
    REVEN=REVEN+(PHI(I,1)-PHI(I,2))*R(I)/DEL
205 RODD=RODD+(PHI(I+1,1)-PHI(I+1,2))*R(I+1)/DEL
    LAST=(PHI(11,1)-PHI(11,2))*R(11)/DEL
    RODD=RODD-LAST
    FRBAR=(4.0*REVEN+2.0*RODD+LAST)*2.0/((PSBAR2-1.0)*30.0)
    IF(FRBAR.LE.1.0)GOTO400
    FRBAR=1.0
    WRITE(2,401)
401 FORMAT(20H INCORRECT FLOW CALC)
400 WRITE(2,206)
```

```
  206 FORMAT(9H      NDLC,15X,5H NDFR)
      WRITE(2,204)WBAR,FRBAR,AWBAR
  204 FORMAT(1PE15.7,6X,1PE15.7,6X,1PE15.7)
      GOTO6
   55 STOP
      END
      FINISH
****
```

COMPUTER PROGRAMME FOR DETERMINING THE DYNAMIC CHARACTERISTICS OF A UNIFORM FILM AIR LUBRICATED POROUS THRUST BEARING USING A COMBINATION OF NUMERICAL METHODS

(BEARING ASSUMED TO HAVE LINEAR CHARACTERISTICS)

```
      MASTER
      DIMENSION A(50),ALAM(50),B(50),EN(50),V(50),PHI(11,11,19)
      DIMENSION P(11),R(11),BE(11),G(11),OLD(11,11,19)
      DIMENSION CON(50),Y(11),CYN(11,11,19)
      DIMENSION THIA(18),PHASE(10),PERT(10)
C USING JONES DARCY THEORY TO SET INITIAL VALUES FOR FILM PRESSURE
      SINH(X)=(EXP(X)-(1./EXP(X)))/2.
      COSH(X)=(EXP(X)+(1./EXP(X)))/2.
      DAG=0.0
      READ(3,*) (A(N),N=1,50)
      READ(1,*)H,OR,PS,PA,PERMY,AK
      IF(AK.EQ.0.0)GOTO 7
      PERMY=PERMY*1.E-10
      PB=PS/PA
      PB2=PB**2
      S=H/OR
      PERMR=PERMY*AK
      DO 8 N=1,50
      ALAM(N)=S*A(N)*SQRT(AK)
    8 B(N)=S17AAF(A(N))
      READ(1,*)FT
      FT=FT*2.54/1000.0
      POR=0.0908
  999 READ(1,*)FREQ,EPSI
      IF(FREQ.EQ.0.0)GOTO7
      FREQ=FREQ*2.0*3.14159265
      IF(DAG.EQ.1.0)GOTO998
      DEL=0.1
      DET=1.0/18.0
      ERR=0.001
      RHO=DEL*DEL/DET
      VISC=0.01812
      BEARNO=12.0*PERMY*OR*OR/(H*FT*(FT*FT + 6.0*PERMR))
      SUMEN=0.0
      DO 11 N=1,50
      EN(N)=ALAM(N)/(A(N)*A(N)*(BEARNO*ALAM(N)+A(N)*A(N)*TANH(ALAM(N))))
   11 SUMEN=SUMEN + EN(N)
```

```
      C2=(PB2 - 1.0)/(BEARNO*BEARNO*SUMEN - BEARNO/8.0 - 1.0)
      DO 12 N=1,50
   12 CON(N)=BEARNO*C2/(B(N)*(A(N)*A(N)*TANH(ALAM(N))+BEARNO*ALAM(N)))
  998 WRITE(2,154)
  154 FORMAT(17H PRESSURE PROFILE,5X,17H PRESSURE SQUARED)
      DO 17 I=1,11
   17 PHI(I,1,1)=PB2
      DO 16 I=1,11
      R(I)=((I*1.0)-1.0)/10.0
      DO 16 J=2,11
      Y(J)=((J*1.0)-1.0)/10.0
      SUM=0.0
      DO 15 N=1,50
      V(N)=S17AAF(R(I)*A(N))
      TERM=CON(N)*SINH(ALAM(N)*Y(J))*V(N)/COSH(ALAM(N))
   15 SUM=SUM+TERM
   16 PHI(I,J,1)=PB2+C2*Y(J)+SUM
      DO 14 I=1,11
      P(I)=SQRT(PHI(I,11,1))
      WRITE(2,13)P(I),PHI(I,11,1)
   13 FORMAT(1PE15.6,6X,1PE15.6)
   14 CONTINUE
C CALCULATING STEADY STATE LOAD AND FLOW VALUES
      RODD=0.0
      REVEN=0.0
      DO 147 I=2,10,2
      REVEN=REVEN+(P(I)-1.0)*R(I)
  147 RODD=RODD+(P(I+1)-1.0)*R(I+1)
      WBAR=2.0*(4.0*REVEN+2.0*RODD)/(30.0*((PS/PA)-1.0))
      FRBAR=C2/(1.0-PB2)
      WRITE(2,153)
  153 FORMAT(7H  THICK,19X,3H OR,12X,3H PS,19X,6H PERMY,15X,3H FT)
      WRITE(2,148)H,OR,PS,PERMY,FT
  148 FORMAT(1P5E21.6)
      WRITE(2,152 )
  152 FORMAT(9H      WBAR,16X,6H FRBAR)
      WRITE(2,149)WBAR,FRBAR
```

```
  149 FORMAT(1P2E21.6)
C ASSUMING PRESSURE TO BE 180 DEG OUT OF PHASE WITH FILM THICKNESS IN
C ORDER TO SET
C INITIALTIME VALUES USING A PRESSURE PERTABATION EQUAL TO ONE TENTH
C OF AN ATMOS
      DO 119 M=1,19
      DO 119 J=1,11
      DO 119 I=1,11
      PHI(I,J,M)=PHI(I,J,1)+ SIN((M-1)*2.0*3.1415926536/10.0)*0.1
  119 CYN(I,J,M)=PHI(I,J,M)
      WRITE(2,100)
  100 FORMAT(26H ENTERING NUMERICAL METHOD)
C
C     USING ROSCOE TECHNIQUE IN CONJUNCTION WITH ALTERNATING DIRECTION
C     IMPLICIT METHOD TO SOLVE COMPRESSIBLE EQUATIONS
C
      IF(DAG.EQ.1.0)GOTO997
  301 READ(1,*)REL
  997 DO 42 M=1,19
      DO 42 J=2,11
      DO 42 I=1,11
      PHI(I,J,M)=CYN(I,J,M)
   42 OLD(I,J,M)=PHI(I,J,M)
      K=0
      L=0
      ALPHA=POR*VISC*H*H*FREQ/(PERMY*PA)*1.E-8
   41 M=1
      L=L+1
      N=0
      K=K+1
   37 M=M+1
      FF=FT+EPSI*SIN((M-1)*DET*2.0*3.14159265)
      BEARNO= 12.0*PERMY*OR*OR/(H*FF*(FF*FF + 6.0*PERMR))
      BETA= 12.0*OR*OR*VISC*FREQ/(PA*(FF*FF + 6.0*PERMR))*1.E-8
      GAMMA=24.0*VISC*OR*OR*EPSI*FREQ*COS((M-1)*DET*2.0*3.14159265)
     6/(PA*(FF*FF + 6.0*PERMR)*FF)*1.E-8
      J=1
```

```
23 J=J+1
   I=0
20 I=I+1
   IF(I.EQ.11)GOTO 21
   IF(I.GT.1)GOTO 19
   W=RHO*ALPHA/(SQRT(PHI(I,J,M)))+ S*S*AK*(1.0+1.0/(EXP(1.0)))/(1.0-
  51.0/(EXP(1.0)))
   W=W*(-1.0)
   BE(I)= S*S*AK*(1.0+1.0/(EXP(1.0)))/(W*(1.0-1.0/(EXP(1.0))))
   G(I)=((2.0-RHO*ALPHA/(SQRT(PHI(I,J,M))))*PHI(I,J,M-1)-(PHI(I,J+1,
  4M-1)+PHI(I,J-1,M-1)))/W
   GOTO 20
19 BO=-(S*S*AK*(1.0+1.0/(EXP(1.0/(I-1))))/((I-1)*(1.0-1.0/(EXP(1.0/
  3(I-1))))) + RHO*ALPHA/(SQRT(PHI(I,J,M))))
   CO=S*S*AK/((I-1)*(1.0-1.0/(EXP(1.0/(I-1)))))
   AO=CO*EXP((-1.0/(I-1)))
   DON=(2.0- RHO*ALPHA/(SQRT(PHI(I,J,M))))*PHI(I,J,M-1)-(PHI(I,J+1,
  9M-1)+PHI(I,J-1,M-1))
   W=BO- AO*BE(I-1)
   G(I)=(DON- AO* G(I-1))/W
   BE(I)=CO/W
   GOTO 20
21 AO=S*S*AK*(1.0+1.0/(EXP(1.0/(I-1))))/((I-1)*(1.0-1.0/(EXP(1.0/(I-1
  8)))))
   BO=-(AO+ RHO*ALPHA/(SQRT(PHI(I,J,M))))
   DON=(2.0-RHO*ALPHA/(SQRT(PHI(I,J,M))))*PHI(I,J,M-1)-(PHI(I,J+1,M-1
  6)+PHI(I,J-1,M-1))
   W=BO- AO*BE(I-1)
   G(I)=(DON-AO*G(I-1))/W
   PHI(I,J,M)=G(I)*REL + (1.0-REL)*OLD(I,J,M)
22 I=I-1
   PHI(I,J,M)=(G(I)- BE(I)*PHI(I+1,J,M))*REL+(1.0-REL)*OLD(I,J,M)
   IF(I.GT.1)GOTO22
   IF(J.EQ.10)GOTO24
   GOTO23
24 J=J+1
   CO=(1.0+1.0/(EXP(1.0)))/(1.0-1.0/(EXP(1.0)))
   W=-(CO+BETA*RHO/(SQRT(PHI(I,J,M))))
```

```
      BE(I)=CO/W
      G(I)=(DEL*BEARNO*(PHI(I,J,M-1)-PHI(I,J-1,M-1))-PHI(I,J,M-1)*
     9BETA*RHO/(SQRT(PHI(I,J,M)))+DEL*DEL*GAMMA*SQRT(PHI(I,J,M-1)))/W
   25 I=I+1
      DON=DEL*BEARNO*(PHI(I,J,M-1)-PHI(I,J-1,M-1))-PHI(I,J,M-1)*
     8BETA*RHO/(SQRT(PHI(I,J,M)))+DEL*DEL*GAMMA*SQRT(PHI(I,J,M-1))
      CO=1.0/((I-1)*(1.0-1.0/(EXP(1.0/(I-1)))))
      BO=-(CO*(1.0+1.0/(EXP(1.0/(I-1))))+BETA*RHO/(SQRT(PHI(I,J,M))))
      AO=CO*1.0/(EXP(1.0/(I-1)))
      W=BO-AO*BE(I-1)
      BE(I)=CO/W
      G(I)=(DON-AO*G(I-1))/W
      IF(I.LT.10)GOTO25
      I=I+1
      PHI(I,J,M)=1.0
   26 I=I-1
      PHI(I,J,M)=(G(I)-BE(I)*PHI(I+1,J,M))*REL+(1.0-REL)*OLD(I,J,M)
      IF(I.GT.1)GOTO26
      M=M+1
      FF=FT+EPSI*SIN((M-1)*DET*2.0*3.14159265)
      BEARNO=12.0*PERMY*OR*OR/(H*FF*(FF*FF+ 6.0*PERMR))
      BETA=12.0*OR*OR*VISC*FREQ/(PA*(FF*FF+ 6.0*PERMR))*1.E-8
      GAMMA=24.0*VISC*OR*OR*EPSI*FREQ*COS((M-1)*DET*2.0*3.14159265
     4)/(PA*(FF*FF+ 6.0*PERMR)*FF)*1.E-8
      I=0
   31 I=I+1
      J=1
   29 J=J+1
      IF(I.GT.1)GOTO27
      IF(J.GT.2)GOTO28
      ROY=S*S*AK*(1.0+1.0/(EXP(1.0)))/(1.0-1.0/(EXP(1.0)))
      DON=(ROY-RHO*ALPHA/(SQRT(PHI(I,J,M))))*PHI(I,J,M-1)-ROY*PHI(I+1,J,
     3M-1)
      BO=-(2.0+RHO*ALPHA/(SQRT(PHI(I,J,M))))
      W=BO
      BE(J)=1.0/W
      G(J)=(DON-PB*PB)/W
```

```
      GOTO29
   28 ROY=S*S*AK*(1.0+1.0/(EXP(1.0)))/(1.0-1.0/(EXP(1.0)))
      DON=(ROY-RHO*ALPHA/(SQRT(PHI(I,J,M))))*PHI(I,J,M-1)-ROY*PHI(I+1,J,
     9M-1)
      BO=-(2.0+RHO*ALPHA/(SQRT(PHI(I,J,M))))
      W=BO-BE(J-1)
      G(J)=(DON-G(J-1))/W
      BE(J)=1.0/W
      IF(J.LT.10)GOTO29
      J=J+1
      AO=-(BEARNO*DEL)
      ROY=(1.0+1.0/(EXP(1.0)))/(1.0-1.0/(EXP(1.0)))
      DON=ROY*PHI(I+1,J,M-1)-(ROY-BETA*RHO/(SQRT(PHI(I,J,M)))+DEL*DEL*
     7GAMMA/(SQRT(PHI(I,J,M-1))))*PHI(I,J,M-1)
      BO=DEL*BEARNO+BETA*RHO/(SQRT(PHI(I,J,M)))
      G(J)=(DON-AO*G(J-1))/(BO-AO*BE(J-1))
      PHI(I,J,M)=G(J)*REL+(1.0-REL)*OLD(I,J,M)
   30 J=J-1
      PHI(I,J,M)=(G(J)-BE(J)*PHI(I,J+1,M))*REL+(1.0-REL)*OLD(I,J,M)
      IF(J.GT.2)GOTO30
      GOTO31
   27 IF(I.EQ.11)GOTO32
      IF(J.GT.2)GOTO33
      W=-(2.0+RHO*ALPHA/(SQRT(PHI(I,J,M))))
      ROY=S*S*AK/((I-1)*(1.0-1.0/(EXP(1.0/(I-1)))))
      DON=(ROY*(1.0+1.0/(EXP(1.0/(I-1))))-RHO*ALPHA/(SQRT(PHI(I,J,M))))*
     7PHI(I,J,M-1)-ROY*(PHI(I+1,J,M-1)+PHI(I-1,J,M-1)/(EXP(1.0/(I-1))))
      BE(J)=1.0/W
      G(J)=(DON-PB*PB)/W
      GOTO 29
   33 BO=-(2.0+RHO*ALPHA/(SQRT(PHI(I,J,M))))
      ROY=S*S*AK/((I-1)*(1.0-1.0/(EXP(1.0/(I-1)))))
      DON=(ROY*(1.0+1.0/(EXP(1.0/(I-1))))-RHO*ALPHA/(SQRT(PHI(I,J,M))))*
     6PHI(I,J,M-1)-ROY*(PHI(I+1,J,M-1)+PHI(I-1,J,M-1)/(EXP(1.0/(I-1))))
      BE(J)=1.0/(BO-BE(J-1))
      G(J)=(DON-G(J-1))/(BO-BE(J-1))
      IF(J.LT.10)GOTO29
```

```
      J=J+1
      AO=-(BEARNO*DEL)
      ROY=1.0/((1.0-1.0/(EXP(1.0/(I-1))))*(I-1))
      DON=ROY*(PHI(I+1,J,M-1)+PHI(I-1,J,M-1)/(EXP(1.0/(I-1))))-(ROY*(1.0
     6+1.0/(EXP(1.0/(I-1))))-BETA*RHO/(SQRT(PHI(I,J,M)))+DEL*DEL*GAMMA/(
     6SQRT(PHI(I,J,M-1))))*PHI(I,J,M-1)
      BO=DEL*BEARNO+BETA*RHO/(SQRT(PHI(I,J,M)))
      G(J)=(DON-AO*G(J-1))/(BO-AO*BE(J-1))
      PHI(I,J,M)=G(J)*REL+(1.0-REL)*OLD(I,J,M)
   34 J=J-1
      PHI(I,J,M)=(G(J)-BE(J)*PHI(I,J+1,M))*REL+(1.0-REL)*OLD(I,J,M)
      IF(J.GT.2)GOTO34
      GOTO31
   32 IF(J.GT.2)GOTO35
      BO=-(2.0+RHO*ALPHA/(SQRT(PHI(I,J,M))))
      ROY=S*S*AK*(1.0+1.0/(EXP(1.0/(I-1))))/((I-1)*(1.0-1.0/(EXP(1.0/(I-
     41)))))
      DON=(ROY-RHO*ALPHA/(SQRT(PHI(I,J,M))))*PHI(I,J,M-1)-ROY*PHI(I-1,J,
     9M-1)
      W=BO
      G(J)=(DON-PB*PB)/W
      BE(J)=1.0/W
      GOTO29
   35 BO=-(2.0+RHO*ALPHA/(SQRT(PHI(I,J,M))))
      ROY=S*S*AK*(1.0+1.0/(EXP(1.0/(I-1))))/((I-1)*(1.0-1.0/(EXP(1.0/(I-
     81)))))
      DON=(ROY-RHO*ALPHA/(SQRT(PHI(I,J,M))))*PHI(I,J,M-1)-ROY*PHI(I-1,J,
     7M-1)
      W=(BO-BE(J-1))
      G(J)=(DON-G(J-1))/W
      BE(J)=1.0/W
      IF(J.LT.10)GOTO29
      J=J+1
      PHI(I,J,M)=1.0
   36 J=J-1
      PHI(I,J,M)=(G(J)-BE(J)*PHI(I,J+1,M))*REL+(1.0-REL)*OLD(I,J,M)
      IF(J.GT.2)GOTO 36
```

```
      IF(M.LT.19)GOTO37
      DO 38 M=1,19
      DO 38 J=2,11
      DO 38 I=1,11
      PER=(PHI(I,J,M)-OLD(I,J,M))/(OLD(I,J,M))
      IF(ABS(PER).GT.ERR)GOTO38
      N=N+1
      IF(N.EQ.2090)GOTO40
   38 OLD(I,J,M)=PHI(I,J,M)
   47 DO 39 I=1,11
      DO 39 J=2,11
   39 PHI(I,J,1)=PHI(I,J,19)
      GOTO 41
   40 WRITE(2,48)
   48 FORMAT(18H SOLUTION OBTAINED)
      DO 50 M=1,19
      WRITE(2,49) (PHI(I,11,M),I=1,11)
   49 FORMAT(11F8.4)
   50 CONTINUE
      DO 200 I=1,10
      DO 201 M=1,18
  201 THIA(M)=SQRT(PHI(I,11,M))
      SUM1=0.0
      SUM2=0.0
      SUM3=0.0
      DO 203 M=1,18
      SUM1=SUM1+THIA(M)
      SUM2=SUM2+THIA(M)*COS((M-1)*DET*2.0*3.14159265)
  203 SUM3=SUM3+THIA(M)*SIN((M-1)*DET*2.0*3.14159265)
      01=SUM1/18.0
      04=-ATAN(SUM2/SUM3)
      02=SUM2/(SIN(04)*9.0)
      03=04*57.2957795
      WRITE(2,204)01,02,03,R(I)
  204 FORMAT(7H PMEAN=,1PE15.6,6H PERT=,1PE15.6,7H PHASE=,1PE15.6,3H R=,
     91PE15.6)
      PHASE(I)=04
```

```
  200 PERT(I)=02
      SUM1=0.0
      SUM2=0.0
      SUM3=0.0
      SUM4=0.0
      DO 205 I=2,10,2
      TERM1=PERT(I-1)*COS(PHASE(I-1))*R(I-1)
      TERM2=PERT(I)*COS(PHASE(I))*R(I)
      TERM3=PERT(I-1)*SIN(PHASE(I-1))*R(I-1)
      TERM4=PERT(I)*SIN(PHASE(I))*R(I)
      SUM1=SUM1+TERM1
      SUM2=SUM2+TERM2
      SUM3=SUM3+TERM3
  205 SUM4=SUM4+TERM4
      DAMP=2.0*(4.0*SUM4+2.0*SUM3)/30.0
      SPRING=2.0*(4.0*SUM2+2.0*SUM1)/30.0
      WRITE(2,206)DAMP,SPRING
  206 FORMAT(6H DAMP=,1PE15.6,8H SPRING=,1PE15.6)
      BETAMAX=12.0*OR*OR*VISC*FREQ/(PA*(FT*FT+6.0*PERMR))*1.E-8
      GAMAX=2.0*EPSI*BETAMAX/FT
      BETAMAX=GAMAX/BETAMAX
      WRITE(2,302)ALPHA,GAMAX,BETAMAX
  302 FORMAT(7H ALPHA=,1PE15.6,3X,7H GAMAX=,1PE15.6,3X,15H GAMAX/BETAMAX
     9=,1PE15.6)
      FIN=SQRT(((WBAR*OR*OR*3.14159265*(PS-PA)*EPSI*FREQ*FREQ/98.0665
     9-SPRING*2.0*3.14159265*OR*OR*PA*10.0)**2)+(DAMP*2.0*3.14159265*OR*
     9OR*PA*10.0)**2)
      CSPRING=SPRING*2.0*3.14159265*PA*OR*OR*10.0/FIN
      CDAMP=DAMP*2.0*3.14159265*PA*OR*OR*10.0/FIN
      WRITE(2,303)CSPRING,CDAMP
  303 FORMAT(4H FK=,1PE15.6,4H FD=,1PE15.6)
      DAG=1.0
      GOTO929
    7 STOP
      END
      FINISH
****
```

APPENDIX EIGHT

PUBLISHED WORK

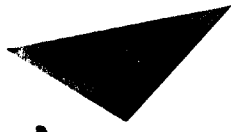

Aston University

Content has been removed for copyright reasons

Aston University

Content has been removed for copyright reasons